2013

GRAPHENE-BASED SEMICONDUCTOR AND METALLIC NANOSTRUCTURED MATERIALS

Abdallah Zedan
Virginia Commonwealth University

GRAPHENE-BASED SEMICONDUCTOR AND METALLIC NANOSTRUCTURED MATERIALS

A dissertation submitted in partial fulfillment of the requirements for the degree of Doctor of Philosophy at Virginia Commonwealth University

by

Abdallah F. Zedan

M.S. Cairo Univ. 2008

Director: M. Samy El-Shall

Professor of Physical Chemistry, Chemistry Department

Virginia Commonwealth University

Richmond, Virginia

May 2013

ACKNOWLEDGMENTS

First, I am grateful to Allah the Exalted and Mighty lord for his mercy, blessings, and gratitude. I always seek his guidance, kindness and forgiveness in this life and in the hereafter. It is my pleasure to acknowledge my research advisor Dr. Samy El-Shall who kindly gave me the opportunity to continue my graduate studies and earn my Ph.D. under his supervision. I acknowledge him for all advices he gave me to solve my research problems. I am grateful for his significant contribution in advancing our research projects and communications. I truly thank him for his time, valuable inputs and the continuous support and help. Many thanks to my advising committee, Dr. James Terner, Dr. Sally Hunnicutt, Dr. Hani El-Kaderi and Dr. Massimo Bertino, for their valuable feedback during the course of my study. I acknowledge Dr. Terner for his collaboration with the Raman measurements. I thank Dr. Hunnicutt for the education skills I learnt from her during the physical chemistry laboratory. I also thank Dr. El-Kaderi for his kind encouragements and I acknowledge Dr. Bertino for his assistance with some TEM measurements. Special thanks to Dr. Sherif Moussa for his collaboration and contribution during our joint research projects. I thank all my colleagues from El-Shall's research group for their help in the laboratory and for the useful discussions I had with them. I thank Natalie Herring for her assistance with some TEM and SAED measurements. I would like also to thank Dr. Dmitry Pestov in nanocharacterization center for his assistance with SEM and XPS measurements and Dr. Joseph Turner in the instrumental facility for his help. I take this opportunity to thank the VCU community

and the Department of Chemistry for the valuable education I have received and for the whole experiences, I learnt. I also acknowledge the National Institute of Laser Enhanced Science for granting me a leave of absence so I could come here to the United States and learn. On a personal note, I owe deep thanks, acknowledgements, appreciations and love to my parents, my parents in law, my wife, my two daughters Rehab and Alzahraa, my son Moaaz, my brothers, my sisters and my all my friends.

TABLE OF CONTENTS

LIST OF TABLES

List of Figures

ABSTRACT

GRAPHENE-BASED SEMICONDUCTOR AND METALLIC NANOSTRUCTURED MATERIALS

By Abdallah F. Zedan, Ph.D.

A dissertation submitted in partial fulfillment of the requirements for the degree of Doctor of Philosophy at Virginia Commonwealth University.

Virginia Commonwealth University, 2013

Director: M. Samy El-Shall, Professor of Physical Chemistry, Chemistry Department

Exciting periods of scientific research are often associated with discoveries of novel materials. Such a period was brought about by the successful preparation of graphene, which is a 2D allotrope of carbon with remarkable electronic, optical and mechanical properties. Functional graphene-based nanocomposites have great promise for applications in various fields such as energy conversion, opteoelectronics, solar cells, sensing, catalysis and biomedicine. Herein, microwave and laser-assisted synthetic approaches were developed for decorating graphene with various semiconductor, metallic or magnetic nanostructures of controlled size and shape. We developed a scalable microwave irradiation method for the synthesis of graphene decorated with CdSe nanocrystals of controlled size, shape and crystalline structure. The efficient quenching of photoluminescence from the CdSe nanocrystals by graphene has been explored. The results provide a new approach for exploring the size-tunable optical properties of CdSe nanocrystals supported on graphene, which could have important implications for energy conversion

applications. We also extended this approach to the synthesis of Au-ceria-graphene nanocomposites. The synthesis is facilely conducted at mild conditions using ethylenediamine as a solvent. Results reveal significant conversion percentages up to 60-70% of CO to CO_2 at ambient temperatures. Gold nanostructures have received significant attention because of the feasibility to tune their optical properties by changing size or shape. The coupling of the photothermal effects of these gold nanostructures of controlled size and shape with graphene oxide nanosheets dispersed in water is demonstrated. Our results indicate that the enhanced photothermal energy conversion of the gold-graphene oxide suspensions could to lead to a remarkable increase in the heating efficiency of the laser-induced melting and size reduction of Au nanostructures. The gold-graphene nanocomposites could have potential in photothermolysis, thermochemical and thermomechanical applications. We developed a facile method for decorating graphene with magnetite nanocrystals of various shapes (namely, spheres, cubes and prisms) by the microwave-assisted-reduction of iron acetylacetonate in benzyl ether. The shape control was achieved by tuning the molar ratio between the oleic acid and the oleyamine. The structural, morphological and physical properties of graphene-based nanocomposites described herein were studied using standard characterization tools such as TEM, SEM, powder X-ray diffraction, XPS and Raman spectroscopy.

CHAPTER 1 INTRODUCTION

1.1 Overview

The most exciting and fruitful periods of scientific research are often associated with discoveries of novel materials that introduce opportunities to revisit and create scientific challenges. Such a period was realized by the discovery of free-standing graphene in 2004.[1] Graphene is a two-dimensional (2D) allotrope of crystalline carbon. Its remarkable intrinsic features and electronic properties give graphene a great deal of research interest in the present and the future. Despite its short history, graphene has already revealed a plethora of new physical and chemical properties to explore along with a cornucopia of potential applications in many technological fields such as nanocomposites, nanoelectronics, sensors, batteries, supercapacitors and hydrogen storage.[2] Graphene-related investigations ranging from fundamental studies to practical devices utilization have been the focus of many research communities from different disciplines. Chemists are busily working on developing new routes to synthesize processable graphene. Physicists are trying to understand and implement the new graphene's properties and phenomena. Engineers are designing novel devices to exploit graphene's extraordinary properties and biologists are working to introduce graphene into biomedical diagnoses and treatments. The existence of such intensive research and wide spread collaborations makes the future of graphene extremely bright.

1.2 Dissertation Outline

This dissertation is focused on the synthesis of functional graphene-based nanocomposites of great promise for applications in energy conversion and storage, opteoelectronics, catalysis and biomedicine. The different chapters in the dissertation are designed in a bottom-up writing approach. The next section in this chapter begins with brief background and literature review on graphene and different classes of nanostructures that is necessary for understanding subsequent sections. Then the statement of research problem is described followed by the objectives of our work. Chapter 2 presents a brief description of the physical techniques used for characterization and studying the properties of our graphene-based nanostructured materials. In chapter three, we describe a microwave irradiation method for decorating graphene with CdSe nanocrystals of controlled size, shape, and crystalline structure. Direct evidence for the quenching of photoluminescence from the CdSe nanocrystals by graphene and the important implications in energy conversion are discussed.

Research in nanocatalysis aims at designing superior nanostructured catalysts that are essential for many technological advances in chemical synthesis and processing, environmental detoxification and improving air quality. Chapter 4 details the ethylenediamine-assisted synthesis of Au-ceria-graphene nanocomposites and their use as heterogeneous catalysts for the low-temperature CO catalytic oxidation. Noble metal nanoparticles have received significant attention for decades because of the feasibility to tune their electronic and optical properties by changing size, shape, composition or dielectric environment. Chapter 5 begins with a section that details the seed-mediated method employed here to develop Au nanostructures of various shapes such as rods, cubes and bipyramids. Next, the coupling of the photothermal effects of these Au nanostructures of controlled size and shape with GO nanosheets dispersed in water is described. The chapter

emphasizes on the enhanced photothermal energy conversion of the Au-GO suspensions and the laser-induced melting of Au nanostructures.

The interest in magnetic nanostructures and their composite materials, with a special emphasis on magnetite, has increased over years owing to their potential applications in electronics, optoelectronics, data storage industries, catalysis and biomedicine. Chapter 6 describes our microwave synthesis of bifunctional magnetite-CdSe nanocomposites. Evidence for dual optical-magnetic properties are presented. In chapter 7, a general microwave-based strategy for decorating graphene with magnetite nanocrystals of various shapes (namely, spheres, cubes and prisms) is outlined. The magnetic properties are compared for different shapes with and without graphene and finally the dissertation is ended with bibliography and vita.

1.3 Background

Prior to 2004, it was generally accepted that as the thickness of a thin film decreases to dozens of atomic layers, the melting temperature rapidly decreases and the thin film becomes thermodynamically unstable. The tendency of very thin films to segregate into islands or decompose requires that they become integrated as a part of three-dimensional (3D) structure or stabilized by a supporting base with matching crystal lattices.[3] Accordingly, 2D crystals of a single atomic plane were presumed not to exist and their growth was thought to be unfavorable, essentially because the growth implies high temperature and therefore thermal fluctuations, which are detrimental to 1D and 2D structures. The presumption continued until 2004 when the free-standing graphene was unexpectedly isolated [1, 4] and confirmed after several follow-up experiments.[5, 6] Since then, the model came into reality and 2D crystals could be obtained on top of non-crystalline substrates, in liquid suspension, and as suspended membranes.[3] Before discussing the earlier work on graphene, it is useful to review the structure and properties of

graphite, the well-known graphene bulk counterpart. Graphite is a naturally occurring, abundant and low-cost mineral. It consists of parallel stacked sheets of graphene layers bonded together by weak van der Waals forces. The most two common types of graphite are the highly oriented pyroelectric graphite (HOPG) and *Kish* graphite. HOPG is synthetic graphite formed by cracking a hydrocarbon at high temperature and subsequent heat treatment that is often combined with high pressure. HOPG is highly oriented along the *c*-axis but less ordered in the in-plane layers. It has been used the most as host material for graphite intercalation compounds (GIC). Kish graphite is obtained by the crystallization of carbon from molten steel during steel manufacturing process. Typical Kish graphite exhibits much higher structural ordering than HOPG, but less ordering and chemical purity than natural single crystal flakes. [7] The layered morphology and the weak dispersion forces between adjacent sheets allow layers to move easily over one another, making graphite ideal for use in dry lubricants. Also its high electrical and thermal conductivity led to the use of graphite in electrodes and heating elements for industrial blast furnaces. Moreover, the high mechanical strength enabled its use in carbon fiber reinforced composites. **Figure 1.1** shows the layered structure of graphite, which accounts for many of its physical properties.

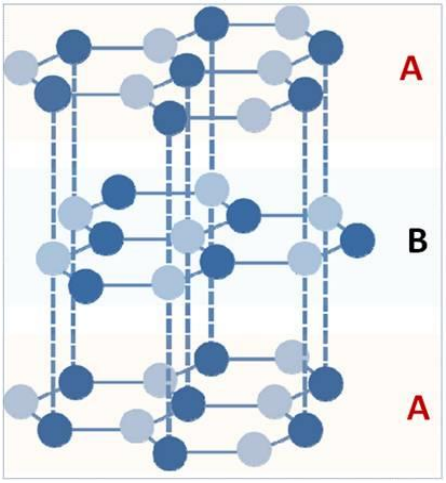

Figure 1-1 Lattice structure of graphite showing ABA stacking arrangement (modified from [8]).

In graphitic layers, each carbon atom adopts three of the four outer energy level electrons to form strong covalent σ bonds to three neighbor carbons in the same basal plane. The resulting strong intraplanar interactions give rise to an extended stiff hexagonal lattice structure. The fourth valence electron on each carbon atom contributes to a delocalized system of electrons that is also a part of the chemical bonding. These delocalized electrons are free to move throughout the plane, so graphite conducts charge and thermal carriers to a greater extent along the basal planes of carbon atoms. The forces of interactions in graphite crystal are highly anisotropic in such a way that the binding forces within the basal planes (intralayer interactions) are much stronger than those at right angle to the basal planes (interlayer interactions). Extended planes in graphite are held by relatively weak attractive forces leading to weak interplanar interactions. The lack of covalent bonding at right angles to the plane and the relatively large interlayer spacing make the propagation of charge or thermal carriers along the *c*-direction extremely weak. Accordingly, the out-of-plane electrical and thermal conductivity are more than one-thousand times lower than the corresponding in-plane counterparts which makes the resistivity in a direction perpendicular to graphitic sheets much greater than parallel to the basal planes. As a result, the electrical conductivity is different where it ranges from insulating behavior in the *c*-axis direction to superconducting in the in-plane direction. [7]

As in metals, parallel electrical resistivity increases with the temperature because of the decreased electron mean free path and the increased electron-phonon interactions that take over the increase in the carrier density. However, the perpendicular electrical resistivity decreases slightly with increasing temperature, possibly because electrons can jump or tunnel from one plane to another due to increased thermal activation.[9] While the inner symmetric 1s orbital in carbon is greatly bound with an energy that is far from the Fermi level, the four valence electrons *2s*, $2p_x$,

$2p_y$ and $2p_z$ have similar energies making their wavefunctions mix easily and facilitating hybridization. This feasibility of hybridization allows carbon to form structures with different geometries such as 3D, 2D, 1D and 0D galleries.[10] Graphite, for example, exhibits sp^2 type hybridization, where *s*, p_x, and p_y atomic orbitals on each carbon atoms hybridize to form strong sp^2 covalent bonds. The remaining p_z orbital overlaps with its three neighbors to form a band of filled π-orbitals (VB) and a band of empty π*-orbitals (CB).

The comparable strength of electron affinity and ionization potential of graphite (4.6 eV) enable graphite to participate in reactions either as an electron donor or acceptor which enriches its chemistry in a great way. The weak attractive force between successive layers in graphite allows the insertion of guest atoms, ions or molecules between the adjacent layers and graphite structures with such galleries are known as graphite intercalation compounds (GIC). These GIC are prepared by the incorporation of atomic or molecular layers of a different chemical species (intercalants) between layers in graphite (host). The strong intraplanar binding along with the weak interplanar binding causes the layers of graphite and intercalants to stay separate. Thus graphite layers in GIC retain the basic properties of pristine graphite and intercalate layers behave similarly to the parent intercalate material. Nevertheless, an expansion along the *c*-axis is observed due to the intercalation.[7] Intercalation in this way allows tuning many physical properties of the host material over a vast range. For example, the intercalation of different chemical species with different densities allows tuning the charge carrier concentration in graphite and thus modulating the electrical or thermal conductivities. Since charge carriers have low mobility in intercalate layers, but extremely high mobility in graphite layers, increasing the concentration of donor or acceptor intercalates leads to a large increase in the in-plane conductivity due to the charge transfer from intercalates to π-electron system in graphite.[7] Reagents that can be intercalated into graphite

include donor or acceptor species. Donor intercalants are typically K, Li, and Cs, whereas acceptor compounds are often based on Lewis acids such as Br_2 and SO_3 or strong Bronsted acids such as H_2SO_4 and HNO_3. The probability of a given chemical species to intercalate depends on the chemical affinities and geometric constraints such as intercalant size or bonding distances.[7]

1.4 Two dimensional graphene: the parent of sp^2 carbon materials

In the past few years, graphene has been profiled as a rapidly rising star on the horizon of materials science and condensed matter physics. Graphene is a flat single layer of $\boldsymbol{sp^2}$-hybridized carbon atoms tightly packed into a 2D honeycomb lattice. Since its first isolation, the status of graphene has changed from being an unexpected newcomer to a rising champion.[3] The importance of graphene has become evident even though commercial products have not appeared. Graphene show electronic properties which are extremely remarkable where charge carriers can travel thousands of interatomic distances before they scatter.[1, 4-6] In the extended carbon network of 2D graphene, adjacent carbon atoms are bonded together with strong covalent interactions and have in-plane nearest neighbor ($a_{c\text{-}c}$) distances of 0.142 nm.[11] The graphene monolayer can be viewed as the basic building block to all other $\boldsymbol{sp^2}$ graphitic materials or carbon allotropes. [3] As shown in **Fig. 1.2**, the 2D monolayer graphene is stacked to form 3D graphite, rolled into 1D buckytube or wrapped into 0D buckyball.

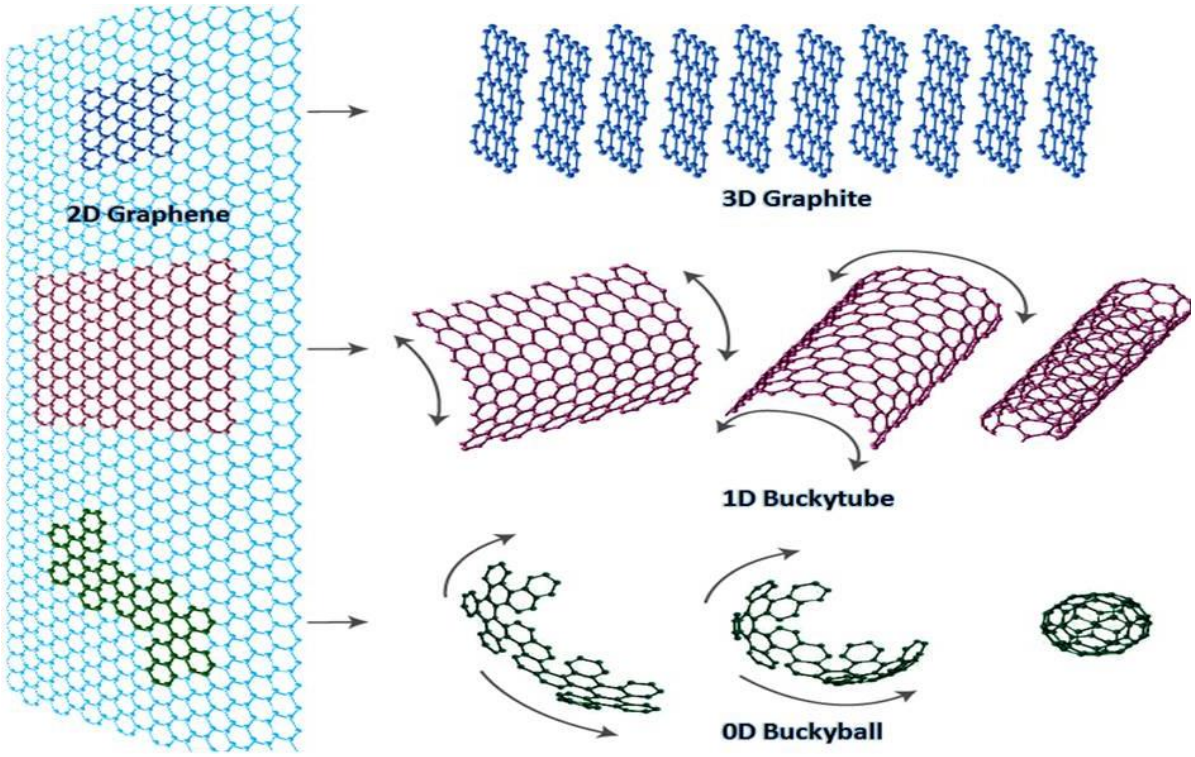

Figure 1-2 Single-layer graphene shown as a basic building block of 3D graphite, 1D buckytube and 0D buckyball (modified from [3]).

1.5 Remarkable features of graphene

The performance of graphene depends on the number of layers and the overall quality of the crystal lattice. Although most remarkable features that will be discussed here are inherent to monolayer graphene, they also still apply to bilayer and few layer graphene if the quality of the crystal structure is maintained. The long-range π conjugation in crystalline graphene allows charge carriers to travel thousands of interatomic distances at room temperature before they scatter, and such behavior features graphene with charge carrier mobility as high as 200,000 $Cm^2/V.s$, mainly because electron scattering mechanisms which often result from phonon interactions, lattice defects, or charge inhomogeneities are less pronounced. [12] Graphene supported on various substrates such as Si or SiO_2 possesses ballistic transport of charge over submicron scales. On the

other hand, freely-suspended graphene shows a lower intrinsic electrical resistivity and presents a low density material that is highly conducting at room temperature.[12]

Moreover, the charge carrier density in graphene can be tuned from electrons to hole charge carriers by electrochemical doping or applying an external voltage. [13] Another interesting feature of graphene is its transparency to radiation from UV to IR which makes graphene a potential candidate for use in the solar cell industry and for transparent electrodes. Compared to indium-tin-oxide (ITO), which suffers from degradation and ion-migration, graphene is much more transparent for wavelengths larger than 1500 nm, and it possesses higher stability.[13] Another remarkable feature is that monolayer graphene is a giant flat molecule that has two faces with no bulk in between, demonstrating an ultimate surface area that reaches 2630 m^2/g.[12] Also, graphene can adsorb and desorb various atoms, molecules, or ions making it potential candidate for application in chemical sensing. Adsorption of donor or acceptor species such as NO_2, NH_3, K, OH changes the charge carrier concentration leaving graphene highly conductive, while adsorption of ions such as H+, OH- (like in GO or single-sided graphene) introduces mid-gap or localized states that results in poorly conductive graphene.[14, 15] Moreover, the robust atomic scaffold structure makes graphene intact during chemical reactions which accounts for its chemical stability, which enables the reversible chemical dressing up and down of graphene during engineered chemical processes. However, retaining these remarkable features of monolayer graphene remains a challenge. As a 2D crystal, graphene tends to increase its intrinsic stability by gentle crumbling in the third dimension. This behavior causes graphene to gain elastic energy and suppresses the thermal vibrations which are originally anomalously large in 2D resulting in total free energy minimization.[12]

1.6 Characterization of graphene flakes

Characterization techniques that are typically used to verify the structure of graphene include optical microscopy, Raman spectroscopy, infrared (IR) spectrometry, UV-Vis spectroscopy, atomic force microscopy (AFM), transmission electron microscopy (TEM) and X-ray photoelectron spectroscopy (XPS). In an ordinary optical microscope, graphene is visualized when placed on top of Si wafer with a specific SiO_2 thickness, due to the interference-like contrast with respect to an empty wafer. Scanning probe microscopy is the most obvious choice for studying graphene topography and verification of crystallite thickness. The step height for successive layers in graphene (0.34 nm) lies well within the detection limits of modern atomic force microscopes (AFMs) making the technique extremely powerful in precise determination of crystallite thickness. In visualization of graphene with AFM, a graphene/solvent dispersion is deposited onto a substrate using spin-coating or drop-casting. The solvent is then allowed to dry very slowly leaving behind graphene layer. However, the existence of a space between the substrate and graphene sheet during the drying process makes the measurement of the actual thickness of graphene sheet challenging. Nevertheless, reliable and accurate measurement of the thickness can be performed under AFM based on folded edges of graphene. Scanning tunneling microscopy (STM) is a second scanning probing technique that has been used to successfully compare the electronic topography of graphite and graphene.[16]

Experimental Raman studies have played a critical role in studying the structure of all $\boldsymbol{sp^2}$ carbon allotropes from 3D to 0D (namely graphite, graphene, carbon nanotubes, and fullerenes) and understanding the behavior of phonons and electrons in graphene.[17] One can draw valuable information on vibrational and crystallographic characteristics, physical properties of electrons, electronic states and phonons and phonon energy dispersion from Raman spectra. Another

advantage is that the electronic structure of graphene is uniquely captured in its Raman spectrum and any changes in the electronic bands between single layer, bilayer and few layers graphene are reflected as Raman fingerprints allowing nondestructive identification of the number of graphene layers in a flake.[18] This makes Raman spectroscopy the most powerful tool to probe the thickness of graphene crystal. The strength of the technique stems also from the nature of the signal. For instance, in resonance Raman spectroscopy the combination of the Raman process with an optical absorption from a lower state to a higher state or an emission from a higher state to a lower state results in significant enhancement in the Raman signal by factor of 10^3, which allows the observation of weak Raman signals from single layer graphene.[17]

1.7 Graphene-based nanocomposite structures

Recently, the syntheses and utilization of functional graphene-based composite materials have been extensively explored for many practical applications in various fields such as energy conversion, optical electronics, composites, electrode materials, batteries, transistors, solar cells, thin coatings, membranes, sensors and catalysis.[19, 20] The extraordinary electron mobility among other unique features granted graphene great promise in nanoscale electronics, photonics and composite strutcres.[21-23] For energy storage applications, graphene can be used as a base for supercapacitors, batteries, interconnects, and field emitters.[24-26]

Functionalized graphene is also suitable in paper industry as a paper material [27] and as an excellent filler for functional nanocomposites.[28, 29] Also because of its lightness and stiffness, graphene has shown promise in nanoelectrochemical systems.[30] The carbon sp^2 network in single and bilayer graphene exhibits a unique 2D electron transport that gives rise to strong conductivity, [31, 32] making conductive graphene sheets and graphene-based films ideal for opteoelectronics.[33-36]

As potential transparent electrode materials, graphene films, for example, can by prepared by thermal annealing of graphene oxide (GO) deposited by dip-coating and then used as electrodes or anodes in dye-sensitized solar cells.

The versatility of graphene extends to chemical sensing applications, and that is mainly due to the large surface-to-volume ratio of the 2D structure, which is essential for high sensitivity. Also, the unique electronic structure and the ambipolarity allows adsorption of either electron withdrawing or donating groups leading to chemical gating of the material.[14, 37] Moreover, graphene can become a routine TEM accessory providing good imaging support for atomic-resolution TEM, because it is a single crystal membrane, one atom-thick, has low atomic mass, is cheap and easy to deposit on grids.[38] A number of studies showed that the potential of graphene in preparing dual or multicomponent functional composite materials. [39-45] Binary or dual functional component structures of graphene and a variety of secondary component such as small organic compounds, metals, metal compounds, insulating or conducting polymers, carbon nanotubes and fullerenes have been explored. These dual composites combine the excellent optical, thermal, electrical and mechanical properties of graphene with the abundant tunable functions of the secondary components. For example, various composite structures of graphene and polymers such as polyvinyl alcohol (PVA), polyacrylamide (PAM), poly(methylmethacrylate (PMMA) and polypropylene (PP) or small organic molecules such porphyrins and metalloporphyrins or metal nanostructures such as Au, Ag, Pd, Pt, Cu, Sn and Co have been explored.[20]

Graphene–based composite materials are often prepared by blending chemically modified graphene with secondary components to form targeted composite structures. In most cases the main driving force that enables various organic or inorganic nanostructures to adsorb onto graphene is the hydrophobic and static interaction. In most of this work, the syntheses of composite

structures of graphene and various semiconductor or metallic nanostructures are achieved in single-step and one-pot procedures that allow simultaneous reduction of the starting graphene oxide (GO) and contemporary synthesis of the secondary nanoparticles. For instance, a facile and direct method to anchor CdSe semiconducting nanostructures onto reduced graphene oxide (RGO) surface was developed. [46] This is a new synthetic route that could be successfully extended to the synthesis of various hybrid architectures based on graphene.

1.8 Inorganic nanostructures

When moving from bulk material towards smaller and smaller aggregates reaching nanoscale dimensions, one begins to enter a new regime where particles start to exhibit dramatic changes in their photochemical, photophysical, photochromic, electronic and optical properties. That is, as size becomes smaller and smaller, a higher percentage of surface atoms are introduced resulting in many new size-dependent phenomena. In that regime, the finite size of the particle confines the spatial distribution of charge carriers into a restricted volume in all three dimensions and electrons inside the particle start to feel the volume limitation "walls" of the particles, resulting in quantized energy levels. [47] The ability to manipulate the physical and chemical attributes of these particles affords researchers the capability to rationally design and make good use of nanoparticles in a various fields such as miniaturized devices, light-emitting diodes (LED), photovoltaic, lasers, optical memory, drug delivery, biomedical fields, catalysis, energy conversion, among others.[48]

Semiconductor nanocrystals or quantum dots (QDs) are highly fluorescent zero-dimensional (0D) particles with radii smaller than the exciton Bohr radius (a_B) of the respective bulk solid. QDs feature optical properties that can be readily customized by changing the size or composition of the particles.[49] QDs combine the most ideal characteristics, such as multiple colors

and brightness, offered by fluorescent organic dyes or semiconductor LEDs. [50] Interestingly, the color of quantum dots - both in absorption and emission - can be modulated to any chosen wavelength by tuning the size, essentially due to the rise of the quantum confinement effect. It is known from elemental quantum mechanics that when electronic charge carriers (electrons or holes) are confined in a volume limited by potential barriers comparable or smaller than the deBroglie wavelength of the particle, their allowed energy states become quantized with an increase in the effective band gap of the material.[51] Consequently, the onset of the optical absorption spectra shift towards the high energy region as the size of the particles is decreased. Thus, semiconductor nanostructures of different sizes may offer optical properties that span the spectrum from ultraviolet to infrared.[52]

Studying metallic nanoparticles attracts great interest because of their unusual chemical and physical properties that make them suitable for many technological applications in catalysis, electronics, optics, and biotechnology. The capability of tuning the optical and electronic properties gradually by controlling the particle size and shape makes metallic nanostructures extremely unique systems. When the size of the metallic nanostructures, particularly the noble metals (i.e. Au and Ag nanoparticles) is reduced to less than the mean free path of the electron, they begin to exhibit a very strong optical absorption in the visible region (that is not present in the spectrum of the bulk metal) due to the collective excitation of the free electrons in the conduction band known as the local surface plasmon resonance (SPR).[53] The position of the surface plasmon absorption peak depends mainly on the shape, size of the particle and the dielectric constant of the environment. For instance, the surface plasmon absorption of spherical Au nanoparticles feature only one absorption peak centered at ~ 520 nm due to transverse resonance. In case of Au nanorods splitting into transverse mode and longitudinal modes is observed. The

longitudinal plasmon band depends linearly on the aspect ratio of the nanorods. As a result the absorption spectrum of Au nanoparticles is tunable from the visible to mid IR regions depending on size and shape of the nanoparticles.

With increased interests in magnetic nanoparticles and owing to their peculiar properties, iron oxide nanostructures of various compositions, sizes and shapes have attracted a considerable attention during the last decades and have become an active research field in the area of magnetism. The increasing attention in these materials as well as other composites is determined by the novel magnetic, electronic, optical and chemical properties, which are different from those of the bulk materials because of the extreme small sizes and the large specific surface areas. Magnetic materials offer many potential applications in electronics, optoelectronics, data storage industries, catalysis and biomedicine. From iron oxide nanostructures, magnetite has received a great deal of interest, primarily because of its ease of preparation, strong superparamagnetic behavior, and oxidative stability.[54-63]

1.9 Statement of the problem

Since the first isolation of free-standing graphene by micromechanical cleavage of bulk graphite in 2004 [1], great efforts have been devoted to the development of reliable methods for synthesizing large quantities of graphene and graphene-based functional materials. The most significant challenge in these syntheses is overcoming the strong exfoliation energy associated with the π-stacked layers in graphite.[64] Methods adopted to overcome such strong interlayer interactions to prepare isolated graphene include mechanical cleavage, substrate-based methods, ultrasonication-assisted direct exfoliation, bottom-up syntheses, and solution based synthetic approaches. In mechanical cleavage, high-quality graphene crystallites up to 100 μm in size can be obtained from bulk graphite by repeated peeling, a piece of graphite is rubbed on a piece of

regular Scotch® tape to produce carbon debris. The scotch tape with the debris is then pressed against a slab of SiO_2 wafer (300 nm width). The debris adheres to the SiO_2 wafer, and small crystallites of graphene can be identified on the top of the wafer using optical or confocal Raman microscope. The cleavage method is extremely laborious, and it yields samples sufficient only for laboratory investigations but not for a wide-scale processing or applications. Another difficulty in exfoliating a single layer stems from the challenge to overcome the van der Waals forces exactly between the first and second layers without disrupting any subsequent sheet.

The synthesis of graphene with substrate-based methods, such as epitaxial growth or chemical vapor deposition, involves the growth of single layer in situ on a substrate that can be then located by STM and electron diffraction. In the Epitaxial growth of graphene, the electrically-insulating SiC is heated-up at very high temperature (1000 ^{o}C) and in ultrahigh vacuum causing the uppermost Si atoms to flee and leave behind small islands of graphitized carbon atoms which rearrange into hexagonal graphene.[65] These methods can give large-area graphene films up to 1 cm^2 that are compatible with the current complementary metal-oxide semiconductor (CMOS), but samples obtained are usually of non-uniform growth of several or few-layer graphene layers with an overall quality that is sensitive to the type of the substrate, and the entire process is somewhat complicated.

Chemical vapor deposition (CVD) involves a transition metal substrate film, typically Cu or Ni, that is saturated with carbon by passing a hydrocarbon gas such as methane or ethylene, which decomposes at high temperature. When the substrate is cooled, the solubility of carbon atoms in metal film decreases, and a thin layer of carbon precipitates from the surface. The primary metallic substrate is then removed by chemical means.[66] The challenge in preparing graphene by CVD is that the conditions after nucleation must be carefully controlled to promote primary crystal

growth to ensure a fine control over the thickness and to avoid seeding to prevent formation of secondary crystal/layer or grain boundaries.

Graphene can be also obtained by the direct exfoliation of graphite layers using ultrasonication. In doing so, graphite is dispersed directly in an appropriate organic solvent, such as DMF, and ultrasonication provides the energy required for exfoliation that is balanced by the solvent-graphene interaction. Although stable dispersions of graphene crystallites in selected organic solvents can be achieved by repeated ultrasonication and centrifugation, it is still a challenge to increase the single-layer yield and the dispersion density.

Graphene can be grown directly from organic precursors such as polyacyclic hydrocarbons, PAHs through bottom-up synthesis. Polyacyclic hydrocarbons (PAHs) are attractive, highly versatile, and can be substituted with a range of aliphatic chains to modify solubility, however the size limitation since increasing the molecular weight generally decreases the solubility and increases the occurrence of side reactions, the low yield and the non-uniform single layers still constitute some challenges to this method.

Wet chemical or solution-based methods for production of graphene rely on generating colloidal suspensions of graphite, graphite derivative (mainly oxide), or graphite intercalation compounds, then the chemical reduction of these colloids. When considering criteria of a proficient synthetic route to graphene, four important factors should be kept in mind to ensure ease of integration: 1) the route should be scalable; 2) it should produce 2D crystal lattice of high quality to ensure highest charge carriers mobility; 3) it should provide fine control over crystallite thickness to ensure uniform device performance and 4) the process should be compatible with complementary metal-oxide semiconductor (CMOS) processing. Many of these ideals are met by the inexpensive and extensive oxidation of bulk natural graphite into GO and the subsequent

reduction back to RGO to restore the electronic conjugation and the conductivity. The chemical reduction of GO constitutes a promising alternative for preparation of graphene due to the feasibility of the process. Among chemical methods to prepare GO, Brodie, Staudenmaier, and Hummers methods are used the most. These methods involve the oxidation of graphite in presence of strong acids and oxidants. GO prepared from these methods has different extents of oxidation depending on the method, reaction conditions, and the graphite precursor.[2] The prepared GO can be then easily exfoliated in water or polar organic solvents and reduced back to graphene. This GO-based preparation is massively scalable, and large quantities of graphene can be produced. The method is versatile and allows the reduction to be performed with strong reducing agents such as hydrazine, dimethylhydrazine, hydroquinone, or $NaBH_4$, or thermally or using UV light.

Moreover, this synthetic approach offers the possibility of obtaining large volume production of processable graphene sheets at a much lower cost relative to other methods. Also, the suitability for the controlled-density deposition of resulting graphene sheets as thin conductive films onto various solid and flexible substrates opens up the wide exploitation of this featured material.[2, 67] Nevertheless, the wet chemical synthetic approach based on reduction of GO to graphene has some disadvantages. Although the $\boldsymbol{sp^2}$-bonded carbon networks are restored upon reduction of the oxidized regions in GO, the crystalline nature of these areas are not as perfect as that of intact graphene. The introduced disordered areas or defects can induce strain as well as in-plane and out-of-plane deformation in the surrounding RGO and this in turn can affect the properties of the material and degrade the device performance.[68] Although the electrical performance or conductivity of RGO is four orders of magnitude higher than that of the semiconducting GO prior to chemical reduction, [69] it still lag behind that of pristine graphene by a factor of 10-100, [70] and this is roughly because of the residual oxygen-containing functional groups

that tend to remain even after a strong reduction. As demonstrated by Wallace et al., [2] the reduction of carboxylic acid groups with hydrazine is unlikely to occur under the given reaction conditions, and these groups are confirmed to remain after reduction of GO. Accordingly, the surface of graphene sheets still be negatively charged and an electrostatic repulsion mechanism could be used to form well-dispersed graphene colloids under controlled pH and concentrations.[2]

Another consequence of the reduction of GO to RGO is that the removal of oxygenated groups causes the RGO sheet to become less hydrophilic and quickly aggregate in solution. Nevertheless, less hydrophilic RGO can be stabilized in a solution using polymers or surfactants, via decoration with small organic molecules or nanoparticles, or by raising the pH during reduction to form charge-stabilized sheets and form colloidal dispersions.[11] Also, during reduction it might be difficult to remove all oxygen-containing functional groups so one may end up with a graphene that is not the same is the pristine and which contains a significant amount of oxygen, and possibly, significant amount of defects. These remnant oxygen-containing functional groups of RGO can enable the subsequent in situ formation of nanostructures by acting as anchor sites on the surface and the edges of the non-fully reduced graphene oxide sheet.[71]

CHAPTER 2 Characterization Techniques

Characterization of nanostructured materials and composites requires studying the size, shape, morphology, composition, electronic, magnetic and optical properties, among others. To achieve this, standard techniques and characterization tools such as UV-Vis spectrophotometry, photoluminescence spectroscopy, transmission and scanning electron microscopy, X-ray diffractometry and photoelectron spectroscopy, Raman and IR spectrometry in addition to vibrating sample magnetometry are typically used. In this chapter, the experimental methods used for characterization of our graphene-based nanostructured materials are described.

2.1 UV-Vis absorption and photoluminescence spectroscopy

UV-Vis absorption spectroscopy involves the measurement of the attenuation of wavelengths from 200-900 nm of light beam after it passes through an absorbing medium. The measurement of absorption spectra of semiconductor and metallic nanostructures can provide valuable information about size and shape of the nanocrystals. In case of semiconductor nanostructures, electronic absorption is directly related to the band-gab, which is characteristic of the materials. Semiconductor nanocrystals of different compositions or sizes absorb radiation at different regions in the UV-Vis range. For metallic nanostructures, UV-Vis measurements are particularly useful in determining size and shape. Moreover, UV-vis spectroscopy provides a tool for tracing growth kinetics of both semiconductor and metallic nanoparticles. It is also an important tool for obtaining valuable information about the electronic structure of graphene and GO.

Photoluminescence spectroscopy is a powerful technique for studying the electronic properties of semiconductor nanocrystals. It provides information about quality, defects, impurity concentrations and bandgaps. When semiconductor nanocrystals are excited with light photons of energy greater than that of the band gap, an electron is elevated to conduction band leaving behind a hole in the valence band. Upon electron-hole recombination, a photon of an energy characteristic to the band gap is emitted. Other useful information about the charge or energy transfer between semiconductor nanocrystals and graphene, for example, can be also obtained from photoluminescence studies.

In this work, UV-Vis absorbance spectra were recorded using HP-8453 spectrophotometer. Diluted suspensions of test samples were placed in 1 cm UV-quartz cuvette and absorption spectra were recorded within the appropriate scan range and using the pure respective solvent as a reference. Photoluminescence spectra of diluted suspension were measured using Varian (CARY) spectrofluorometer equipped with xenon lamp as an exciting source. Both excitation and emission slits were set at 5 nm and the excitation wavelength was chosen according to the absorption characteristics.

2.2 Transmission and scanning electron microscopy

Electron microscopes utilize electrons which have short wavelengths and thus allow observation of matters with atomic resolution. The two microscopy techniques adopted here are the transmission electron microscopy (TEM) and the scanning electron microscopy (SEM). Both techniques provide valuable means to acquire morphological, crystallographic and surface topographic information. In TEM, electron shots are sent with high acceleration voltage through thin layered-sample and the changes associated with transmitted beam are imaged. Direct

information about size, shape and morphology can be obtained from the difference in contrast of the sample and the background.

In SEM the surface of an object is scanned by measuring electrons scattered back from scanning electron beam. SEM can produce images of the surface of the sample, yielding 3D appearance that helps identifying surface topography. The spatial resolution of a SEM image depends on the size of the electron spot, which in turn depends on both the wavelength and the magneto-electro-optical system that generates the scanning beam. Unlike TEM, the SEM resolution is not high enough to image atomic features since both spot size and interaction volume could be larger than the interatomic distances.[72] Nevertheless, the ability to image relatively large sample areas and bulk solids is an advantage of SEM over TEM.

Energy dispersive X-ray spectroscopy (EDAX) was used for elemental analysis of some composite structures. The technique is based on the fact that every element has a unique atomic structure which makes different atomic structures exhibit different X-ray characteristics. In EDAX the incident electron beam excite an electron from a low-energy inner shell, resulting in its ejection and formation of a hole. An electron from a higher-energy shell then fills the hole and the excess energy is emitted as X-rays which are then analyzed by energy-dispersive spectrometer.

In this work, TEM studies were conducted on Joel JEM-1230 electron microscope operated at 120 kV equipped with Gatan UltraScan 4000SP 4K × 4K CCD camera. Samples for TEM were prepared by placing a droplet of colloid suspension in respective solvent on a Formvar carbon-coated, 300-mesh copper grid (Ted Pella) and allowing them to evaporate in air at ambient conditions. Size distribution and average size were determined using imageJ analysis software package. SEM, STEM and EDAX measurements were carried out using a Quantum DS-130S dual stage electron microscope.

2.3 Powder X-ray diffraction (XRD)

X-ray diffractometry (XRD) is the most essential tool to study and evaluate the crystal structure of a material. The powder XRD measurements are based on the well-known Bragg's law ($\lambda = 2d \sin\theta$). it is generally accepted that XRD reflection peaks of nancorystalline solids are broader than those of bulk counterpart solids. In our work, the X-ray diffraction (XRD) patterns of the powder samples were measured at room temperature with a standard X'Pert Philips Materials Research diffractometer with Cu $K_{\alpha 1}$ radiation. The database used for the identification of crystal structures of materials investigated in this work is the Joint Committee on Powder Diffraction Standards-International Center for Diffraction Data (JCPDS-ICCDD) system. In some instances, the average crystallite size was evaluated from diffraction patterns using Sherrer's formula and was compared to that obtained from TEM analysis. Lattice constants were calculated from XRD peaks using typical formulas.

2.4 X-ray photoelectron spectroscopy (XPS)

Tailoring the properties of materials requires an effective understanding of how a solid or a liquid interacts with its surroundings and how it is perceived by the surrounding environment. This in turn is defined by the outer 1-10 nm region of any solid substrate or liquid material. Often cases, the surface layer in a given material is different from the underlying bulk both chemically (composition or types of atoms) and structurally (bond angles or lengths). Accordingly, the surface elemental composition and speciation (chemical environment) need to be defined in an effective manner.[73] Among the experimental spectroscopic techniques that provide electronic information about atoms, molecules, ions, compounds and solid surfaces by measuring the kinetic energy of electrons ejected from investigated materials are surface analytical tools such as X-ray

photoelectron spectroscopy (XPS, formerly known as electron spectroscopy for chemical analysis, ESCA), UV photoelectron spectroscopy (UPS) and Auger electron spectroscopy (AUS).

In UPS UV radiation is employed to investigate valence/outer-shell levels and thus valence bands and changes in Fermi levels of materials can be studied. XPS uses soft X-rays (200-2000 eV) to examine core/inner-shell levels. XPS in particular is an extremely powerful analytical tool that identifies elemental composition, chemical state, empirical formula and electronic states of the elements within the outer 1-10 nm region of any solid surface, down to 0.1 atomic %.[73] Spectra are obtained by bombarding a given sample with a beam of Al or Mg X-rays and simultaneously measuring the kinetic energy and the number of electrons that escape from the top surface (1-10 nm) of the sample. The technique allows revealing the speciation or the chemical environment with minimal sample preparation, easy analysis, surface specificity (<10 nm) and high sensitivity (>0.05 atomic %).[73]

Photoelectron emission is a one-step process in which an electron initially bound to an atom/ion is ejected by a photon. Since a photon is a package of energy, chargeless and massless (zero rest mass) and an electron is charged with a rest mass, the photon–electron interaction involves an annihilated complete energy transfer from the impacting photon to the electron. When initiating photon energy is high enough, this causes ejection of the electron from the atom/ion or solid surface. The ejected electron will have a kinetic energy ($K.E._{XPS}$) and this kinetic energy is the quantity that is measured in XPS. However, when constructing the energy spectrum, derived binding energy ($B.E._{XPS}$) which is specific to a certain element in a certain environment is used instead of the kinetic energy [73]. Apparently, the $K.E._{XPS}$ is dependent on initiating X-ray photon energy ($\boldsymbol{E_{Ph}}$), whereas $B.E._{XPS}$ is not, according to **Eq. 2.1**, where ϕ_{XPS} is the work function of

the instrument (the minimum energy required to remove an electron from the instrument in contact with a conducting material).

$$K.E._{XPS} = E_{Ph} - \phi_{XPS} - B.E._{XPS} \qquad \textbf{Eq. 2.1}$$

The B.E. of an electron is defined by the attraction between the positively charged protons in nucleus and the negatively charged electron. The fact that B.E. is specific to a certain element in a certain environment arises because B.E. is function of i) the number of protons in the nucleus; ii) the distance between core electrons and their nuclei; iii) the density of electron around the respective atom/ion, molecule or solid (bonding type); and iv) the electron-electron interactions present. Although X-rays can penetrate micrometers below the surface, an electron has a finite flight path (<10 nm) within a solid before it loses some fraction of its energy. Accordingly, for almost all photoelectrons ejected from atoms/ions situated deeper than 10 nm below the surface, energy is lost and quenched. Consequently, all signals from underlying substrate will disappear within the spectral background and only those signals arising from the surface region remain resulting in observed spectral peaks. This phenomenon grants XPS higher sensitivity and specificity to separate surface signals relative to signals from underlying region (bulk) [73].

The sensitivity of XPS is greatly affected by the vacuum extent since it controls the density of molecules in gas phase, controls flight path of any ejected photoelectron, redistricts passage of an electron from sample to detector and decreases contaminant overlays within analysis timescales. For the work described herein, XPS measurements were performed on a Thermo Fisher Scientific ESCALAB 250 using a monochromatic Al Kα X-ray of ~ 1.4 keV.

2.5 Vibrating sample magnetometry (VSM)

Characterization of magnetic properties of nanostructures is generally carried out by measuring the magnetization curves using a vibrating sample magnetometer (VSM). In transverse-coil configuration VSM, the vibration (z) axis is perpendicular to the field applied by the electromagnet, and the pickup coils are arranged to sense the moment along the field direction. When a material is placed within a uniform magnetic field and made to undergo sinusoidal motion (i.e. mechanically vibrated), there is some magnetic flux change. This induces a voltage in the pick-up coils (Hall sensor), which is proportional to the magnetic moment of the sample. With VSM one can obtain magnetization versus field or versus temperature data, and from these curves information about size and magnetic behavior can be drawn. In studying ferromagnetic materials, for example, one observes a decrease in transition temperature with a decrease in particle size and when the particle size is very small (<10–15 nm), the particles become superparamagnetic. Magnetization curves reported herein were acquired using cryogen-free cryocooler-based 3-tesla VSM – VersaLab that has a temperature range of 50 to 400 K.

2.6 Raman spectroscopy

In Raman spectroscopy, light scattering is employed to study molecular vibrations. Raman spectroscopy complements IR absorption spectroscopy. A molecular vibration is only IR-active if there is a change in the dipole moment during the vibration and is Raman active only if there is a change in polarizability or distortion of the electron cloud around the vibrating molecule. When a bond shortens or lengthens during vibration, the distortion becomes harder or easier, resulting in a change in polarizability. Although molecular vibrations in homonuclear diatomic molecules with no dipole moment such as Cl_2 are IR-inactive, the bond stretch leads to change in polarizability and this makes vibrations Raman-active.

Raman spectroscopy is based on the inelastic scattering of light by matter. It can probe the structure of gases, liquids and amorphous or crystalline solids. When a monochromatic beam of radiation is passed from an intense excitation laser source through a sample, most of the radiation is scattered by molecules in the sample. If the collision between incident photons and molecules is elastic with only slight interaction and no energy loss, the scattered radiation is of the same frequency as the source radiation, and is known as Rayleigh scattering. If the collision is inelastic, photons are scattered with a slight shift in wavelength, frequency or energy. Scattered photons of energy less than the excitation source give rise to Raman Stoke lines and those with more energy give rise to Raman Anti-Stoke lines. A sketch of different scattering processes involved in laser-matter interaction is presented in **Fig. 2.1**. A typical Raman spectrum is a plot of the intensity of the inelastically scattered light as a function of the shift of the radiation energy in wavenumber where each peak in the spectrum relates to one or more vibration modes.

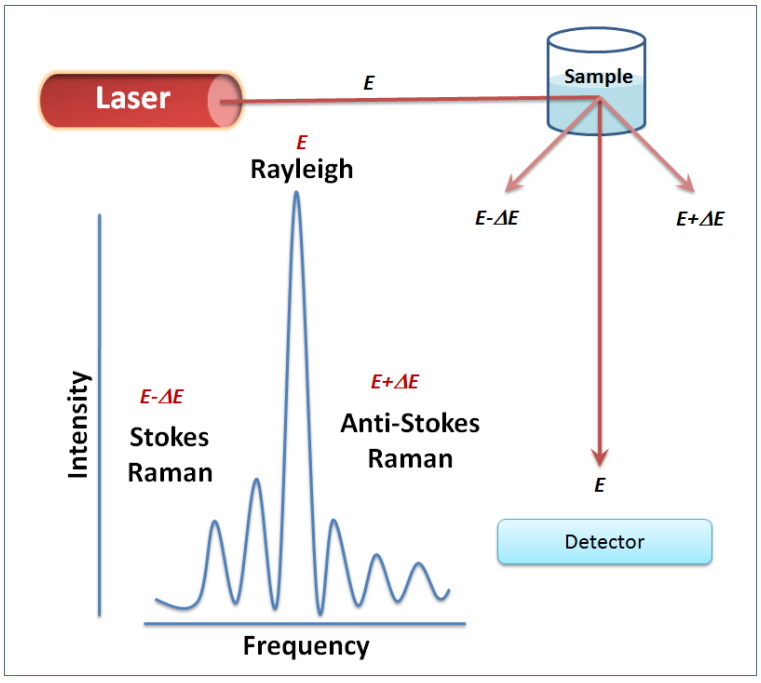

Figure 2-1 Laser interactions with matte showing elastic and inelastic scattering processes.

Unlike photon energy absorption, the process of Stokes scattering is not quantized and the molecule is thought of as existing in an imaginary state of energy between the ground and the first electronic excited state, as shown in **Fig. 2.2**. It should be noted that ΔE corresponds to the frequency of IR vibration and if it is active there would be a peak in the IR spectrum at frequency equal to ΔE. Also Raman shifts are completely independent of the wavelength of the excitation source and normal Raman spectra are obtained when UV, visible or NIR source is used, except for shift due to instrumental variation or when resonance condition applies. Because of the low intensity of the Anti-Stokes Raman lines, they are less important to analytical chemists except when the sample is highly fluorescent, since fluorescence interferes with Anti-Stokes lines to a much lesser extent than with Stokes lines. When a scattering system has an absorption band close to the excitation frequency, as it is the case in resonance Raman, the signal intensity becomes several orders of magnitude higher than that of normal Raman scattering.

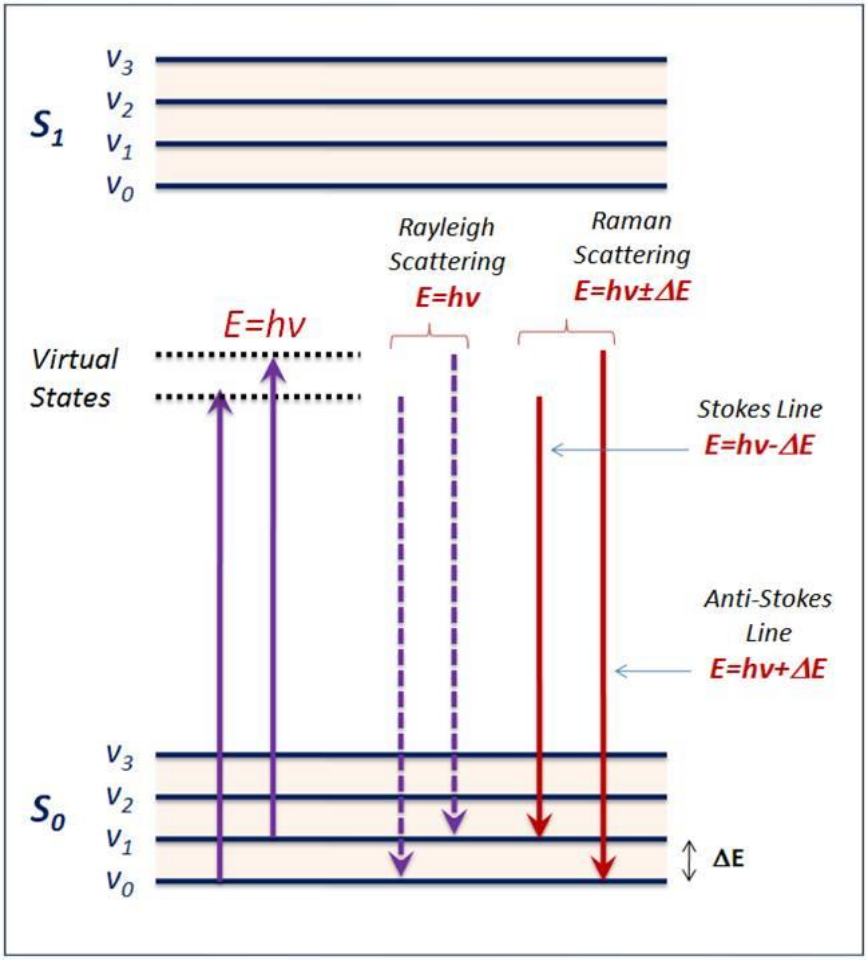

Figure 2-2 Scheme of Stokes and Anti-Stokes transitions from a virtual state.

2.6.1 Dispersive and Fourier transform Raman instrumentation

A typical Raman spectrometer consists of a light source, sample holder, a wavelength selector or an interferometer and a detector. Since the Raman signal is directly proportional to the power of the light source, laser which is both monochromatic and very intense is an ideal desirable light source for Raman spectroscopy. Lasers used for Raman spectroscopy include Nd/YAG laser (1064 nm), HeNe laser (633 nm), Ar ion laser (488 or 457.9 nm) and Kr ion laser (531 nm). The intensity of the Raman signal is directly proportional to the fourth power of the frequency and inversely proportional to the fourth power of the wavelength and this makes green and blue lasers

better than red lasers for improved signal, however, they posses higher probabilities of fluorescence and photobleaching or photodecomposition. In dispersive Raman spectrometer shown in **Fig. 2.3**, a monochromator device (grating) is used to separate the Raman scattered light into its constituent frequencies which are directed onto CCD detector. Dispersive Rama spectrometer often employs visible lasers such as 473 nm, 532 nm, 632, and 780 nm as radiation sources and sensitive Si devices as detectors.

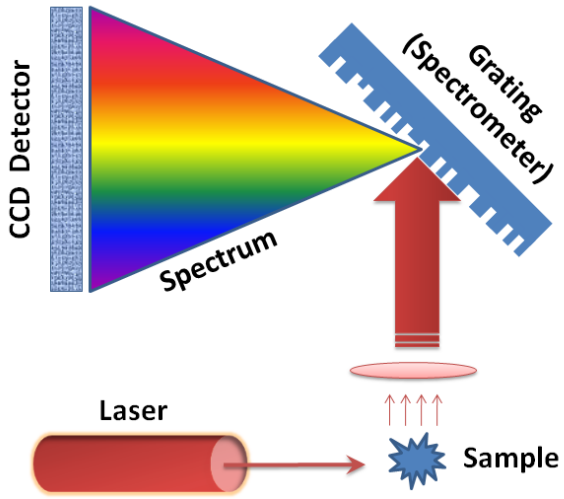

Figure 2-3 Basic components of a dispersive Raman spectrometer.

FT Raman spectrometer generally uses a NIR laser source (Nd/YAG, 1064 nm) and a Michelson interferometer, as depicted in **Fig. 2.4**. FT Raman spectrometer has many of the advantages of FT-IR such as high light throughout, simultaneous measurement of all wavelengths, the increased S/N ratio by averaging and the high precision in wavelength. Also the use of the NIR laser causes dramatic reduction in background fluorescence. However, since the 1064 nm laser line is very close to the IR absorption band of water, aqueous solutions cannot be studied as easily as they can be with visible laser lines. Also since the Raman intensity is inversely proportional to the fourth power of the wavelength, Raman signal is weak. Instead of CCD detectors, NIR

detectors such as InGaAs are used. A Michelson interferometer, like in IR spectroscopy, converts the Raman signal into an interferogram, allowing the acquirement of the entire spectrum simultaneously.

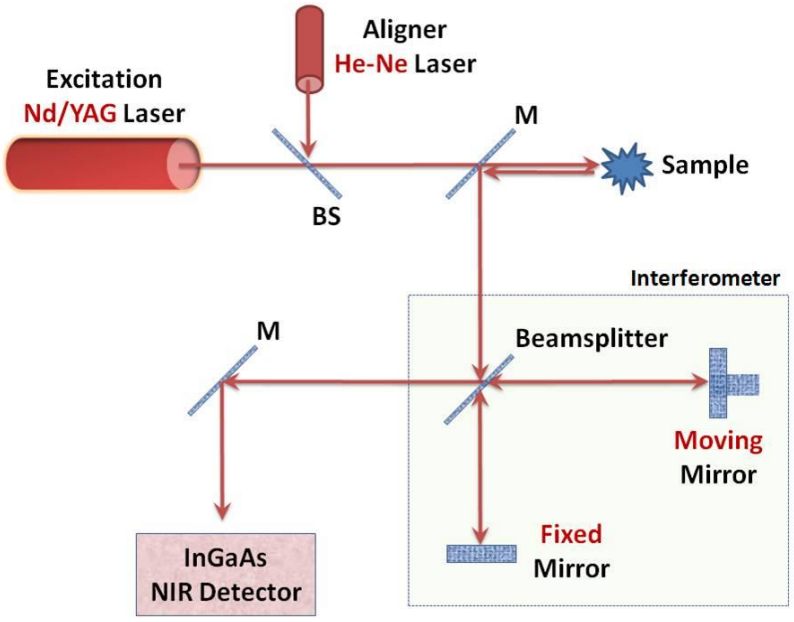

Figure 2-4 Typical components of a FT-Raman spectrometer.

2.6.2 Advantages and applications of Raman spectroscopy

Raman measurements are advantageous in a number of ways. Because the laser beam can be focused into small spot, very small specimens (few µgs or µls) can be analyzed by Raman spectroscopy when placed at the focal point of an intense laser beam. Nondestructive analysis of liquid and solid samples can be conducted in glass capillary or NMR tubes with minimal or no sample preparation. Because water is a very weak Raman scatterer, aqueous solution can be analyzed with minimal water interference. Gases do not scatter radiation efficiently and so contribution to the Raman signal from atmospheric CO_2 or H_2O in air in the optical path is insignificant compared to IR absorption. Raman spectroscopy is useful for qualitative and quantitative analysis of organic and inorganic compounds.

In normal Raman spectroscopy, a monochromatic light of a frequency that cannot be absorbed by the sample is used. When a laser excitation line that falls within an excited state is used, the intensity of some Raman lines increases by great factor (10^3-10^6) over the intensity in normal Raman spectroscopy, facilitating the analysis of low concentration analytes. This resonance effect leads to the powerful resonance Raman spectroscopy (RRS), providing the molecule possess a chromophore that can absorb UV or visible radiation. Tunable dye lasers that generate wavelengths over the UV-Vis range of 200-800 nm are often used. A schematic of processes involved in resonance Raman is shown in **Fig. 2.5**.

In this work two different Raman set-ups were used to study Raman features of prepared nanocomposites. In some instances, Raman spectra were measured at room temperature using a 457.9 nm Ar ion laser (Spectra-Physics model 2025). The samples were pressed into a depression at the end of a 3 mm diameter stainless steel rod, held at a 30 degree angle in the path of the laser beam. The laser beam was focused to a 0.10 mm diameter spot on the sample with a laser power of 1 mW. The Raman scattered light was collected by a Canon 50 mm f/0.95 camera lens. The detector was a Princeton Instruments 1340 x 400 liquid nitrogen CCD detector, attached to a Spex model 1870 0.5 meter single spectrograph with interchangeable 1200 and 600 lines/mm holographic gratings (Jobin-Yvon). Though the holographic gratings provided high discrimination, Schott and Corning glass cut-off filters were used to provide additional filtering of reflected laser light, when necessary.

In other instances, Raman spectra were recorded using Thermo Scientific DXR SmartRaman Spectrometer with 532 nm excitation laser source. The laser power was 5 mW, the spectral resolution was ~ 4 cm^{-1} and the spectrum acquisition consisted of 100 accumulations with a total acquisition time of 15 min.

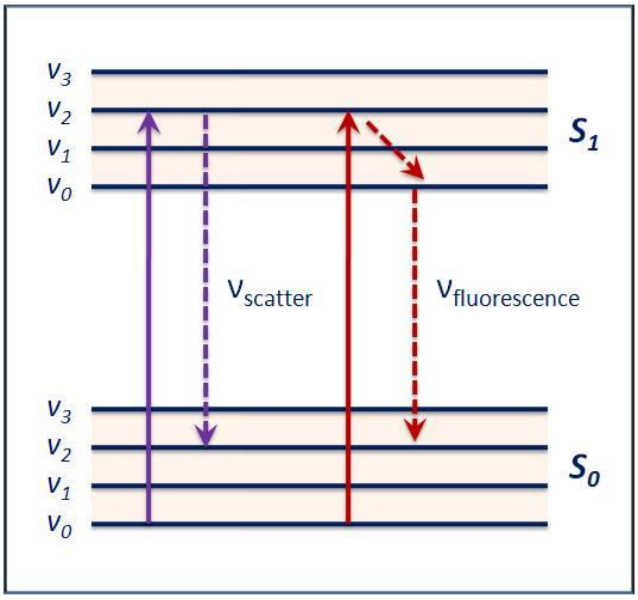

Figure 2-5 A schematic of resonance Raman process

2.6.3 Fourier-Transform IR spectrometry

Molecules with covalent bonds may absorb IR radiation and the absorption is quantized where only certain IR frequencies are absorbed. The energy associated with IR radiation is sufficient to cause molecules to rotate and vibrate when possible and the absorbing molecule is elevated to a higher energy state. The energy needed to cause an electron transition to rotational level is smaller than energy needed to cause transition to vibrational level. When the IR energy is between 1-100 μm (high), the molecule will be excited to higher vibrational state and when the energy is greater than 100 μm (weaker), the molecule is excited to higher rotational states in the gas phase. Since each vibration level has multiple rotational levels associated with it, IR spectrum of a liquid or solid sample consists of a broad vibrational absorption bands and not narrow lines.

When an IR radiation is passed through a sample, some of the radiation is absorbed by the sample and some passes through. The resulting spectrum represents the molecular absorption and transmission, creating a molecular fingerprint of the sample with absorption peaks that correspond

to the frequencies of vibration between the bonds of the atoms making up the material. A simple IR spectrometer layout is depicted in **Fig. 2.6**. A beam of IR energy radiated from the source (usually a glowing black-body) is passed through an aperture which controls the amount of energy delivered to the sample/detector. When the beam enters the interferometer, spectral encoding takes place and the resulting interferogram leaves the interferometer as a signal. In the sample compartment, certain IR frequencies which are unique to the test sample are absorbed. Finally the transmitted beam passes to the detector where a unique interferogram signal is measured. The signal measured is digitized and sent to the computer. After the Fourier transformation process, a final IR frequency spectrum is generated.

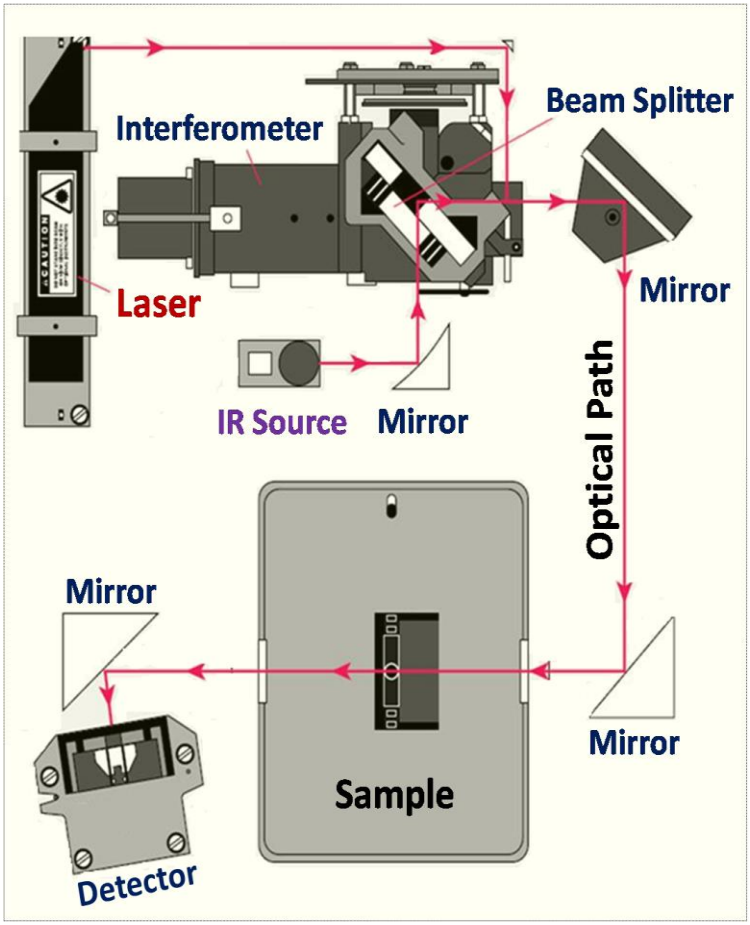

Figure 2-6 Schematic representation of a typical FT-IR spectrometer layout (adapted from [74]).

Typical components of a FTIR spectrometer include IR source (usually a glowing black-body source that emits radiation through an aperture which controls the amount of energy delivered to the sample/detector), interferometer (composed of beam splitter, fixed and moving mirror), laser for aligning the mirrors and for internal calibration and a detector. When two beams of light of the same wavelength are brought together in phase they reinforce each together and continue down the light. When the two beams are out of phase destructive interference takes place. FT spectrometers are based on Michelson interferometer where passing radiation is separated by a beam splitter into two perpendicular beams of approximate intensity. The two beams are then reflected by mirror back to the beam splitter when they recombine and are reflected together onto the detector one of the mirrors is fixed in position and the other mirror can move toward or way from the beam splitter changing the path length of that arm. As the moving mirror is moved the signal falling on the detector is a cosine wave with the usual maxima and minima when plotted against the travel of the mirror. Since real IR sources are polychromatic, each wavelength will generate a unique wave the signal at detector is a result of the summation of the all cosine waves. The interferogram holds spectral info from the sample in a time domain (intensity vs time based on the speed of the moving mirror). Now the contribution from each wavelength can be obtained if the unique cosine waves can be extracted from interferogram when these individual wavelengths are reconstructed give spectrum infrequency domain (usual spectrum). To convert the time domain spectrum into frequency domain spectrum use Fourier transform. It expresses mathematical function of time as function of frequency.

FTIR measurements are practically advantageous, limitless, extremely more accurate and reproducible compared to those measured with dispersive technique. Some major advantages are the fast speed, improved sensitivity, mechanical simplicity and internal calibration. i) Speed: since

all frequencies are measured simultaneously (sample is exposed to all source wavelengths at once and all wavelengths are measured simultaneously in less than a second), FTIR measurements can increase scan speed and decrease collection rate from several minutes to few seconds (many spectra from sample can be collected in a very short time, averaged added electronically improved s/n increased sensitivity); ii) Sensitivity: the fast measurement in FTIR allows the co-addition of several scans together which ratio out the random noise and improves sensitivity dramatically. The improved sensitivity permits analysis and detection of even the lowest of unknown contaminants; iii) Mechanical simplicity: FTIR spectrometer features little possibility of mechanical breakdown since only a single optical part (mirror) is moving in the interferometer; iv) Internally calibration: modern FTIR spectrometers employ a He-Ne laser as an internal self-calibrating standard, eliminating the need to be calibrated by the user.

The model of the FTIR spectrometer utilized in this work is Nicolet 6700 FTIR. As a first step a background IR spectrum due to the absorption by optical elements of the instrument itself and the gaseous species (CO_2 and/or H_2O) in ambient air is measured with no sample in the beam and then compared to the measurement with the sample in the beam to determine the percent transmittance. Next, an IR spectrum that contains absorption bands from the sample as well as the background is collected. Now the ratio between the sample spectrum and the background spectrum gives the adjusted spectrum of the sample. In this way, when the background is measured and removed, the resulting spectral features in IR spectrum can be ascribed strictly to the test samplle. In all IR spectra in this work, the %transmittance is plotted versus wavenumber in cm^{-1} and frequencies were compared to values from literature to determine the possible functional groups responsible for absorption.

CHAPTER 3 Shape-Controlled CdSe-Graphene Nanocomposites: Photoluminescence Quenching by Graphene

3.1 Overview

We have developed a facile, fast, and scalable microwave irradiation method for the synthesis of graphene and CdSe nanocrystals of controlled size, shape, and crystalline structure dispersed on graphene sheets. The reduction of GO into graphene takes place in DMSO within two minutes of microwave irradiation as opposed to 12 hrs of conventional thermal heating at 180 ^{o}C. The method allows the simultaneous reduction of GO and the nucleation and growth of CdSe nanocrystals using a variety of capping agents. Cubic and hexagonal CdSe nanocrystals with an average size of 3-4 and 5-7 nm, respectively have been prepared by the proper choice of the capping agent within a few minutes of microwave irradiation. High quality, nearly monodisperse CdSe nanocrystals have been supported on graphene with no evidence for aggregation. Direct evidence is presented for the efficient quenching of photoluminescence from the CdSe nanocrystals by graphene. The results provide a new approach for exploring the size-tunable optical properties of CdSe nanocrystals supported on graphene that could have important implications for energy conversion applications such as photovoltaic cells where CdSe quantum dots, the light-harvesting material, are supported on the highly conducting flexible graphene electrodes.

3.2 Introduction

Graphene, a two-dimensional nanometer-thick highly conducting and thermally stable material, has sparked great excitement in the fields of chemistry, physics and materials sciences and continues to attract extensive interest for fundamental scientific inquiry and for the prospects of potential applications and new advanced technologies. [3, 5, 75] This unusual activity is attributed to the extraordinary properties of this unique material which include the highest intrinsic carrier mobility at room temperature of all known materials and very high mechanical strength and thermal stability. [1, 3-6, 12, 23, 76] Graphene promises a diverse range of potential applications in many technological fields such as nanocomposite materials, nanoscale electronics, sensors, batteries, supercapacitors, hydrogen storage, and quantum dots. [1-3, 35, 77-79]

Although graphite and GO have been known to be in existence since the last century, [80] it is only recently that graphene has been prepared and characterized in a systematic way. [1, 4-6] Mechanical cleavage of ordinary graphite, the process originally led to a discovery of free-standing graphene, [1] is the technique currently used in most experimental studies of graphene. However, the difficulty of this method to scale-up and produce graphene sheets in large quantities for applications has led to the rise of chemical conversion of graphite as an efficient and low cost approach for bulk production of graphene and graphene based composite materials. [2]

Several solution-based routes of preparation of graphene has been demonstrated including the chemical oxidation of graphite to hydrophilic GO, [80] which can be readily exfoliated as individual GO sheets by ultrasonication. As reported by Ruoff and co-workers, [81] the electrically-insulating GO can be converted back to conducting graphene by chemical reduction with hydrazine hydrate for example. However, hydrazine is highly toxic and potentially explosive [12] and its use

should be minimized or even eliminated. Because of the fact that most unique properties of graphene are associated mainly with individual sheets, prevention of aggregation and keeping sheets individually separated is of particular importance. The tendency of graphene sheet to form irreversible aggregates or even to restack forming graphite through van der Waals interactions has been a major obstacle to exploiting most proposed applications. [2] This challenge has been encountered in so many efforts through either attachment of polymers onto the sheets or chemical reduction and decoration with small molecules and nanoparticles. [45, 79, 81-86] Initial efforts to support metallic and semiconductor nanoparticles on carbon structures and graphene have been already reported. [83, 87-91] A one step method to deposit CdS nanocrystals on graphene sheets in dimethyl sulfoxide (DMSO) has been demonstrated by Aoneng Cao et al. [91] In our quest to further explore the supporting of semiconductor nanocrystals on graphene, we adopted the most readily available and least expensive carbon material, ordinary graphite, as a source for the synthesis of graphene sheets, and we decorated these graphene sheets with the first QD system to be successfully prepared with extremely high quality and also the first system that has been extensively studied and understood in much detail, CdSe quantum dots. Controlled syntheses of cubic and hexagonal CdSe crystalline phases were successfully achieved. The entire synthesis was conducted in a facile way so that CdSe nanocrystals were synthesized and simultaneously deposited on the graphene sheets which were obtained by DMSO-reduction of GO upon MWI.

The chemical reduction of GO is the most widely applied technique used for preparing RGO. Various effective organic and inorganic reducing agents such hydrazine monohydrate, dimethylhydrazine, phenylhydrazine, strong alkaline solutions such as ammonia and potassium hydroxide, sodium borohydride, hydroquinone, high-temperature alcohol vapors, among others have been explored for the chemical and solvothermal reduction and removal of oxygen-

containing functional groups of GO. Upon such treatments, most of the oxygenated groups are eliminated from GO and the π-electron conjugation is partially restored within the aromatic system of graphite. As a result, the π-stacking interaction and hydrophobic characters are increased causing RGO sheets to precipitate from the reaction mixture. [20] The use of hydrazine and its derivatives as reducing agents has several disadvantages. They exert potential hazard to the environment and personnel and are highly flammable and corrosive. In addition, they are expensive and residual traces may alter the performance of RGO in devices. To avoid using hydrazine, we developed a solvothermal reduction of GO in polar organic solvent, dimethylsulfooxide (DMSO). The resulting RGO can be dispersed in polar organic solvents such as DMSO and DMF with a concentration of 0.1 mg/ml and can be filtered into shiny black films. The combination of highest carrier mobility, thermal, chemical and mechanical stability of graphene with the size-tunable properties of metal and semiconductor nanocrystals offers many interesting applications in a wide range of fields including heterogeneous catalysis, nanoelectronics and devices. [67, 78, 92, 93] Specifically, semiconductor nanocrystals of controlled size and shape assembled on the surface of graphene are expected to play major roles in the development of new generation nanostructured solar cells, fuel cells, light emitting diodes, lasers, sensors, and novel energy conversion devices. [45, 91, 94-96]

The study of the zero-dimensional CdSe quantum dots deposited on two-dimensional graphene is scientifically intriguing for understanding the interaction between excited semiconductor nanocrystals and graphene. [45, 91, 94-96] CdSe quantum dots are model systems for studying quantum size effects, and they have provided many textbooks with examples of the size- and shape-tunable structural, electronic and optical properties of semiconductor nanocrystals. [97-99] From a practical point of view, the size-tunable optical properties of CdSe nanocrystals coupled

with the extremely high carrier mobility of graphene present an ideal system for energy conversion applications such as photovoltaic cells where CdSe quantum dots, the light-harvesting material, are supported on the highly conducting flexible graphene electrodes. [100, 101] Fast electron transfer from the photoexcited CdSe nanocrystals to graphene could result in high carrier transport through the nanocrystals and efficient charge collection at the graphene electrodes. However, resonant energy transfer can also take place from the excited CdSe quantum dots exciting electron-hole pairs in graphene. Brus and co-workers have recently demonstrated efficient energy transfer from individual CdSe/ZnS nanocrystals to single- and few-layer graphene films. [96] They suggested that resonant energy transfer is much faster than photoexcited electron transfer due to the weak electronic coupling between the semiconductor nanocrystals and graphene. Very recently, RGO decorated with CdSe nanoparticles have been prepared by a two-step process where RGO (prepared separately by the hydrazine/ammonia reduction of GO for 24 hrs) was added into the reaction solution during the synthesis of the CdSe nanoparticles. [102] Although CdSe-RGO nanocomposites produced by these processes show enhanced photoresponse over pure CdSe nanoparticles and bare RGO films, definitive evidence of GO reduction is questionable based on the reported XPS spectra which indicate significant presence of the epoxy/ether, C=O and C(O)O functional groups in GO. [102]

In this work, [46] we present a facile, fast, and scalable one-step, one-pot microwave synthesis of phase-controlled small CdSe nanocrystals supported on highly RGO sheets. The main feature of the method reported here is the simultaneous efficient reduction of GO and the controlled synthesis of phase-selected CdSe nanocrystals on the RGO sheets within a few minutes of microwave irradiation. Through ligand-controlled synthesis, the reported method allows the synthesis of cubic or hexagonal CdSe nanocrystals with an average size of 2-3 or 4-7 nm,

respectively, well-dispersed on the surface of the chemically converted graphene sheets. We also report on the efficient quenching of the CdSe photoluminescence in solution by graphene which could have important implications for the separation of the photogenerated electrons and holes in the CdSe nanocrystals and the possible transfer of these carriers to the graphene sheets [46].

3.3 Experimental

3.3.1 Chemicals and reagents

Graphite (natural, high purity,-200 mesh, 99.9999%, metal basis, Alfa Aesar), sulfuric acid (Fisher Scientific, Certified ACS), potassium permanganate (Analyt Reag., low in mercury, Mallinckrodt), hydrogen peroxide (30%, KMG), cadmium oxide (99.99% metal basis, Sigma-Aldrich), selenium (powder,-100 mesh, 99.99% metal basis, Aldrich), 1-hexadecylamine (tech. grade, 90%, Aldrich), trioctylphosphine oxide (tech. grade, 90%, Sigma-Aldrich), oleic acid (tech. grade, 90%, Aldrich), tributylphosphine (tech. 90%, Aldrich), and dimethyl sulfoxide (ACS 99.9%, Alfa Aesar).

3.3.2 Synthesis of GO

GO was synthesized from graphite powder by a modified Hummers method as presented by Nogueira and co-workers. [80, 103] Micron sized graphite powder (20 g) was put into cold (0 ^{o}C) sulfuric acid (460 ml). $KMnO_4$ (60 g) was added gradually with stirring and under cooling, so that the temperature of the mixture was kept below 20 ^{0}C. The mixture was then stirred for 2 h at 35±2 ^{o}C and cold DI-H_2O (920 ml) was added. The reaction was terminated by adding excess DI-H_2O (2.8 L) and 30% H_2O_2 (50 ml), after which the color of the mixture turned bright yellow. The mixture was filtered, washed with large amount of hot DI- H_2O, filtered and dried in a

hydrothermal oven at 45 ^{0}C for 5 h. As-prepared GO was suspended in dimethylsulfoxide (DMSO) to give a 0.1 mg/ml yellow-brown dispersion.

Exfoliation to GO was achieved via ultrasonication (Branson 3510, 40 KHz*)* for 1 hour. Such dispersion of exfoliated GO in DMSO was stable for several months. When GO is exposed to sonication waves in an appropriate solvent (in our work DMSO or water), the large particles or platelets are reduced in size and thickness into smaller and thinner ones. An illustration of the exfoliation process is presented in **Fig. 3.1**. The compression and agitation caused by the high-frequency (20-40 kHz) waves causes local bubbles or cavitations that collapse, leaving behind an enormous localized temperature and pressure as high as 5,000 K and 500 atm, respectively. Such treatment enables an efficient exfoliation of GO platelets into few-layers GO.

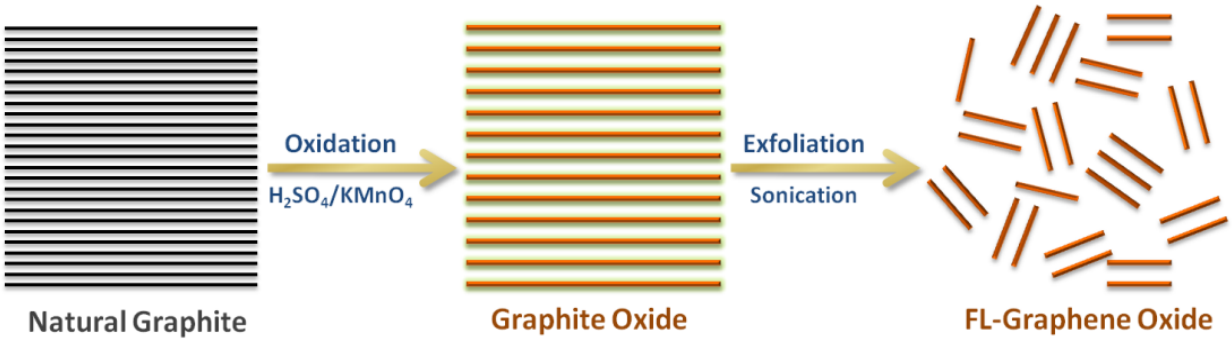

Figure 3-1 Schematic illustration of exfoliation of graphite into GO.

3.3.3 Microwave synthesis of graphene

In a typical experiment, 30 ml of a clear homogeneous sonicated GO-DMSO solution in a 50 ml reaction vessel was placed in a conventional microwave oven (Oster, 1200 W, 1.4 cu. ft. countertop microwave: Model OGG21401) and microwaved at a full power for 5 s and off with stirring for 5 s. Different solutions were irradiated for different times between 40 s and up to 2 min. The color change from yellow-brown to black indicates the completion of the reduction

process and the formation of graphene dispersion. For further characterization, graphene dispersion was centrifuged (eppendorf centrifuge 5804) at 5000 rpm for 10 min, then the segregated solid was transferred to a 20 ml capacity Al dish and put in a hydrothermal oven at 55 ^{o}C for 8 hours to dry.

3.3.4 Microwave synthesis of CdSe-graphene nanocomposite

Synthesis of cubic CdSe nanocrystals supported on graphene involved the addition of cadmium oxide powder (120 mg) to an oleic acid solution (5 ml), followed by microwave irradiation (MWI) till the complete dissolution of CdO and a colorless solution was obtained. A mixture of trioctylphoshpine oxide (1.93 g) and hexadecylamine (1.93 g) was then added to the colorless solution, and the reaction mixture was further microwaved allowing the solid TOPO-HDA mixture to dissolve. A clear homogeneous solution of GO dispersed in DMSO (400 µl) was added to the reaction vessel with the subsequent addition of selenium powder (118 mg) that was pre-dissolved in tributylphosphine (3 ml), (Se-TOP). To allow nucleation and growth of CdSe nanocrystals with the simultaneous reduction of GO to graphene, the reaction vessel was further MW irradiated for 2 min; on for 5 sec and off for 10 sec until the growth and reduction processes were complete. The synthesis of hexagonal CdSe nanocrystals supported on graphene adopted the same method as that of cubic CdSe except that the TOPO-HDA mixture was not added. The as-prepared composite structures were precipitated with ethanol, centrifuged, and re-dispersed in chloroform for further analyses and characterization.

3.3.5 Characterization

TEM images were obtained using a Joel JEM-1230 electron microscope operated at 120 kV equipped with a Gatan UltraScan 4000SP 4K x 4K CCD camera. Samples for TEM were

prepared by placing a droplet of a colloid suspension in toluene on a Formvar 300-mesh, carbon-coated copper grid (Ted Pella) and allowed to dry in air. The small angle X-ray diffraction (SA-XRD) patterns were measured at room temperature with an X'Pert Philips Materials Research Diffractometer using Cu $K_{\alpha 1}$ radiation. The X-ray photoelectron spectroscopy (XPS) analysis was performed on a Thermo Fisher Scientific ESCALAB 250 using a monochromatic Al KR. Absorption spectra were recorded using a Hewlett-Packard HP-8453 diode array spectrophotometer. Emission spectra were recorded using a Varian, Inc. - Cary Eclipse Fluorescence Spectrofluorimeter. The UV-Vis absorption spectra were acquired between 400 and 750 nm with a slit width of 5 nm. Nanocomposites solutions were placed in a 1 cm thick quartz cuvette and the spectra were taken against toluene as respective solvent reference. The photoluminescence spectra were collected between 480 and 700 nm using an excitation wavelength of 430 nm with a slit width of 5 nm for both excitation and emission. IR spectra were collected with a Nicolet 6700 FT-IR system using the transmission mode. Raman spectra were measured using an excitation wavelength of 457.9 nm provided by a Spectra-Physics model 2025 argon ion laser. The laser beam was focused to a 0.10 mm diameter spot on the sample with a laser power of 1 mW. The samples were pressed into a depression at the end of a 3 mm diameter stainless steel rod, held at a 30 degree angle in the path of the laser beam. The detector was a Princeton Instruments 1340 x 400 liquid nitrogen CCD detector, attached to a Spex model 1870 0.5 meter single spectrograph with interchangeable 1200 and 600 lines/mm holographic gratings (Jobin-Yvon). The Raman scattered light was collected by a Canon 50 mm f/0.95 camera lens. Though the holographic gratings provided high discrimination, Schott and Corning glass cut-off filters were used to provide additional filtering of reflected laser light, when necessary. [87]

3.3.6 Quenching of CdSe photoluminescence by graphene

A homogenous graphene-DMSO stock solution, 0.1 mg/ml, was prepared by adding 5 mg of the prepared graphene to 50 ml of DMSO, and the suspension was sonicated for 1 h. A stock solution of 0.1 mg/ml of cubic CdSe nanocrystals, prepared using a mixture of TOPO and HDA in DMSO, was made by weighing out 5 mg of CdSe and dissolving in 50 ml chloroform. Seven solutions were made by adding 3 ml of the CdSe-chloroform solution to 0, 0.5, 0.6, 0.7, 0.8, 0.9, and 1.0 ml of the graphene-DMSO solutions, and the volume of each mixture was brought to 4 ml by adding DMSO, resulting in final graphene concentrations of 0, 12.5, 15, 17.5, 20, 22.5, and 25 μg/ml, respectively. The CdSe concentration in each solution was thus 75 μg/ml. All solutions showed an absorbance value of ~0.41 at the excitation wavelength of 430 nm.

3.4 Results and Discussion

3.4.1 Microwave synthesis of graphene using DMSO as a solvent

Since its isolation in 2004 by Geim and co-workers [1], graphene has attracted an increasing interest due to the one-atom thick 2D structure and superior electrical, thermal and mechanical properties. Up to date several effective solution-based routes and techniques have been developed for the conversion of low cost GO into high quality graphene and graphene based composite materials for potential applications in nanoelectronics, among others. [11, 70, 81, 82, 87, 104, 105] We have recently developed a facile, convenient, and scalable microwave assisted chemical reduction method for the synthesis of graphene as well as metallic and bimetallic nanoparticles supported on graphene using a simple household microwave oven. [87] The main advantage of MWI over other conventional heating methods is rapid and uniform heating of the reaction mixture. Due to the difference in the solvent and reactant dielectric constants, selective dielectric heating can provide

a significant enhancement in the transfer of energy directly to the reactants, which causes an instantaneous internal temperature rise. [106-108] In the present work, we modified our MWI synthesis approach by utilizing the high microwave absorbing solvent dimethyl sulfoxide (DMSO) for the MW assisted reduction of GO. Recently, it has been suggested that dimethyl sulfoxide (DMSO) at higher temperatures (180 °C for 12 hours) could result in the reduction of GO. [91] By taking advantage of the high polarity of DMSO (μ = 3.96 Debye) and its characteristic high efficiency of converting electromagnetic radiation into heat, [106] we were able to convert GO into graphene within 1-2 minutes of MWI instead of 12 hours by the conventional thermal process.

GO, the oxidation product of bulk graphite, is a layered material with the same structure of natural graphite with the difference being that constituting graphene layers are functionalized with oxygen containing groups such the hydroxyl, epoxy, carbonyl and carboxylic groups. As a result the sp^2-bonded carbon network is strongly disrupted by these functional groups and the interlayer separation increases as well. [11] Upon oxidation, the electronic conjugation is lost and graphite loses its excellent electrical properties and essentially becomes a semiconductor or an insulator according to the oxidation level. In the most popular structural model, [109] GO is portrayed or depicted as a combination of randomly distributed non-oxidized regions and oxidized regions. Whereas carbon atoms in the non-oxidized regions retain the sp^2 hybridization, the oxidized regions are bearing oxygen-containing functional groups and thus have sp^3 hybridization. In this view the sheets of GO have their basal planar planes decorated mostly with major epoxy and hydroxyl groups, while minor carbonyl and carboxylic groups are populated at the edges. The existence of large regions functionalized with oxygen-containing functional groups attached to the edges and basal planes makes GO hydrophilic; therefore, it can be readily exfoliated in water to generate stable aqueous colloidal dispersion by simple sonication or stirring for long time enough.

The hydrophilic nature of GO allows water to easily intercalate between the layers; accordingly, the interlayer distance can increase from 6 to 12 A^o with increasing relative humidity. As revealed by the measurement of the surface charges (zeta potential) of graphite or GO sheets in water, the ionization of carboxylic acid and phenolic hydroxyl groups existing on surfaces leaves the sheets highly negatively charged and apparently the colloidal stability in water is presumed to be a result of an electrostatic repulsion rather than the hydrophilicity. [2, 11] The concentration of GO in stable aqueous dispersions can be as high as 3 mg/ml. Also, it can be dispersed in polar organic solvents such as DMSO, DMF, THF and NMP at about 0.5 mg/ml.[11]

The oxidation process with a mixture of $H_2SO_4/KMnO_4$ functionalizes the GO with various hydroxyl and epoxy groups, in addition to carbonyl and carboxyl groups along the edges and basal planes of the sheets. [82, 110] The layering in GO is evident from its XRD pattern. The peak in the XRD pattern of a typical GO at 10.7^o corresponds to an interlayer distance between sheets (*d-spacing*) of about 0.78 nm that agrees with literature [33, 104] compared to 0.34 nm of natural native graphite. [12] This increase in the interlayer spacing means a significant reduction in the van der Waals forces between adjacent sheets, which indicate that exfoliation can be utilized as a route to obtain single layers of graphene. [12] In our synthesis, DMSO acts as a solvent for GO and a capping agent for CdSe in case of protocol 2. The possible mechanism of the reduction of GO to graphene may be attributed to heating effect upon microwave irradiation. This thermal reduction approach in presence of DMSO has been suggested by Aoneng Cao et al. [91] and a similar reduction of GO into graphene via thermal treatment has been reported by Mullen and co-workers. [34, 111]

The successful reduction of GO by DMSO under MWI conditions was verified by monitoring the X-ray diffraction (XRD), X-ray photoelectron spectroscopy (XPS), FT-IR, and UV absorption spectroscopy. The XRD pattern of the RGO shows the disappearance of the

characteristic peak of GO at $2\theta = 10.9^{o}$ after 1.5 min of MWI in DMSO, as shown in **Fig. 3.2-a**, indicating that most of the GO has been converted into graphene. [11, 81, 82, 87] On the other hand, even after 7 hrs of heating at 180 ^{o}C, a significant amount of GO remains unreduced as evident by the presence of the XRD peak of GO shown in **Fig. 3.2-b**. The shift of the XRD peak to lower 2θ values indicate that the separation between the GO layers has increased above the 8 Å distance corresponding to the $2\theta = 10.9^{o}$. Only after 12 hrs of heating the DMSO solution at 180 ^{o}C, is a complete disappearance of the GO peak observed and the color of the solution changes from golden yellow to black (**Fig. 3.2-d**) indicating the conversion of GO into graphene. With the MWI method (1200 W power), this process is completed in 2 minutes as shown in **Figs. 3.2-a and 3.2-c**. The MWI time required for the deoxygenation of GO varies between a few and several minutes depending on the MW power, the concentration of GO and the volume of the solution.

To further probe the deoxygenation and reduction of GO in DMSO using both the conventional thermal heating at 180 ^{o}C and MWI, the C1s XPS spectra were measured for samples prepared after different reaction times. As shown in **Fig. 3.3**, the C1s spectrum of GO shows peaks corresponding to oxygen-containing groups between 285.5 and 289 eV in addition to the sp^2-bonded carbon C=C at 284.5 eV. Typically, peaks at 285.6, 286.7, 287.7 and 289 are assigned to the C1s of the C-OH, C-O, C=O, and HO-C=O groups, respectively [112, 113]. As expected, significant reduction of the oxygen-containing groups is observed after the thermal heating or the MWI of GO in DMSO as shown in **Fig. 3.3**. It is interesting to note that MWI for 40 s results in a degree of deoxygenation of GO similar to that obtained after 2 hrs of heating at 180 ^{o}C as shown in **Fig. 3.3**. The XPS data clearly indicates that most of the oxygen-containing groups in GO are removed after 100-120 s of MWI. This confirms that MWI of GO in DMSO can provide a fast and simple route for the production of graphene.

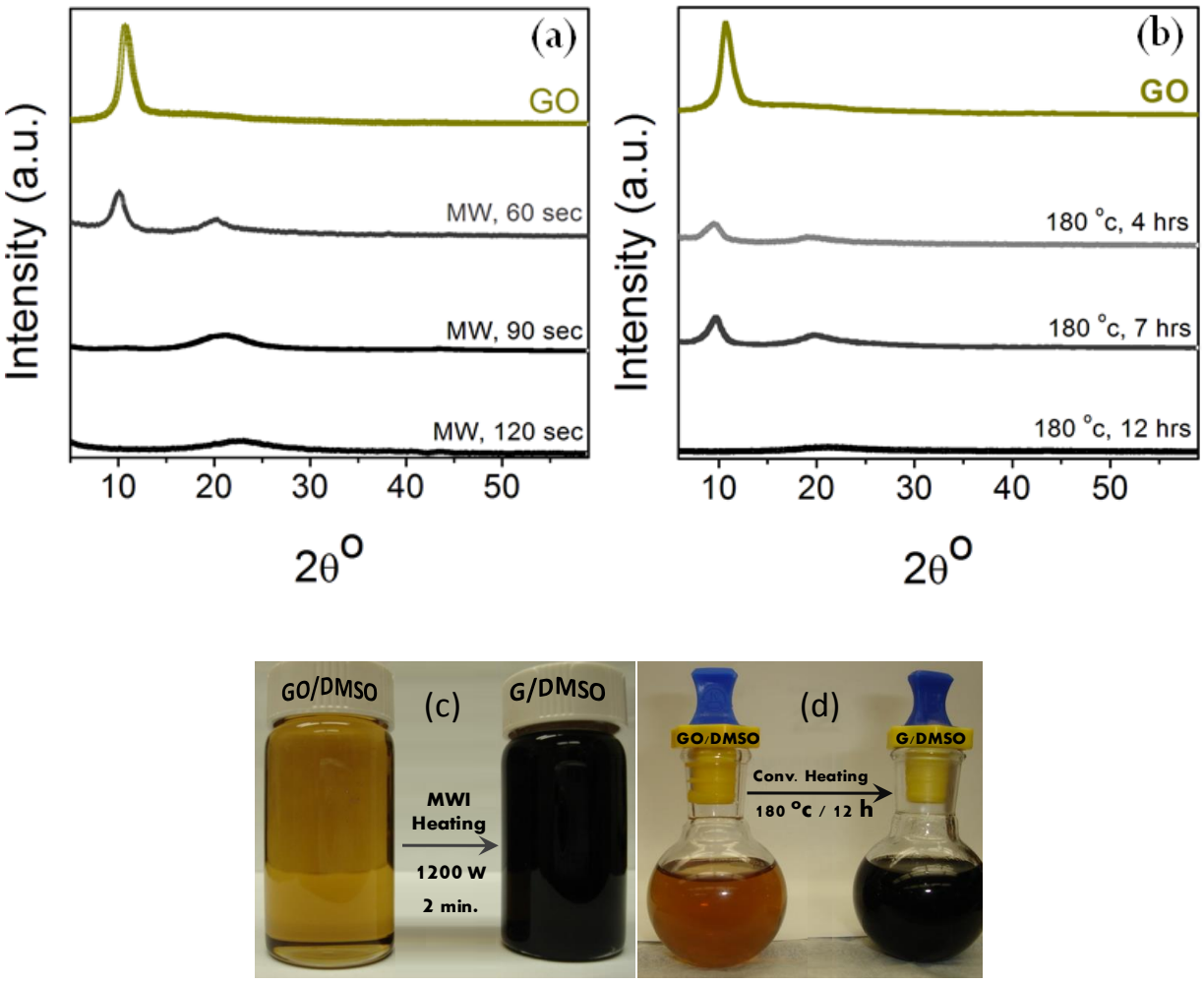

Figure 3-2 (a), (b) Changes in the XRD pattern of GO from (a) MW reduction after 1, 1.5 and 2 min, and (b) thermal reduction after 4, 7 and 12 hrs. (c), (d) Digital images of GO and graphene (G) colloidal suspensions in DMSO for (c) MW and (d) thermal syntheses.

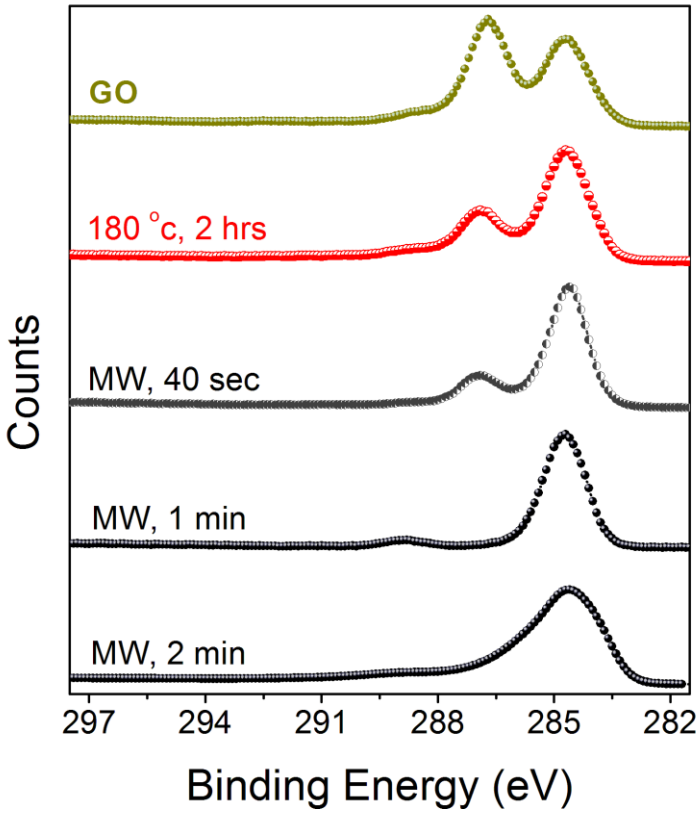

Figure 3-3 Changes in the C1s XPS spectra of GO after 2 hrs of heating at 180 ºC in DMSO, and after 40 s, 1 min and 2 min of MWI in DMSO.

Additional structural and chemical composition information on the sample prepared by the MWI of GO in DMSO for 2 min was obtained using FT-IR and UV absorption spectroscopy (Supporting Information, SI). The FT-IR spectrum clearly showed the disappearance of the C-O peaks at 1400 cm^{-1} (carboxy) and 1220 cm^{-1} (epoxy) as well as the C=O stretching vibrations of the COOH groups at 1740 cm^{-1}, and the O-H deformations of the C-OH groups at 1350-1390 cm^{-1} (**Fig. 3.4**). [112, 114] The UV absorption spectrum of GO shows the characteristic shoulder at 305 nm attributed to n→π* transitions of C=O bonds.[35] This shoulder disappears after the 2 min MWI of GO and a new absorption peak appears at 283 nm attributed to π→π* transitions of extended aromatic C-C bonds typical of RGO (**Fig. 3.5**). [2, 115] Raman spectroscopy is a sufficiently powerful,

sensitive, nondestructive and rapid analytical technique that can provide information about the structural and electronic properties of carbon nanostructures and graphene. **Figure 3.6** compares Raman spectra of GO (**Fig. 3.6-a**) and RGO (**Fig. 3.6-b**). For GO, two distinct bands are clearly observed at 1345 and 1589 cm^{-1} due to the D and G bands, respectively. In case of RGO, the same two distinct bands observed for GO can be seen also in RGO. The band at 1350 cm^{-1} is the disorder mode band that is related to the defects and disorder induced modes in graphene, and the band at 1599 cm^{-1} is attributed to the vibration of sp^2-bonded carbon atoms in the planar hexagonal graphite lattice. The reduced D/G ratio (0.33) between the two bands compared to GO (0.79) is an approximate indication of the disorder degree in RGO by the solvothermal treatment.

Typical TEM images of the synthesized graphene sheets by MWI in the presence of DMSO are shown in **Fig. 3.7**. The TEM images show a few stacked layers and a lateral size up to a few micrometers. Also the TEM images show that some of the graphene layers are folded on one edge with isolated small fragments on the surfaces. It should be mentioned that the electron beam of the TEM induces the folding and entanglement of the graphene sheets due to the intrinsic nature of the 2D structure of the sheets where they become thermodynamically more stable via folding. [24]

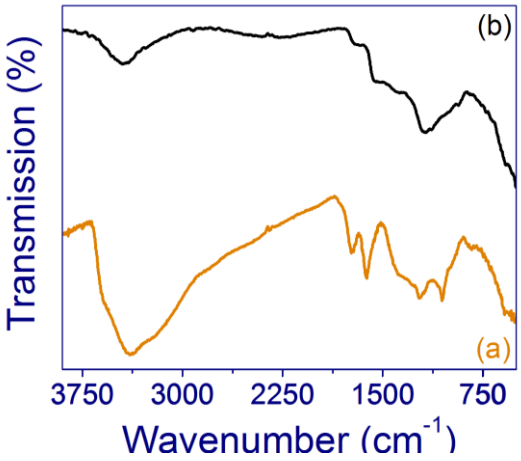

Figure 3-4 IR spectra of GO and graphene prepared by MWI in DMSO.

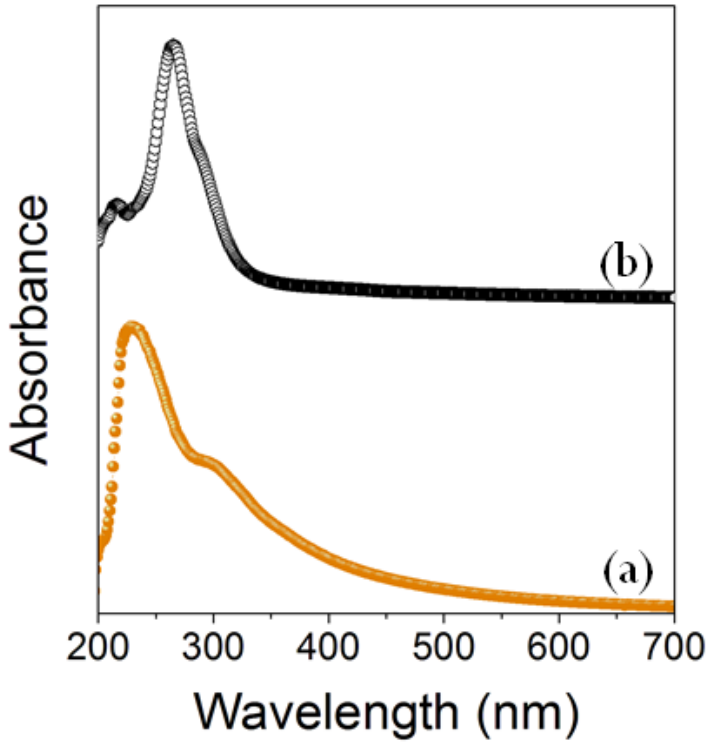

Figure 3-5 UV-Vis spectra of GO (a) and graphene (b) prepared in DMSO.

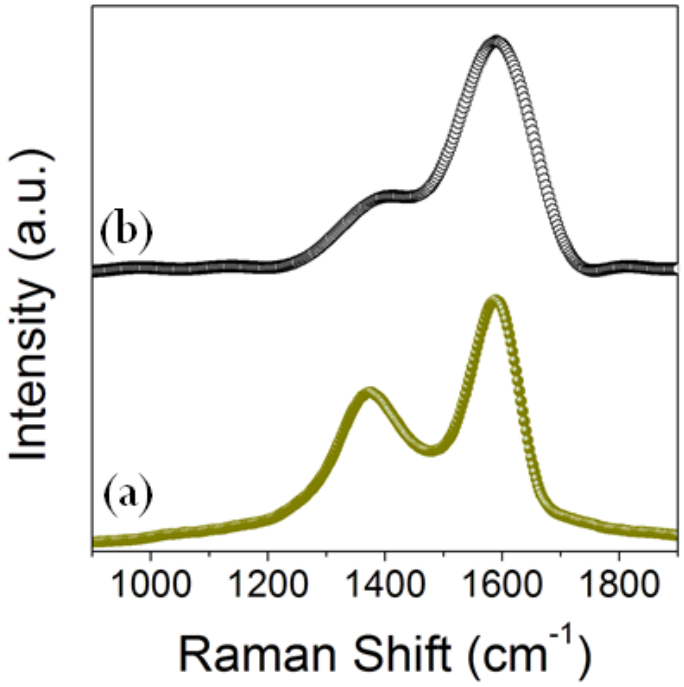

Figure 3-6 Raman spectra of GO before (a) and after (b) 2 min-MWI in DMSO.

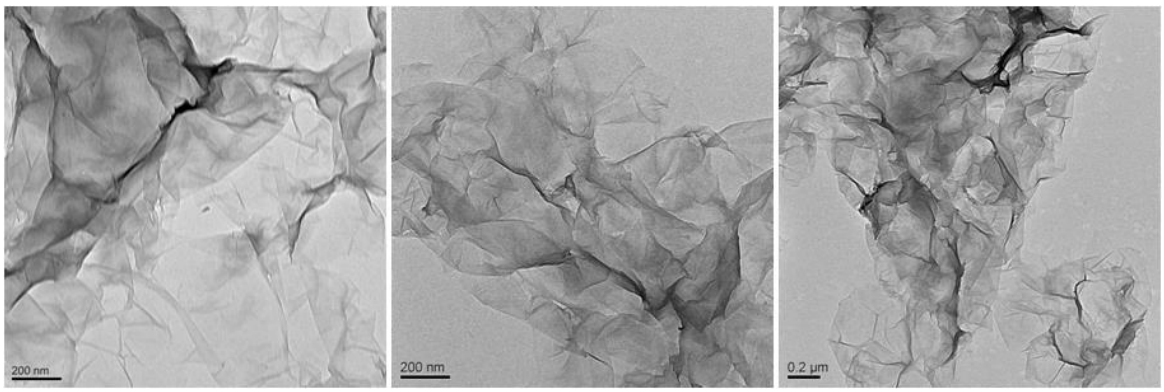

Figure 3-7 TEM images of graphene sheets prepared by MWI of GO in DMSO.

3.4.2 Cubic and hexagonal CdSe nanocrystals by microwave synthesis

In order to synthesize high quality CdSe nanocrystals supported on graphene using the DMSO-MWI approach, we first developed a ligand-controlled method for the synthesis of CdSe nanocrystals in DMSO using MWI. In this case, DMSO was used as a solvent for the reaction between the Cd and Se precursors (cadmium oleate and TOP-Se, respectively). We investigated the effect of adding two different coordination ligands TOPO (trioctylphosphine oxide) and HDA (hexadecylamine) on the size and phase of the CdSe nanocrystals formed by the MWI method.

Figure 3.8 displays the XRD patterns of CdSe nanocrystals formed by MWI using TOPO, HDA and TOPO-HDA mixtures as coordination ligands to the CdSe nanocrystals in DMSO. The results clearly indicate that CdSe nanocrystals prepared in the presence of HDA or HDA + TOPO have a cubic (zinc blende, ZB) structure, as can be seen from the three characteristic ZB peaks of the (111), (220), and (311) planes between $2\theta = 25^{o}$ and 49^{o}, and the absence of the (102) and (103) diffractions characteristic of the hexagonal (wurtizite, WZ) structure at $2\theta = 35^{o}$ and 47^{o}, respectively (**Fig. 3.8-a,b**). [116, 117] In the presence of TOPO alone (or DMSO only) the hexagonal structure of CdSe is evident (**Fig. 3.8-c,d**). By increasing the amount of TOPO relative to HDA,

the XRD pattern reveals a change in the crystalline structure from a cubic to a hexagonal structure as suggested by the multiple structures of the (111) ZB peak and the emergence of the (103) peak of the WZ structure.

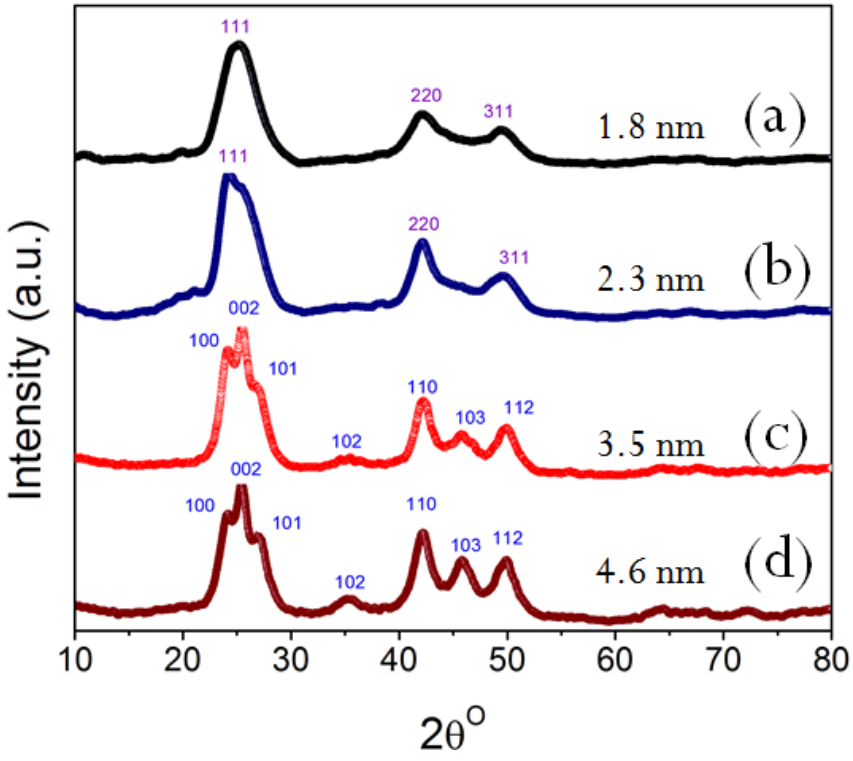

Figure 3-8 XRD patterns of CdSe nanocrystals prepared by MWI of cadmium oleate and TOP-Se in DMSO (d), and with the addition of: (a) TOPO + HDA, (b) HDA only, and (c) TOPO only. The crystallite sizes indicated are calculated based on Debye-Scherrer equation.

The change in the crystalline structure from ZB to WZ is accompanied by a decrease in linewidth of the diffraction peaks indicating an increase in the crystallite size of WZ nanocrystals. In the cubic CdSe, the crystallite size ranges from 1.8 to 2.3 nm, whereas in hexagonal CdSe it varies between 3.5-4.6 nm as calculated from the width of the diffraction peaks using the Debye-Scherrer equation. [118] This trend is consistent with the correlation between particle size and absorption peak for CdSe nanocrystals prepared by the conventional thermal heating route. [119] This

trend is also confirmed by the TEM images of the CdSe nanocrystals prepared by the MWI method as shown in **Fig. 3.9**. It is clear that the WZ nanocrystals are faceted and some of the hexagonal facets can be clearly seen in the TEM image. The analysis of several TEM images indicates the particle size of the nanocrystals prepared in the presence of HDA or HDA-TOPO ranges from ~2 to 3 nm while those prepared in the presence of TOPO (or DMSO only) range from ~4 to 7 nm.

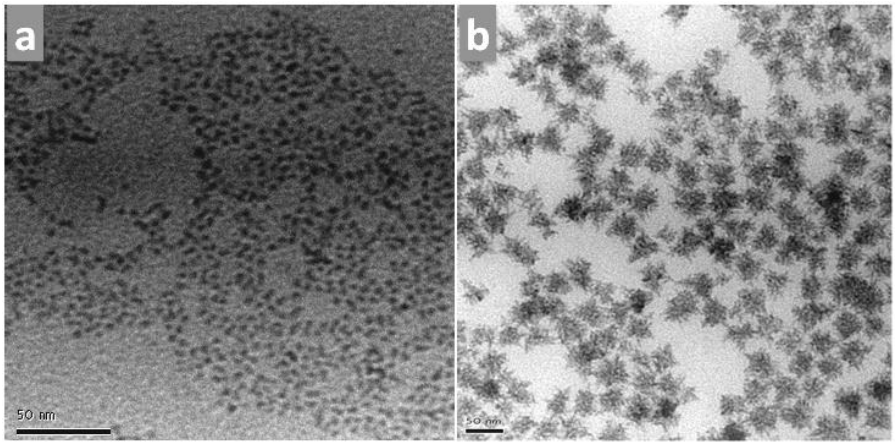

Figure 3-9 TEM images of CdSe nanocrystals with (a) cubic and (b) hexagonal structures prepared by MWI of cadmium oleate and TOP-Se in DMSO (hexagonal), and with the addition of TOPO and HDA (cubic). The scale bar is 50 nm.

The observed effects of the coordination ligands on controlling the size and phase of the CdSe nanocrystals prepared by the MWI in DMSO are consistent with previous results on CdSe nanocrystals prepared by conventional thermal heating at 275 ^{o}C. [120-123] Because of the small energy difference between the ZB and WZ structures of CdSe (9 meV/2 atom), the kinetics that govern the growth of the nanocrystals can be controlled by using a mixture of coordination lignads which can promote the formation of the metastable cubic nuclei. [120-123] In the present case, the addition of the less sterically hindered primary amine HDA allows the formation of a denser coordination layer on the nanocrystals' surface than the highly hindered trialkylphosphine compounds TOP and TOPO, thus stabilizing the cubic phase relative to the hexagonal phase of

CdSe. [120-123] Additionally, the phase change from cubic to hexagonal is probably due to the increase in the crystallite size and change in the atomic configuration of CdSe nanocrystals.

The absorption and emission spectra of the CdSe nanocrystals prepared in DMSO in the presence of HDA/TOPO as a function of MWI time are shown in **Fig. 3.10**. The solution contained cadmium oleate (0.2 mM), TOP-Se (0.5 mM), HDA (8 mmol), TOPO (5 mmol) in DMSO and the reaction was performed in a 1200 W domestic microwave oven. The systematic red shift in the absorption and emission peak is attributed to the growth of the CdSe nanocrystals. The data demonstrates the effectiveness of the MWI method in preparing size-selected nanocrystals since the reaction time can be controlled within the time scale of the nucleation and growth of nanocrystals.

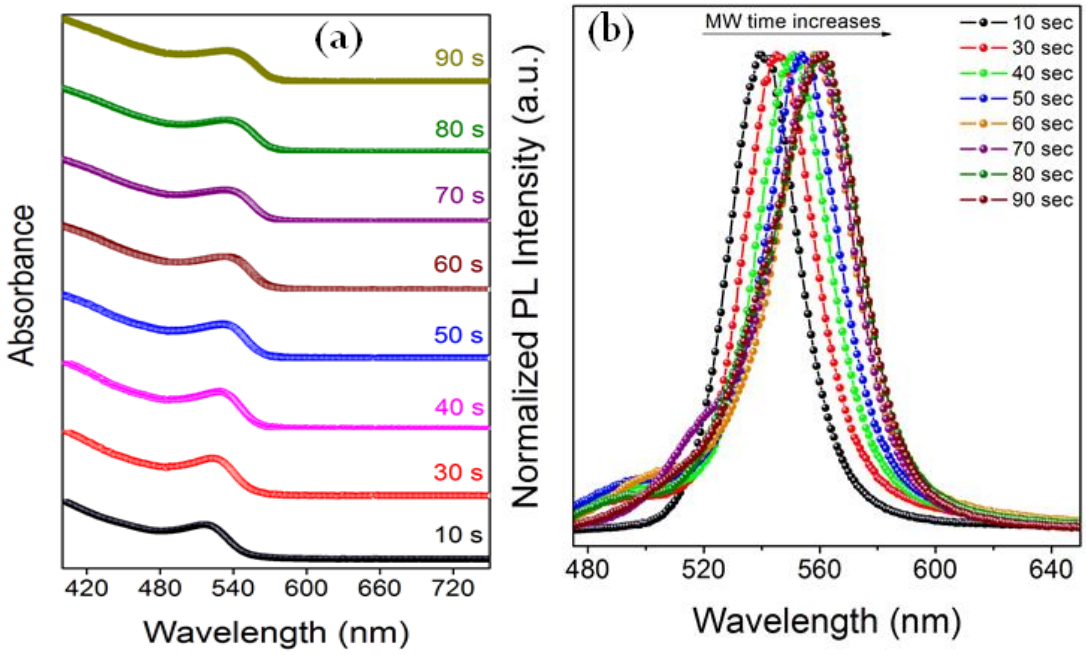

Figure 3-10 (a) UV-Vis absorption and (b) emission spectra of cubic CdSe nanocrystals prepared by MWI of cadmium oleate and TOP-Se in DMSO with the addition of TOPO and HDA at different microwave irradiation times.

3.4.3 Cubic and hexagonal CdSe nanocrystals supported on graphene

Following the development of the DMSO-MWI approaches for the conversion of GO into graphene and the synthesis of ligand-controlled CdSe nanocrystals, a combined synthesis approach was developed to prepare cubic or hexagonal CdSe quantum dots supported on graphene. To allow nucleation and growth of CdSe nanocrystals along with the simultaneous reduction of GO to graphene, the reaction mixture consisting of cadmium oleate, TOP-Se and GO in DMSO was microwave irradiated for 2 min which resulted in the formation of hexagonal CdSe on graphene. For the formation of cubic CdSe nanocrystals on graphene, a HDA or TOPO-HDA mixture was added to the reaction mixture before the MWI.

The simultaneous reduction of GO to graphene and the formation of CdSe quantum dots on graphene is clearly evident from the XRD, XPS, TEM, UV-Vis absorption, and photoluminescence data of the CdSe-graphene nanocomposites prepared by the DMSO-MWI method as discussed below. The XRD spectra of cubic and hexagonal CdSe nanocrystals supported on graphene (**Fig. 3.11**) match well with the corresponding spectra of the unsupported nanocrystals, thus confirming the synthesis of crystalline phase-selected CdSe quantum dots on graphene.

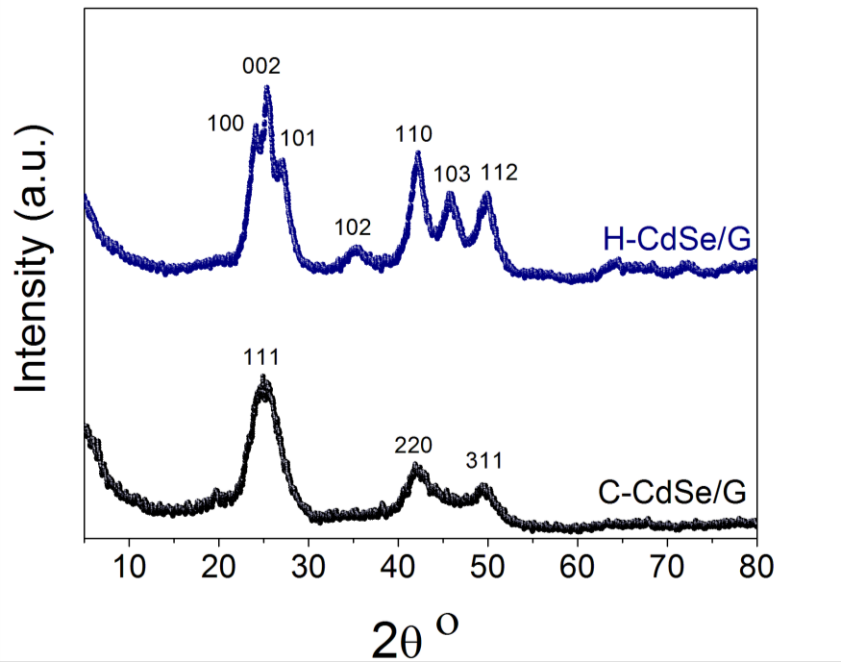

Figure 3-11 X-ray diffraction patterns of hexagonal and cubic CdSe on graphene.

The C1s, Cd3d and Se3d XPS spectra of the CdSe supported on graphene are compared to the corresponding spectra of pure GO and CdSe nanocrystals as shown in **Fig. 3.12**. The C1s spectra of both the cubic (C-CdSe/G) and hexagonal (H-CdSe/G) graphene nanocomposites shown in **Fig. 3.12-a** are similar to that of the RGO (**Fig. 3.3**) indicating the conversion of GO into graphene during the MWI synthesis of the CdSe nanocrystals. However, the extent of GO reduction appears to be more in the C-CdSe/G than in the H-CdSe/G composites as indicated by the complete absence of all C1s peaks corresponding to oxygen functional groups in the XPS spectrum of C-CdSe/G nanocomposite. This is can be attributed to the enhanced reducing environment created by the addition of HDA during the synthesis of C-CdSe/G nanocomposite.

The binding energies of $Cd3d_{5/2}$ and $Se3d_{5/2}$ electrons in the CdSe nanocrystals observed at 405.0 eV and 53.8 eV, respectively (**Fig. 3.12**) correspond to Cd (+II), and Se (-II). [124] Noticeable shifts of the Cd3d and Se3d binding energies towards lower energies are observed in

both the C-CdSe/G and H-CdSe/G nanocomposites as shown in **Fig. 3.12**. This may suggest a change in the oxidation state or chemical environment of the Cd and Se atoms present in the graphene matrix. Therefore the XPS data provides evidence for a strong interaction between the CdSe nanocrystals and graphene. This is consistent with the robust nature of the CdSe/G nanocomposites and their stability against ultrasonication which suggest that the current synthesis approach produces CdSe/G nanocomposites with good interfacial properties.

The decoration of the 2D graphene sheet surface with the CdSe nanocrystals can be easily observed by TEM as shown in **Fig. 3.13**. Both the cubic (**Fig. 3.13-a,b**) and the hexagonal (**Fig. 3.13-c,d**) nanocrystals are well dispersed on the graphene sheet surface. The average sizes of the cubic and hexagonal nanocrystals on graphene are 3-4 and 5-7 nm, respectively. No apparent aggregation of CdSe nanocrystals can be seen on the graphene sheets, and no significant areas of the graphene sheets are lacking the CdSe decoration. The cubic CdSe nanocrystals appear to assemble in well organized patterns on the surface of the graphene (**Fig. 3.12-b**) probably because of their small sizes and the high degree of monodispersity. There appear to be some larger particles (4-5 nm) which could be a result of additional particles laying on the assembled ones.

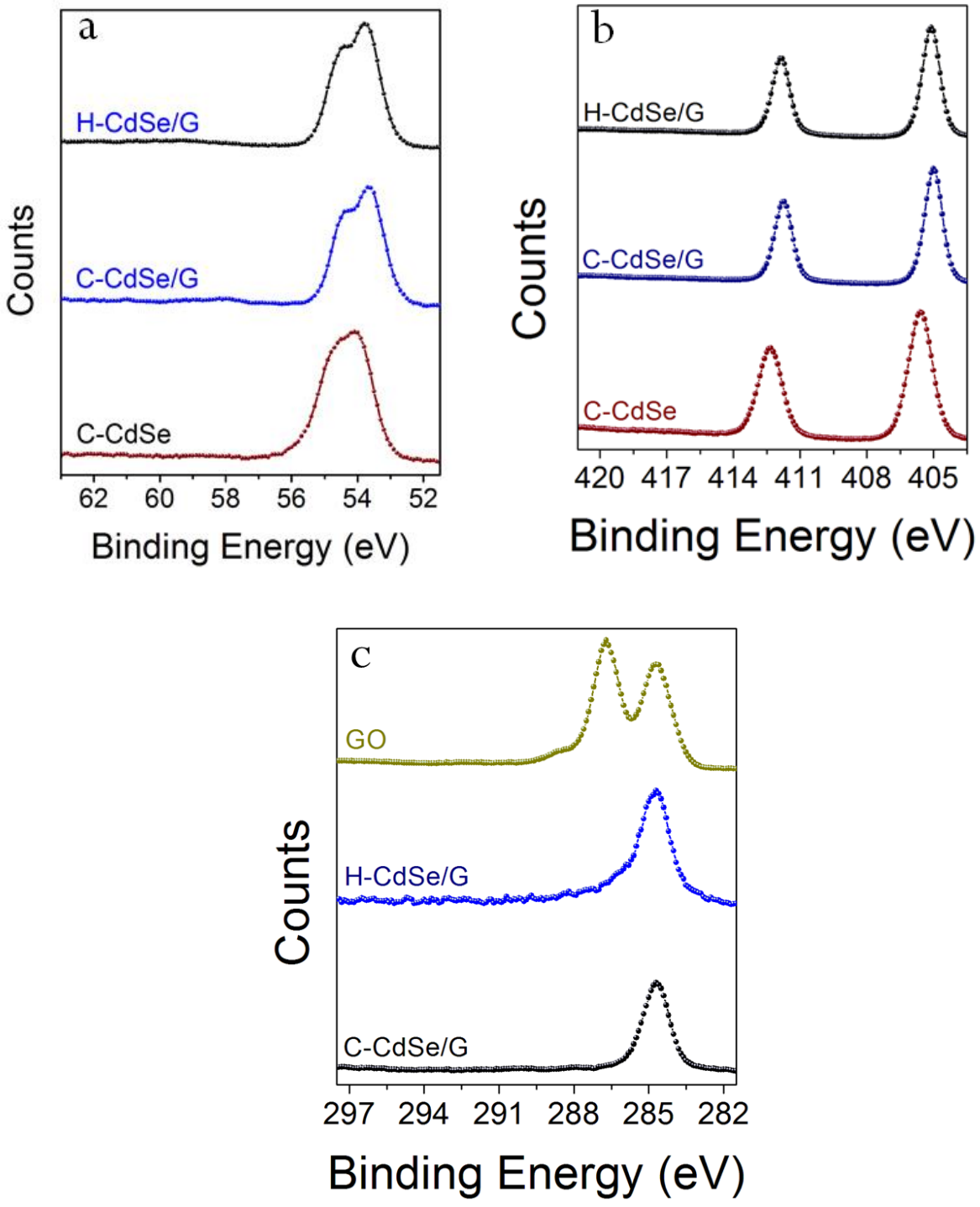

Figure 3-12 (a) C-1s XPS spectra of GO and graphene decorated with hexagonal (H-CdSe/G) and cubic (C-CdSe/G). Cd-3d (b) and Se-3d (c) XPS spectra of H-CdSe/G, C-CdSe/G, and unsupported C-CdSe nanocrystals.

The small increase in the size of the CdSe nanocrystals in the CdSe/G nanocomposites relative to the free CdSe nanocrystals is probably related to the nucleation and growth mechanism of CdSe nanocrystals in the presence of GO. One possibility is that the CdSe nanocrystals are directly nucleated on the existing GO sheets followed by reduction of GO and the growth of the CdSe nanocrystals on the RGO sheets. The presence of the oxygen functional groups in GO may actually create attractive heterogeneous nucleation sites for the CdSe nuclei which would decrease the barrier for the homogeneous nucleation process [125]. However, at present we do not have direct evidence for such a mechanism and more efforts are to be made in the future to compare the homogeneous and heterogeneous nucleation rates of CdSe nanocrystals in order to elucidate the growth mechanism of CdSe nanocrystals in the presence of GO or RGO sheets.

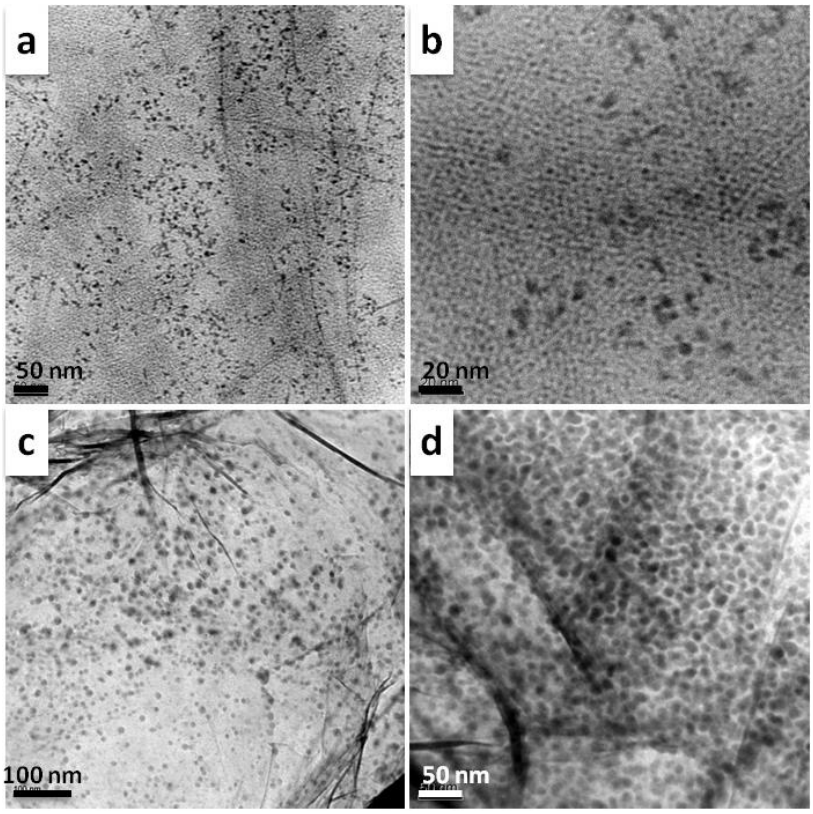

Figure 3-13 TEM images of (a, b) cubic and (c-f) hexagonal CdSe nanocrystals supported on graphene.

3.4.4 Shape-controlled synthesis of CdSe nanorods supported on graphene

The optical and electrical properties of semiconductor nanocrystals sensitively depend on both the size and the shape. Typical synthesis of CdSe nanorods involves the Cd precursor as CdO and ODPA in TOPO, and the Se precursor as elemental Se dissolved in TOP. The Se precursor is injected into Cd precursor at 320 °C. UV-Vis and PL spectra for CdSe nanorods obtained from this reaction after 2 min following injection in absence and in presence of GO sheets are shown in **Figs. 3.14**. A well-defined exciton peak at 540-553 nm due to the absorption in the visible region is evident, along with the corresponding emission peak between 560-600 nm in the PL spectrum. CdSe nanocrystals can grow either cubic (zincblende, ZB) or hexagonal (wurtizite, WZ) lattice structure where the energy difference between zincblende (ZB) and wurtzite (WZ) structures is very small (<9 meV/2 atom).

TEM images of CdSe nanorods prepared in absence of GO (**Fig. 3.15)** and CdSe nanorods anchored on graphene sheets **(Fig. 3.16)** indicate that the final nanocrystals are nonbranched nanorods, suggesting the growth is due to wurtzite nuclei because growth from zinc blende nuclei would likely result in branched nanoparticles. In principle, the reaction of CdSe monomers to form CdSe nanocrystals is very simple; monomers nucleate to form very small clusters which subsequently grow into nanocrystals. Nevertheless, the case becomes complicated by the presence of two different energetically accessible crystal phases, wurtzite and zinc blende. The crystal phase is critical in controlling the shape because different crystal facets of the growing nanoparticles may have different reactivities, and this determines the final morphology of the nanocrystals. The crystal phase and the reaction kinetics are controlled by thermodynamics of the reaction solution, which in turn are determined by temperature and chemical composition of the reaction mixture.

High temperatures favor the formation of wurtzite nanocrystals, while zinc blende nanocrystals are grown at lower temperatures. [126]

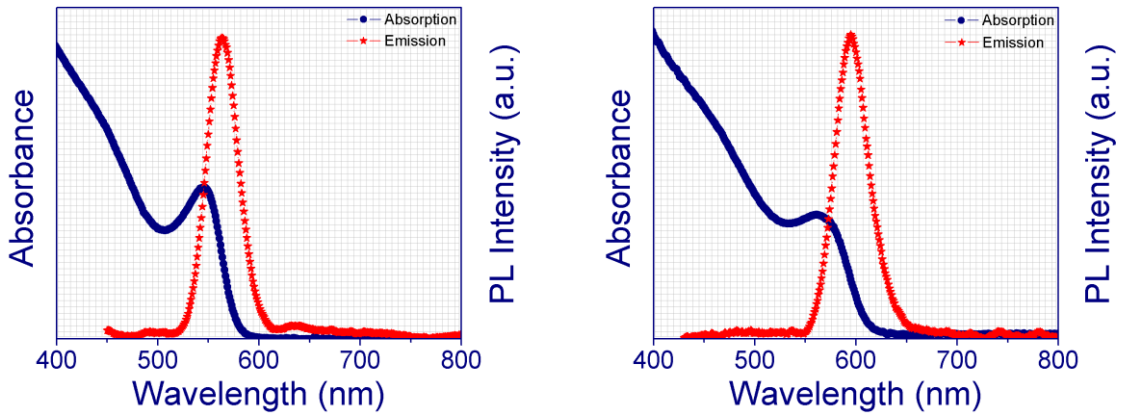

Figure 3-14 UV-Vis and normalized PL spectra of CdSe annorods (left) and CdSe nanorods anchored on graphene (right).

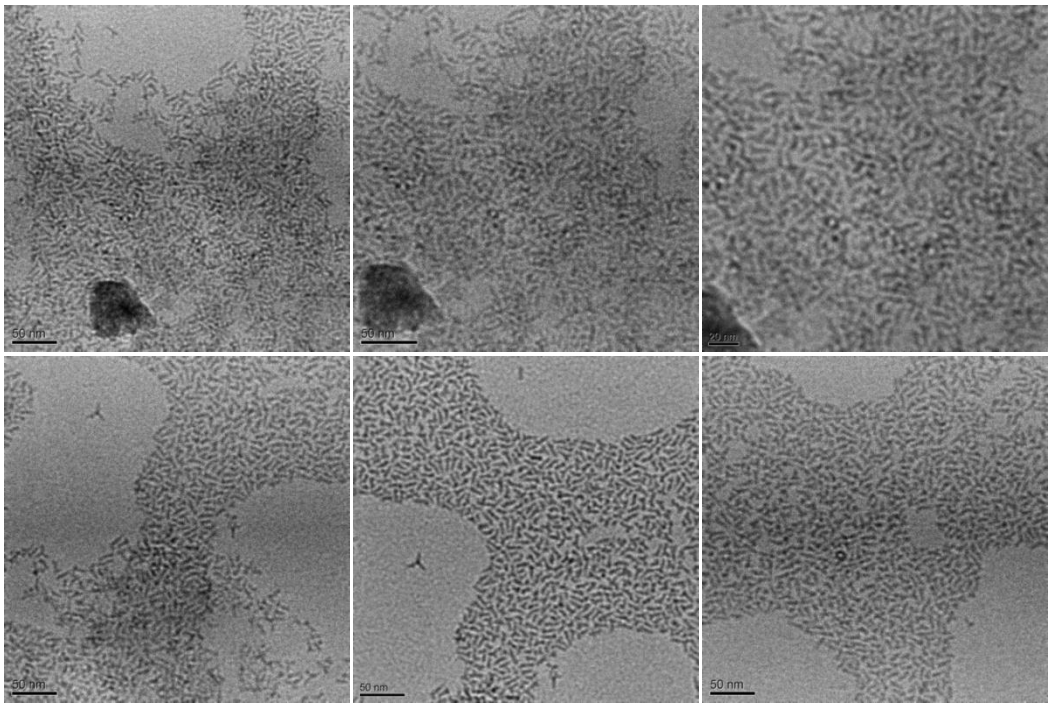

Figure 3-15 TEM images of CdSe nanorods prepared in DMSO/ ODA mixture.

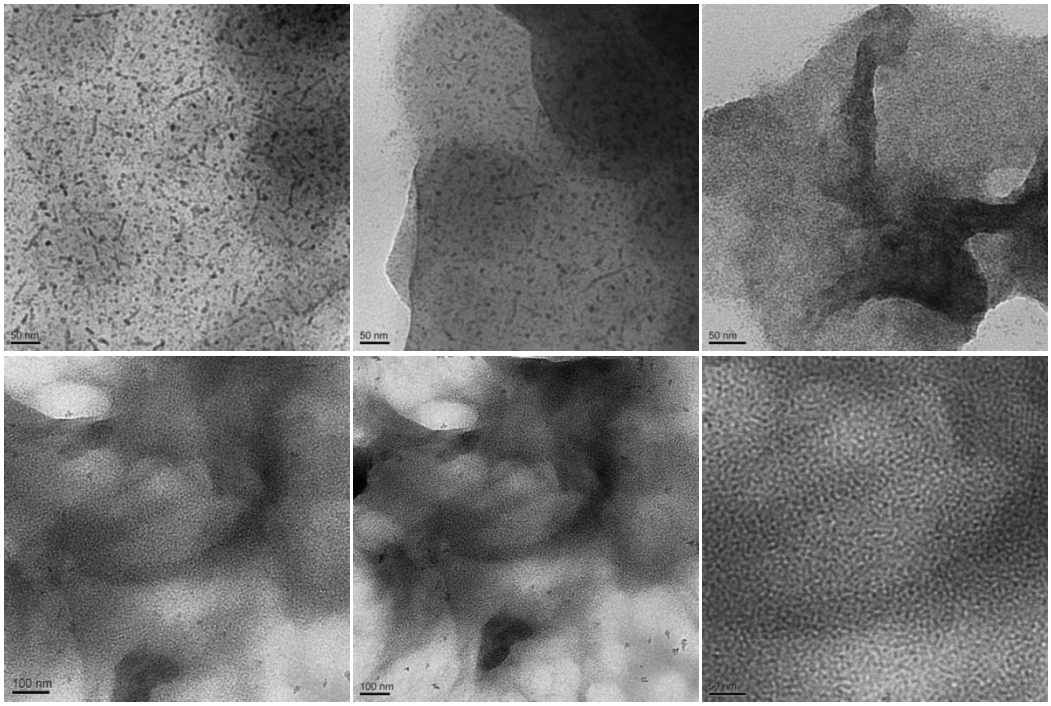

Figure 3-16 TEM images of CdSe nanorods anchored on graphene sheets prepared in DMSO/ODA mixture.

On the basis of the experimental results, a mechanism that interprets the deposition of nanocrystals and formation of CdSe nanorods/graphene nanocomposites can be illustrated as in **Fig.. 3.17**. The epoxy and hydroxyl functional groups at the surface of the basal planes and the carboxylic or carbonyl functional groups at the edges might be retained during the course of the GO reduction. During nucleation and growth these groups can act like anchor sites that enable the in situ deposition of nanocrystals attaching on the surface and the edges of the sheets [71]. Initially, the addition of tetradecylphosphonic acid (TDPA) to CdO leads to formation of metal complex. Then Cd^{2+} ions that are formed by the thermal decomposition and dissolution of CdO-TDPA metal complex in TOPO, might favorably bind to the O atoms of the negatively charged oxygen-containing functional groups on partially RGO sheets by an electrostatic force. With the addition of Se-TOP solution at a relatively high temperature (~300 ^{o}C), a large number of nuclei are formed in a very short time. The further increase in temperature by lengthening the MW irradiation time

allows primary crystals to grow while being anchored on the oxygen-containing groups or defect sites. In case of the formation of CdSe rods, the ratio of CdO/Se and the TDPA along with the injection temperature play an important role in determining the morphology of the deposited nanocrystals. As a result, the overall crystal had only single preferable growth direction, yielding CdSe rods. Significantly the temperature and the manner of adding Se-TOP exerts an influence on the stacking of the nuclei and formation of the rods in the crystal growth mechanism. A superheated mixture of CdO-TDPA/TOPO has to be obtained first prior to adding the Se-TOP mixture. A rapid addition of Se-TOP to the superheated mixture causes the burst of large amount of growing species in a very short time. Further investigations on the effects of other reaction parameters such as precursor's concentration, CdSe/GO ratio and reaction time on the mechanism of the simultaneous growth and reduction are still needed.

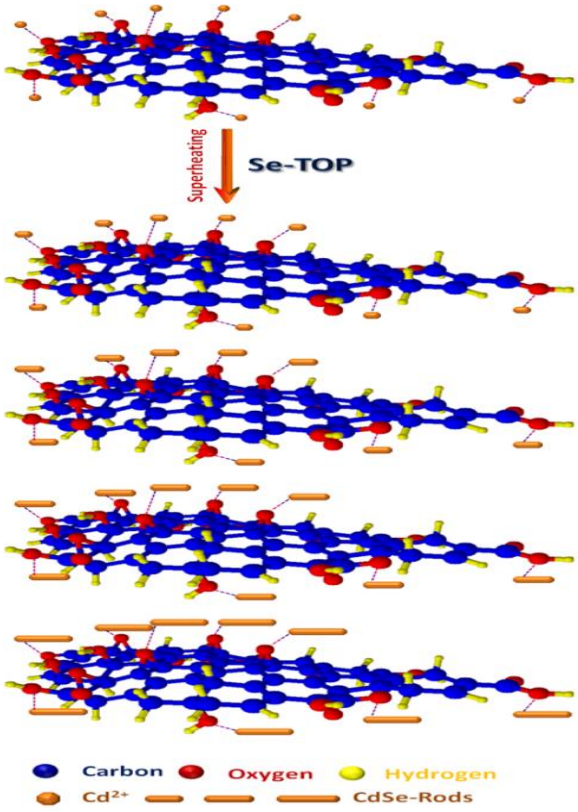

Figure 3-17 Illustrations CdSe nanorods growth in presence of GO.

3.4.5 Quenching of CdSe photoluminescence by graphene

The absorption and emission spectra of the cubic and hexagonal CdSe nanocrystals prepared by MWI in DMSO in the presence of HDA/TOPO and TOPO, respectively with the simultaneous reduction of GO are shown in **Fig. 3.18**. In comparison to the spectra obtained under identical preparation conditions except for the presence of GO, noticeable spectral shifts in both the absorption and emission peaks are observed. For the hexagonal nanocrystals, the absorption and emission peaks shift from 540 and 590 nm, respectively in the absence of graphene to 560 and 625 nm, respectively when GO is present during the MWI synthesis. For the cubic nanocrystals, the magnitude of the spectral shifts due to the presence of graphene was much less (absorption and emission bands at 489 and 542 nm, respectively in the absence of graphene and 500 and 555 nm, respectively in the presence of graphene). The red spectral shift is attributed to the growth of the CdSe nanocrystals where the presence of GO may have altered the nucleation and growth mechanisms. Another possibility is the effect of GO on the adsorption of the capping agents on the CdSe nuclei. It is interesting that the extent of the red spectral shifts due to the presence of GO is much more pronounced for the hexagonal than for the cubic CdSe nanocrystals. This is also consistent with the observed larger size of the hexagonal nanocrystals. Although a significant quenching of the fluorescence is observed from both the cubic and hexagonal CdSe nanocrystals when the particles are prepared in the presence of GO, again the extent of PL quenching is more pronounced in the hexagonal crystals. This quenching is attributed to the efficient electron accepting ability of graphene which could result in electron transfer from the excited CdSe nanocrystals [46].

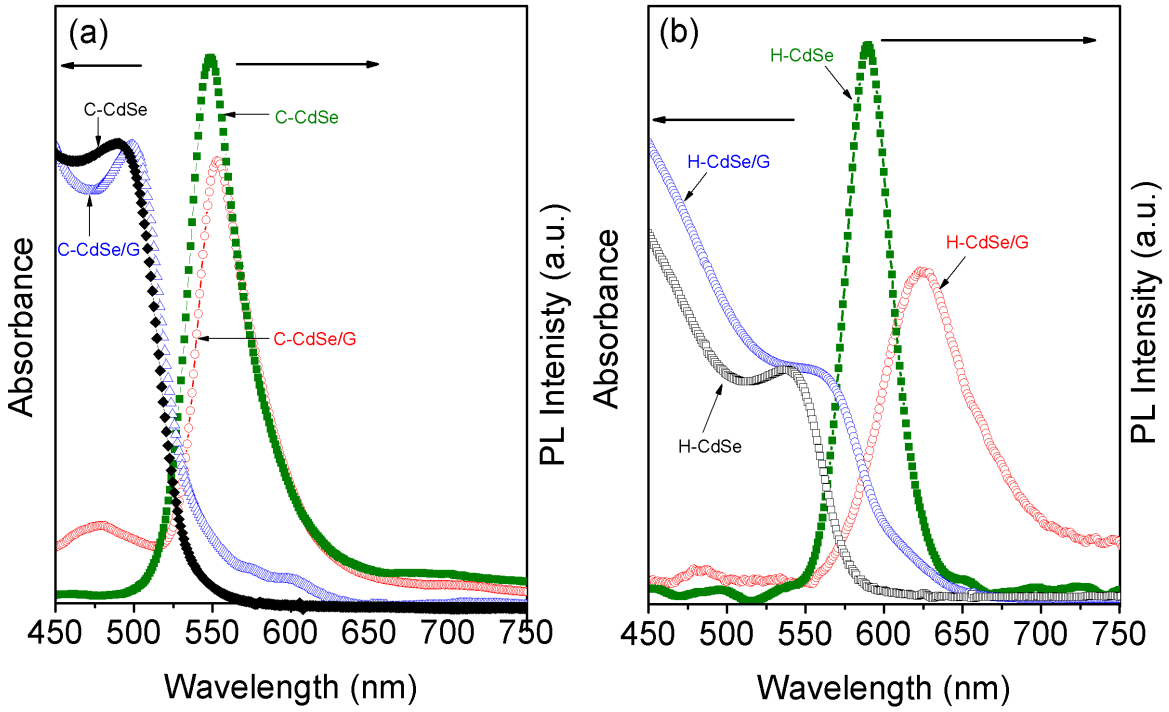

Figure 3-18 Comparison of UV-Vis absorption and photoluminescence spectra for (a) cubic and (b) hexagonal CdSe nanocrystals with and without graphene.

A qualitative trend of decreasing the fluorescence from both the cubic and hexagonal CdSe nanocrystals is observed by increasing the starting amount of GO in each synthesis. However, comparing the PL behavior of CdSe nanocrystals prepared in the absence and presence of GO cannot yield accurate quantitative data due to the possible role of GO in altering the nucleation and growth mechanisms of the CdSe nanocrystals and the extent of the adsorption of capping agents on the crystal surfaces. In order to assess the quenching effect of graphene on the emission from CdSe nanocrystals in a more quantitative manner, the fluorescence spectra of the CdSe nanocrystals dispersed in chloroform were measured as a function of the concentration of graphene added to the CdSe solution. We chose chloroform because the C-CdSe nanocrystals prepared without GO can be easily dispersed in chloroform as shown in solutions photographic images shown in **Fig. 3.19**. The concentration of C-CdSe nanocrystals was kept constant (75 µg/ml) in all

the solutions containing variable concentrations of graphene (0, 12.5, 15, 17.5, 20, 22.5, and 25 μg/ml) using the procedure outlined in the experimental section in order to eliminate any errors due to dilution. As shown in **Fig. 3.19**, all solutions showed an absorbance value of ~0.41 at the excitation wavelength of 430 nm and thus the number of the absorbing nanocrystals will be comparable and the corresponding fluorescence spectra should show the effect of the graphene concentration on the emission intensity. Indeed, the emission spectra displayed in **Fig. 3.19** clearly show that the addition of graphene quenches the fluorescence from the C-CdSe nanocrystals.

The quenching mechanism of the PL from the CdSe nanocrystals could be explained by either electron or energy transfer from the excited nanocrystals. Efficient energy transfer from individual CdSe/ZnS nanocrystals to single- and few-layer graphene films has been recently demonstrated by Brus and co-workers [96]. They suggested that resonant energy transfer is much faster than photoexcited electron transfer due to the weak electronic coupling between the core CdSe nanocrystal and graphene due to the presence of the insulating ZnS outer shell. In the present work, CdSe nanocrystals can directly interact with the graphene sheets without the presence of an isolated shell and this may lead to increasing the rate of electron transfer relative to that of energy transfer. It may also be possible to increase the rate of electron transfer by increasing the ordered assembly of the nanocrystals and thus the interfacial interaction between the CdSe nanocrystals and graphene. Ultrafast pump-probe time-resolved spectroscopy may help to understand the quenching mechanism in more detail.

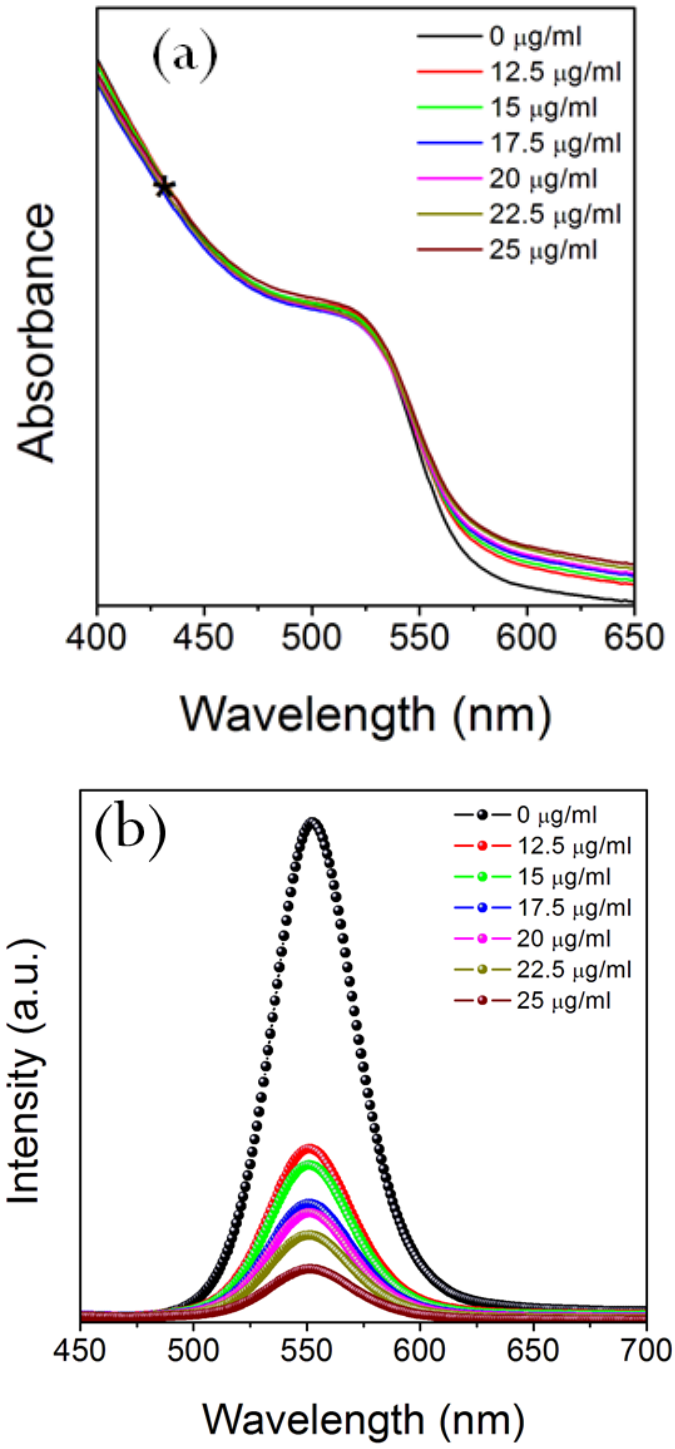

Figure 3-19 Absorption (a) and photoluminescence (b) spectra of CdSe-graphene solutions in $CHCl_3$-DMSO containing different amounts of graphene suspensions as indicated.

3.5 Conclusions

In summary, we have developed a facile and fast microwave irradiation method for the synthesis of graphene and CdSe nanocrystals of controlled size, shape, and crystalline structure dispersed on the graphene sheets. The reduction of GO into graphene takes place in DMSO within two minutes of microwave irradiation as opposed to 12 hrs of conventional thermal heating at 180 ^{o}C. The method allows the simultaneous reduction of GO and the nucleation and growth of CdSe nanocrystals using a variety of capping agents. Cubic and hexagonal CdSe nanocrystals with an average size of 3-4 and 5-7 nm, respectively have been prepared by the proper choice of the capping agent within a few minutes of microwave irradiation. High quality nearly monodispere CdSe nanocrystals have been supported on graphene with no evidence of aggregation. Direct evidence is presented for the efficient quenching of photoluminescence from the CdSe nanocrystals by graphene. The large surface areas of the graphene sheets and the highly dispersed semiconductor nanocrystals such as CdSe raises the potential of these composites as exciting material for use in future optoelectronics, and we believe that anchoring CdSe nanocrystals to graphene by means of this approach may bring fascinating chemical and physical properties to explore. The results of this work provide a new approach for exploring the size-tunable optical properties of CdSe nanocrystals supported on graphene, which could have important implications for energy conversion applications such as photovoltaic cells where CdSe quantum dots, the light-harvesting material, are supported on the highly conducting flexible graphene electrodes.

CHAPTER 4 Solvothermal Synthesis of Ceria-Graphene Nanocomposites: Low-Temperature CO Catalytic Oxidation

4.1 Overview

Herein, a facile single-step solution-based synthesis of ceria-graphene (CeO_2/RGO) nanocomposites is reported for the first time. The method is based on ethylenediamine-assisted solvothermal treatment of GO, which allows controlled reduction of GO to graphene (RGO) with by controlling the reaction temperature. The approach is potential for large scale production and low cost processing, The same approach was modified and utilized to synthesize CeO_2/RGO nanocomposites with different oxygen content in a contemporarily fashion using a mixture of GO and cerium nitrate in ethylenediamine (EDA) solution at different temperatures. Through this synthetic approach, an even distribution of 4-5 nm spherical CeO_2 nanoparticles of uniform size and shape was successfully achieved in situ on the high surface area RGO sheets in one-pot reaction and without post-preparation treatments. Different conditions to control the crystallinity and morphology of the nanocomposite structures are examined. We also show that the CeO_2/RGO nanocomposites can be utilized as an active support for noble metals for an efficient low-temperature CO catalytic oxidation. The results provides a new simple, efficient, scalable, environmentally-friendly and economically-favorable approach for large scale production of metal oxide nanostructures supported on graphene which could have important implications for industrial and environmental remediation.

4.2 Introduction

Graphene, a highly versatile carbon material, has received a great attention in recent years because of its extraordinary structural, optical, thermal, mechanical and electrical properties. [3, 75, 127] Such intriguing and unique features make graphene promising in wide array of potential applications such as nanocomposites, sensors, supercapacitors, nanoelectronics, transparent conducting films, batteries, paper-like materials and others. [20] The unique two-dimensional nature and the extremely high surface area of graphene sheets make this carbon material an ideal support for the deposition of various inorganic nanoparticles. [44-46, 71, 87, 90, 95, 128-133] The combination of highest carrier mobility, thermal, chemical and mechanical stability of graphene with the size-tunable properties of metal and semiconductor nanocrystals offers many interesting applications in a wide range of fields including heterogeneous catalysis, nanoelectronics and devices. [46, 128, 132] Fueled with major and exciting advancements in the past few years, the cubic fluorite-structured oxide, ceria constitutes the most important class of the rare earth oxide nanostructures. [134] Because of the unique redox properties, the high oxygen storage capacity, the high refractive index (1.6 – 2.5 at 633 nm), the strong absorption in the UV range, the optical transparency in the visible range and the interesting catalytic and free radical scavenging properties, [135, 136] cerium oxides structures have received a significant attention from the research communities. They have been extensively studied for application in fast ion conduction in solid oxide fuel cells, [137] as environmental heterogeneous catalysts support, [138] as UV absorbers in UV-blocking, [139] in oxidation-resistance coatings, [140] three-way catalysts and diesel fuel, [141] gas sensing, oxygen pumps, amperometric oxygen monitors, fine chemical synthesis, mechanical polishing, and recently in toxicity and biomedical applications. [134, 142-144]

Unsurprisingly such wide applications of ceria have been supported by wide research and literature devoted to synthesis, characterization and applications of cerium oxide nanostructures. Several solution-based routes have been developed for the conversion of low cost GO into graphene and graphene based composite materials. In this regard, there is much need to find a solvent which can act as a reducing agent for GO under mild reaction conditions and meanwhile can provide an environment for the synthesis of targeted nanostructures. The ability of the bidentate ligand ethylenedimaine (EDA, $NH_2CH_2CH_2NH_2$) as a molecular precursor to react with various inorganic precursors at mild conditions has been utilized by various groups to develop architectures of various metal, metal oxide and semiconductor nanostructures. Doussier-Brochard et al. [145] demonstrated a solvothermal route in ethylenediamine for the synthesis of p-type transparent conductor LaOCuS nanoparticles. In addition, $Zn_xCd_{1-x}S$ alloy nanocrystals have been fabricated facilely by Kim and co-workers [146] using ethylenediamine as a solvent-coordinating molecular template in water. In a similar study, Biswas et al. [147] reported the synthesis of high-aspect ratio alloy semiconductor nanowires $Cd_{1-x}Zn_xS$ using an ethylenedimaine-assisted solvothermal approach. Moreover, Kar and co-workers recently utilized the dual role of the ethylenediamine as a catalyst and reducing agent in the direct synthesis of ultrsmall water-dispersible ceria nanoparticles at room temperature. [148] Herein, we further extend the ethylenediamine-assisted solvothermal approach to the controlled synthesis of nanocomposite structure of CeO_2 nanoparticles and chemically synthesized graphene (RGO). The new developed synthetic approach described here permits the controlled reduction of GO to RGO with the synchronized growth and anchoring of CeO_2 nanoparticles evenly on the surfaces of RGO sheets.

4.3 Experimental

4.3.1 Chemicals and reagents

Graphite (natural, high purity,-200 mesh, 99.9999%, metal basis, Alfa Aesar), sulfuric acid (Fisher Scientific, Certified ACS), potassium permanganate (Analyt Reag., low in mercury, Mallinckrodt), hydrogen peroxide (30%, KMG), cerium (III) nitrate hexahydrate (99.99% trace metal basis, Aldrich), ethylenediamine (ReagentPlus, >99%, Sigma-Aldrich) and Gold(III) chloride solution in dil HCl (99.99% trace metals basis, Sigma-Aldrich).

4.3.2 Characterization

Samples were characterized by UV-Vis, PL, TEM, SEM, EDX, XRD, XPS and Raman spectroscopy. The optical absorption and the photoluminescence spectra were measured using HP-8453 spectrophotometer and Varian (CARY) spectrofluorometer, respectively. The X-ray diffraction (XRD) patterns of the powder samples were measured at room temperature with an X'Pert Philips Materials Research diffractometer with Cu $K_{\alpha 1}$ radiation. Crystallite size was calculated from diffraction patterns with Sherrer's equation and compared to that obtained from TEM analysis. Lattice constants were calculated from XRD peaks using formulas reported in the literature. To investigate the size, shape and morphologies of CeO_2 and CeO_2-RGO nanocomposites, transmission electron microscopy studies (TEM) were conducted using a Joel JEM-1230 electron microscope operated at 120 kV equipped with a Gatan UltraScan 4000SP 4K × 4K CCD camera. Samples for TEM were prepared by placing a droplet of colloid suspension in respective solvent on a Formvar carbon-coated, 300-mesh copper grid (Ted Pella) and allowing them to evaporate in air at ambient conditions. The X-ray photoelectron spectroscopy (XPS) analysis was performed on a Thermo Fisher Scientific ESCALAB 250 using a monochromatic Al

Kα X-ray. Scanning electron microscopy (SEM) and energy dispersive X-ray spectroscopy (EDX) were carried out using a Quantum DS-130S dual stage electron microscope. Raman spectra were recorded on Thermo Scientific DXR SmartRaman Spectrometer with 532 nm excitation laser source. The laser power was 5 mW, spectral resolution was ~ 4 cm-1 and the spectrum acquisition consisted of 100 accumulations with a total acquisition time of 15 min.

4.3.3 Graphene synthesis by EDA

GO was synthesized from graphite powder by a modified Hummers method as presented by Nogueira and co-workers [80, 149]. The oxidation results in carboxyl and hydroxyl functional groups on the ends and surfaces of GO sheets and this made exfoliation to GO easily achieved via ultrasonication (Branson 3510, 40 KHz) for 1 hour. Unless otherwise mentioned, a clear homogenous bright yellow dispersion of GO in DI-H_2O of 0.1 mg/ml was prepared and used for all experiments. For the EDA-assisted synthesis of RGO, a mixture of GO-H_2O and EDA (1:3 vol. ratios) was first sonicated for 15 min, then stirred and refluxed at 110^oC for 24 hour under atmospheric pressure. Upon completion, the reduction of the GO to RGO was indicated by the disappearance of the bright yellow color and formation of black flakes at the bottom of the flask. The mixture was cooled to room temperature and the black flakes of RGO were centrifuged, separated and repeatedly washed with DI-water (until the pH of the supernatant reached 7) and finally with ethanol. The washed flakes were dried in an oven at 60 ^oC overnight for further characterization. A similar synthesis of partially RGO was achieved by running the reaction between GO and EDA at room temperatures overnight.

4.3.4 Spherical CeO_2 nanoparticles synthesis by EDA

To investigate the effect of the temperature and heating source on the properties of CeO_2 nanostructures, different syntheses were performed using $Ce(NO_3)_3.6H_20$ as the same precursor for the Ce ions but with different conditions. The details of the different methods are outlined in the next section. The CeO_2 nanoparticles prepared from all protocols were separated by centrifugation and repeatedly washed first with DI-water until the pH of the supernatant reached 7 and finally with ethanol. Nanoparticles were then dried in an oven at 60^oC overnight.

Spherical CeO_2 nanoparticles were first prepared at room temperature as described by Kar et al. [148] with a little modification. A solution of 1 mmol of $Ce(NO_3)_3.6H_20$ in 50 ml ethylenediamine (EDA) was aged under vigorous stirring for 24 h, sample denoted as CeO_2-RT. After complete washing and drying, as described above, a portion of the as-prepared powder was calcinated by heat treatment in a muffle furnace under air. The furnace temperature was ramped to 450 ^oC at a rate of 25 ^oC/min. and then held at 450 for 3 hours. The calcinated powder was then cooled to ambient temperature and crushed. This calcinated sample is denoted here as CeO_2-RTC. A typical synthesis similar to that of CeO_2-RT was carried out but under reflux for 24 h at relatively low temperature of 110^oC using a conventional hot plate. Upon completion, the precipitate was treated the same way as before without further calcination. This sample is denoted as CeO_2-CH. For comparison, a solution of 1 mmol of $Ce(NO_3)_3.6H_20$ in 50 ml ethylenediamine (EDA) was irradiated in a domestic microwave oven for 2 min at 1200 W. The CeO_2 nanoparticles from this method is denoted as CeO_2-MW.

4.3.5 CeO_2/graphene nanocomposites synthesis by EDA

In a similar way described above for the synthesis of RGO assisted by EDA, the CeO_2/RGO nanocomposite was prepared as follow: a mixture of GO-H_2O and EDA (1:3 vol. ratios) was first sonicated for 15 min, then a pre-determined amount of $Ce(NO_3)_3.6H_20$ was added and then the whole mixture was vigorously stirred and refluxed at 110 ^oC for 24 hour under atmospheric pressure. The addition of EDA to GO led to an instantaneous color change from yellow-orange to grey and finally to black after the reaction is complete. Upon completion and after cooling the mixture to ambient temperature, the final product was separated and then washed six times with DI water and finally with ethanol and then left in an oven at 60 ^oC overnight to dry out. The same protocol was applied to synthesize CeO_2 nanoparticles on partially RGO by conducting the in situ reduction and growth at room temperature. To test the effect of the composition ratio between CeO_2 and RGO, the initial ratio between the Ce precursor and GO was varied.

4.3.6 Au-CeO_2/graphene ternary nanocomposites for CO catalytic oxidation

The ternary composites of Au loaded onto CeO_2/RGO have been assessed in CO conversion. General protocols of catalyst preparation, data measurement and analysis are outlined in this section. The colloidal deposition of Au nanospheres on the composite support (CeO_2, CeO_2-GO, CeO_2-partially RGO and CeO_2-RGO) or on the individual components was achieved as follows: 20 mg of the solid support was suspended in 20 ml DI water and sonicated at room temperature for 15 min. A few drops of NaOH aqueous solution were added to the obtained suspension to adjust the pH to the isoelectronic point of CeO_2 [150] and hence maximize Au loadings. A designated amount of $HAuCl_4$ dissolved in water (20 ml, 1 mM) was added to the suspension while stirring. The mixture was brought to boiling while stirring and 10 ml of 1% aqueous solution of trisodium citrate was added. After the reaction has complete, the mixture was centrifuged and

the precipitate was washed three times in boiling DI water to remove excess tetrachloauric acid and residual anions and finally was dried in an oven at 80 ^{o}C overnight.

Chloroaurate is commonly employed as a precursor for preparation of Au-based catalysts and thus chloride ions are among the residuals that can be retained in the catalysts and reduce their activities. It is well established that chloride (Cl^-) content even as low as 0.0006 (atom ratio), can have a significant detrimental effect on the catalytic activity of Au catalysts in a concentration-dependent manner. [151] Since halides have a high affinity to Au and can have high mobility on the surface of a hydroxylated support, Cl^- can cause Au species to agglomerate during the heat treatment of a catalytic reaction and thus lowers the catalytic activity. It might also modify the active sites on the metal surface either electronically or by physical adsorption onto CO active sites of Au nanoparticles (poisoning). Hindering the reducibility of gold may deactivate Au metal. [152-156] For these reasons, multiple washings were conducted to eliminate or minimize the presence of Cl^- or other halide species in our prepared catalyst.

To address the critical role of intensive washing in increasing the chances of CO adsorption and improving the catalytic activity of Au-based catalyst, two experiments were done on the same catalyst without washing and after an intensive washing of the catalyst with the standard procedures. The detrimental effect of residual chloride in Au catalysts was seen. It is generally accepted that chloride can affect the activity in two ways. One way is to cause agglomeration of nanosized Au particles upon heat treatment or to poison the active sites at the metal surface. [151] Beside halides, it is know that anions like phosphates and sulfates can suppress the catalytic activity of solid-supported Au. No detailed studies exist on whether or how nitrate would negatively affect Au catalysis. [157] The nature of the wash solution is critical and can result in an active or inactive catalyst. For these reasons, after centrifugation, the solid was repeatedly washed

with hot DI water. As determined from ICP measurements for representative catalysts, the Au content in Au-CeO_2 and Au-CeO_2-GO ranges between 4.3 to 5% by weight.

Experiments for the CO catalytic oxidation were performed using a fixed bed-programmable flow tube furnace reactor (Thermolyne 2100) [107] as shown in **Fig. 4.1**. In a typical experiment, 20 mg of the test catalyst was dispersed in glasswool and placed inside a pyrex glass tube. The sample and furnace temperatures were measured by a thermocouple placed in contact with the catalyst bed and in the middle of the tube furnace, respectively. Signals from thermocouples were processed using an SC-2345 data acquisition board. To plot temperatures and other measurement parameters, a data acquisition software using Labview was utilized. A gas mixture consisting of 4 wt % CO and 20 wt % O_2 in balance helium was passed over the sample at a flow rate of 100 cm^3/min while the temperature was ramped to 400^oC at maximum. The flow rate was controlled by a set of MKS digital mass flow meters. The conversion of CO to CO_2 was monitored using an online infrared gas analyzer (ACS, Automated Custom Systems Inc.) to detect the exit gas, which is then vented to outlet.

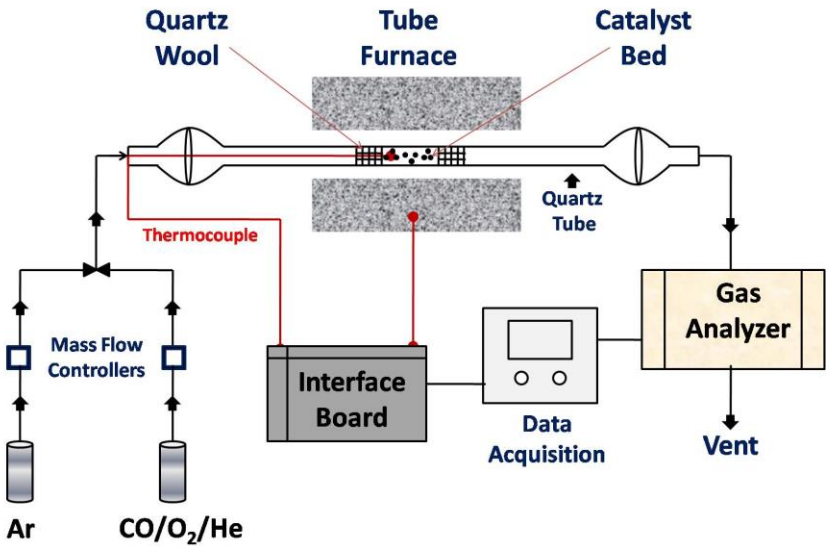

Figure 4-1 Schematic representation of typical set up used in CO catalytic oxidation

4.4 Results and Discussion

4.4.1 Controlled reduction of GO to RGO by EDA

The successful controlled reduction of GO to RGO with different extents of oxygen containing functional groups by EDA under solvothermal conditions of both room temperature and 110^{o}C was verified by monitoring the UV absorption spectroscopy, X-ray diffraction (XRD) and X-ray photoelectron spectroscopy (XPS). The UV-visible spectrum of GO dispersion in water is featured by two absorption bands in the range of 200-400 nm; a little shoulder at the lower energy part (~305 nm) due to the n-π* electronic transitions associated with the bonding in oxygen containing functional groups and a maximum absorption peak in the higher energy part around 230 nm due to the π-π* electronic transitions associated with the C-C bonds. [115, 128, 158] **Figure 4.2 (a-c)** compares the UV-Vis spectra of GO prior to and post the solvothermal treatment in EDA at room temperature and at 110^{o}C for 24 hours. As indicated, the characteristic shoulder of GO at 305 nm disappears after EDA-assisted reduction, and the absorption peak of GO at 230 nm shifts due to the π-π* transitions of extended aromatic C–C bonds as the electronic conjugation within graphene that is being restored in the RGO. [115, 128, 132, 158]

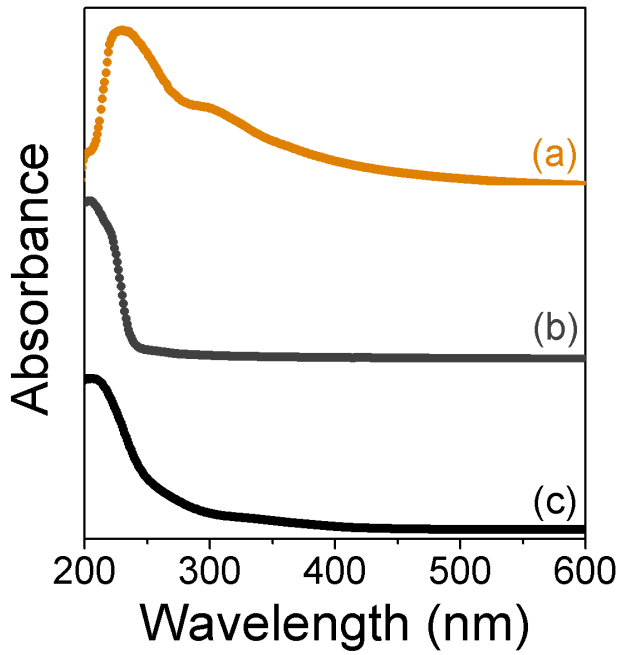

Figure 4-2 UV-vis spectra of a) GO suspension in DI water, b) partially RGO prepared by EDA-solvothermal reaction at room temperature and c) RGO prepared by reduction of GO in EDA at 110ºC .

As a result of the oxidation treatment of graphite, the XRD diffraction pattern of the exfoliated GO is featured by a peak at $2\theta = 10.7^{o}$ with a d-spacing of 8.14 Å (compared to a typical value of 3.34 Å in graphite) resulting from the introduction of carboxyl groups along the lateral and terminal sides of the sheets and epoxy and hydroxyl groups between the carbon sheets. [16-18,21] **Figure 4.3 (a-c)** compares the XRD diffraction pattern of GO (**Fig. 4.3-a**) after overnight reflux in EDA at room temperature (**Fig. 4.3-b**) and conventional heating of the GO solution in EDA at 110 ºC overnight (**Fig. 4.3-c**). Following the EDA-solvothermal treatment for 24 h, the intensity of the $2\theta = 10.7^{o}$ peak (**Fig. 4.3-a**) decreased significantly indicating the conversion of GO into RGO (**Fig. 4.3-c**) while the intensity for the sample prepared at room temperature exhibits features characteristic to Go and RGO phases (**Fig. 4.3-b**).

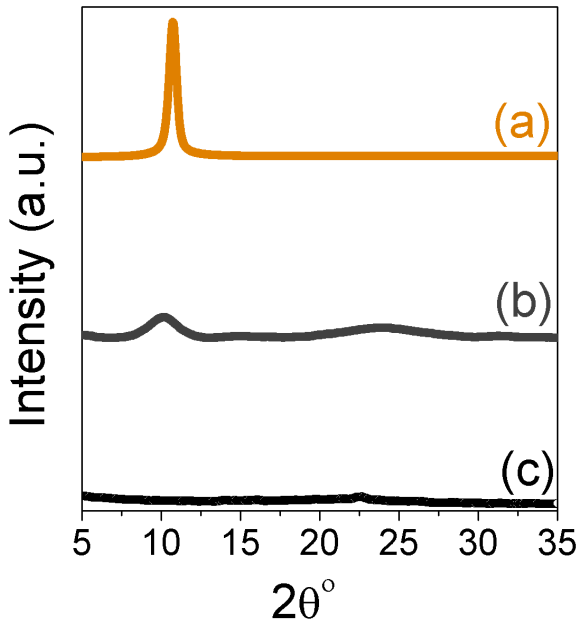

Figure 4-3 XRD diffraction patterns of a) GO b) partially RGO by EDA at RT and c)RGO by GO treatment in EDA at 110 ºC for 24 h.

To further verify the extent of reduction of GO in EDA after reflux for 24 h at room temperature and 110 ºC, the XPS spectra of C1s and O1s were measured and compared with that of GO prior to the solvothermal treatment. **Figure 4.4-a** shows the C1s spectrum of GO with the characteristic peak to the sp^2-bonded carbon C=C at 284.5 eV, in addition to peaks corresponding to oxygen-containing functional groups between 285.5 and 289 eV. Typically, peaks at 289, 287.7, 286.7 and 285.6 are assigned to the C1s of the HO-C=O, C=O, C-O and C-OH groups, respectively. [112, 113] As expected, significant decrease of the peaks corresponding to oxygen-containing functional groups is observed after the solvothermal treatment of GO in EDA at room temperature as shown in **Fig. 4.4-b**. A much higher and more significant reduction deoxygenation can be observed by looking at C1s spectrum of RGO synthesized at 110ºC in EDA as displayed in **Fig. 4.4-c**. The UV-Vis, XRD and XPS data clearly indicates that most of the oxygen-containing functional groups in GO are removed after solvothermal treatment in EDA at temperature low as

110ºC. This confirms that EDA-solvothermal treatment of GO can provide a simple and mild route for the production of RGO with controlled level of oxygen extent. Comparisons of high resolution XPS spectra of O1s of GO, partially RGO and RGO is shown in **Fig. 4.5**.

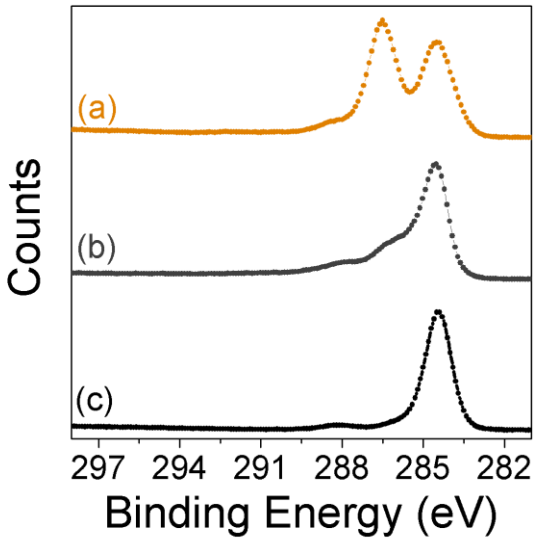

Figure 4-4 High resolution XPS spectra of C1s of a) GO b) partially RGO by RT treatment in EDA and c) RGO prepared by EDA at 110 ºC for 24 h.

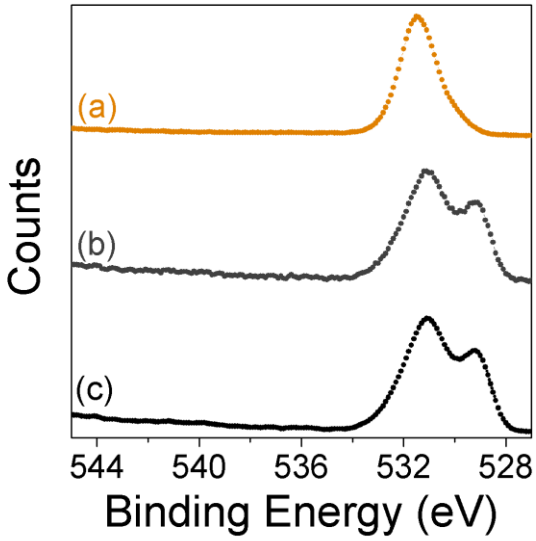

Figure 4-5 High resolution XPS spectra of O1s of a) GO b) partially RGO by RT treatment in EDA and c) RGO prepared by EDA at 110 ºC for 24 h.

Typical TEM images of the synthesized RGO sheets by solvothermal treatment of GO in EDA are shown in **Fig. 4.6**. The TEM images clearly show the 2D nature of graphene sheets with the naturally-wrinkled and partially folded layers. These parts that are observed as folded and entangled with each other are basically due to the intrinsic nature of 2D structure of graphene sheets where they become thermodynamically stable via folding. [159] Also large areas which are covered with the sheets can be observed with lateral dimensions up to a few microns in length. From these observations, the silk-like nature, the smooth surface and the flexibility of the RGO sheets can be inferred.

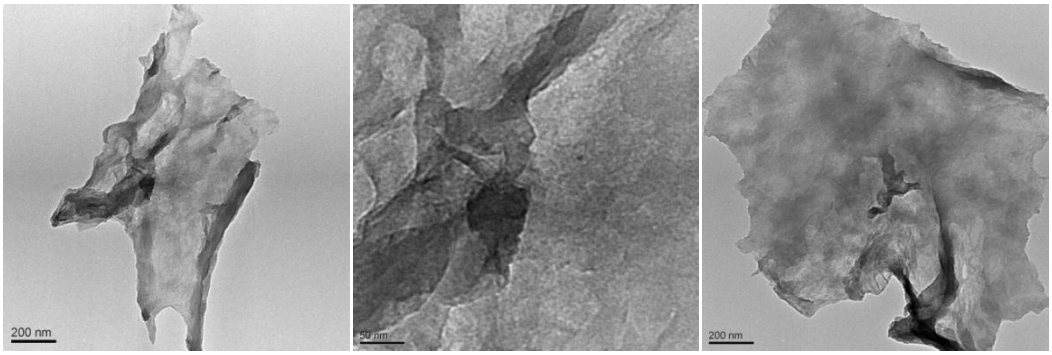

Figure 4-6 TEM images of RGO prepared by EDA-assisted solvothermal reduction at high temperature.

Raman spectroscopy is a powerful, sensitive, nondestructive and rapid analytical technique that can provide information about the structural and electronic properties of carbon nanostructures and graphene. **Figure 4.7** compares Raman spectra of graphite (**Fig. 4.7-a**), GO (**Fig. 4.7-b**) and RGO (**Fig. 4.7-a**). For graphite, the G band can be observed at 1580 cm^{-1} and no significant defects as indicated by the absence of the D band. For GO, two distinct bands are clearly observed at 1345 and 1589 cm^{-1} due to the D and G bands, respectively. In case of RGO, same two distinct bands observed for GO can be seen also in RGO. The band at 1350 cm^{-1} is the disorder mode band that is related to the defects and disorder induced modes in graphene and the band at 1599 cm^{-1} is

attributed to the vibration of sp^2-bonded carbon atoms in the planar hexagonal graphite lattice. The increased D/G ratio (~2.54) between the two bands compared to GO (~1.52) is an approximate indication of the disorder degree in RGO by the solvothermal treatment.

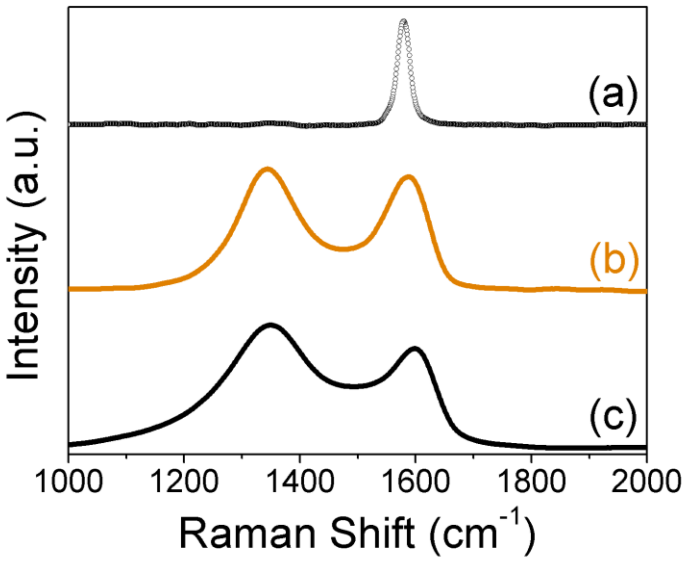

Figure 4-7 Raman spectra of a) graphite b) GO and c) RGO prepared by EDA-solvothermal treatment. G band is positioned at 1580, 1589 and 1599 cm^{-1} for graphite, GO and RGO, respectively. D band is located at 1345 and 1350 cm^{-1} for GO and RGO, respectively. D/G ratio of GO and RGO is 1.52 and 2.54, respectively.

4.4.2 Controlled synthesis of CeO_2 and CeO_2-RGO

X-ray diffraction is very useful in interogating the bulk crystalline structure of solids. The analysis of the peak position, broadening, and shape symmetry can provide information about the crystal phase, the mean crystallite size and the strain, respectively. [72] In this work, the grain size was calculated using Sherrer equation and the microstrain was evaluated using the single line method by analyzing the line broadening. The Sherrer equation is given as

$$D = \frac{k.\lambda}{\beta.\cos\theta}$$

where *D* is the mean crystallite grain size, *k* is the so-called shape factor (usually takes a value of 0.9), λ is the wavelength of the X-ray used (1.54056 nm for Cu-$K_{\alpha 1}$), β is the line broadening and θ is the angle of the X-ray reflection. For this purpose we used the broadening from the (111) and (220) XRD reflections which are manifested at lower angular values. Since strain effects could result in broadening the XRD reflections and this makes Sherrer's formula valid only for unstrained grains, so the lattice constant has to be calculated first before applying the Sherrer's equation in estimating the average crystallite size. For the cubic fluorite-structured cerium oxide grains, the lattice constant α can be calculated from the *d* spacing of the lattice planes as described in [135] using the equations

$$\boldsymbol{d_{hkl}} = \frac{\boldsymbol{\alpha}}{\sqrt{\boldsymbol{h^2+k^2+l^2}}} \qquad\qquad \boldsymbol{\alpha} = \frac{\boldsymbol{\lambda.\sqrt{h^2+k^2+l^2}}}{\boldsymbol{2\ sin\theta_{hkl}}}$$

where *d* is the *d*-spacing, α is the lattice constant, and *h,k,l* are the Miller indices.

The lattice constants for all samples were calculated and compared to that of corresponding to bulk ceria (5.410 A^o), as shown in **Table 4.1**. From the calculated lattice constant, the relative strain (*s*) value can be estimated as $\boldsymbol{s} = \frac{\boldsymbol{\alpha - \alpha_{bulk}}}{\boldsymbol{\alpha_{bulk}}}$, where α_{bulk} is the lattice constant value of unstrained bulk ceria [135]. From these calculations, we could see that the relative strain values listed in **Table 4.1** are relatively small to broaden the widths of XRD peaks and it is reasonable to use Sherrer's formula in determining the average crystallite size.

The XRD diffraction patterns of nanosized ceria powder prepared by EDA under different conditions are shown in **Fig. 4.8**. All patterns exhibit well-resolved, broad XRD reflections characteristic of the single phase fluorite-type structure of cerium oxide (CeO_2, ICCD 00-034-0394) from the database, without any reflections from impurity phases. The characteristic XRD peaks, peak positions, and crystallite size of different samples are shown in **Table 4.1**. As listed in

the table, the peaks can be indexed to the (111), (200), (220), (311), (222), (400) and (331) planes characteristic to a cubic fluorite-structure CeO_2 with space group Fm3m. The mean crystallite size of the particles was found to be dependent on the preparation conditions. The mean crystallite size of ceria prepared at room temperature is less than 3 nm and the size was found to increase to 5 nm upon calcinations. The heat treatment for 3 h at 450 ^oC likely led to sintering and formation of larger particles and as a result of this annealing, the crystal size increases by a factor of ~ 200%. The weak reflections in case of as-prepared CeO_2-RT sample indicate either amorphous nature of the ceria or the ultrafine size of the crystals and from the calculation of average size based on Sherrer formula, the size of these CeO_2-RT nanoparticles was found to be about 2.5 nm. The presence of well-defined peaks in as-prepared samples by MW (CeO_2-MW) or with conventional heating (CeO_2-CH) without calcinations treatments indicates the enhanced crystalline nature of samples in these preparations, as well as that with the grapheme (CeO_2-RGO).

Table 4-1 XRD measurements parameters and calculations

Crystal Plane	Peak Position (2θ) Degrees				
	CeO_2-RT	**CeO_2-RTC**	**CeO_2-CH**	**CeO_2-MW**	**CeO_2-RGO**
(111)	28.8	28.4	28.9	28.7	28.7
(200)	32.7	32.9	33.7	33.2	33.3
(220)	47.4	47.4	47.5	47.6	47.8
(311)	56.3	56.2	56.5	56.4	57.0
(222)	58.0	58.9	59.1	59.2	59.1
(400)	69.8	69.3	69.6	69.4	69.2
(331)	76.0	76.7	76.2	76.8	76.5
(420)	79.2	79.0	78.7	78.9	78.4
(422)	87.4	88.4	88.7	88.4	88.8
Crystallite Size (nm)	**2.5**	**5.7**	**2.7**	**5.1**	**3.3**
Lattice Constant (A^o)	**5.37**	**5.42**	**5.34**	**5.38**	**5.35**
Stress	**-0.138**	**0.044**	**-0.231**	**-0.094**	**-0.188**
Diameter (TEM)	**7.2 nm**	**9.5 nm**	**7.7 nm**	**9.6 nm**	**5 nm**

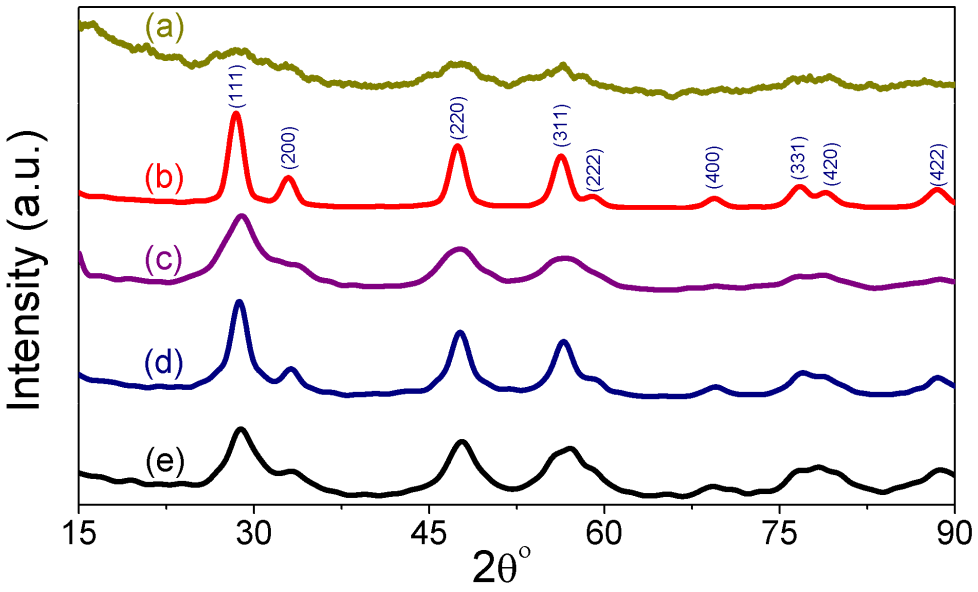

Figure 4-8 XRD diffraction patterns of a) CeO_2-RT, b) CeO_2-RTC, c) CeO_2-CH, d) CeO_2-MWI and e) CeO_2-RGO.

Semiconductor nanoparticles such as cerium oxide and others are widely characterized by absorption and fluorescence techniques. Optical systems in such techniques are not expensive and data acquisition is relatively fast. In addition, measurements are done while samples are in colloidal dispersions, thus retaining the chemistry at the surfaces. As shown in **Fig. 4.9**, samples strongly absorb UV light due to band-gap absorption, while there is much weaker absorption in the visible range. The optical absorption spectra dominated by a band at 300 nm confirm the presence of the Ce ions in the solution. The contribution of RGO to absorption at around 230 nm can be seen in the UV-Vis spectrum shown in **Fig. 4.9-e**. A typical photoluminescence spectrum of CeO_2-RTC nanoparticles and the corresponding excitation spectrum are shown in **Figs. 4.10-a-b**, respectively. The spectra show the wide band gap of the as-prepared ceria sample.

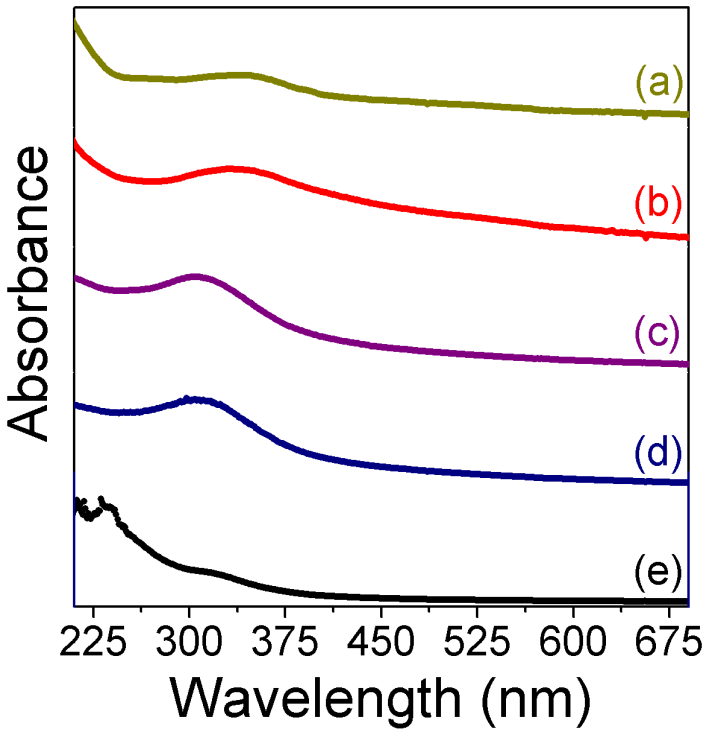

Figure 4-9 UV-Vis spectra of a) CeO_2-RT, b) CeO_2-RTC, c) CeO_2-CH, d) CeO_2-MWI and e) CeO_2-RGO.

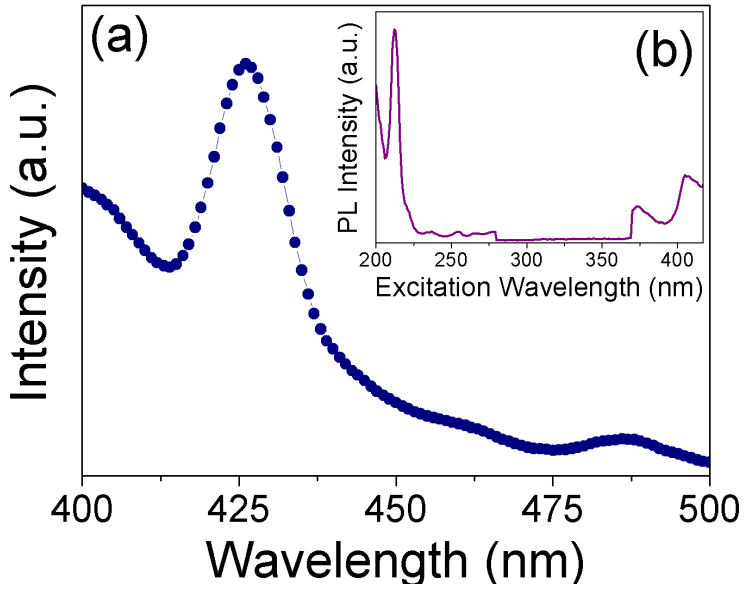

Figure 4-10 (a) PL spectrum of CeO_2-RTC and (b) excitation spectrum

Transmission electron microscopy TEM was used to analyze the size, shape and microstructure of ceria nanoparticles prepared under different conditions. It is clear from all images shown in **Fig. 4.11 (A-D)** that CeO_2 are structured as agglomerates of 20 nm in average constituting 3-5 nm individual nanoparticles. Due to the high surface stress, ceria nanoparticles exhibit high instabilities and under normal nucleation and growth conditions where capping agents are absent, they tend to grow beyond their nanoscale size either by aggregating or undergoing Ostwald ripening. [160] For instance, samples prepared at RT (**Fig. 4.11-a**), with conventional heating source at 110^{o}C (**Fig. 4.11-c**) and with MWI (**Fig. 4.11-d**) exhibit spherical morphologies with some other irregular shapes. The size distribution plots for different ceria samples are presented in **Fig. 4.12. (A-D**).

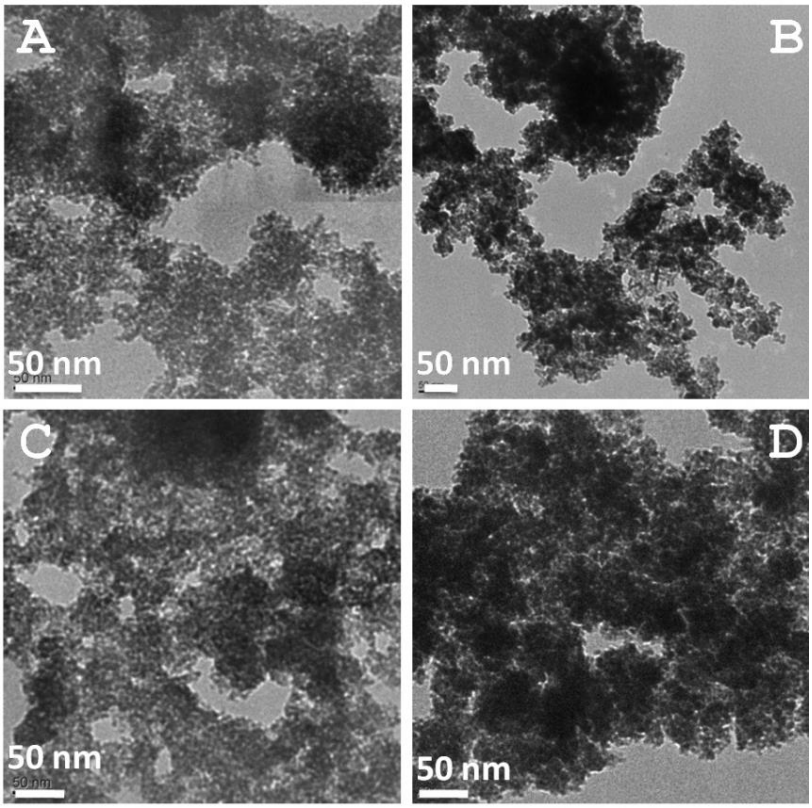

Figure 4-11 TEM images of a) CeO_2-RT, b) CeO_2-RTC, c) CeO_2-CH and d)) CeO_2-MW. Average size from analysis for A is 7.2 nm, B is 9.5 nm, C is 7.7 nm and D is 9.6 nm.

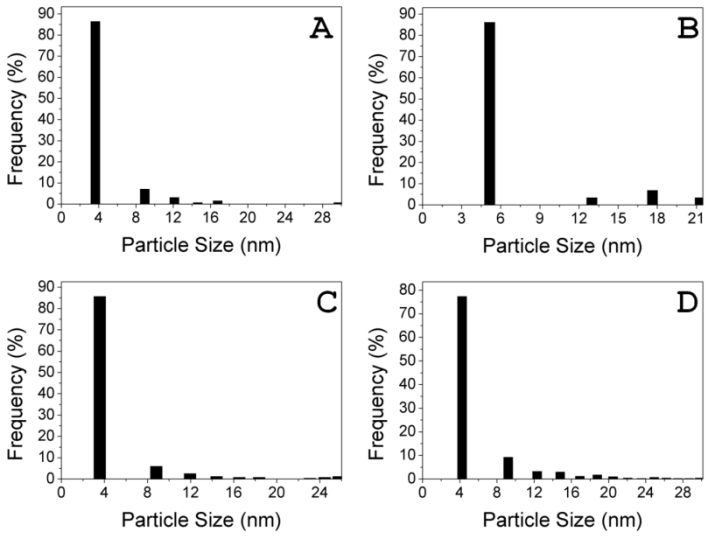

Figure 4-12 Size distribution analysis of a) CeO_2-RT, b) CeO_2-RTC, c) CeO_2-CH and d)) CeO_2-MW.

The structure, morphology and surface ornamentation of RGO sheets with CeO_2 nanoparticles are clearly visible in TEM images of CeO_2-RGO composite shown in **Fig. 4.13-A-D**, the size distribution analysis in **Fig. 4.14** and EDX mapping images shown in **Fig. 4.15**. The TEM analysis shown in **Fig. 4.14** reveals that the agglomeration tendency decreases significantly with the presence of graphene sheets. In this case individual nanoparticles of 3-5 nm can be observed. The good contrast between the composite counterparts (decorated graphene sheets and CeO_2 nanoparticles) allows distinction of the CeO_2 nanoparticles (showing up as black fine dots) from RGO. Images clearly show that surfaces of RGO sheets are evenly decorated with a homogenous distribution of CeO_2 nanoparticles of uniform size and spherical shape. The evident even and homogenous distribution of the nanoparticles on the surface suggests that the nucleation process was even and abrupt and that the growth conditions were uniform in the system. The image analysis shows that the average size of CeO_2 nanoparticles in this case is ~ 5 nm which is in agreement with that calculated from XRD measurements (~ 3-4 nm) using Sherrer equation.

Compared to all samples of CeO_2 nanoparticles prepared as a comparison without graphene and although the corrugated nature of the layers, neither apparent agglomeration nor significant CeO_2-void areas on the graphene sheets can be seen. The layered sheets possess large surface areas and even dispersion of CeO_2 nanoparticles anchored on the surface. Such integration of 2D graphene with its large surface area and the highly dispersed nanoceria can be an exciting material for use in heterogeneous catalytic applications for both industrial and environmental applications. Anchoring CeO_2 nanoparticles to graphene sheets by means of this approach may bring fascinating chemical and physical properties to explore and this can lead to a wide array of potential implementations of this composite material. It is worth discussing the role of RGO/GO on the growth of CeO_2 nanoparticles and show how this influenced the final size and morphology. The different morphologies of unsupported CeO_2 and that CeO_2 anchored on graphene indicate that RGO plays a fundamental role in controlling the agglomeration process. The interaction with GO sheets initially promotes a covering of the sheets surfaces establishing some nucleation sites due to interaction with C-OH, C-O-C, and C-OOH groups exposed on GO surfaces and then during the growth processes nanoparticles are anticipated to form on these nucleation sites and remain dispersed while anchored to the sheets. Therefore the morphology of ceria nanoparticles on RGO is completely different from free-standing ceria that apparently are larger and agglomerated.

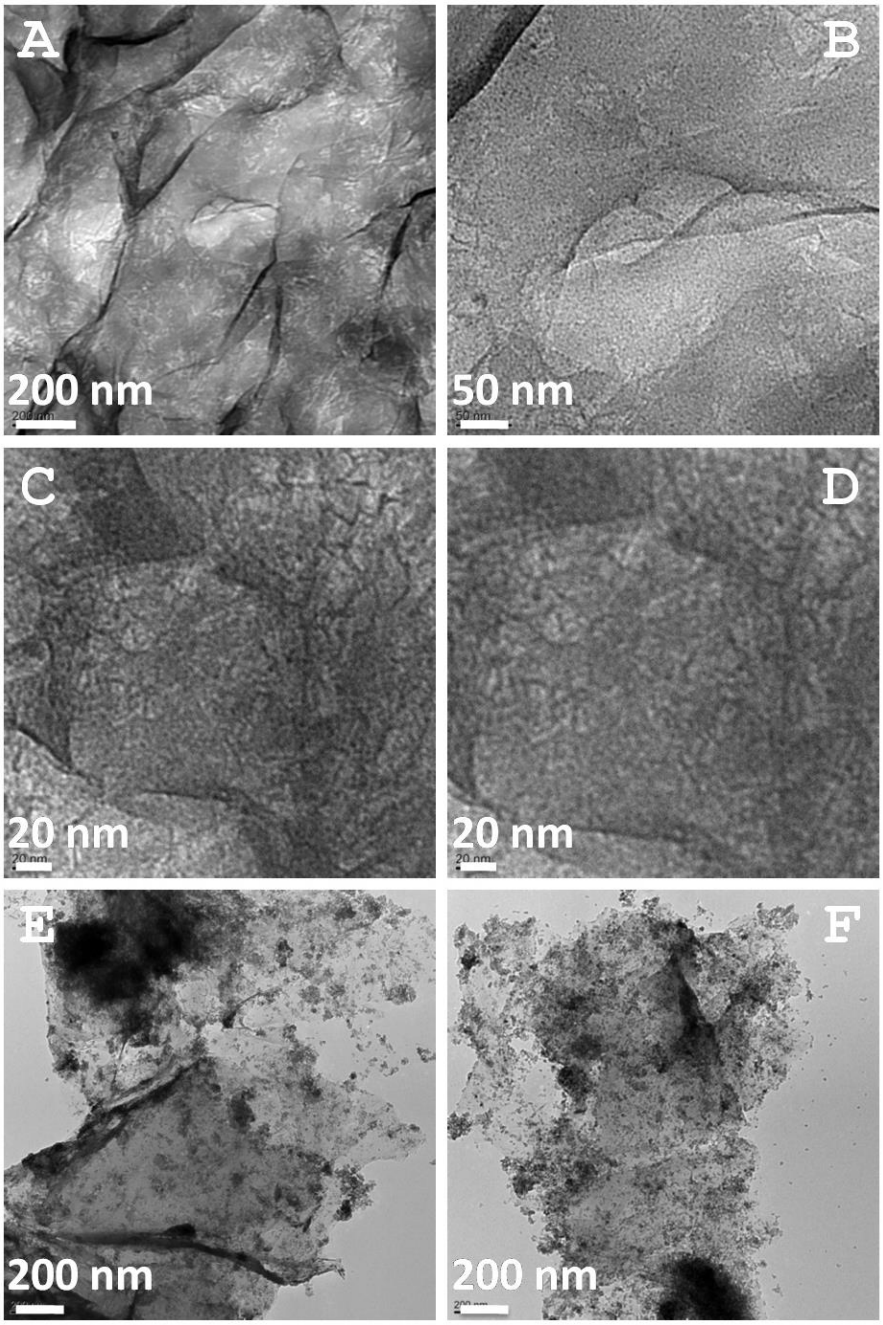

Figure 4-13 TEM images of CeO_2-RGO (a-c) 1% RGO and (d-e) 20% RGO (mass ratio).

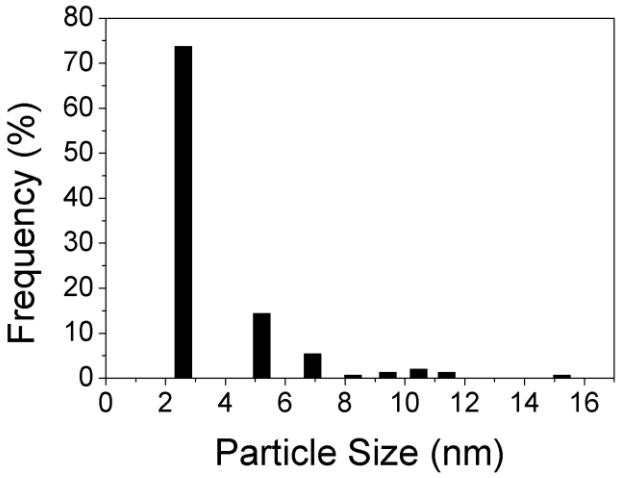

Figure 4-14 Size distribution analysis for ceria graphene and calculated average size is 5.04 nm.

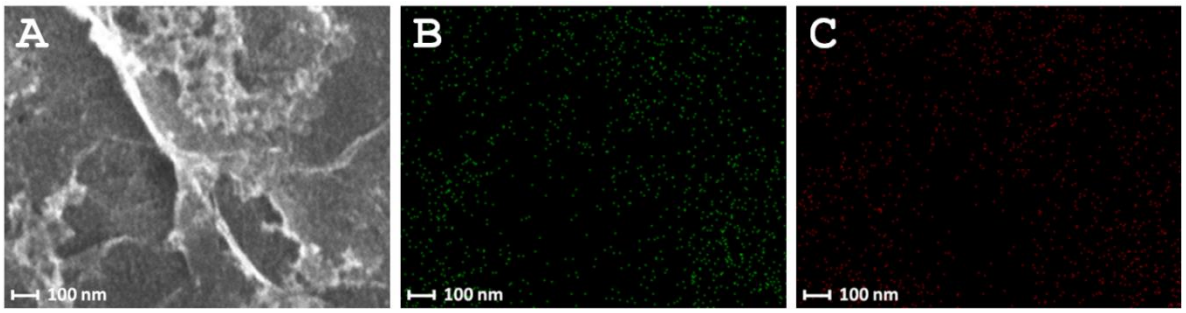

Figure 4-15 a) SEM image of CeO_2-RGO and b-c) EDX mapping of CeO_2-RGO showing cerium (b) and oxygen (c) mapping.

X-ray photoelectron spectroscopy is a powerful and sensitive technique in surface analysis. In XPS, irradiating the specimen with monochromatic X-rays under ultrahigh vacuum conditions (~ 10^{-9} Torr) results in generation of photoelectrons. The kinetic energies of these ejected photoelectrons are then measured. The binding energy of the core level electron (E_k) can be determined from the incident photon energy ($h\nu$) and the binding energy of the electron (E_B) using the equation ($E_k = h\nu - E_B$). The binding energy is characterized by the element; however, it can be affected by the chemical environment. For example, factors such as oxidation state, particle size

and surface adsorbates can shift the binding energy. Therefore, information from XPS about chemical shifts should be treated with care.

To determine the oxidation state of the elements, XPS measurements/analyses was performed on a Thermo Fisher Scientific ESCALAB 250 imaging system using an Al K_α monochromatic X-ray source. Pass energy of 160 eV was used to conduct a survey on all samples and an energy of 23.5 eV with an operating pressure of 5 x 10^{-8} was used to conduct a high-resolution scan for analyzing the oxidation state of the elements, Ce3d for example. From XPS measurements, the stoichiometry and bonding type in ceria can be determined from the characteristic peaks observed for O1s and Ce3d.

Generally, XPS spectrum of Ce3d in CeO_2 is featured by ten peaks constituting two sets; a set of 5 peaks of Ce $3d_{5/2}$ level with *v* structure and a set of five peaks of Ce $3d_{3/2}$ level with *u* structure. The assignment of these ten peaks is shown in **Table 4.2**. As described in the literature, [135, 141, 148, 161, 162] six of those ten peaks are attributed to Ce^{4+} ($v, v'', v''', u, u'', u'''$) and the remaining four are attributed to Ce^{3+} (v_o, v', u_o, u'). From the corresponding sums of the integrated areas of peaks related to the Ce^{4+} and Ce^{3+} XPS signals, the relative concentrations or proportions of Ce^{4+} and Ce^{3+} can be calculated as described in [141] using the following equations:

$$[\boldsymbol{Ce^{3+}}] = \frac{\boldsymbol{Ce^{3+}}}{[\boldsymbol{Ce^{3+}} + \boldsymbol{Ce^{4+}}]}$$

$$[\boldsymbol{Ce^{4+}}] = \frac{\boldsymbol{Ce^{4+}}}{[\boldsymbol{Ce^{3+}} + \boldsymbol{Ce^{4+}}]}$$

$$\boldsymbol{Ce^{4+}} = \boldsymbol{v} + \boldsymbol{v''} + \boldsymbol{v'''} + \boldsymbol{u} + \boldsymbol{u'} + \boldsymbol{u''}$$

$$\boldsymbol{Ce^{3+}} = \boldsymbol{v_o} + \boldsymbol{v'} + \boldsymbol{u_o} + \boldsymbol{u'}$$

From the ratios of integrated peaks areas of Ce^{3+} to that of total Ce^{3+} and Ce^{4+} the atomic fraction of Ce^{3+} was calculated as follow: where A_x integrated area corresponding to peak x

$$[Ce^{3+}] = \frac{[A_{v_o} + A_{v'} + A_{u_o} + A_{u'}]}{[A_{v_o} + A_v + A_{v'} + A_{v''} + A_{v'''} + A_{u_o} + A_u + A_{u'} + A_{u''} + A_{u'''}]}$$

XPS spectra of all samples reveal the prominent presence of oxygen and mixed valence state cerium ions (Ce^{4+} and Ce^{3+}) species. The comparison of Ce3d spectra of different CeO_2 and CeO_2-RGO samples are presented in **Fig. 4.16.** In all spectra the observed overlapping peaks are attributed to the trivalent Ce^{3+} and the tetravalent Ce^{4+} oxidation states. In analyzing the relative proportions of Ce^{3+} and Ce^{4+} in these CeO_2 and CeO_2-RGO samples, Ce3d spectra curves were fitted with ten peaks using Gaussian functions, as described in the literature. [141, 148, 161] The parameters obtained from fitting included the peak position, intensity, area, area ratio and the full width at half maximum (FWHM) for each peak and the relative proportions of Ce^{3+} and Ce^{4+} determined for different samples are shown in **Table 4.3.** The results of peak fitting of Ce3d spectra of ceria samples prepared under different conditions and that in CeO_2-RGO nanocomposites along with the calculation of the corresponding [Ce^{3+}] and [Ce^{4+}] are summarized in **Table 4.4**. As can be seen in **Fig. 4.16** the 3d core level spectra of Ce ions are in the range of 870-925 eV. The fitted peaks on the graph labeled ($v,\ v'', v''',\ u,\ u'\ and\ u''$) are corresponding to Ce^{4+} and overlapping peaks labeled ($v_o, v', u_o\ and\ u'$) are corresponding to Ce^{3+}.

The results of Gaussian fitting reveal that the proportion of Ce^{3+} is 45.0 % for CeO_2 prepared at room temperature, 50.0 % for sample calcinated at 450 ^oC for 3 h, 37.0 % for sample prepared by MWI for 2 min at 1200 W, while it is only 33 % for the sample prepared by reflux at 110 ^oC for 24 h with a conventional hot plate, both run on the CeO_2 and CeO_2-RGO. The high

concentration of Ce^{3+} in case of CeO_2-RT revealed by the quantitative analysis of Ce3d spectra reflects that ceria nanoparticles prepared under such conditions are highly defective. However, the thermal treatment of these CeO_2-RT nanoparticles led to a reduction of the [Ce^{3+}] which infers the enhanced crystalline structure upon calcinations. The peaks characteristic to Ce^{3+} (v' and u') were reduced when the syntheses were done at higher temperature whether from microwave or conventional heating sources. The defects [Ce^{3+}] decreased from 37 % in case of CeO_2-MW to 33 % for CeO_2 in CeO_2-CH and CeO_2-RGO and such decrease in oxygen vacancies or defect concentration may indicate larger sizes of CeO_2 nanoparticles in such cases [141]. Nonetheless, the concentration of defects in all CeO_2 samples is relatively high and these defects were found to activate oxygen [163] which increases the potential of such structures as active supports for Au-based catalysts in CO oxidation. A considerable proportion of trivalent Ce^{3+} ions were detected in XPS measurements but no reflections due to the crystalline Ce_2O_3 were observed in the XRD diffraction patterns. This may indicate the Ce_2O_3 phase is amorphous and that amorphous nature of the Ce_2O_3 indicates that this phase is located at the grain boundaries and grain surface [135]. Among challenges that some researchers have experienced in investigating ceria and ceria-based structures by XPS is the charging problem. Such challenges can lead to different results and hence different interpretations [141] and in our case this may account for the small shifts of peaks to relatively lower or higher binding energies, which in turn may indicate the relative increase in the content of the respective species.

The XPS spectra of O1s are shown in **Fig. 4.17**. All spectra exhibit 2 peaks; a main peak at 529.5 eV [135] which is ascribed to O^{2-} ions and a less intense peak shifted to higher energy which can be ascribed to OH^- ions of surface hydroxyl groups. We notice that this peak is much smaller in case of calcinated sample (CeO_2-RTC). Upon calcinations and heat treatment, the hydroxyl content decrease and thus the corresponding peak intensity also decreases. Comparison of high-resolution XPS C1s spectra is presented in **Fig. 4.18**.

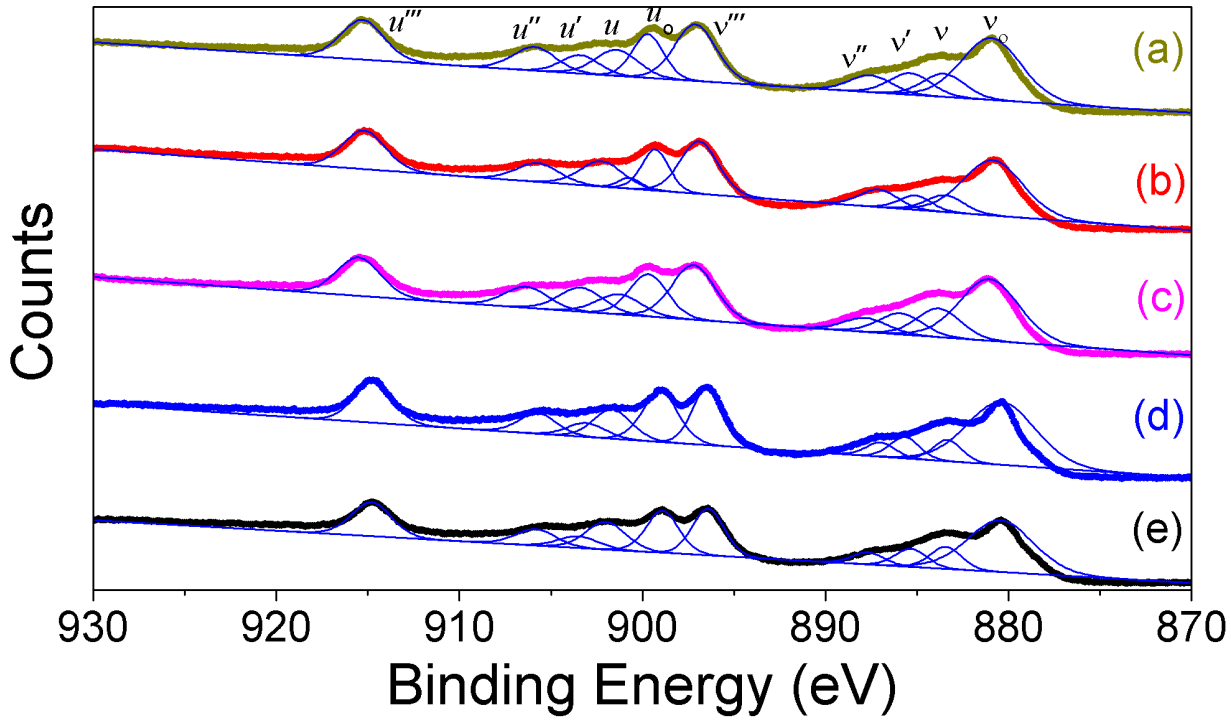

Figure 4-16 XPS Ce3d a) CeO_2-RT, b) CeO_2-RTC, c) CeO_2-CH d) CeO_2-MW and e) CeO_2-RGO.

Table 4-2 Gaussian peak parameters of the two series of peaks assigned to Ce3d XPS spectra

Series	Set	Origin	Shift (eV)					Intensity					Produced by …state
			RT	RTC	CH	MW	RGO	RT	RTC	CH	MW	RGO	
Ce $3d_{5/2}$	v	Ce^{4+}	883.54	883.47	880.39	881.05	880.44	8358.34	5356.82	14377.99	22167.82	14815.44	$Ce\ 3d^9\ 4f^2\ L^{n-2}$
	v''	Ce^{4+}	887.54	887.11	883.34	883.81	883.43	6120.45	5641.6	4815.02	10347.72	6292.25	$Ce\ 3d^9\ 4f^1\ L^{n-1}$
	v'''	Ce^{4+}	897.1	896.9	885.67	885.89	885.34	20408.17	16931.48	4952.64	7593.85	5205.19	$Ce\ 3d^9\ 4f^0\ L^{n}$
	v_o	Ce^{3+}	880.94	880.85	887	887.8	887.67	22361.93	17818.42	3268.65	5038.44	3448.71	$Ce\ 3d^9\ 4f^2\ L^{n-1}$
	v'	Ce^{3+}	885.37	885.1	896.48	897.2	896.4	7778.77	4567.73	13141.7	19640.2	13427.09	$Ce\ 3d^9\ 4f^1\ L^{n}$
Ce $3d_{3/2}$	u	Ce^{4+}	901.41	900.7	899.02	899.67	898.9	9448.8	3424.88	11519.2	15259.7	11963.08	$Ce\ 3d^9\ 4f^2\ L^{n-2}$
	u''	Ce^{4+}	905.9	905.73	901.64	901.28	901.99	8502.59	6056.96	6721.47	7258.33	7854.13	$Ce\ 3d^9\ 4f^1\ L^{n-1}$
	u'''	Ce^{4+}	915.3	915.2	903.06	903.36	903.49	14386.54	12404.36	3209.44	8663.71	3327.5	$Ce\ 3d^9\ 4f^0\ L^{n}$
	u_o	Ce^{3+}	899.7	899.3	905.72	906.35	905.82	15807.74	13251.12	4679.94	7574.56	4671.6	$Ce\ 3d^9\ 4f^2\ L^{n-1}$
	u'	Ce^{3+}	903.4	902.25	914.7	915.5	914.8	6631.87	8198.92	9702.8	13888.83	9668.76	$Ce\ 3d^9\ 4f^1\ L^{n}$

Table 4-3 Fitting parameters of the two series of peaks assigned to Ce3d XPS spectra for different ceria samples

Series	Set	Origin	Area					Area%					FWHM				
			RT	RTC	CH	MW	RGO	RT	RTC	CH	MW	RGO	RT	RTC	CH	MW	RGO
Ce	v	Ce^{4+}	24298.88	14065.97	68915.65	92394.3	67924.94	6.64	5.24	32.18	24.48	29.65	2.68	2.42	4.42	3.85	4.23
$3d_{5/2}$	v''	Ce^{4+}	17793.03	14813.76	9633.01	31483.99	13702.95	4.87	5.53	4.5	8.35	5.99	2.68	2.42	1.85	2.81	2.01
	v'''	Ce^{4+}	59116.82	44458.8	9908.31	23105.05	11389.85	16.25	16.66	4.64	6.13	4.98	2.67	2.42	1.85	2.81	2.02
	v_o	Ce^{3+}	93203.35	74266.21	6539.32	15329.97	7510.43	25.46	27.65	3.06	4.07	3.29	3.85	3.85	1.85	2.81	2.01
	v'	Ce^{3+}	22614.01	10185.35	26428.41	59757.31	29380.79	6.19	3.8	12.42	15.94	12.91	2.68	2.06	1.86	2.81	2.02
Ce	u	Ce^{4+}	27961.54	5281.65	28446.77	40069.01	27174.5	7.7	1.98	13.38	10.7	11.95	2.73	1.42	2.28	2.42	2.1
$3d_{3/2}$	u''	Ce^{4+}	25161.23	17924.01	17439.17	22008.58	21769.17	6.94	6.74	8.21	5.88	9.59	2.73	2.73	2.39	2.8	2.56
	u'''	Ce^{4+}	42573.26	36707.52	8327.05	26269.93	9222.78	11.79	13.86	3.92	7.02	4.06	2.73	2.73	2.39	2.8	2.56
	u_o	Ce^{3+}	33931.19	25129.63	12142.34	22967.43	12948.21	9.34	9.43	5.73	6.15	5.71	1.98	1.75	2.39	2.8	2.56
	u'	Ce^{3+}	17414.01	24262.59	25275.47	41968.72	26798.75	4.8	9.11	11.97	11.28	11.86	2.42	2.73	2.4	2.79	2.56

Table 4-4 comparison of concentrations of Ce III and Ce IV in different ceria samples prepared under different conditions

	CeO2-RT	CeO2-RTC	CeO2-CH	CeO2-MW	CeO2-RGO
$[Ce^{4+}]$	54.19	50.01	66.83	62.56	66.22
$[Ce^{3+}]$	45.79	49.99	33.18	37.44	33.77

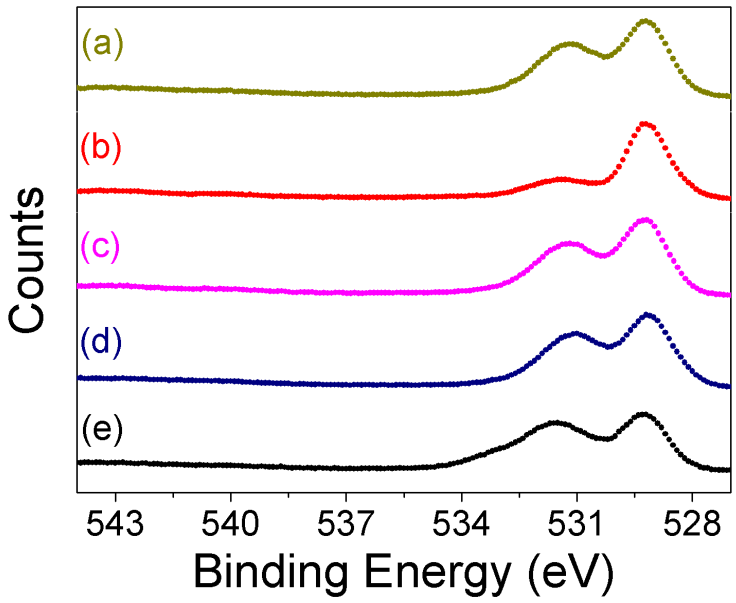

Figure 4-17 XPS O1s a) CeO_2-RT, b) CeO_2-RTC, c) CeO_2-CH d) CeO_2-MW and e) CeO_2-RGO.

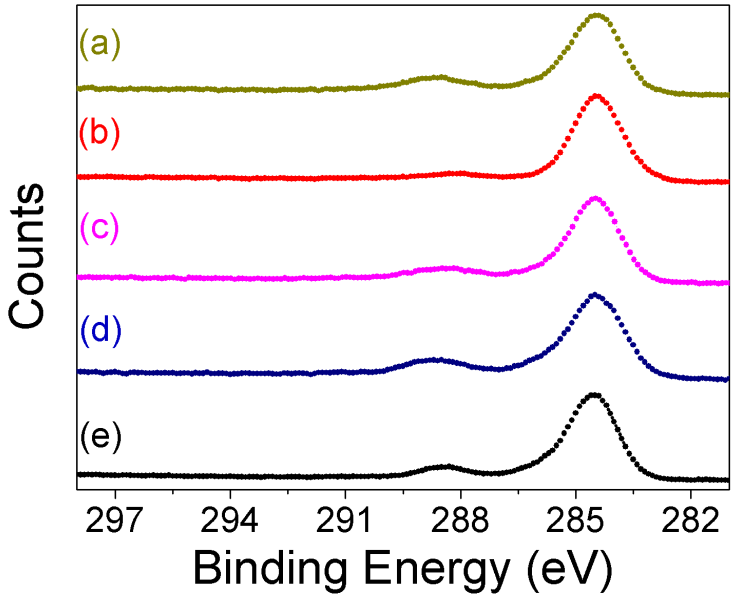

Figure 4-18 XPS spectra of C1s of a) CeO_2-RT, b) CeO_2-RTC, c) CeO_2-CH d) CeO_2-MW and e) CeO_2-RGO.

Raman spectroscopy is a powerful, sensitive, nondestructive and rapid analytical technique that can provide accurate information about the structural, symmetrical and electronic properties of nanostructures. Owing to the strong sensitivity of the phonon characteristics to the crystalline nature of the material, at a local level, the frequency shift and asymmetric broadening of Raman bands and can be useful for systematic characterization of nanomaterials. Therefore, Raman studies have been frequently used to investigate the structure and properties of ceria-based structures. [164] It is worth mentioning that changes in size of spherical nanoparticles can result in different Raman shifts according to the relationship of phonon dispersion for the phonon branch characteristics to which the Raman active mode belongs. For example, the frequency/peak position of F_{2g} Raman band in CeO_2 down-shifts to lower energy, whereas that of E_g band in TiO_2 shifts to higher energy as the crystallite size decreases. [160] In case of ceria, decreasing the particles size causes lattice expansion and changes lattice constants and this in turn leads to a shift in the F_{2g} peak position (originally 464 cm^{-1}) to lower energies and broadens the Raman line-width. [165] The direct relation between softening and broadening of Raman modes to the nanoparticles size makes Raman spectroscopy very useful to estimate the average size as a quick check of the nanocrystals size. The data measurement is advantageous in being readily available, non-destructive, no requirement special sample preparation applicable to different ceria-based samples. A one consequence of phonon confinement in spherical nanocrystals is that the frequency of an acoustic Raman mode scales as the inverse of particles dimensions. This observation has been used in estimating the average size of nanoparticles, particularly in the low-frequency region. The rare earth oxide, CeO_2, is a typical example in which the line-width and frequency of Raman active modes vary with the size and thus an average size of the particles can be estimated based on the Raman spectra. [160, 166, 167]

Fluorite-structured solids such as CeO_2 has six optical-phonon branches, which yield three zone center frequencies, 272 cm^{-1}, 545 cm^{-1} and 465 cm^{-1} due to the doubly degenerate TO mode, the non-degenerate LO mode and the triply degenerate Raman active mode, respectively. The triply degenerate active F_{2g} mode at ~ 464 cm^{-1} is given directly by measuring the Raman spectrum of bulk cubic-fluorite phase ceria. [164, 167, 168] As the crystals size decreases the peak of this active F_{2g} mode near 464 cm^{-1} down-shifts to lower energies and the line-shape gets asymmetric and broadened due to the inhomogeneous strain broadening introduced by the phonon confinement and dispersion in particles sizes. [164, 168] Several Raman studies have shown that the Raman peak energy of CeO_2 nanocrystals at room temperature decreases and the line-width increases with decreasing the particle size and this can serve as a quick check for the size. Mazali et al. [160] showed that the frequency of the F_{2g} mode exhibits a quadratic dependence on *1/d*, where *d* is the average size of the particles.

Figure 4.19 shows Raman spectra of ceria nanoparticles prepared under different conditions. The Raman shift due to F_{2g} phonon mode (455 cm^{-1}) [169] is presented in all samples. The main band at about 460 $^{cm-1}$ corresponds to the triply-degenerate allowed F_{2g} mode of fluorite CeO_2. [170] It can be seen that with decreasing size down to few nanometers (samples a-d), the line-shape of the Raman allowed mode becomes progressively broader and asymmetric changes in the signal profile as well as a decrease in the intensity are observed, compared to bulk CeO_2 (sample e). [171] As compared with micron-sized CeO_2 the frequency shift from 464 cm^{-1} to 455 cm^{-1} is a size-induced property that has been described in ceria based material based on the phonon confinement model. [160] The narrowing of the F_2g band after calcinations reflects an increase in the size of crystals resulting from sample annealing. The size increased by a factor of two as calculated from XRD.

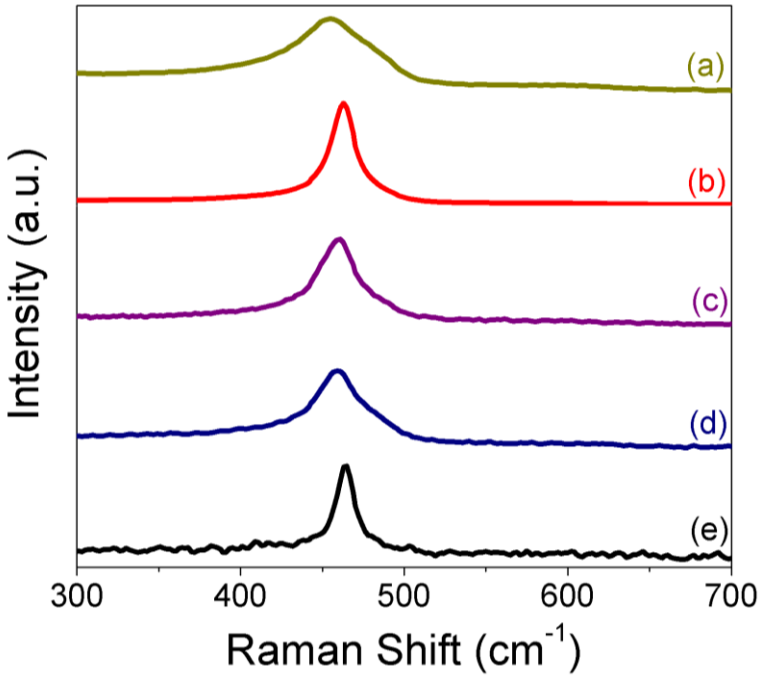

Figure 4-19 Raman spectra of a) CeO_2-RT, b) CeO_2-RTC, c) CeO_2-CH d) CeO_2-MW and e) commercial micro-sized CeO_2 nanoparticles using 5 mW 532 nm excitation laser.

Ceria has fluorite structure belonging to the space group Fm3m and have a simple vibrational spectrum with one IR active phonon and one Raman active phonon in the spectral region (300-700 cm^{-1}) where graphene shows a very small negligible contribution to the Raman spectra in this range (**Fig. 4.20**). In Raman spectrum of CeO_2-graphene, two distinct bands are clearly observed: the band at 1313 cm^{-1} is the disorder mode band that is related to the defects and disorder induced mode in graphene and the band at 1598 cm^{-1} is attributed to the vibration of sp^2-bonded carbon atoms in the planar hexagonal graphite lattice. The increased D/G ratio (~2.64) between the two bands compared to GO or RGO might reveal surface reconstruction of RGO induced by CeO_2 nanoparticles anchored on the surface.

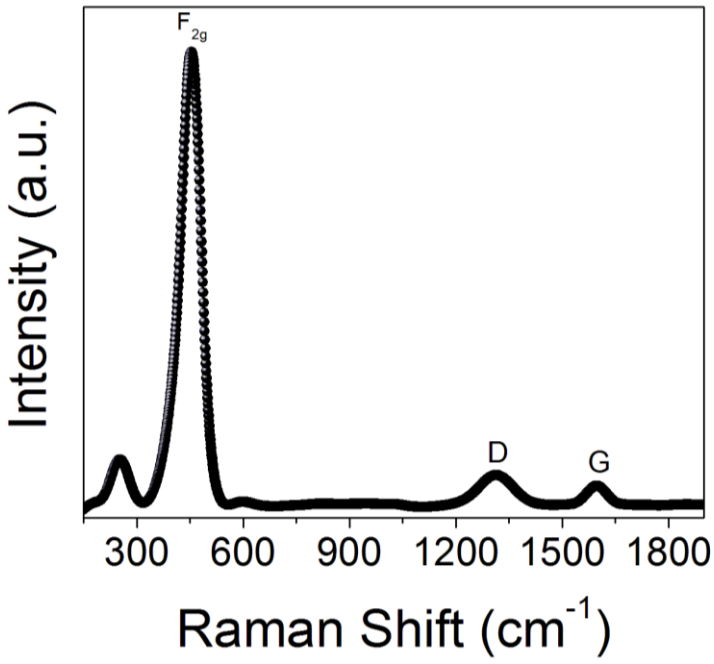

Figure 4-20 Raman spectra of CeO_2-RGO nanocomposites using 532 nm excitation laser (5 mW) showing the F_{2g} mode of CeO2 posiitoned at 453 nm and the D and G bands of graphene at 1313 and 1598 nm, respectively.

Our preparation of such CeO_2/RGO nanocomposites with a high-degree of crystallinity, homogenous composition and controllable morphology with simple solvothermal route is very advantageous in a number of ways. First, the EDA-assisted synthesis of CeO_2/RGO nanocomposite is facilely conducted in a single-step at mild conditions without post-synthesis treatments and at a relatively low temperature of 110^{o}C. Second, the reaction proceeds in EDA, which is safer than other toxic or explosive organic reducing agents such as hydrazine and hydrazine derivatives, and no additional reagents are added, making it an environmentally-friendly and economically-favorable approach. Third, the one-pot synthesis is simple and scalable facilitating the potential for large scale production with low cost synthesis and processing. Fourth, this EDA-assisted synthetic approach is shown to be compatible for shape controlled-fabrication of ceria nanoparticles. The method can serve also as a general strategy for decorating graphene

with various kinds of metal oxides, metals and semiconductor nanostructures of controlled size and morphology could be demonstrated. Fifth, such nanocomposite structure held the advantage of the unique extended microstructure of graphene sheets and the nanosized structure of ceria nanoparticles. Compared to traditional un-supported ceria nanoparticles, the overall size of this composite is larger, which could facilitate the separation and recycling in homogenous catalysis and environmental remediation processes. Sixth, the structure also retains the extremely high surface area of graphene sheets with the interconnected ceria nanoparticles uniformly dispersed on the surface. Because of the high catalytic activity of the CeO_2/RGO nanocomposites in simultaneous catalytic CO oxidation, the composite structure may be a promising candidate in various potential catalysis applications, environmental remediation as well as other energy (promising anode materials for Li-ion batteries) and biomedical systems.

4.4.3 CO Catalytic Oxidation

Heterogeneous catalytic oxidation of carbon monoxide (CO) to carbon dioxide (CO_2) using noble metal-based catalysts has been studied extensively as a model reaction. The popularity of CO oxidation as a model system stems from reaction simplicity where only diatomic molecules are involved and product formation takes place over few steps. It is also an important practical modality for CO removal in many environmental and industrial applications such as air purification, closed-cycle CO_2 lasers, polymer electrolyte membrane (PEM) fuel cells, [172, 173] purification of H_2 from CO traces in H_2 fuel cells, removing toxic CO in effluents and car exhaust. [174] Oxidation of CO can be catalyzed with highly dispersed noble transition metals, particularly Au, Pd and Ru, on various reducible oxides as supports at low temperature. [138, 175, 176] Moreover, the sensitivity of CO molecules to the structure of the surface and can be used to probe active sites on metal surfaces, which can help understanding the nature and mechanism of active coordination

sites. [177] Adsorption of CO on the surfaces can be simply traced by IR spectroscopy, among others. Nevertheless, a critical point in CO catalytic oxidation is to develop simple strategies for preparing catalysts with higher reactivity and stability by increasing the metal-support interaction. [178]

Different catalyst supports possess different activation energies, so reducible metal oxides such as CeO_2, TiO_2 and Fe_2O_3 are preferred in catalyzing CO oxidation compared to irreducible metal oxides such as Al_2O_3, SiO_2 and ZrO_2. Such metal oxide support can directly catalyze activation of the molecular oxygen, [179] favor electronic interaction with transition metal catalyst [180] or impose strains on metal clusters. [181] Metal support structures of nanocrystalline size are more active than larger sized crystals. Among reducible metal oxides, CeO_2, has gained particular interest and is widely used in catalytic industry and as an active and thermally stable support for noble and transition metal-based catalysts, such as Au, Pd, and Cu. Ceria nanostructures possess high oxygen storage capability under reducing reaction conditions which allow generation of oxygen vacancies and lead to enhanced activity. These oxygen vacancies are mobile on the surface, can form oxygen vacancy clusters, [182] prevent the sintering of metal clusters [183] and provide nucleation sites for metal structure. [184]

Although bulk Au is considered relatively to be inert and catalytically inactive, [177, 185] Au in nanosize regime has very rich and varied chemistry [186] and 2-10 nm Au nanospheres for example are exceptionally active catalysts. [107, 187] These nanostructures of gold metal of small size, high surface area and dense population of unsaturated coordination sites have shown increased activity over conventional catalysts in catalyzing number of inorganic and organic reactions. [107] Some examples include catalyzed conversions such as hydroamination of alkynes and alkenes and

hydrochlorination of acetylene and alkynes over oxide-supported Au nanostructures. [188] Also Au-based catalysts have been intensively used for oxidation of CO to CO_2 at low temperature [107, 188].

The rationale behind the change in CO catalytic oxidation activity between bulk and nanosized Au is the nature of the active sites. The low activity of bulk Au is attributed to the lack of defect sites such as steps, edges and corners on the surface. [189] Accordingly, neither molecular nor dissociative oxygen is chemisorbed on the surfaces of clean single crystals of Au nor CO is only weakly adsorbed non-dissociatively. [190] However, CO and O_2 were found to be adsorbed with lower adsorption energies on Au atoms with lower coordination numbers, [191] which is the case in Au nanoparticles and clusters, and on the rough surfaces of microcrystalline Au or evaporated Au films. [192] Thus the activity of Au can be enhanced if the density of surface defects is increased. Such abundance of low-coordinated Au atoms at corners and edges can favor adsorption of CO and hence increases the catalytic efficiency. [193] In low-temperature CO oxidation, the binding of CO and O_2 to the solid-supported Au is the key factor that activate the O-O bond to a peroxide-like (or superoxide-like) adsorbable states. [187]

In addition to size, morphology and local coordination, the ability of gold to catalyze CO oxidation depends also on the oxidation state of the Au active species, whether cationic, anionic or zerovalent as well as the extent of interaction between Au and the metal support. [188, 194] For instance, Guzman et al. [195] reported that positively charged Au species are more reactive than zerovalent species for catalyzing ethylene hydrogenation at 353 K and that the activity declines upon He treatment due to the reduction and aggregation of Au. However, preparing cationic Au catalysts which can stay stable during the reaction without reduction and formation of zerovalent state Au remains a challenge. Indeed the stability of Au in a given oxidation state (Au^0, Au^{1+}or Au^{3+}) during a reaction is sensitive to reaction conditions and the nature of the solid support. [188]

Another important aspect in CO oxidation is the catalyst-support nature and the metal support interaction. In supported metal catalysts in general and Au in particular, the reducibility and surface area of the support are critical parameters in determining the efficiency of CO oxidation. Assuming the same loading percentage, the higher the specific surface area of the support, the farther apart the metal particles will be and in such case, they will likely retain their small size during the course of the catalytic reaction. A one challenge in CO oxidation studies is that comparing results from different groups is difficult even for the same type of catalyst and with similar size. The challenge is clear when we look at literature survey listed in **Table 4.5** where catalysts with same chemical compositions show different trends even under similar experimental conditions. The difficulty arises from the differences in the operation conditions, the synthetic methods and the catalysts pretreatment protocols. For instance, among the reasons a wide variation in the activity of Au catalysts is reported in the literature as can be seen in the survey shown in **Table 4.5** is the poisoning by the chloride. Also since Au cations are relatively easy to reduce in such a way that the details in the preparation procedure can cause variations in the activity. Also During the thermal reaction the size and oxidation state of Au can easily change. [157] For example, Au cations can be reduced at room temperature by light or air-borne reductants during preparation or storage. [196] Another challenge is elucidating the identities of the active species or reaction intermediates giving rise to reactivity of a catalyst. In this aspect, only average inference based on information such as the products of the catalytic reaction and the nature of the catalyst precursors rather than physical characterization can be drawn. [188] In many cases the use of tetrachloroaurate can lead to Au particles of relatively different shapes and sizes, among other nonuniform and complicated species. Thus the progress in understanding reaction mechanisms and catalysts structures is remarkably low since it requires an in-situ characterization of the catalyst under

reaction conditions due to the easy change of Au state [157, 188] and the sensitivity to differences in preparation procedures, pretreatment protocols and operation conditions [151] which makes comparing results from different groups difficult even for the same type of catalyst with similar size and compositions.

In this study, representative catalysts prepared by colloidal deposition of Au nanostructures on CeO_2/RGO were characterized by UV-Vis, photoluminescence and TEM studies. A UV-Vis spectrum of representative CeO_2/RGO catalyst exhibiting absorption features of both CeO_2 at 305 nm and Au at 521 nm is displayed in **Fig. 4.21**. **Figure 4.22** shows PL spectrum of CeO_2/RGO (**Fig. 4.22-a**) and the corresponding excitation spectrum (**Fig. 4.22-b**). Representative TEM images of the catalyst showing the decoration of CeO_2/RGO nanocomposites with Au nanostructures is shown in **Fig. 4.23**.

Table 4-5 Literature survey of CO oxidation activity of Au-CeO_2 nanostructures of various sizes and shapes

	Catalyst	Method	Au (wt %)	100% T (ºC)	Ref
1	Au/CeO_2	Support built around preformed Au	1 %	125	197
		Support built around preformed Au	3%	150	197
	Au/CeO_2	DPU (urea)	1 %	>200	197
		DPU (urea)	3%	~125	197
2	Au/CeO_2	DP (Deposition Precipitation)	1%	175	198
	Au/CeEu	DP	1%	150	198
3	Au/CeO_2 spheres	Reduction with NaBH4		165	199
	Au/CeO_2 Rods	Reduction with NaBH4		220	199
4	Au/CeO_2 Spheres	DP ($_{Na2CO3}$)	3%	295	200
	Au/CeO_2 Rods	DP (Na_2CO_3)	3%	295	200
5	Au/CeO_2	DP (Na_2CO_3)	3%	301	201
6	Au/CeO_2 Bulk	DP (Na_2CO_3)	2.8	~ 100	202
	Au/CeO_2 (flower-like)	DP (Na_2CO_3)	2.7	~ 100	202
7	Au/CeO_2	Cotemporary	5	327	107
8	Au/CeO_2	Cotemporary	2	245	138
	Au/CeO_2	Cotemporary	5	211	138
	Au/CeO_2	Cotemporary	10	156	138
9	Au/CeO_2	DP (NaOH)	2.8	20	203
10	Au/CeO_2	DP (KOH)		-50	204
11	Au/CeO2 (Flower-like)	DP	4.7	~100	161
12	Au/CeO_2	LVCC	5	163	205
13	Au/CeO_2	Hydrothermal DP Hydrothermal Precipitation		20 50	206
14	Au/CeO_2	NaBH4	1	~ 75	178
15	Au/CeO_2	DP (NaOH)	1.5	200	207
16	Au/Ceria (Hollow-spheres)	DP NaOH		RT	208
17	Au/CeTi	DP (NaOH)		20	209
18	Au/CeO_2	DP, Thermal Treat.	0.09	20	210
20	Au/Ceo_2	Double impregnation method (DIM)	1	150	211
21	Au/ Ceo_2	Double impregnation method	1	75	212
22	Au/ Ceo_2 Rods	DP, Heat		150	213
23	Au/ Ceo_2	DP (NaOH)		330	214
24	Au/ Ceo_2	DP urea		150	215
25	Au/ Ceo_2	Direct anionic exchange (DAE)	1.79	75	216
26	Au/ Ceo_2	DP (NaOH)		40	217

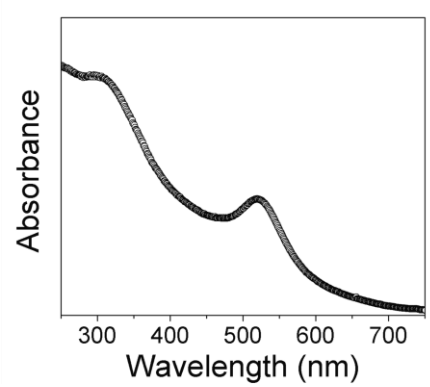

Figure 4-21 UV-Vis spectrum of Au-CeO2/RGO showing two absorption peaks due to Au and CeO_2 nanoparticles.

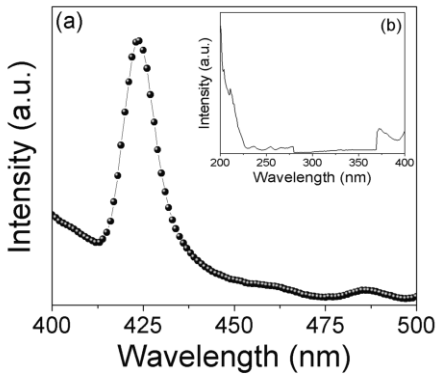

Figure 4-22 (a) Photoluminescence spectrum of Au-CeO2/RGO tertiary composite with an emission peak at 424 nm due to CeO_2 using 370 nm excitation wavelength; b) an excitation spectrum with emission filter set at 427 nm.

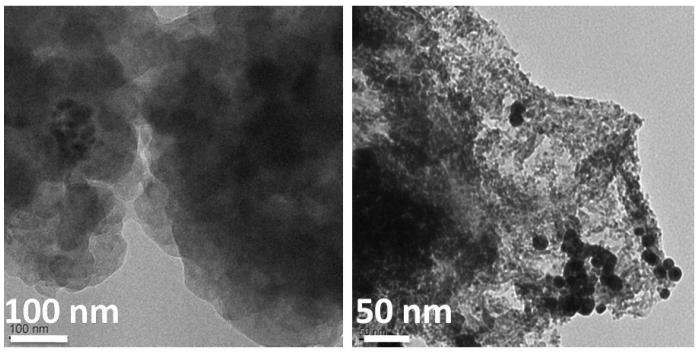

Figure 4-23 TEM image of Au-CeO_2/RGO catalyst prepared by loading Au nanostructures onto the CeO_2-RGO nanocomposites prepared in EDA at 110ºC.

It is generally accepted that the catalytic activity strongly depends on the particle size and dispersion which in turn is very sensitive to the procedure of preparation and pre-or post-treatments. [152-157, 218] Plots of CO conversion percentages versus temperature for different composites are shown in **Figs. 4.24 and 4.25**. It can be seen that increasing the reaction temperature inside the tune furnace lead to a gradual ramp in percentages of CO conversion. The catalytic efficiency of CeO_2 is apparently much less than different CeO_2-Au nanostructures. For instance, the CeO_2-RGO composite structure shows higher activity where a 100% CO conversion is achieved at 285 ^oC compared to 340^oC of pure CeO_2. The even distribution of CeO_2 nanoparticles on the surface of RGO and the strong interaction between the metal oxide and the carbon network might have enhanced the metal support-interaction and provided even accessible catalytic centers with fewer tendencies to agglomeration.

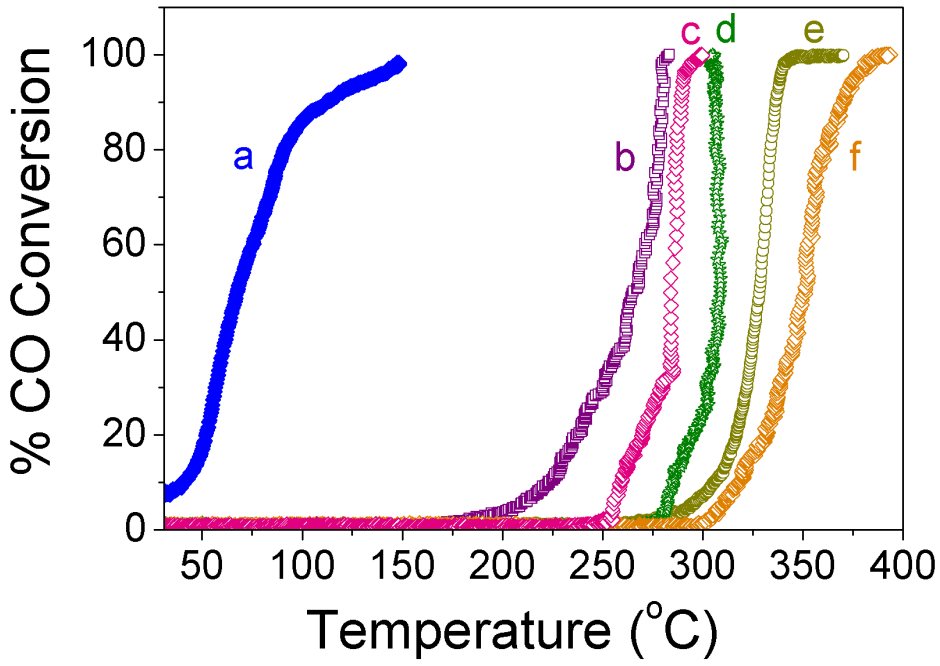

Figure 4-24 CO conversion percentages as function of temperature for different catalysts: a) Au-CeO_2/RGO with high graphene content, b) CeO_2/RGO, c) Au-GO, d) Au-partially RGO, e) pure CeO_2 and f) Au-RGO.

The increased catalytic activity and enhanced performance in case of the binary composite of CeO_2 and RGO (CeO_2/RGO) relative to individual pure CeO_2 may be due to uniform and efficient dispersion of CeO_2 nanoparticles which is the reactive metal oxide phase on the surface of RGO sheets as revealed from TEM images in **Fig. 4.13 (A-D)**. The very small particle size of CeO_2 and the large average dimensional area of graphene along with the interaction between the metal oxide and RGO sheets could have led to a more uniform dispersion of the reactive oxide on graphene layers. In addition, the fine size of CeO_2 nanoparticles led to a higher surface area and since the oxygen storage capability of CeO_2 is size dependent where presence of oxygen defects in ceria nanoparticles smaller than 5 nm leads to much higher activity. The introduction of graphene enhanced the dispersion of the metal oxide support and thereby its catalytic activity.

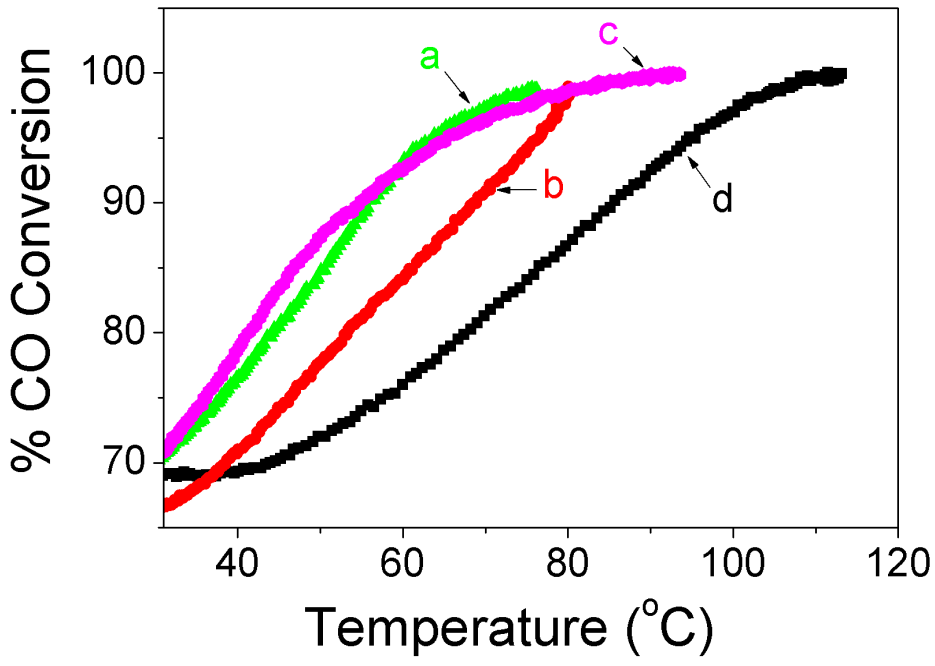

Figure 4-25 CO conversion percentages as function of temperature for different catalysts: a) Au-CeO_2/RGO b) Au-CeO_2/GO, c) Au-CeO_2/partially RGO and d) Au-CeO_2.

The activity of metal catalysts prepared by loading Au onto RGO, partially RGO, GO and CeO_2/RGO with higher graphene content was quite low compared to catalysts prepared by loading Au onto pure CeO_2, CeO_2/GO CeO_2/partially RGO and CeO_2/RGO with low content graphene, that is, there is no strong effect on the catalytic oxidation of CO at low temperature in case of carbon structure dominate the support. **Figure 4.24** reveals a 100% conversion of CO to CO_2 was reached at temperatures of 394, 305, 300 and 149^oC for Au-RGO, Au-partially RGO, Au-GO and Au-CeO_2/RGO with high graphene content, respectively, and no significant activity of these catalysts was observed at room temperature. On the other hand, it is clear from **Fig. 4.25** that binary composite of Au-CeO_2 and the tertiary composites of Au-CeO_2/GO, Au-CeO_2/partially RGO and Au- CeO_2/RGO showed higher catalytic activities and significant conversion percentages between 65-72% can be clearly observed at ambient temperature. For Au-CeO_2, a reaction temperature of 113 ^oC was needed to achieve a 100% CO conversion and for Au-CeO_2/GO, Au-CeO_2/partially RGO and Au- CeO_2/RGO a 100% oxidation was reached at 80, 94 and 76 ^oC, respectively. In addition, more than 67% conversion was observed at room temperature. Despite the similar trend of catalytic performance of CeO_2 and CeO_2/RGO composite, the later catalyst showed relatively little higher catalytic activity and is much easier to be handled and recycled and regenerated in practical applications, mainly because of the microscale dimensions of graphene sheets. The performance in catalytic oxidation of CO could be improved dramatically by controlled variation in the catalyst synthesis method, the dispersion uniformity and the catalyst composition.

4.5 Conclusions

In summary, a facile synthesis of ceria-graphene (CeO_2/RGO) nanocomposites is reported for the first time. Adopting EDA-assisted solvothermal approach that is potential for large scale production and low cost processing, controlled reduction of GO to RGO with controllable different extents of reduction were achieved by controlling the reaction temperature. The same approach was modified and utilized to synthesize CeO_2/RGO nanocomposites with different oxygen contents in a contemporarily fashion using a mixture of GO and cerium nitrate in EDA solution at different temperatures. An even distribution of 4-5 nm spherical CeO_2 nanoparticles of uniform size and shape was successfully achieved in situ on the high surface area RGO sheets in one-pot reaction and without post-preparation treatments. Different conditions to control the crystallinity and morphology of the nanocomposite structures are examined. The CeO_2/RGO nanocomposites were used as active Au-supports for efficient low-temperature CO catalytic oxidation. The results provides a new simple, efficient, scalable, environmentally-friendly and economically-favorable approach for large scale production of metal oxide nanostructures supported on graphene which could have important implications for industrial and environmental remediation.

CHAPTER 5 Laser-Driven Size Reduction and Photothermal Energy Conversion by Shape-Controlled Au-GO Nanostructures

5.1 Overview

Noble metal nanoparticles have received significant attention for decades because of the ability to tune their electronic and optical properties by changing size, shape, composition or dielectric environment. In this chapter, the seed-mediated synthesis of different Au nanostructures is described. The coupling of the photothermal effects of these Au nanostructures of controlled size and shape with GO nanosheets dispersed in water is demonstrated. Our results indicate that the enhanced photothermal energy conversion of the Au-GO suspensions could to lead to a remarkable increase in the heating efficiency of the laser-induced melting and size reduction of Au nanostructures. These resulting ultrasmall Au nanoparticles of 2-4 nm diameters are end up anchored to the laser-induced defects of the RGO nanosheets. The ultrasmall Au-graphene nanocomposites are potential materials for photothermolysis. In addition they may serve as promising photoabsorbers for the efficient conversion of solar energy into usable heat in variety of thermal, thermochemical and thermomechanical applications.

5.2 Introduction

The type of motion of electrons is what determines the physical and chemical properties of a material. [219] The 2D graphene, for example, is a distinct material because of the remarkable behavior electrons and the electronic motion. But the motion itself is determined by the space

accessible to electrons which in turn depends on the shape and so for quantum confinement size matters and so does shape. Unconfined electrons in metals or semiconductors with a very low degree of spatial confinement have motion that is not quantized and hence can absorb any amount of energy. But once an electron is bound or confined, its motion becomes highly confined and quantization sets in. [53] Accordingly, new chemical, optical or thermal properties that are belonging to neither the metal nor the atom can be observed. [53]

A typical example of such phenomena is the local surface plasmon resonance (SPR) in noble metals. SPR is an extremely interesting behavior of noble metals when their size is decreased below the electron mean free path. In the interaction between metal nanoparticles and incident light, the electrons in the conduction band undergo a coherent collective oscillation, with a frequency in resonance with that of the incident light. These collective oscillations of electrons lead to an induced charge separation between the free electrons and the ionic metal core. The metal core then exerts a restoring Coulombic force causing electrons to oscillate back and forth on the nanoparticle surface creating a dipole oscillation. The dipole oscillation induces a strong absorption of the incident light, as can be seen very clearly in a UV-Vis spectrum of Au or Ag nanoparticles. This unique interaction of plasmonic nanoparticles (Au in particular) with the incident light gives rise to brilliant, pretty and very intense colors of their colloidal dispersions. [219] Due to SPR, the radiative properties of noble metal nanoparticles such as light absorption, scattering or fluorescence are enhanced by orders of magnitude. They can be tuned to a great extent by changing the size, shape, composition, structure, interparticle separation, orientation, morphology or the dielectric properties of the metal or the surrounding medium. [53] All these factors affect the charge density on the nanoparticle surface that changes the SPR characteristics.

Au nanostructures have a remarkable capacity to absorb and scatter light over a broad range of the visible and near-infrared regions depending on the particles' size and shape. [220-223] These interactions also trigger photothermal effects where electronic oscillations at the particle surface are converted to heat which raises the particles' temperature as determined by the surface plasmon resonance (SPR). [220, 222, 224-226] These phenomena have been extensively investigated for a variety of applications in biomedical imaging, [222, 226-228] cancer therapy and diagnosis, [226, 229, 230] catalysis, [231] sensors, [232] and photonic devices. [233]

As in Au nanoparticles, photothermal energy conversion by carbon nanotubes (CNTs) has been also studied for therapeutic applications. [234-237] Most recently, interest has been focused on graphene and GO, [238-240] which have emerged as novel nanocarbon materials with potential uses in energy applications including photothermal energy conversion in addition to nanoelectronics, supercapacitors, batteries, photovoltaics and related devices. [3, 76] The large surface area (2600 m^2g^{-1}) of graphene and the strong optical absorption across the spectrum (2.5 % of the white light) coupled with its high thermal and chemical stability can lead to a rapid temperature rise and subsequent energy transfer to the host medium, thus offering an efficient way of heating the medium [3, 76]. This has been recently demonstrated by the development of a facile laser reduction method for the synthesis of Laser Converted Graphene (LCG) which provides a solution processable synthesis of individual graphene sheets [128, 132]. In this process, irradiation of GO suspended in water using the second or the third harmonic of a Nd-YAG laser (532 nm or 355 nm, respectively) results in significant deoxygenation of GO and the formation of LCG. This remarkable photothermal conversion of energy results in a significant temperature rise of water from room temperature to 75 °C in a few minutes of laser irradiation (532 nm of nanosecond pulses at 30 Hz with an average power of 6 W) [128].

The interaction of Au nanoparticles with pulsed laser light tuned to the SPR bands of the gold nanostructures can result in a sequence of heating, melting and evaporation processes which can lead, in addition to the photothermal energy effects, to significant size reduction of the original gold nanoparticles. [241-246] The coupling of the SPR of gold nanostructures with the photothermal effects of GO could enhance the melting and evaporation of the Au nanostuctures and the formation of ultrasmall Au nanoparticles attached to the large surface area of the laser converted graphene sheets. Herein, we report on the enhanced photothermal energy conversion by gold nanoparticles of well-defined size and shape dispersed in GO solutions as efficient photothermal materials for a variety of applications involving rapid heating of water. Furthermore, we demonstrate that the enhanced photothermal energy conversion by the gold-GO aqueous solutions can be tuned by controlling the shape of the Au nanostructures from spherical particles to short and long nanorods. We also report the synthesis of ultrasmall gold nanoparticles with diameters of 2-4 nm well-dispersed on the laser converted graphene nanosheets. The coupling of the laser-induced size reduction of the gold nanoparticles with the laser conversion of GO into graphene (LCG) provides a novel method for the synthesis of ultrasmall gold nanoparticles from much larger particles with different sizes and shapes. These ultrasmall gold-graphene nanocomposites are proposed as novel photothermal energy convertors for a variety of thermochemical and thermomechanical applications, in addition to photothermal therapy, such as heating and evaporation of liquids by solar energy, ignition of solid fuels, and welding of composite materials.

5.3 Experimental

5.3.1 Chemicals and reagents

Graphite powder (99.9999%, 200 mesh, Alfa Aesar), Sulfuric acid (ACS reagent, Sigma), potassium permanganate (ACS reagent, Sigma), hydrogen peroxide (30%, Sigma), gold (III)

chloride solution (99.99% trace metals basis, 30 wt. % in dilute HCl, Sigma), hexadecyltrimethylammonium bromide (≥98%, Sigma), L-ascorbic acid (99%, Sigma), sodium citrate triabsic dihydrate (ACS reagent, ≥99.0%, Sigma-Aldrich) and silver nitrate (ACS reagent, ≥99.0%, Sigma).

5.3.2 Preparation of GO and Au nanoparticles

In these experiments, GO was prepared by the oxidation of high purity graphite powder according to the method of Hummers and Offeman [80] and as described earlier. The yellowish-brown GO was washed repeatedly with hot water, followed by drying overnight at 60 ^{o}C. A stock solution of GO in water was prepared by dissolving 2 mg of the dried GO in 10 ml of DI water followed by sonication until a homogeneous yellow dispersion was obtained.

Spherical Au nanoparticles were prepared by the standard citrate reduction procedure as described in the literature. [247] A 100 ml of 1 mM $HAuCl_4$ aqueous solution was heated until boiling and then 10 mL of 38 mM trisodium citrate solution was added under continuous stirring for 15 min. Au nanoparticles of different shapes were prepared utilizing the seed-mediated method, [248-250] with little modifications. In this method, a relatively low concentration solution of Au ions is first reduced by a strong reducer to yield 3-4 nm Au nanospheres. A growth solution containing higher concentration of Au ions, a shape-directing surfactant, a weak reducing agent, and silver ions is prepared in a separate flask. The weak reducing agent employed here is ascorbic acid and just by itself is not capable of reducing the Au ions all the way to Au atoms. But when both the seed and growth solutions are mixed, an autocatalytic reaction (by metal atoms in seeds) is thought to take place on the surface of the seed to produce larger anisotropic Au nanoparticles. [250] In typical synthesis, the Au-seed solution was prepared by the addition of aqueous $NaBH_4$ (300 µl, 10^{-2} M) to a mixture of $HAuCl_4$ (2.5 ml, $5x10^{-4}$ M) and CTAB (2.5 ml, $2x10^{-1}$ M) at room temperature

under vigorous stirring. For the synthesis of different shapes, an 80 µl of the freshly prepared Au-seed solution was added to various growth solutions to initiate anisotropic growth of Au nanoparticles with different shapes. The different growth solutions contained the same $HAuCl_4$ and CTAB concentrations but different amounts of $AgNO_3$ were utilized to grow various morphologies, namely, spheroids, short rods, long rods, bipyramids, rounded-corner rectangles, sharp-corner rectangles, cubes and dog-bones. Each of the growth solutions was prepared by first mixing $HAuCl_4$ (25 ml, 10^{-3} M) and CTAB (25 ml, $2x10^{-1}$ M) solutions followed by the addition of 70 µl of ascorbic acid ($78.8 x10^{-3}$ M) which resulted in discoloration of the yellowish Au-CTAB mixture due to the partial reduction of Au ions. Then the designated amount of $AgNO_3$ was added to the colorless mixture followed by the subsequent addition of the seed to catalyze the growth. All growth solutions were kept undisturbed at a temperature of 25-28 ^oC for two hours. The absorption spectra of different Au nanoparticles were recorded for the as-prepared fresh samples diluted in DI water. The final concentrations of $AgNO_3$ in the growth solutions required for the growth of different shapes are as follows: spheroids ($4 x 10^{-7}$ M), short rods ($8 x 10^{-7}$ M), long rods ($8 x10^{-6}$ M), bipyramids ($12 x10^{-6}$ M), rounded-corner rectangles ($13 x10^{-6}$ M), sharp-corner rectangles ($14 x10^{-6}$ M), cubes ($16 x 10^{-6}$ M) and dogbones ($32 x10^{-6}$ M). All chemicals used were 99.99 % purity as obtained from Sigma-Aldrich, USA.

5.3.3 Laser-driven synthesis of Au-graphene nanocomposites

For the laser irradiation and photothermal synthesis of ultrasmall Au-graphene nanocomposites, an aqueous dispersion of GO and preformed selected-shape Au-nanoparticles was prepared by mixing 1 ml of Au-nanoparticles solution with 2 ml GO solution (2 mg/10 ml), and the mixture was irradiated in a quartz cuvette with the unfocused beam of the second and third harmonics of a Nd:YAG laser (2nd harmonic λ=532 nm, average power 4 W, hν =2.32 eV, or 3rd

harmonic λ = 355 nm, average power 2 W, $h\nu$ = 3.49 eV, pulse width τ = 7 ns, repetition rate = 30 Hz, fluence ~ 0.1 J/cm^2, Spectra Physics LAB-170-30). The beam diameter was measured to be 7-9 mm for both the 532 nm and 355 nm. The solutions were magnetically stirred during the irradiation. For the Au-size reduction experiments in the absence of GO, 1 ml of the shape-selected Au-nanoparticles solution was irradiated under similar laser conditions as described above (irradiation for 10 min corresponding to 18,000 laser shots). The temperature of the solution was monitored during irradiation using a thermocouple immersed in the solution.

5.3.4 Morphological, optical and Raman characterization

TEM images were acquired using a Joel JEM-1230 electron microscope operated at 120 kV equipped with a Gatan UltraScan 4000SP 4K x 4K CCD camera. Absorption spectra were recorded using a Hewlett-Packard HP-8453 diode array spectrophotometer. The Raman spectra were measured using an excitation wavelength of 457.9 nm provided by a Spectra-Physics model 2025 argon ion laser. The laser beam was focused to a 0.10 mm diameter spot on the sample with a laser power of 3 mW. The samples were pressed into carbon tape supported on glass cover slip, held at a 30 degree angle in the path of the laser beam. The detector was a Princeton Instruments 1340 x 400 liquid nitrogen CCD detector, attached to a Spex model 1870 0.5 meter single spectrograph with interchangeable 1200 and 600 lines/mm holographic gratings (Jobin-Yvon). The Raman scattered light was collected by a Canon 50 mm f/0.95 camera lens. Though the holographic gratings provided high discrimination, Schott and Corning glass cut-off filters were used to provide additional filtering of reflected laser light, when necessary.

5.4 Results and Discussion

Gold nanostructures of anisotropic morphologies can be prepared by a number of approaches including seeded and seedless chemical approaches, electrochemical method, UV-assisted reduction, solvothermal methods, bioreduction, proton beam irradiation, x-ray irradiation, and microwave irradiation, among others. [251, 252] Since its development in 2001, [253] the seed-mediated growth has become the most popular and easiest method for growing anisotropic Au nanostructures. The popularity of the methods stems from the feasibility of preparing high quality products with large yield, high degree of size control and flexible structural modification yet in a simple procedure that can executed in water, under air and at room temperature due to. [221, 248, 254-257] In this method and as described in the experimental section, a low density Au solution is first reduced to yield 3-4 nm Au seeds and a predetermined volume of the seed solution is added to the growth solution. When both the seed and growth solutions are mixed, a presumed autocatalytic reaction driven by Au atoms in seeds takes place on the surface of the seed leading to formation of larger anisotropic Au nanoparticles. [250]

Figures 5.1-5.3 display displays TEM images and UV-Vis absorption spectra of the as-prepared shape-controlled Au nanostructures using the seed-mediated growth method, [248-250] with some modifications. These modifications (see experimental section) allow fine tuning and morphological control of the Au nanostructures by systematically varying the concentration of the silver ions in the growth solution. By increasing the concentration of the Ag ions in the growth solution, gold nanostructures with well-defined shapes of spheroids (hexagonal plates), short-rods (SR), bipyramids, dog-bones, long-rods (LR), round-corner rectangular plates, sharp-corner rectangular plates, and cubes can be prepared as shown in **Figs. 5.1-5.3**, respectively. The careful manipulation of the kinetic and thermodynamic parameters of the experimental system using

additives, thermal energies, light or their possible combinations provides means to control the size, shape and structure of nanoarchitectures. [258] In seeded growth, fine tuning and morphological control of Au nanoparticles is achieved by systematic variation of parameters involved in the synthesis, for example the quantity of $AgNO_3$. The factors directing shape control in the synthesis of anisotropic Au nanostructures have been explanted with different mechanisms based on the selective adsorption of surfactant and accordingly blocking the growth at specific crystallographic faces. [248-250, 259, 260] The most common of these mechanisms to explain the growth of Au nanorods, for instance, relies on the preferential adsorption of the cationic surfactant (CTAB) molecules on the surface. [248] According to that hypothesis, which is based on high resolution TEM studies, faceted seeds with pentatetrahedral structure have been shown to exist. When the headgroups of the positively charged CTAB micelles bind to these primary seeds, they can bind preferentially onto the side surfaces. The selective binding can be understood on steric hindrance basis, that is, the spacing on the side surfaces which are fcc faces is more comparable to the headgroups of CTAB+ than the hexagonal close packed faces at the tips of the rods. As a result the side faces will be covered with much of the CTAB micelles and will be protected and stabilized more than the ends. Accordingly, Au atoms can add only along the common axis 111 faces at the exposed ends.

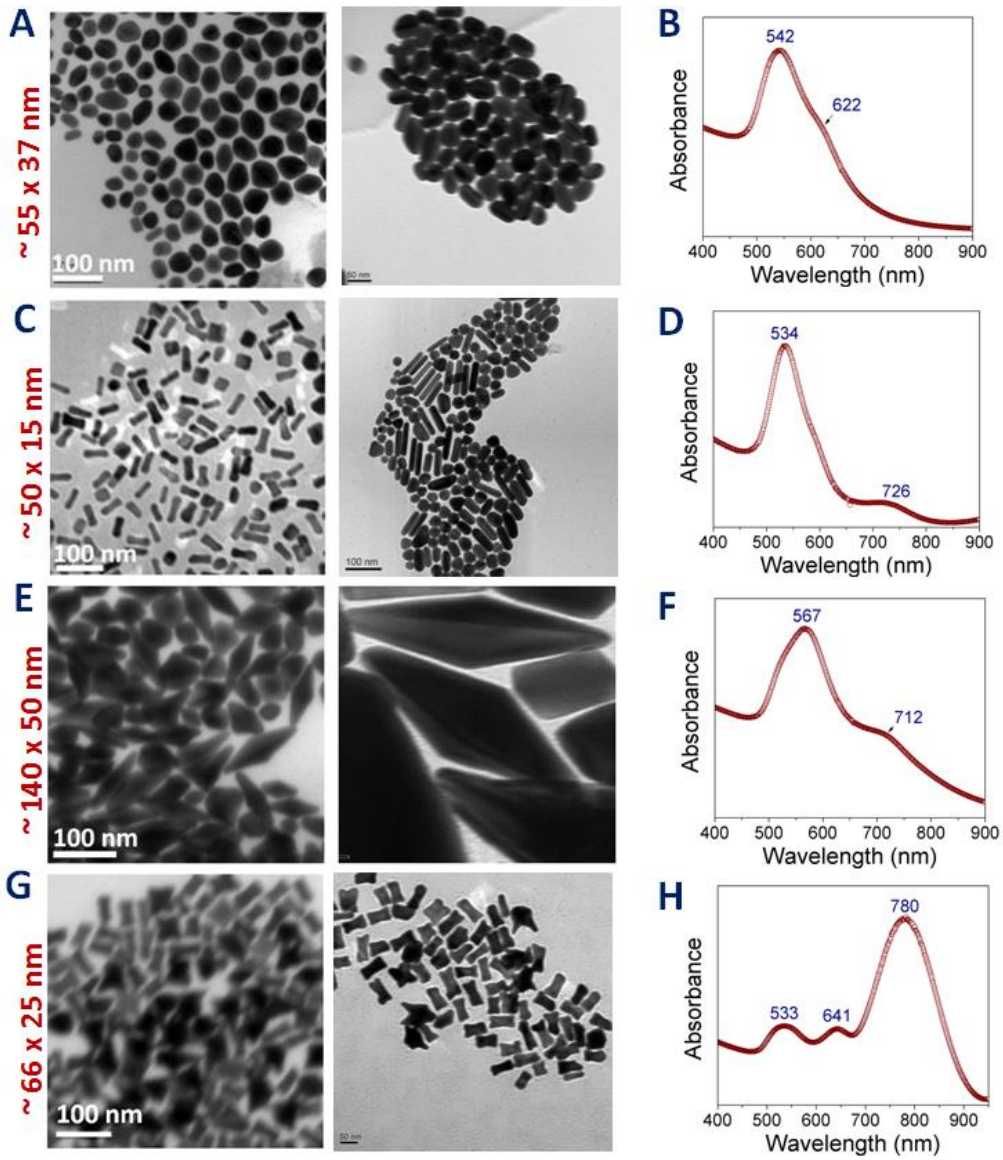

Figure 5-1 TEM images and UV-Vis absorption spectra of Au nanostructures with different shapes: (A,B) spheroids, hexagonal plates, (C,D) short-rods, SR, (E,F) bipyramids and (G,H) dog-bones.

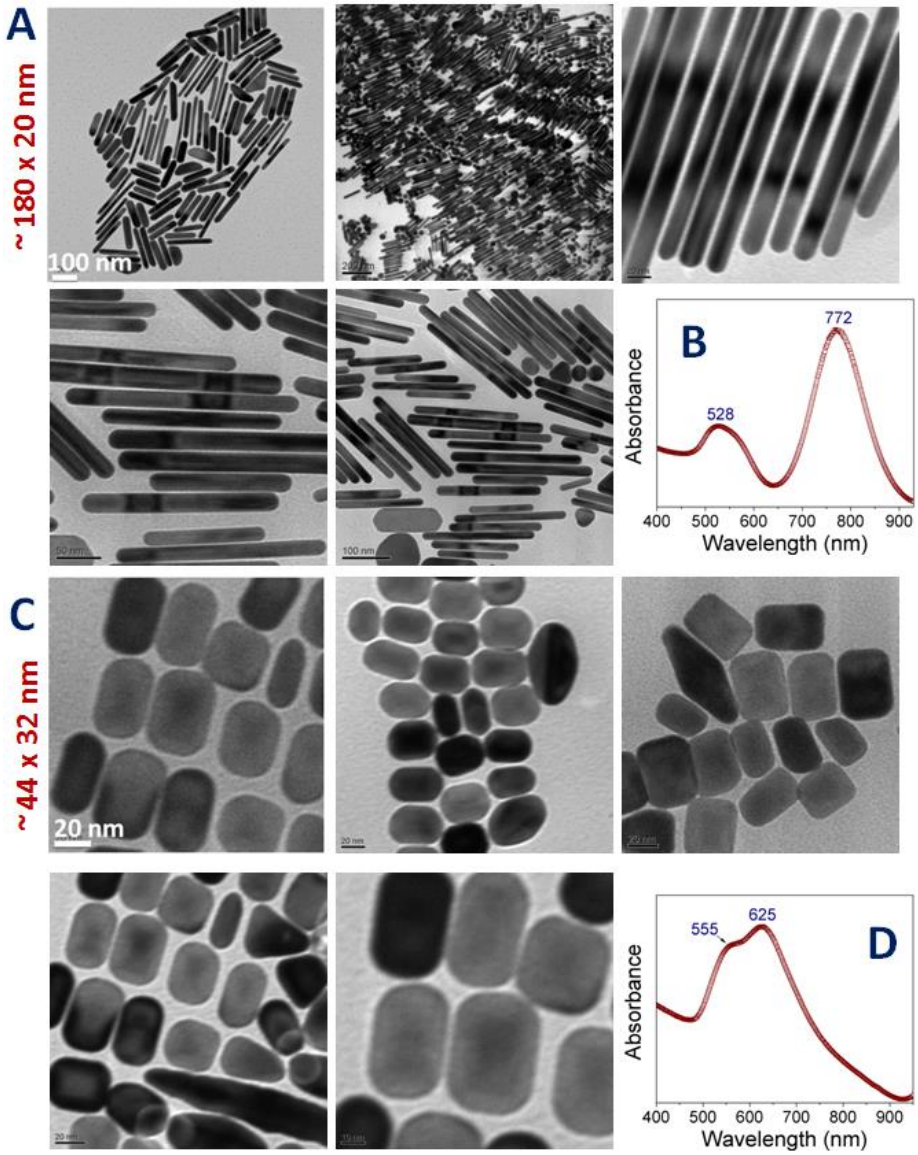

Figure 5-2 TEM images and UV-Vis absorption spectra of Au nanostructures with different shapes: (A,B) long rods and (C,D) round-corner rectangles.

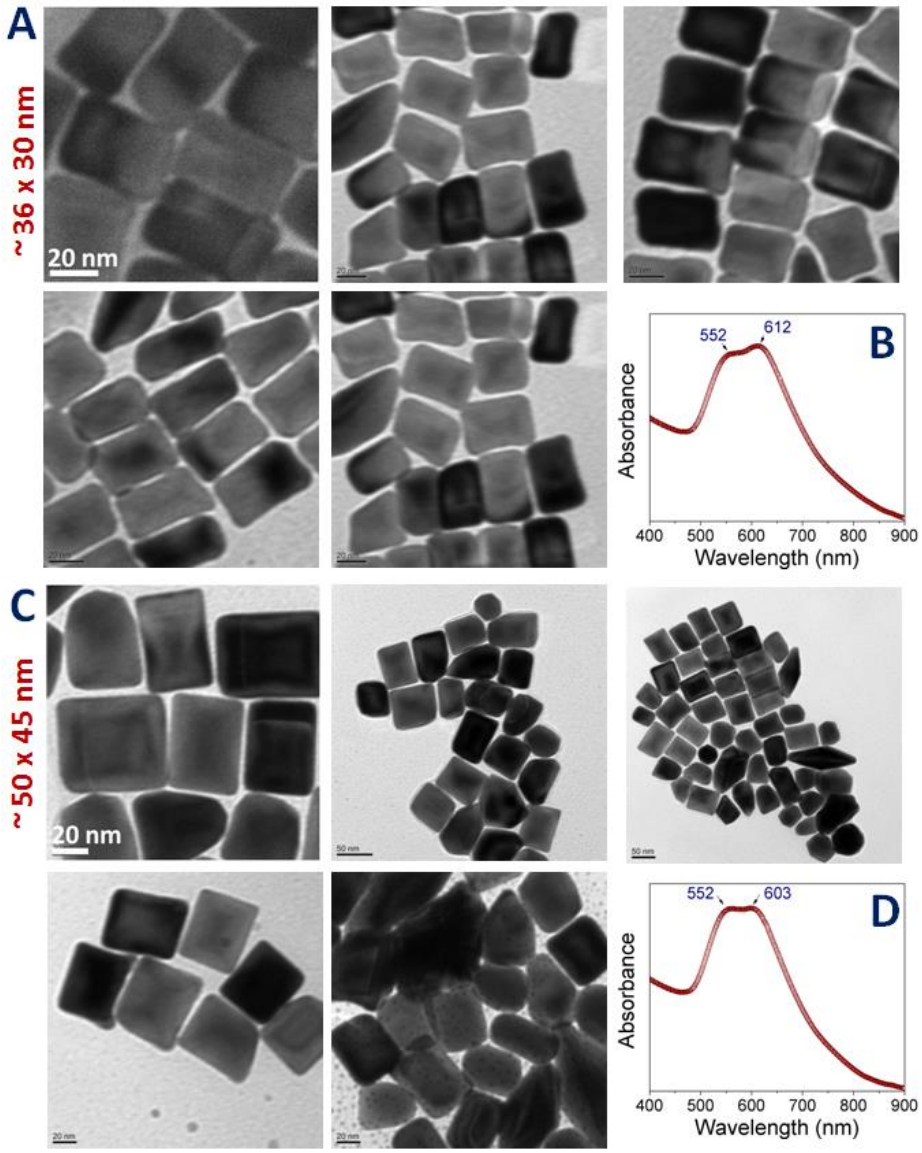

Figure 5-3 TEM images and UV-Vis absorption spectra of Au nanostructures with different shapes: (A,B) sharp-cornerrectangles and (C,D) cubes.

The evolution of the SPR bands of the Au nanostructures with the shape changes is clearly evident in the UV-Vis absorption spectra shown in **Figs. 5.1-5.3 (B,D,F,H)**. The results show the same trends reported in the literature where no SPR is observed for ultrasmall Au nanoparticles with 2-4 nm diameters [261] as can be seen in case of the seed particles shown in **Fig. 5.4**, and a single band around 520-530 nm, weakly dependent on the particle size, is observed for spherical particles of an average size of 15 nm **(Fig. 5.5)** as shown in the UV-vis spectrum shown in **Figs. 5.6.** [248-250, 259, 260] Gold long-rods (**Fig. 5.2-B**) exhibit two SPR bands, near 528 nm and 772 nm, due to the transverse and the longitudinal electronic oscillations, respectively [224, 249, 250, 259]. In such case the polarization of light or the coherent collective oscillation is induced in the two directions along the short and the long axes of the rod. The excitation and oscillation along the short axis give rise to an absorption band in the higher energy region (528 nm), similar to that of Au nanospheres which is called the transverse band. The excitation and plasmon oscillation along the long axis give rise to a relatively much stronger absorption band in the lower energy region (772) which is called the longitudinal band. While the absorption maximum of the transverse band is insensitive to the width of the rod, that of the longitudinal band is largely red-shifted from the visible to the near-IR region as the length increases. [53, 250, 262] The axial ratio between the length and the width represents the size of a nanorod and the linear proportionality between the axial ratio, and the longitudinal band makes it possible to tune the optical properties of Au nanorods by changing the axial ratio or changing the length. Gold nanoparticles with prism or quasi prism shapes have three SPR bands due to the in-plane dipole plasmon resonance, the in-plane quadrupole resonance, and the out-of plane quadrupole resonance (**Figs. 5.1-F and 5.1-H**). [224, 249, 250, 259, 260] The out-of plane dipole resonance is sufficiently weak and broad that it is barely discernible as a shoulder on the in-plane resonance (**Fig. 5.1-F**). The in plane dipole plasmon

resonance is very sensitive to the sharpness of the tips on the triangles. [224, 249, 250, 259, 260] These unique optical properties of anisotropic gold nanocrystals enable the tuning of SPR to any wavelength specific to a particular application from the visible to the NIR spectral regions. [221, 223, 226]

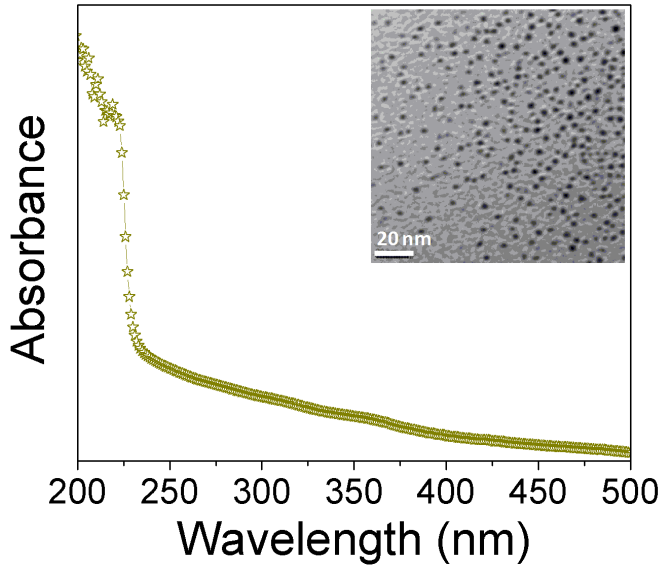

Figure 5-4 UV-Vis absorption spectrum and TEM image of the Au seed nanoparticles.

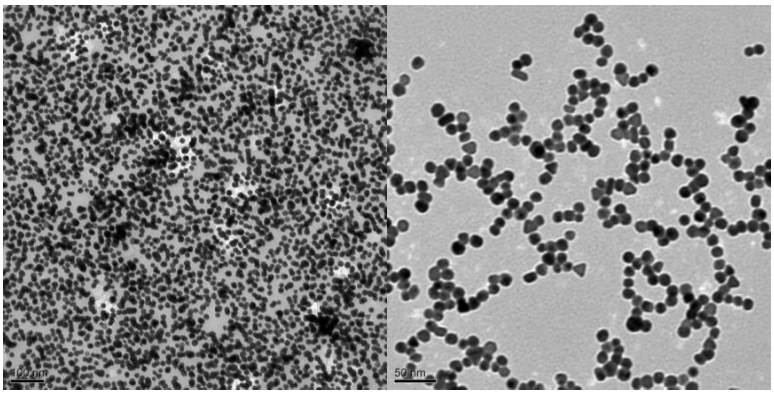

Figure 5-5 TEM images of the Au nanospheres (average diameter ~ 15 nm).

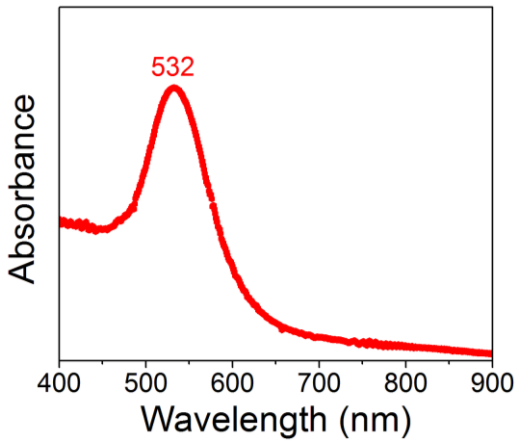

Figure 5-6 UV-Vis absorption spectrum of 15 nm Au nanospheres prepared by citrate reduction.

We selected five distinct shapes of the gold nanostructures shown in **Figs. 5.1-5.3** namely, spheroids (**Fig. 5.1-A**), short-rods (SR, **Fig. 5.1-C**), bipyramids (**Fig. 5.1-E**), long rods (LR, **Fig. 5.2-A**), and cubes (**Fig. 5.3-C**) in addition to the small spheres prepared by citrate reduction method[37] (**Fig. 5.5**) to investigate the photothermal energy effects and laser-induced size reduction of these Au nanostructures in the absence and presence of GO. For each selected shape, two solutions containing similar concentrations of Au nanoparticles of the same shape with and without GO were laser irradiated under identical conditions. Absorption spectra and TEM images were recorded for each solution before and after the laser irradiation. The temperature rise in each solution was also monitored during the laser irradiation. The results are presented in **Figs. 5.7-5.12** and are discussed below.

Figures 5.7-A and 5.7-B display TEM images of the spherical Au nanoparticles after the 532 nm laser irradiation in the absence and presence of GO (TEM images of the as prepared spherical particles are shown in Fig. S2, SI). The TEM images shown in **Fig. 5.7-A** indicate a slight decrease in the average size of the spherical particles from 13 ± 2 to 10 ± 2 nm following the laser irradiation in water. The corresponding SPR band exhibits a small blue shift from 532 nm

to 512 nm as shown in **Fig. 5.7-C**, consistent with the weak dependence of the SPR of spherical Au nanoparticles on particle size [224, 260]. In presence of GO, the 532 nm laser irradiation resulted in almost the disappearance of the SPR band as shown in **Fig. 5.7-C** suggesting more effective melting and evaporation of the Au nanoparticles during the laser irradiation of Au-GO suspension. This, indeed, is confirmed by the TEM images shown in **Fig. 5.7-B** which indicate that the diameters of the Au-nanoparticles significantly decreased from 13 ± 2 nm to 5.4 nm upon laser irradiation in the presence of GO. Thus, both the absorption spectra and the TEM micrographs clearly show that after the 532 nm laser irradiation in the presence of GO, the Au nanoparticle sizes become profoundly smaller than in the absence of GO under identical laser irradiation conditions. This result implies that the temperature of gold nanoparticles during the irradiation is much higher in presence of GO than in pure water. This is consistent with the measured temperature changes caused by laser irradiation of the three solutions of spherical Au nanoparticles in water; GO in water and spherical Au-nanoparticles dispersed in a GO-water mixture under identical experimental conditions as shown in **Fig. 5.7-D**.

The temperature of the GO solution containing spherical Au-nanoparticles reaches **69.3 °C** after 10 minutes of laser irradiation (532 nm, 4 W, 30 Hz) in comparison with the same concentration of spherical Au nanoparticles in water, and the GO solution without Au nanoparticles which reach **47.5 °C** and **56 °C**, respectively under identical experimental conditions. The higher temperature rise observed for the Au nanoparticles dispersed in the GO solution demonstrates that the coupling of the photothermal effects of Au nanoparticles and GO can result in highly efficient photothermal energy convertors. The temperature rise during the irradiation of the Au nanoparticles-GO solution assists in anchoring the nanoparticles to the defect

sites created by the laser reduction of GO thus resulting in uniform dispersion of the small Au particles among the RGO nanosheets as shown by the TEM image of **Fig. 5.7-B**.

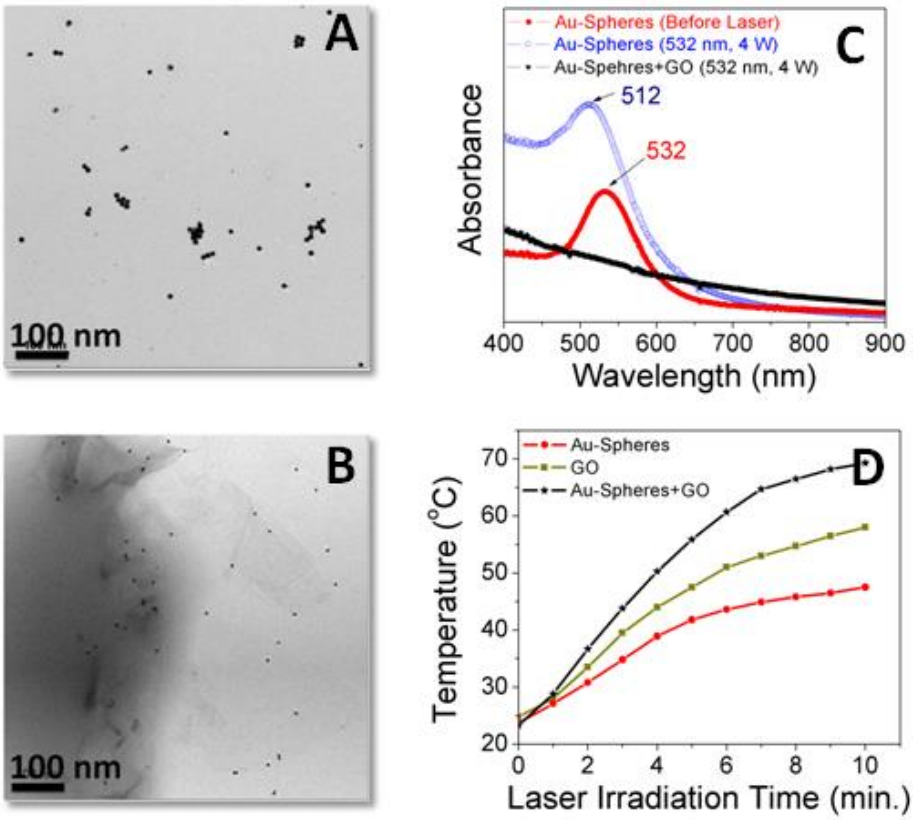

Figure 5-7 TEM images of Au nanospheres after the 532 nm laser irradiation in absence (A) and presence of GO (B); UV-Vis absorption spectra after laser irradiation in water and in GO (C); temperatures profiles showing the increase of the solutions temperatures (D).

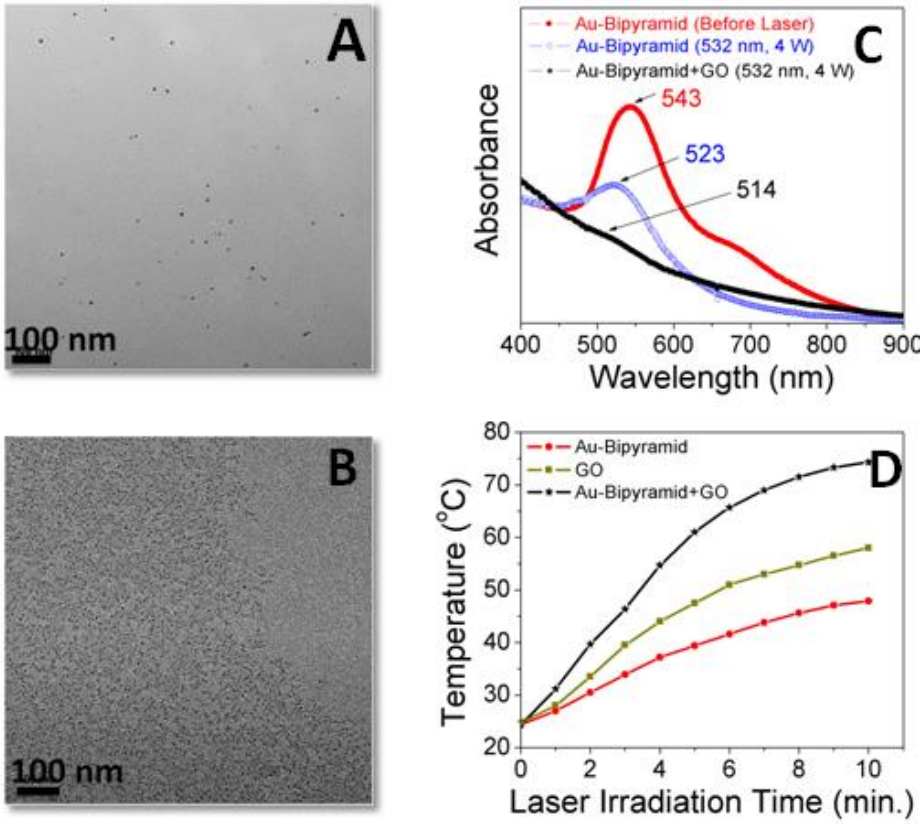

Figure 5-8 TEM images of Au bipyramids after the 532 nm laser irradiation in absence (A) and presence of GO (B); UV-Vis absorption spectra after laser irradiation in water and in GO (C); temperatures profiles showing the increase of the solutions temperatures (D).

Figures 5.8-A and 5.8-B display TEM images and UV-Vis absorption spectra of the as-prepared bipyramidal Au nanoparticles after the 532 nm laser irradiation in the absence and presence of GO. The absorption spectra of the as-prepared bipyramidal nanoparticles (**Fig. 5.8-C**) show two absorption bands at 567 and 712 nm corresponding to the transverse and the longitudinal SPR bands. Both bands disappear following the laser irradiation in water, as shown in **Fig. 5.8-C**, with the appearance of one SPR band at 523 nm indicating the melting of the Au-bipyramidal nanoparticles and the reforming of Au- nanospheres during the laser irradiation process. This is confirmed by the TEM image displayed in **Fig. 5.8-A** which shows spherical particles with an average size of 4.3±1.5 nm as compared to the dimensions of the original bipyramidal particles of

140 x 50 nm (shown in **Fig. 5.1-E**). Interestingly, the same laser irradiation in the presence of GO converts the bipyramidal particles into ultrasmall spherical particles with an average diameter of 1.6±0.6 nm as shown in **Fig. 5.8-B**. This size reduction is accompanied by rapid increase in solution temperature reaching about **74.3 ºC** in 10 min of laser irradiation, compared to **47.9 ºC** without GO**,** as shown in **Fig. 3-H**. This increase in temperature reflects the net heat transfer to water resulting from the coupled photothermal effects of the Au bipyramidal nanoparticles and GO.

Figures 5.9-A, and 5.9-B display TEM images and UV-Vis absorption spectra of the as-prepared Au SR after the 532 nm laser irradiation in the absence and presence of GO. The as-prepared Au short rods, **shown in Fig. 5.1-C,** are characterized by average dimensions of 50±5 x 15±2 nm (aspect ratio ~ 3.3) and exhibit two SPR bands at 534 nm and 726 nm as shown in **Fig. 5.1-D**. Following the laser irradiation in the absence of GO, only the transverse band around 520 nm is observed in the absorption spectrum as shown in **Fig. 5.9-C** consistent with the formation of small spherical nanoparticles with average diameters of 5.3±1.9 nm as evident from the TEM image in **Fig. 5.9-A**. However, the Au nanoparticles formed following the laser irradiation of the particles dispersed in the GO solution have an average diameter of 2.4±0.55 nm as shown in **Fig. 5.9-B**, consistent with the near disappearance of the SPR band except for a small shoulder at 517 nm as shown in **Fig. 5.9-C**. The formation of these ultrasmall Au nanoparticles is accompanied by a strong enhancement in the photothermal energy conversion of the Au SRs dispersed in the GO solution where the solution temperature reaches **70.5 °C** after 10 minutes of laser irradiation (532 nm, 4 W, 30 Hz) as compared to **47.2 °C** and **56 °C** for the Au SRs in water and the GO solution, respectively under identical experimental conditions as shown in **Fig. 5.9-D**.

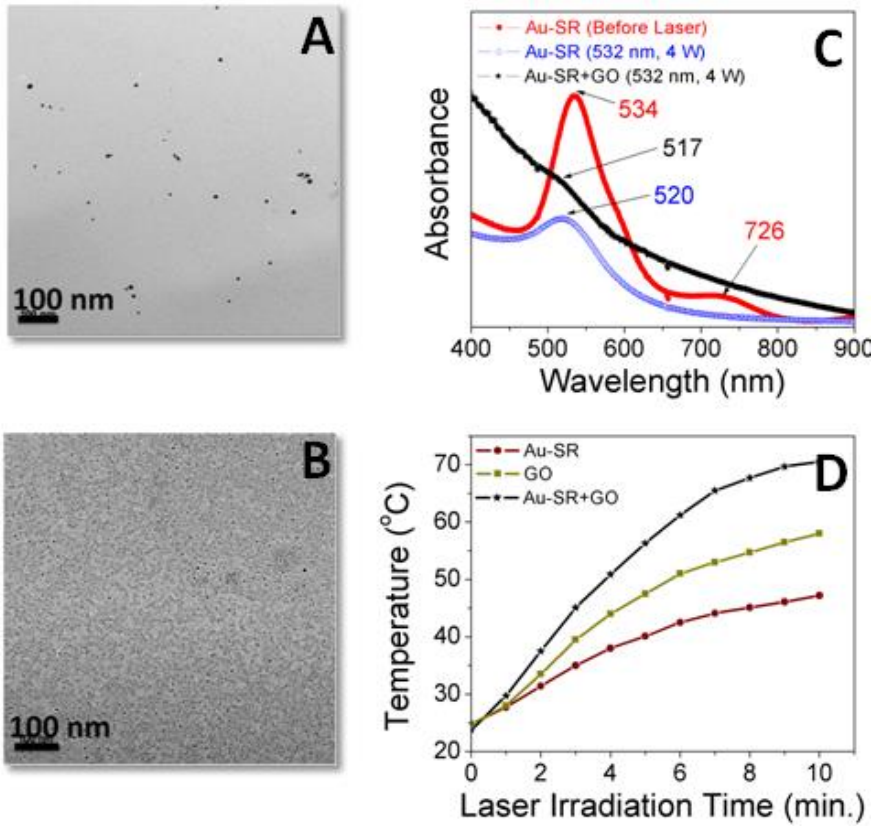

Figure 5-9 TEM images of Au short rods after the 532 nm laser irradiation in absence (A) and presence of GO (B); UV-Vis absorption spectra after laser irradiation in water and in GO (C); temperatures profiles showing the increase of the solutions temperatures (D).

The as-prepared Au LRs, , **shown in Fig. 5.2-A,** have average length and width of 180±20 nm and 20±5 nm, respectively (aspect ratio ~ 9), and exhibit two SPR bands, the transverse near 528 nm and the longitudinal near 772 nm (**Fig. 5.2-B**). Following the 532 nm laser irradiation, the longitudinal band disappears and the transverse band shifts to 523 nm indicating the transformation of the Au LRs into smaller spherical particles. This is clear in the TEM image shown in **Fig. 5.10-A** where spherical particles with an average diameter of 5.5±1.9 nm are observed. Again, laser irradiation of the Au LRs in the presence of GO results in well-dispersed ultrasmall Au nanoparticles with an average diameter of 2.9±1.7 nm as shown in **Fig. 5.10-B**. Accordingly, the transverse SPR band almost disappears following the laser irradiation of the Au LRs in GO as

shown in **Fig. 5.10-C**. The measured temperature change caused by laser irradiation of the Au LRs in the GO solution indicates that the solution temperature reaches **70.2 °C** after 10 minutes of laser irradiation (532 nm, 4 W, 30 Hz) as compared to **55.1 °C** and **56 °C** for the Au LRs in water and the GO solution, respectively under identical experimental conditions as shown in **Fig. 5.10-D**. Again, similar to the Au spherical and SR particles, the presence of GO results in a significant enhancement in the observed photothermal effects.

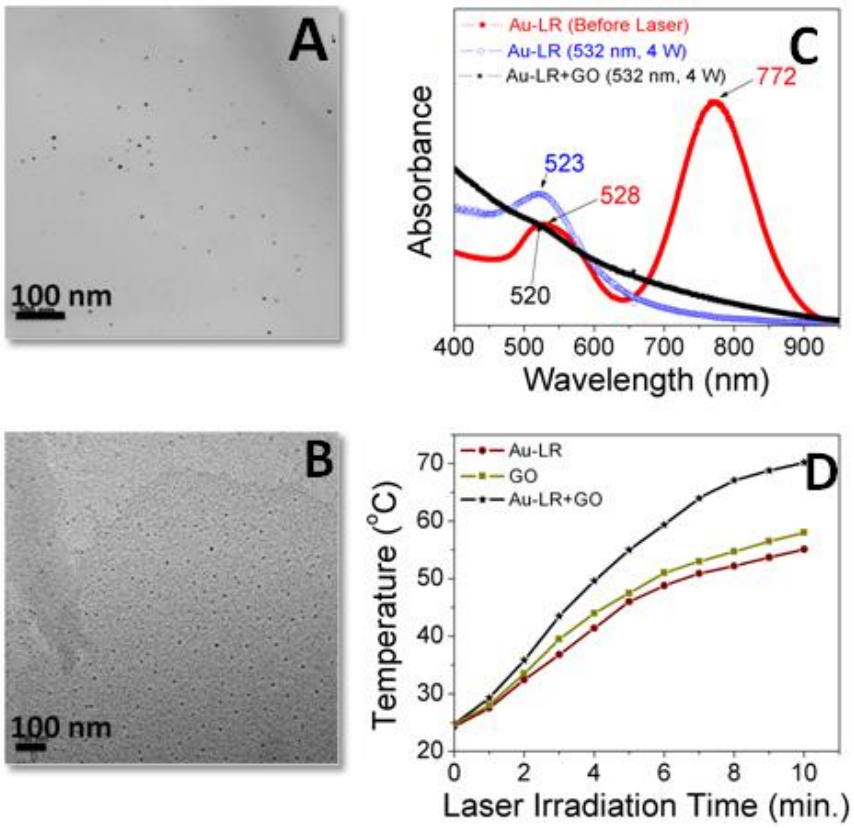

Figure 5-10 TEM images of Au long rods after the 532 nm laser irradiation in absence (A) and presence of GO (B); UV-Vis absorption spectra after laser irradiation in water and in GO (C); temperatures profiles showing the increase of the solutions temperatures (D).

The results for the Au spheroids (shown in **Figs. 5.11-A to 5.11-D)** and Au cubes (shown in **Figs. 5.12-E to 5.12-H)** follow the same general trends observed for the other Au shapes thus leading to generalized findings. Typically, laser irradiation in the presence of GO results in smaller spherical Au nanoparticles well-dispersed on the RGO nanosheets accompanied by a strong enhancement in the photothermal effect as evident by the significant increase of the temperature of the Au-GO solution as compared to the individual Au and GO solutions. However, the size reduction of the Au spheroids and cubes (**Figs. 5.11-5.12; B**) is not as much as with the other shapes (spherical, bipyramids, short-rods and long-rods) where ultrasmall Au nanoparticles with no SPR peaks [261] were observed following the laser irradiation of the Au particles in the presence of GO (**Figs. 5.7-5.10; B**), as compared in **Fig. 5.13**. This appears to be related to the volume of the particles where the large volumes of the spheroids and cubes may require longer irradiation times and higher laser powers in order to effectively melt and vaporize the large Au nanoparticles [241]. The melting of the nanoparticles leads to the shape change from nonspherical to spherical particles and the size reduction is due to the vaporization of the particles. According to the theoretical estimation and experimental results of Pyatenko et al. [245], under low laser energy flow density (less than 10^{12} W/m^2 similar to the conditions of the current experiments), the particle-heating-melting-evaporation mechanism is solely responsible for the size reduction of the nanoparticles.

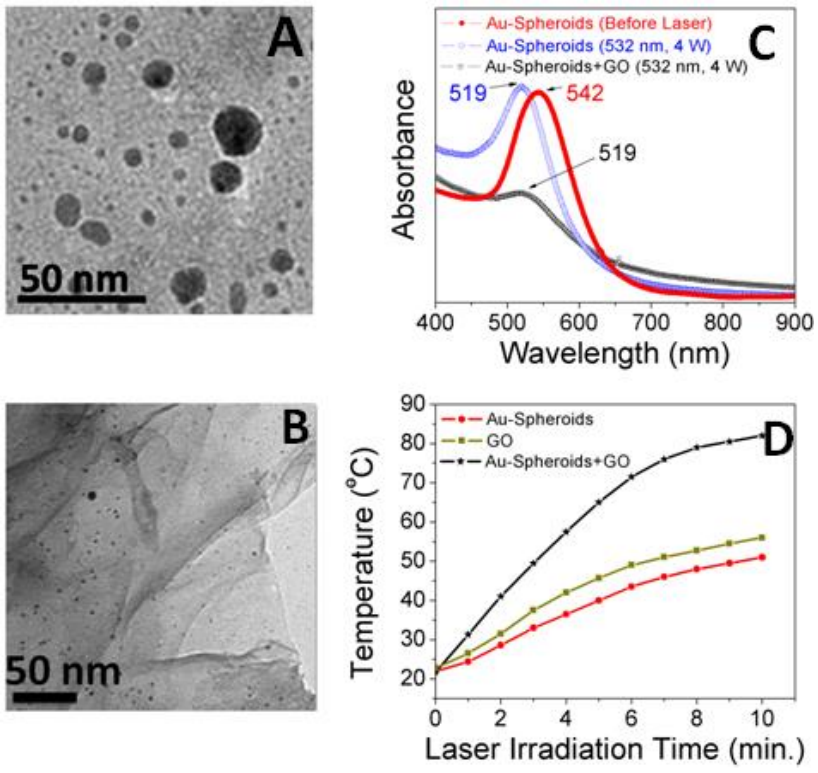

Figure 5-11 TEM images of Au spheroids after the 532 nm laser irradiation in absence (A) and presence of GO (B); UV-Vis absorption spectra after laser irradiation in water and in GO (C); temperatures profiles showing the increase of the solutions temperatures (D).

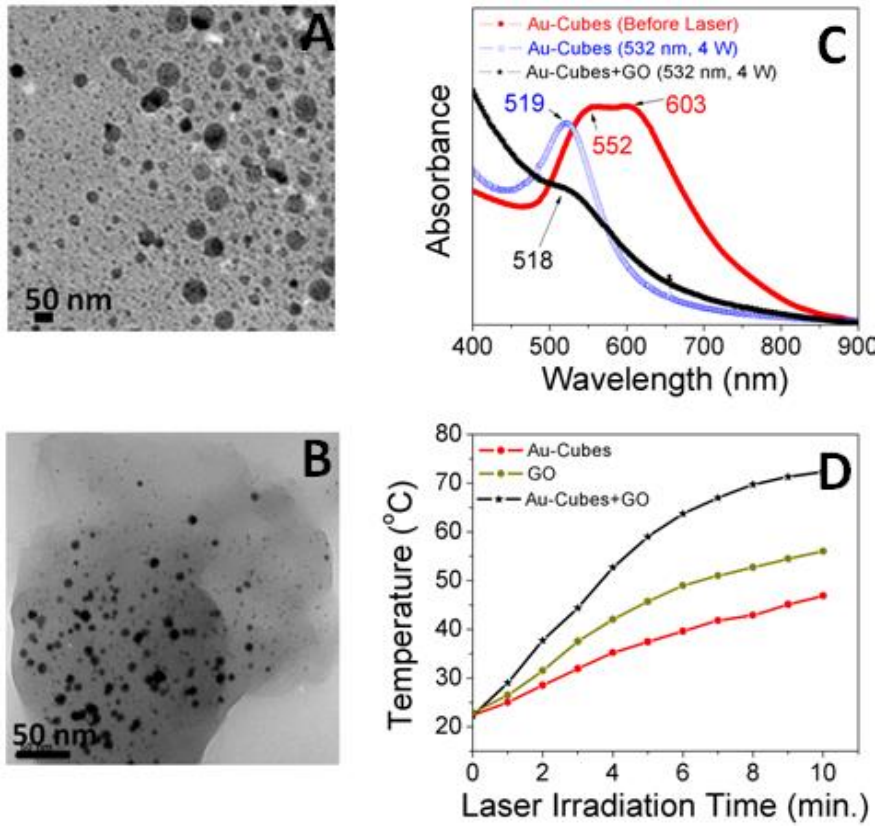

Figure 5-12 TEM images of Au cubes after the 532 nm laser irradiation in absence (A) and presence of GO (B); UV-Vis absorption spectra after laser irradiation in water and in GO (C); temperatures profiles showing the increase of the solutions temperatures (D).

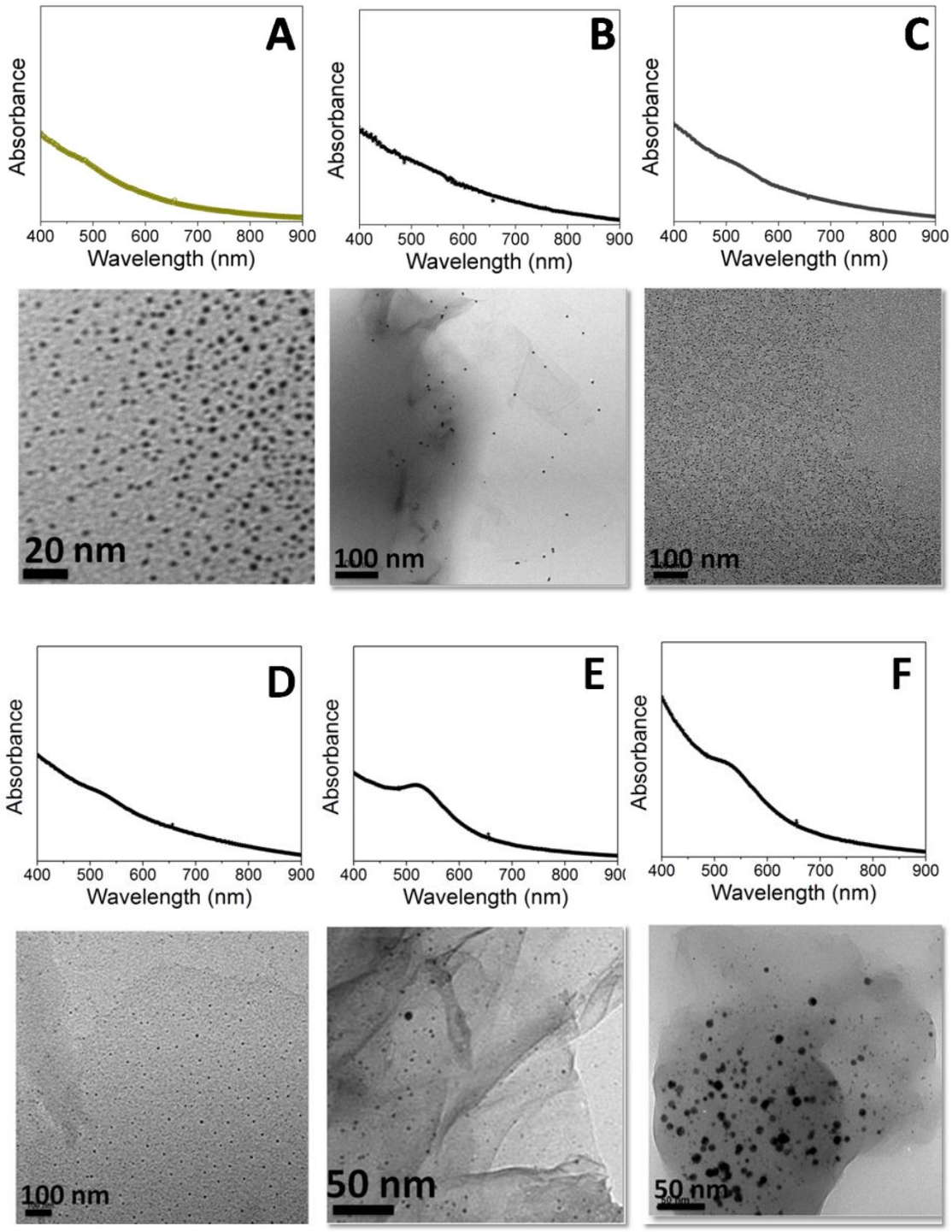

Figure 5-13 Comparison between the absorption spectra and TEM images of laser irradiated Au-nanoparticles of different shapes in GO solutions (A: seed for comparison; B: Au nanospheres; C: Au-bipyramids, D: Au-LRs; E: Au-spheroids; F: Au-cubes).

The observed temperature rise reflects the steady state net heat transfer from Au nanoparticles and RGO nanosheets to the solution. **Fig. 5.14** compares the extent of temperature rise for different shapes of Au nanostructures in the absence and presence of GO during 532 nm laser irradiation. **Table 5.1** lists the maximum temperature rise observed for different shapes of Au nanoparticles following the 532 nm laser irradiation in the presence and absence of GO under identical experimental conditions. Temperature rise profiles obtained under irradiation from 355 nm Nd-YAG laser are presented in **Fig. 5.15** for. The results reveal that the spheroid particles display the highest temperature rise **(82°C)** followed by the various cubes **(72.3-77.5 °C),** then the bipyramids and dog-bones **(74.3-75 °C)**, then the long and short rods **(70.2-70.5 °C),** and finally the small spheres **(69.3 °C).** The observed trend appears to be related again to the volume of the particles and the melting temperatures of different shape nanostructures. For example, the larger volume of the hexagonal plates (spheroids) and probably their lower melting temperature result in more heat being transferred to water and thus elevating the temperature of the solution to **82 °C**. Similarly, the large volumes of the rounded-corner nanocubes result in a significant temperature rise of water **(77.5 °C).** For comparison, the smaller volumes of the small spherical Au particles (**Fig. 3-A**), lead to less photothermal effect and consequently less temperature rise of water (**69 °C**). For the Au nanorods both the small volumes and probably the higher melting temperatures result in less heat transferred to the solution which increases the temperature to only ~**70 °C** as compared to **82°C** for the hexagonal plates.

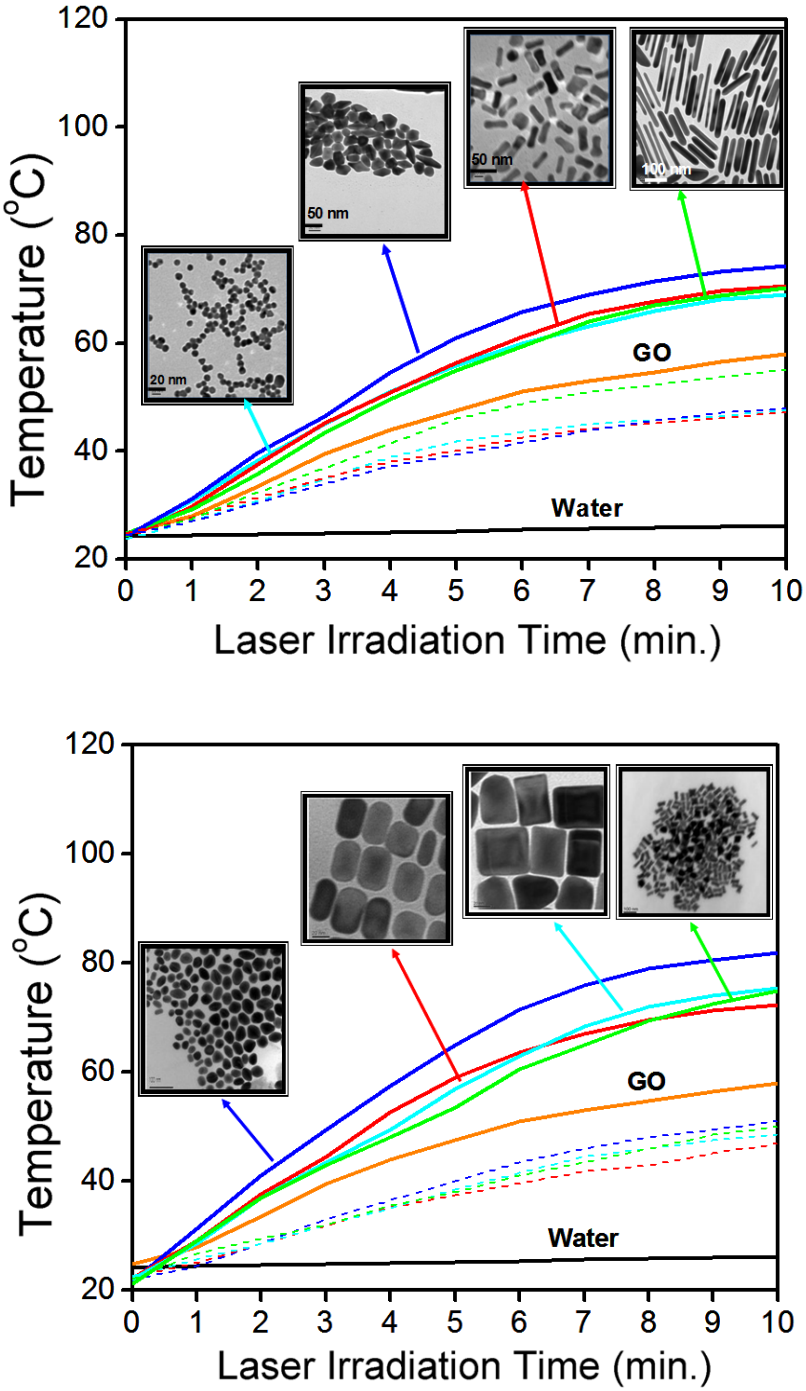

Figure 5-14 Temperature rise during 4 W, 532 nm laser irradiation of different shapes Au nanoparticles without (dashed lines) and with (solid lines) GO; (Top) spheres, bipyramids, short rods and long rods; (Bottom) spheroids, round-corner rectangles, cubes and dogbones.

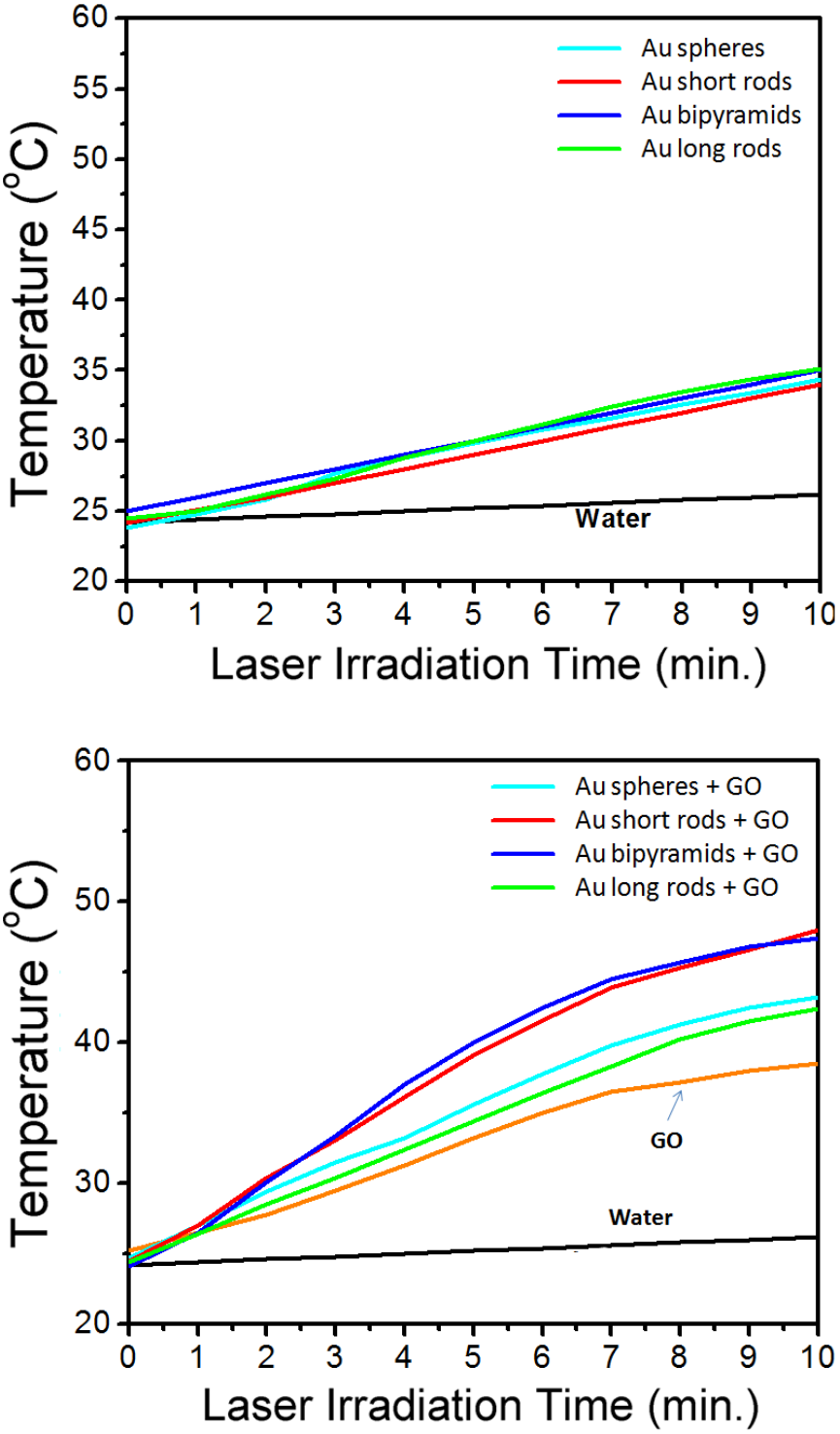

Figure 5-15 Temperature rise during 4 W, 355 nm laser irradiation of selected Au nanoparticles without (top) and with (bottom) GO dispersed in water.

The results clearly indicate that the presence of GO enhances the heating efficiency of the Au nanostructures following the absorption of the 532 nm photons which leads to the subsequent melting and evaporation processes resulting in the formation of monodisperse ultrasmall Au nanoparticles supported on the LCG nanosheets. Previous work has demonstrated that the 532 nm laser irradiation of the Au nanoparticles resulted in a significant size reduction from an initial diameter of 54±7 nm to an average diameter of 6 nm but with a bimodal size distribution [246]. The bimodal size distribution is attributed to Ostwald ripening process where the initially formed small particles with higher surface energies are consumed in the growth of the large particles with lower surface energies at longer irradiation times [246]. The absence of bimodal size distributions in the Au nanoparticles formed by laser irradiation in the presence of GO in the present work suggests that the mobility of the particles is significantly reduced to a degree that does not allow for the dynamic Ostwald ripening process. This can be explained if the small Au particles are anchored to defect sites on the RGO nanosheets which can restrict their mobility.

It is well established that that both the chemical and laser reduction of GO result in the formation of graphene nanosheets with a significant number of defect sites including vacancies, disorder, defective edges, and many others [68, 263-268]. In the laser converted graphene, the nature of these defects depend on the oxygen functional groups interacting with the photogenerated electrons and holes within GO [68, 267, 268]. **Figure 5.16** compares the extent of temperature rise 4 W, 532 nm laser irradiation of Au binary mixtures each composed of nanoparticles of two different shapes in absence and in presence of GO. A similar trend in temperature rise was observed for Au binary mixtures with GO under irradiation of 532 nm laser of 4 W and 5 W. Generally Au binary mixtures with GO exhibited higher temperature rises compared to those mixtures without GO after 10 min of laser irradiation from 4 and 5 W (532 nm) Nd-YAG laser, as shown in **Figs. 5.16 and**

5.17, respectively. A comparison between temperature rise profile of Au binary mixtures with GO obtained under 4 and 5 W laser irradiation (532 nm) is presented in **Fig. 5.18.**

Table 5-1 Maximum solution temperature rise after 10 min of laser irradiation of the Au nanoparticles with different shapes with and without GO using the 532 and 355 nm wavelengths.

Solution	Temperature (ºC) after 10 min.				
	4 W, 532 nm		5 W, 532 nm		4 W, 355 nm
		+GO		+GO	
GO		**58**	NA	NA	**37**
Nanospheres	**47.5**	**69.3**	NA	NA	**32**
Bipyarmids	**47.9**	**74.3**	NA	NA	**33**
Short rods	**47.2**	**70.5**	NA	NA	**34**
Long rods	**55.1**	**70.2**	NA	NA	**34**
Spheroids	**51**	**82**	NA	NA	**43**
Cubes	**46.9**	**72.3**	NA	NA	**47**
Round-Corner Rectangles	**44.5**	**77.5**	NA	NA	**48**
Sharp-Corner Rectangles	**48.5**	**75.5**	NA	NA	**42**
Dogbones	**50**	**75**	NA	NA	NA
Long Rods + Short Rods	**50**	**72.5**	**66**	**87.9**	NA
Long Rods+ Cubes	**51**	**71.5**	**67.8**	**85.8**	NA
Spheroids + Cubes	**59**	**77**	**82**	**94.5**	NA

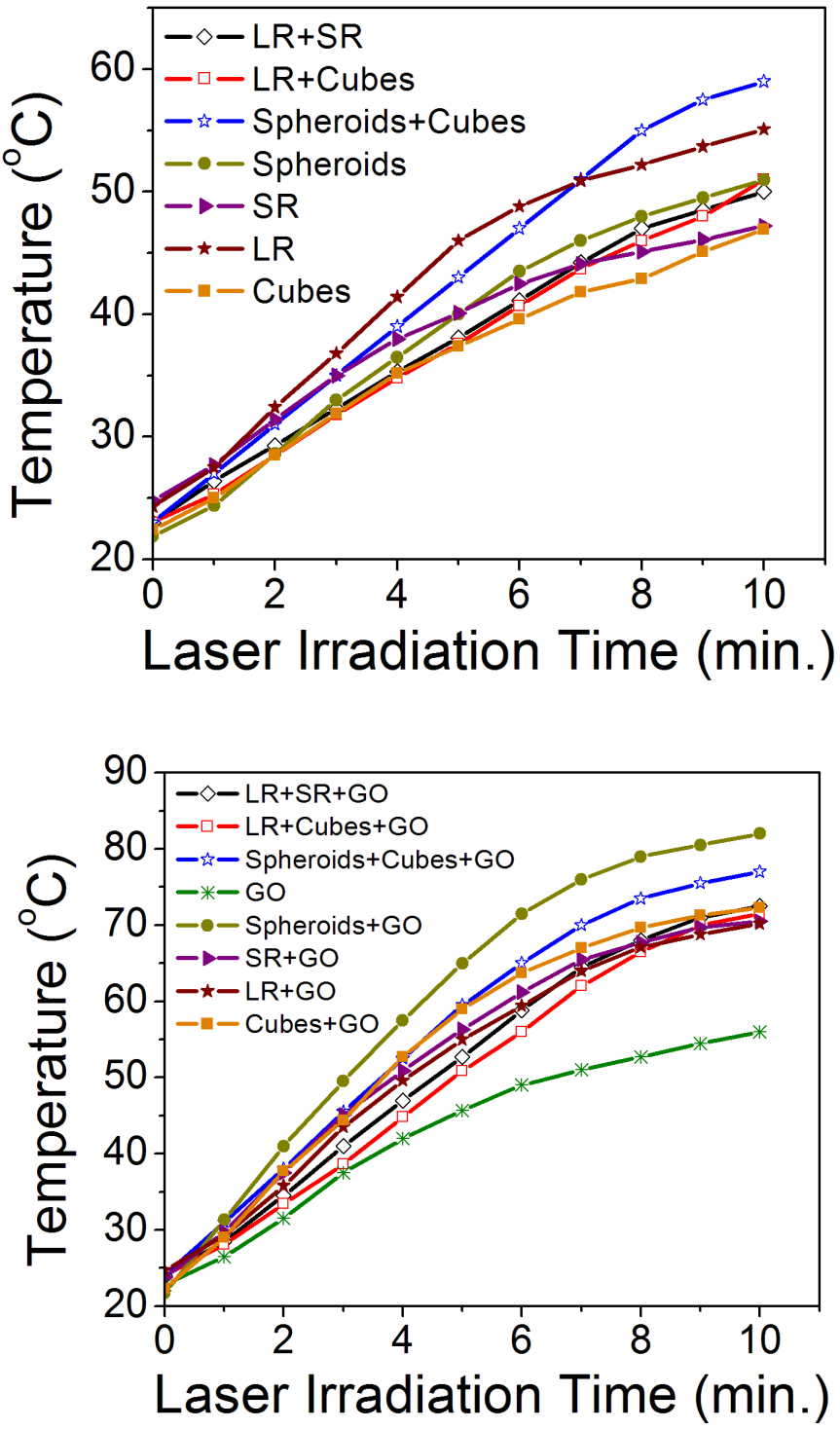

Figure 5-16 Temperature rise during 4 W, 532 nm laser irradiation of Au binary mixtures each of two different shapes without (top) and with (bottom) GO and compared to individual shapes.

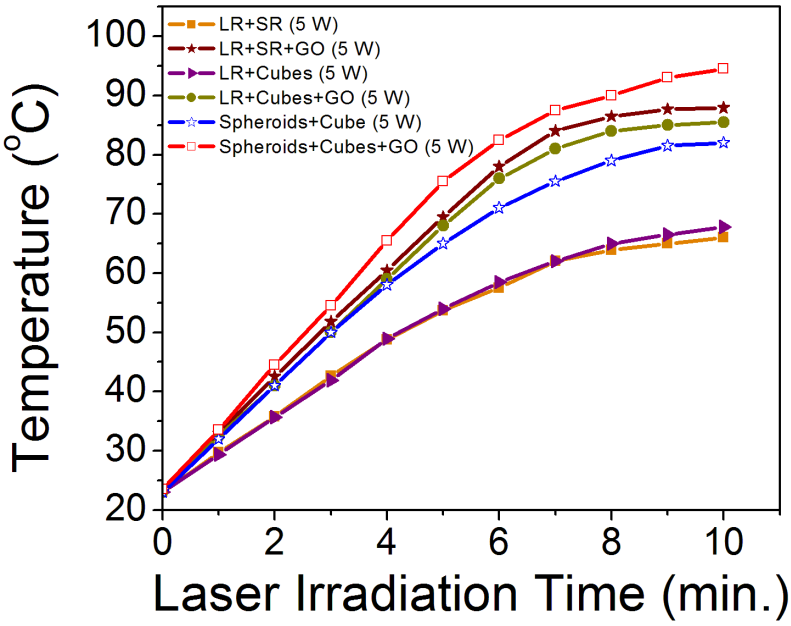

Figure 5-17 Temperature profile during 532 nm laser irradiation at 5 W of Au binary mixtures without and with GO.

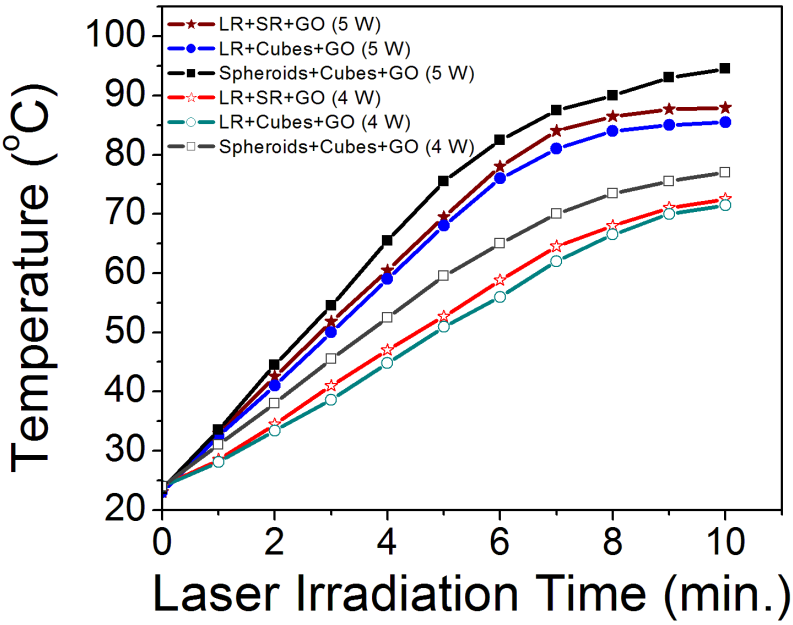

Figure 5-18 Comparison between temperature rise profiles of selected Au binary mixtures with GO irradiated with 532 nm laser at 4 and 5 W laser power for 10 min.

Raman spectroscopy is one of the most useful techniques that can identify the nature of defects and disorder in the graphene and Au-graphene nanosheets [269-272]. To gain information on the extent of defects in the Au-graphene nanosheets, we have applied Raman spectroscopy to compare the LCG with the graphene-containing Au nanoparticles both formed by laser irradiation of GO. **Figure 5.19-A** compares the Raman spectra of GO before and after the 532 nm laser irradiation (10 min, 4 W, 30 Hz). The spectrum of the exfoliated GO exhibits the characteristic G-band (1594 cm^{-1}) and the D-band (1354 cm^{-1}) with a D to G intensity ratio of about 0.70. The G-band arises from the vibration of the sp^2 bonded carbon atoms and the D-band is attributed to structural disorder at defect sites with the D/G ratio usually taken as a measure of the quality of the graphitic structures since for highly ordered pyrolitic graphite, this ratio approaches zero [269-271].

Following the 532 nm laser irradiation of GO, the D/G ratio decreases to 0.40 indicating a significant reduction of the degree of disorder and defect sites in the LCG. However, no decrease in the intensity of the D band relative to the G-band is observed following the laser irradiation of the GO-Au nanoparticle solutions as shown in **Figs. 5.19-B** and 5.19-**C** for the Au long rods and cubes, respectively. In fact, the D/G ratio increases to 0.8 (higher than the D/G ratio of GO) after the laser irradiation of the GO solutions containing either the Au nanorods or the nanocubes. Furthermore, a significant shift of the G-band to higher frequency is observed following the laser irradiation of the GO solutions containing the Au nanorods or the nanocubes (1603 cm^{-1} and 1601 cm^{-1}, respectively compared to1594 cm^{-1} in the absence of Au nanoparticles). This shift is consistent with doping graphene with electron acceptors thus, the Au nanoparticles are acting as week electron acceptors that induce a charge transfer from graphene to the Au nanoparticles [272]. The increase in the D/G intensity ratio compared to the LCG (**Fig. 5.19-A**) and the blue shift of

the G-band are taken as evidence for the presence of more structural defects in the graphene lattice induced by laser irradiation of GO in the presence of Au nanoparticles. These defect sites in the RGO nanosheets act as favorable nucleation sites for the ultrasmall Au nanoparticles which by occupying these vacancies are no longer mobile for Ostwald ripening process to take place and thus the formation of large Au nanoparticles and aggregates is significantly decreased.

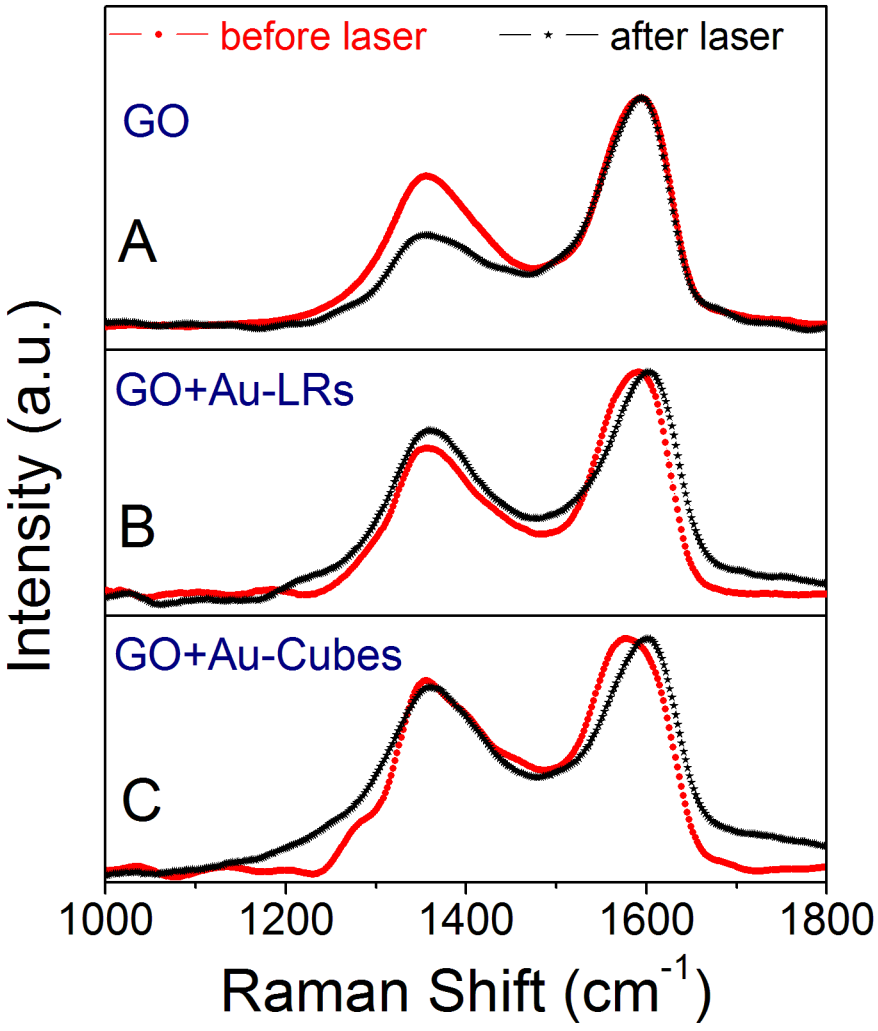

Figure 5-19 Raman spectra of GO (A), GO + Au nanorods (B) and GO + Au nanocubes (C) before (red) and after (black) laser irradiation for 10 min (532 nm, 4W, 30 Hz) in solution.

The advantage of our Au-GO nanocomposites over Au nanostructures used in photothermal therapy stems from the enhanced phothermal energy conversion of the Au-GO compared over individual Au or GO. The strong light absorbing capabilities of Au nanostructures in the NIR region is clearly demonstrated in this work. This optical absorbance in NIR region is expected to dramatically increase if our Au-GO nanocomposites are properly functionalized. As evident in this work, when exposed to a 532 nm laser of 4 W, the temperature rise in Au-GO mixtures is higher than in case of corresponding Au or GO alone. Although the dependence of absorption wavelength on the size is limited in Au nanospheres which limits their use in biomedical applications, in composites of GO with ultrasmall Au assemblies, the optical absorption can be readily tuned by the proper functionalization of GO sheets while taking the advantage of the enhanced optical properties of Au when integrated with GO. In one study, the integration of GO with Au nanostructures have been shown to significantly enhance the two-photon excitation processes and 4-fold an enhancement factor was observed for Au-GO composites compared to pure Au [273].

Since small to intermediate-size Au nanostructures are expected to exhibit higher photoabsorption compared to larger ones and thus are more suitable for photothermal treatment [274], this infers the promise of ultrsmall Au nanoparticles assembled on GO reported herein, provided the proper coating of GO. The decrease in the size results in a decrease in the extinction and accordingly the relative contribution of scattering due to the decreased radiative damping in small nanoparticles compared to larger ones [274, 275]. Also ultrasmall Au-GO composites may serve to overcome the decrease in the absorbance of Au nanostructures under laser irradiation which is a challenge in Au-based photothermal therapeutic modality [276] and they are expected to have higher photostability compared to larger ones of other shapes which melt under laser irradiation. A

number of very recent studies have shown the promise of using GO-based composites in various areas of biomedicine such as cancer therapy and imaging, drug delivery and biomodulation [239, 240, 277-287]. In most of these studies, the optimization of the surface chemistry (PEGylation for example) on GO is shown to be critical for potential *in vivo* or *in vitro* biomedical applications [240, 277-280, 282, 283, 286, 287]. Moreover, the internalization of GO into cells has been shown to depend on both GO lateral dimensions, size distribution and cell type [283, 284]. For instance, macrophage cells possessed equal tendency to internalize GO with two different dimensions of 2 and 0.35 μm [284]. It has been found that properly-functionalized RGO sheets are potentially stable in physiological environments and are non-toxic to cells in mice *in vivo* [239]. This study showed that functionalized GO tended to accumulate selectively in tumor cells with lower tendency for passage through reticuloendothelial pathways.

The Au-based photothermal therapy demonstrated in earlier literature work [226, 233, 288-293], if combined with efficient photothermal energy conversion reported herein, may bring great opportunities for cancer treatment. However, substantial work remains in fine tuning of the surface chemistry of Au/GO nanocomposites and the lateral dimensions to optimize their uptake and non-toxicity behaviors for *in vitro* or *in vivo* biomedical applications. Currently, experiments to investigate the effect of polymer coating on the *in vitro* behaviors of Au/GO composites and their physiological stability and cellular uptake are underway. It is worth mentioning that a very recent study showed that functionalized GO could be delivered into mammalian cells and used as sensitive SERS probes after in-situ intracellular formation of Au nanoparticles [279]. A similar study of using PEGylated GO as a nanovector for delivery proteins into cells is also another evident for the ability of GO to permeate cells after proper coating [282].

5.5 Conclusions

In summary, various shaped-Au nanoparticles nanorods of controlled axial ratio, bipyarmids, spheroids and cubes of controlled edges and edge lengths have been synthesized adopting slightly-modified seed-mediated approach. The coupling of the surface plasmon resonance of these Au nanoparticles with the laser reduction of GO leads to significant enhancement of the efficiency of photothermal energy conversion by the gold nanoparticles-GO mixtures. The enhanced photothermal effects can be tuned by controlling the shape and size of the gold nanostructures, which result in a remarkable increase in the heating efficiency of the laser-induced melting and size reduction of gold nanostructures. The large surface areas of the laser RGO nanosheets with multiple defect sites and vacancies provide efficient nucleation sites for the ultrasmall gold nanoparticles to be anchored to the graphene surface. This defect filling mechanism decreases the mobility of the ultrasmall gold nanoparticles and thus stabilizes the particles against the Ostwald ripening process which leads to a broad size distribution of the laser-size reduced gold nanoparticles. The ultrasmall gold-graphene nanocomposites are proposed as novel photothermal energy convertors for a variety of thermochemical and thermomechanical applications, in addition to photothermal therapy, such as heating and evaporation of liquids by solar energy, ignition of solid fuels, and welding of composite materials.

CHAPTER 6 Microwave Synthesis of Bifunctional Magnetic-Luminescent (Fe_3O_4/CdSe) Nanocomposites

6.1 Overview

In this chapter a rapid microwave-assisted synthesis and detailed characterization of a bifunctional nanocomposite, composed of a magnetic core, Fe_3O_4, and a semiconductor shell, CdSe is described. Magnetite Fe_3O_4 nanoparticles are synthesized and used as seeds for the heterogeneous nucleation and growth of the CdSe nanoshells. The optical properties of the nanocomposites are assessed by UV-Vis and photoluminescence measurements. Additionally, the crystalline phase and size distribution of the nanocrystals are determined by XRD and TEM, respectively. The results indicate that the as prepared nanocomposites are nearly monodisperse with an average size of 10 nm and a quantum yield of 13%. The synthesized nanocomposites clearly provide both magnetic and luminescent properties which could be useful for simultaneous detection and separation possibly in biomedical applications.

6.2 Introduction

In the past few years, the colloidal synthesis of inorganic nanostructures has been directed in part towards integrating different functional components (e.g. metal, magnetic and semiconductor) in a hybrid single structure that possesses dual-or multifunctionality.[294-317] The controlled synthesis of such multicomponent nanostructures has been one of the important goals of nanoparticles' research due to their novel properties and many advantages over the more-limited

single component counterparts. For example, Kim et al. reported the synthesis of Co/CdSe nanocrystals which display both magnetic and photoluminescence properties.[317] Jinhao et al. demonstrated the use of external magnetic field in the intracellular manipulation of fluorescent/magnetic nanocrystals.[298, 299] Deka et al. developed a colloidal two-step seeded-growth approach to synthesize a multicomponent magnetic/semiconductor structure.[304] Water-soluble Fe_3O_4/CdTe magnetic/fluorescent nanocrystals were reported by Sun et al.[312] Similarly, Xu et al. have synthesized biocompatible luminescent superparamagnetic nanostructures for guided fluorescence imaging.[313] Liu et al. reported a sonochemical generalized aqueous route for the synthesis of nanocomposites of magnetic and different semiconductor structures.[301] Also bifunctional Fe_3O_4/Se bundles have been synthesized by Lu et al.[311] Other magnetic/semiconductor hybrid structures such as Fe_2O_3-CdS [296, 308] and FePt/In_2O_3,[316] FePt-CdS dumbbells,[303] FePt-ZnO core-shell,[314] FePt-PbS and FePt-PbSe [310] have been also synthesized using magnetic nanocrystals as seeds.

The importance of such highly functional materials stems from the tailored and enhanced novel proprieties, such as increased stability, surface area, magnetic, optical and catalytic properties which are different from that of the individual single-component counterpart.[318] Because of the integrated magnetic and fluorescent properties, they can be applied in a variety of fields such as the simultaneous detection and separation in biological analyses and immunoassays as well as the fluorescence-based imaging for detection and diagnosis.[312, 319, 320] However, synthesis of hybrid nanostructures is a big challenge and needs a great control over the reaction parameters to generate functional materials with tunable properties. In this regard, variant synthetic approaches have been devoted to the synthesis of different kinds of hybrid structures.[294, 295, 302, 306, 321, 322]

Microwave irradiation (MWI) has been used successfully as a simple and fast route for the large-scale synthesis of high crystalline nanostructures that minimizes the thermal gradient effects.[46, 87, 107, 260, 323, 324] Heating of a substance by microwave irradiation is based on dipole rotation and ionic conduction, that is, by reversal of solvent dipoles and the resulting replacement of charged ions of a solute. Due to the difference in the solvent and reactant dielectric constants, selective dielectric heating can provide significant enhancement in reaction rates. The rapid transfer of energy directly to the reactants causes an instantaneous internal temperature rise. Thus, the activation energy is essentially decreased as compared with conductive heating and the reaction rate increases accordingly. This also allows the rapid decomposition of the precursors thus creating highly supersaturated solutions where nucleation and growth can take place to produce the desired nanocrystalline products.[46, 107, 260, 324]

In this work, we demonstrate the application of MWI for the synthesis of Fe_3O_4/CdSe magnetic/luminescent nanocomposites where luminescent CdSe nanoshells are grown around magnetic Fe_3O_4 nanocrystalline seeds. Our choice of the Fe_3O_4 and CdSe components was motivated by their excellent magnetic and optical properties, respectively, and the great attention paid to these systems over the past two decades.

6.3 Experimental

6.3.1 Chemicals and reagents

Iron III acetylacetonate (Aldrich, 99.95%), oleic acid (Aldrich, tech 90%), oleylamine (Aldrich, tech), cadmium oxide (Aldrich, 99.99%), selenium powder (Aldrich, 100 mesh, 99.99%), trioctylphosphine oxide (Sigma, 90%), hexadecylamine (Aldrich, 90%), and trioctylphosphine (Sigma, 90%).

6.3.2 Microwave synthesis of Fe_3O_4 seeds

In a typical synthesis of spherical Fe_3O_4 nanocrystals, 200 mg iron acetylacetonate was dissolved in 1 ml dimethylformamide (DMF) and stirred vigorously until complete dissolution and then a mixture of 1 ml oleic acid and 2 ml oleylamine was added to the solution under stirring. The resulting mixture was then placed in a domestic microwave oven and irradiated for 5 min for 6 nm seeds and 25 min for 10 nm particles (1 min cycles , on for 50 s and off for 10 s) at 33% of 650 W. after the reaction. Upon microwave irradiation, the reaction mixture turned rapidly into dark red and finally to black when temperature was about 280 ^{o}C. After cooling down to room temperature, the formed magnetite particles were separated with ethanol and centrifuge and washed with hexane/ethanol cycles. Although the prepared nanocrystals respond to external filed from a small magnet and can be collected using a permanent magnet, separation was conducted using centrifugation.

6.3.3 Synthesis of CdSe nanocrystals by microwave irradiation

In a typical synthesis of CdSe nanocrystals, cadmium oxide powder (100 mg) was added to an oleic acid solution (5 ml), followed by microwave irradiation until the complete dissolution of CdO which resulted in a colorless solution. A mixture of trioctylphoshpine oxide (2.0 g) and hexadecylamine (2.0 g) was then added to the colorless solution, and the reaction mixture was further microwaved allowing the solid TOPO-HDA mixture to dissolve. The subsequent addition of selenium powder (100 mg) that was pre-dissolved in trioctylphosphine (3 ml), (Se-TOP) allowed nucleation and growth of CdSe nanocrystals within few seconds of microwave exposure. The as-prepared particles were precipitated with ethanol, centrifuged, and re-dispersed in toluene for further analyses and characterizations.

6.3.4 Microwave synthesis of Fe_3O_4/CdSe nanocomposites

For the synthesis of Fe_3O_4/CdSe core shell nanocomposites, a seed-mediated approach was adopted using Fe_3O_4 nanocrystals as seeds. First, cadmium oxide powder (100 mg) was added to an oleic acid solution (5 ml) and the mixture was microwaved for 10 min until the complete dissolution of CdO and a colorless solution of cadmium oleate was obtained. A mixture of trioctylphoshpine oxide (2.0 g) and hexadecylamine (2.0 g) was then added to the colorless solution, and the reaction mixture was further microwaved to dissolve the solid TOPO-HDA mixture. An appropriate amount of seed solution (400 µl of 36 mg/ml) was added under vigorous stirring followed by the subsequent addition of Se-TOP (100 mg/3 ml) solution. The microwave irradiation of the whole mixture allowed the growth of the CdSe on the surface of the existing seeds to give core/shell structure. The reaction mixture was held under MWI for 3 min with 10 s off per min for stirring. The color change of the solution from the black to red indicated the formation of CdSe shell on the Fe3O4 core. After the completeness of the reaction, the prepared nanocomposites were separated and washed with ethanol/toluene cycles using centrifuge.

6.3.5 Characterization

TEM images were recorded using a Joel JEM-1230 electron microscope operated at 120 kV equipped with a Gatan UltraScan 4000SP 4K x 4K CCD camera. The X-ray diffraction (XRD) patterns were obtained with an X'Pert Philips Materials Research Diffractometer at room temperature using Cu $K_{\alpha 1}$ radiation. Absorption spectra were recorded using a Hewlett-Packard HP-8453 diode array spectrophotometer. Emission spectra were recorded using a Varian, Inc. - Cary Eclipse Fluorescence Spectrofluorimeter.

6.4 Results and Discussion

Microwave irradiation (MWI) constitutes a powerful approach for the synthesis of plethora of nanocrystals of controlled structure and morphology, yet in a simple and rapid fashion. The rapid, uniform and selective heating causes an instantaneous temperature rise and direct transfer of heat energy to the reactants, allowing achieving very high effective reaction temperature for the rapid decomposition of the precursors.[108] Magnetic iron oxide nanocrystals (e.g. magnetite Fe_3O_4) are particularly promising in many applications such as soft magnetic materials, electromagnetic shielding, drug delivery, color imaging and others.[325] They have been brought into sharp focus mainly due to their superior magnetic properties, low toxicity and biocompatibility.[326] The microwave-driven decomposition of iron III acetylacetonate in the presence of oleic acid and oleylamine led to formation of nearly monodisperse Fe_3O_4 spherical nanocrystals. The crystal phases of prepared nanocrystals were confirmed by XRD. As shown in **Fig. 6.1 (a-b)**, the Fe_3O_4 nanocrystals possess the spinnel lattice and all diffraction peaks can be indexed to cubic structure which is in a good agreement to the literature.[327]

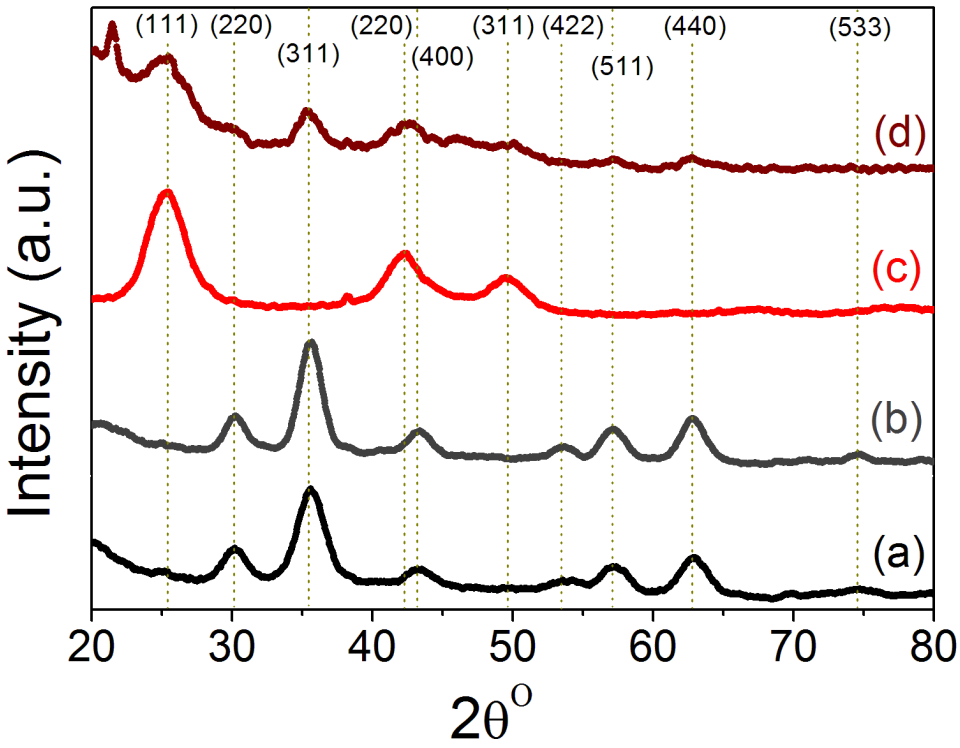

Figure 6-1. XRD patterns of a) 6 nm Fe_3O_4 nanocrystals, b) 10 nm Fe_3O_4 nanocrystals, c) CdSe nanocrytslas and d) Fe_3O_4/CdSe core-shell nanocomposites prepared by MWI.

The size of prepared particles can be easily tuned by controlling the microwave irradiation time. For the synthesis of 6 nm spherical Fe_3O_4 nanocrystals, the reaction was held for 5 min while it was held for 25 min in case of the 10 nm nanocrystals. **Figiure 6.2 (a-f)** shows typical TEM images for representative as-prepared Fe_3O_4 nanocrystals. It is clear that the Fe_3O_4 nanocrystals are spherical, uniform and monodispersed with a mean size of ~6 nm in diameter for those microwaved for 5 min and 10 nm in diameter for those microwaved for 25 min. A representative TEM image of CdSe nanocrystals prepared by MWI is displayed in **Fig. 6.3 (a-b)**. It is observed that CdSe nanocrystals have a relatively narrow size distribution and the mean size is about 3-4 nm. The crystal phase of these nanocrystals was evidenced from XRD pattern displayed in **Fig. 6.1-c** showing that CdSe nanocrystals possess cubic structure.

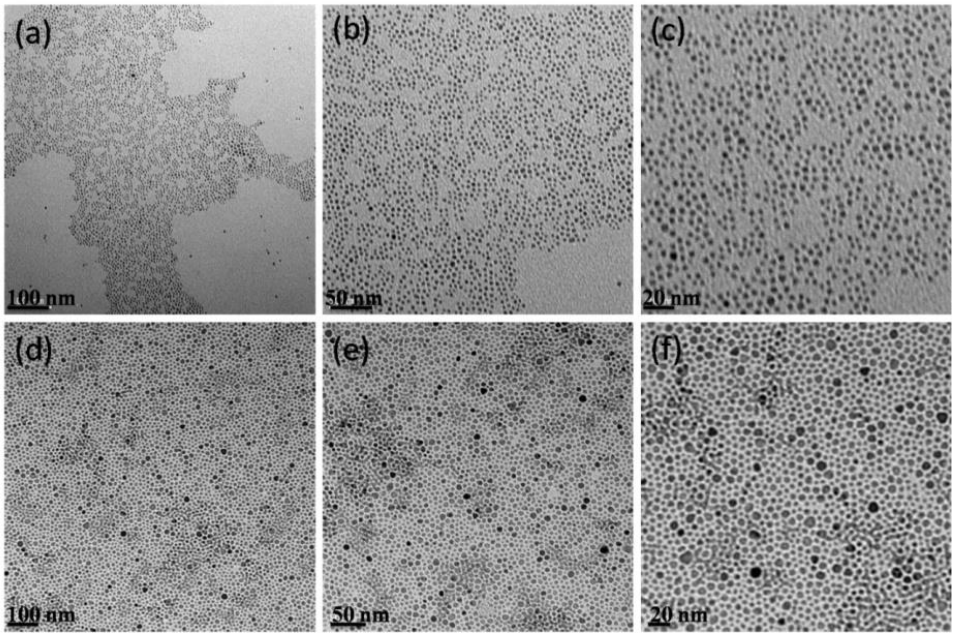

Figure 6-2. TEM images of a-c) 6 nm and d-e) 10 nm Fe_3O_4 nanocrystals prepared by MWI.

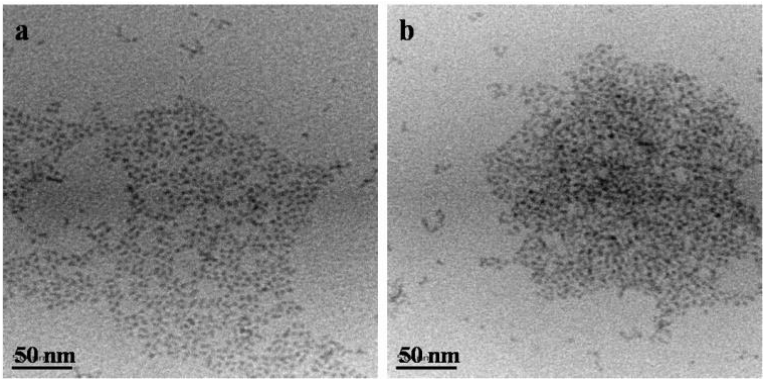

Figure 6-3. TEM images of CdSe nanocrystals prepared by MWI.

For the microwave-assisted synthesis of Fe_3O_4/CdSe nanocomposites, a Se-TOP solution was injected into a reaction mixture of monodispersed Fe_3O_4 nanocrystals (originally stabilized with oleic acid and oleylamine), Cd-oleate complex dissolved in a TOPO-HDA mixture. Fe_3O_4 nanocrystals played the role of seeds for the heterogeneous nucleation of CdSe phase whose morphology and size were controlled by the microwave irradiation time and the ligands present in the reaction mixture. The microwave irradiation of the reaction mixture after the Se-TOP injection

led the CdSe domains to nucleate, grow and eventually form nanoshells onto the Fe_3O_4 nanocrystal surfaces, due to the incompatibility of the lattices of Fe_3O_4 and CdSe and the effect of surface tension.[296, 298] **Figure 6.1 (a-d)** compares the powder X-ray diffraction patterns of **(a-b)** Fe_3O_4 cores, **(c)** CdSe and **(d)** Fe_3O_4/CdSe nanocomposites. The differences in the crystal lattice structures between the single components and the hybrid nanocomposite structure are clearly evident. All patterns reflect the good crystallinity of the as-prepared pure nanocrystals and hybrid nanocomposites. Compared to the XRD patterns of pure Fe_3O_4 **(Fig. 6.1 (a-b)** and CdSe **(Fig. 6.1-c)**, the diffraction peaks in **Fig. 6.1-d** can be indexed to the spinnel structure which reveals the presence of Fe_3O_4 phase in the as-synthesized Fe_3O_4/CdSe nanocomposites as well as the cubic CdSe phase. Both CdSe prepared alone and CdSe shells deposited on the surface of the Fe_3O_4 nanocrystals crystallizes in the wurtzite structure as indicated by the characteristic peaks in the 2θ range of 25-45^o.[46] The diffraction peaks from CdSe component in the Fe_3O_4/CdSe nanocomposites matched the reflections of reported in the literature, showing that no lattice strain is encountered in the CdSe shell in the Fe_3O_4/CdSe nanocomposites structures. TEM images of the Fe_3O_4/CdSe nanocomposites shown in **Fig. 6.4 (a-b)** confirmed the core shell morphology. Compared to Fe_3O_4 and CdSe nanocrystals, the Fe_3O_4/CdSe nanocomposites retain the same spherical shape and uniformity but they are about 3-5 nm larger in diameter, so final core-shell nanocomposites are about 10-15 nm in diameter. The shell thickness could be controlled by MWI time and the amounts of cadmium and injected sulfur precursors. The monodispersity of the prepared nanocomposites reflects the well control over the growth of the CdSe shell on the magnetic core.

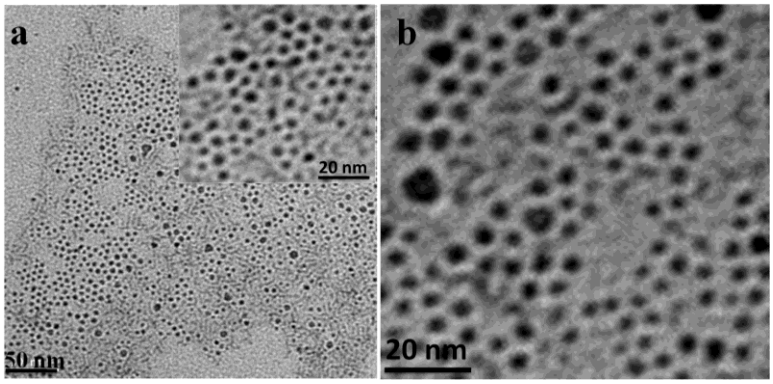

Figure 6-4 TEM images of Fe_3O_4/CdSe nanocomposites prepared by MWI a) Low magnification image with a scale bar of 50 nm, inset in (a) and image b) are higher magnification images with 20 nm scale bar showing the contrast between the core and the shell.

The successful synthesis of Fe_3O_4/CdSe nanocomposites was evidenced also by the optical measurements of the absorption and fluorescence spectra using UV-Vis and photoluminescence spectroscopy. As displayed in **Figs 6.5 and 6.6**, the UV-Vis spectra are featured by a distinct absorption due to the CdSe nanocrystals and narrow emission bands are demonstrated with emission maxima between 540 and 602 nm depending on the microwave time. Compared to the individual CdSe nanocrystals, the integration of Fe_3O_4 cores into CdSe nanocrystals fades out the sharp excitonic features inherited to monodispersed CdSe samples and this effect might be due to inhomogenous and homogenous broadening. However, the photoluminescence properties of Fe_3O_4/CdSe were retained, emission peaks are nearly symmetric like pure CdSe and the fluorescence intensity of as-synthesized Fe_3O_4/CdSe nanocomposites was comparable to that of the pure CdSe prepared under similar conditions. A typical sample of as-prepared Fe_3O_4/CdSe nanocomposites possessed a quantum yield of 0.13 vs. R-6G.

Figure 6.6-b shows the extent of Stoke's shift in the as-prepared Fe_3O_4/CdSe nanocomposites after 240 s of MWI. Moreover, the excellent magnetic property of the nanocomposites was evident. They could be easily separated under an external magnetic field from

a small magnet. A color change from the orange to transparent is observed when an external magnetic field is applied showing the enriching process, as displayed in **Fig. 6.7**. When the magnetic field is removed, the aggregation can be readily dispersed by stirring. From the optical measurements, it can be concluded that Fe_3O_4/CdSe nanocomposites show undisrupted and strong emission and the desired magnetic properties as well. These magnetic and luminescent properties of Fe_3O_4/CdSe derived from Fe_3O_4 counterpart make the nanocomposites ideal to be used in the areas of biolabelling, bioseparation, immunoassays and other diagnostic applications.[299]

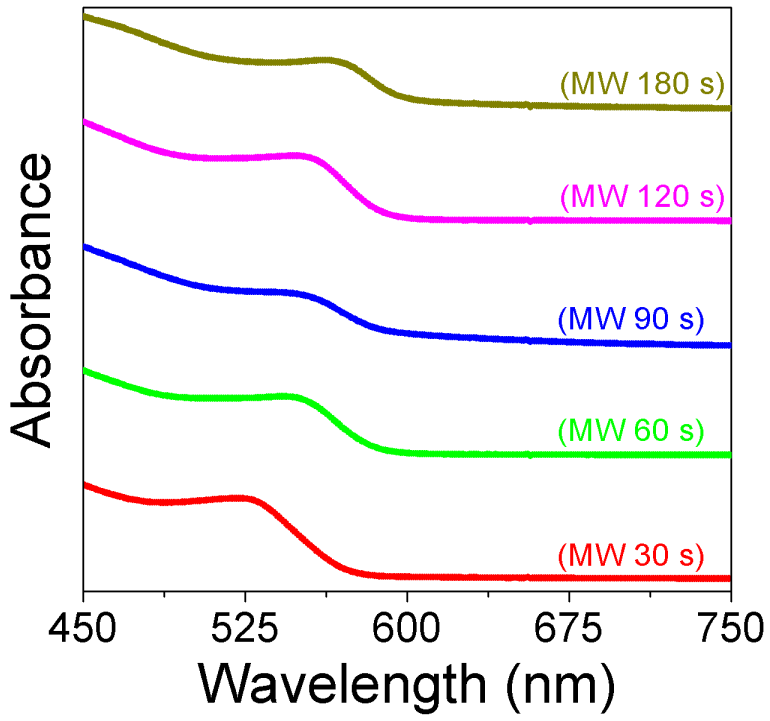

Figure 6-5 UV-Vis spectra of Fe_3O_4/CdSe nanocomposites prepared under different MWI times.

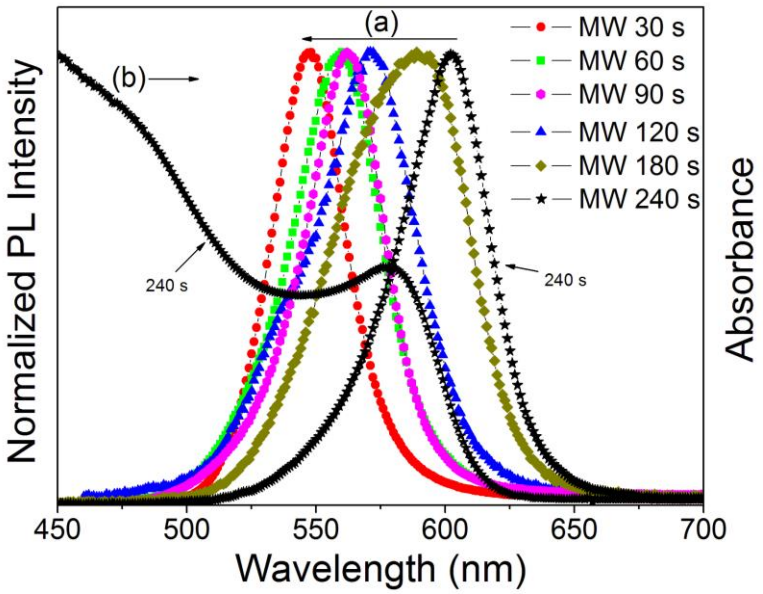

Figure 6-6 Photoluminescence spectra of Fe_3O_4/CdSe nanocomposites prepared under different MWI times (a) and a comparison to UV-vis spectrum of sample prepared at 240 s to show the extent of Stokes shift.

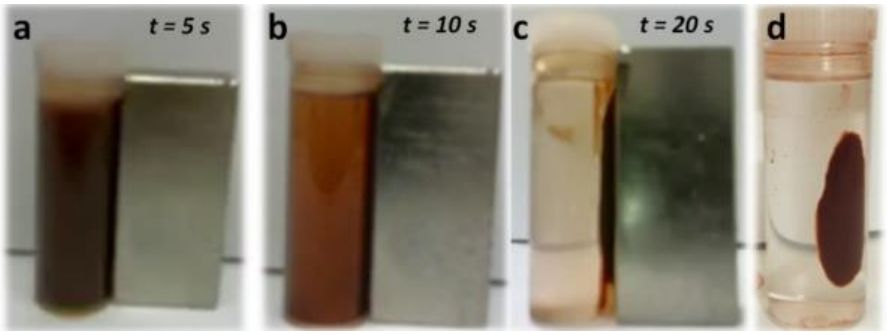

Figure 6-7 A digital image of Fe_3O_4/CdSe nanostructures showing the rapid magnetic separation in an external field in 20 s. In images (a-c) the magnet is in contact with the glass vial and then was taken away from the vial in image (d) to better show magnetic decantation.

6.5 Conclusions

In summary, we presented a facile and rapid microwave-based procedure for the synthesis of Fe_3O_4-CdSe core-shell nanocomposites with tunable optical emission features in an organic environment. The absorption and emission properties of the nanocomposite structures could be easily tuned by changing the microwave irradiation time which also can be used to control the luminescent shell thickness. It would be interesting to extend the experimental approach based on the direct formation of CdSe quantum dots and their simultaneous deposition on the magnetite core to the fabrication of other hybrid nanostructures of semiconductor and magnetic nanocrystals.

CHAPTER 7 Microwave Synthesis of Fe_3O_4/Graphene Architectures: Surfactant-assisted Control of Morphology and Magnetic Properties

7.1 Overview

Herein, a rapid general one-step microwave irradiation method for growing magnetite nanocrystals on reduced graphene oxide sheets is described. The strategy developed allows decorating graphene sheets with magnetite nanocrystals of various well-defined morphologies (spheres, cubes and triangles by microwave-driven reduction of $Fe(acac)_3$ in benzyl ether using oleylamine and oleic acid as surfactants. The size and shape control was achieved by tuning the mole ratio of two surfactants while keeping the amount of $Fe(acac)_3$ fixed. The results demonstrate the feasibility of our microwave synthetic approach to control the morphology of the magnetite nanocrystals anchored on conducting graphene sheets. The morphology of the magnetite nanocrystals grown on graphene can be tailored by tuning the molar ratio of the two surfactants and the iron precursor. Moreover, the introduction of graphene sheets which contribute to the nucleation and growth provided a mean to control the morphology of the magnetite nanoplates anchored on graphene. Our microwave synthetic strategy can be extended to synthesize a wide variety of metal and metal oxide architectures on graphene.

7.2 Introduction

Graphene, a highly versatile carbon material, has received a great attention in recent years because of its extraordinary structural, optical, thermal, mechanical and electrical properties.[3, 75, 127] Such intriguing and unique features make graphene promising in wide array of potential applications such as nanocomposites, sensors, supercapacitors, nanoelectronics, transparent conducting films, batteries, paper-like materials and others.[20] The unique two-dimensional nature and the extremely high surface area of graphene sheets make this carbon material an ideal support for the deposition of various inorganic nanoparticles.[45, 46, 87, 90, 95, 105, 129-131, 328-330] For example, Zedan et al.[46] deposited CdSe quantum dots on chemically synthesized graphene sheets which served as an electron acceptor matrix for CdSe fluorescence quenching. Siamaki et al. [330] loaded Pd nanoparticles on graphene sheets and applied them as catalysts to the carbon–carbon cross-coupling reactions.

In this regard, anchoring superparamagnetic iron oxide nanostructures on chemically synthesized graphene will impart the desirable superparamagnetic features into graphene, making such graphene-based composite material promising for a wide range of fields such as magnetic energy storage, magnetic fluids, catalysis, electromagnetic materials and coatings, environmental remediation, aligned substrates for nanodevices, magnetic separation and biological imaging.[43, 331-339] The control of the morphology, size and magnetic features of magnetic nanoparticles has gained considerable attention in the past few years due to the significance in fundamental understanding and wide technological applications in catalysis, high density magnetic and energy storage media, drug delivery, color imaging, electromagnetic shielding, spintronics, ferrofluids and biological separations.[340-342]

The size and morphological changes in magnetite nanostructures, in particular, have been shown to significantly affect the magnetic features such as coercivity and saturation magnetization.[343-346] In addition, Fe_3O_4 have been brought into sharp focus due to their superior magnetic properties, low toxicity and biocompatibility. To control the size and shape of magnetic nanocrystals, various synthetic methods adopting hydro- or solvothermal treatment, wet chemical etching, reverse-micelles or polyol molecules have been introduced to prepare a variety of structures such as magnetite nanospheres,[54] nanopyarmids,[342] 1D nanowires,[311, 347] nanocubes,[345, 348] nanooctahedra,[341, 349] and nanorods.[350] Chemical synthetic routes offer large scale production of graphene-based composite materials with potentially low cost. Recently, composite structures of graphene or graphene oxide and magnetic nanostructures prepared by the wet chemical methods have been synthesized and applied to arsenic removal, catalysis, magnetic-controlled switches, magnetic resonance imaging (MRI), and targeted drug carriers.[331-338, 351] Cong et al. [333] decorated graphene oxide sheets with Fe_3O_4 nanoparticles and used them as contrast agents for magnetic resonance imaging (MRI). Chandra et al. [334] synthesized magnetite-graphene hybrid structures as efficient absorber for As(III) and As (IV). Chen et al. [336] anchored Fe_3O_4 on graphene oxide sheets for a controlled targeted anticancer drug delivery. Fu et al.[331] reported the use of a magnetically separable ZnFe2O4-graphene nanocomposites as photocatalysts for the degradation of methylene blue. Liang and co-workers [337] fabricated graphene/Fe_3O_4 films and proposed their use in magnetic-controlled switches. Su et al. [338] reported one-pot hydrothermal synthesis of Fe_3O_4-graphene nanocomposites for improved lithium storage. Lin et al. [332] adopted solvent-free microwave heating for instantaneous formation of magnetic metal and metal oxide nanoparticles on graphene. Shen and others [351] deposited both Fe_3O_4 and γ-Fe_2O_3 on graphene sheets using high temperature reaction of Fe $(acac)_3$ in 1-methyl 2-pyrrolidone (NMP). Wang et al. [352] utilized

graphene oxide sheets with different degrees of oxidation to grow Fe_2O_3 hexagonal nanoplates on graphene in a two-step solvothermal method.

Despite these significant efforts, the shape-controlled synthesis of iron oxide magnetic nanoparticles supported on graphene sheets still lacking and to the best of our knowledge such shape-controlled synthesis has not been yet reported. Microwave irradiation (MWI) constitutes a powerful approach for the synthesis of plethora of nanoparticles of controlled structure and morphology, yet in a simple and rapid fashion. The rapid, uniform and selective heating causes an instantaneous temperature rise and direct transfer of heat energy to the reactants, allowing achieving very high effective reaction temperature for the rapid decomposition of the precursors.[46] Herein, a facile strategy to control the shape of magnetite nanocrystals, both free standing and those attached to graphene sheets is explored, integrating in such way the superparamagnetic properties of magnetite nanoparticles of different morphologies and the superior conductivity of graphene in a single compartment composite structure. Compared with the previous reports, the work reported here holds various advantages. First, the preparation method is simple, rapid and single-step with the contemporaneous reduction of graphene oxide to graphene and the in situ formation of Fe_3O_4 on the surface of graphene sheets. Second, the shape of the anchored magnetite nanocrystals can be readily tuned from spheres, cubes to prisms by tuning the molar ratio of the surfactants used (oleylamine and oleic acid). Third, the syntheses show even deposition of Fe_3O_4 on the surfaces of graphene sheets with dense coverage. Fourth, the Fe_3O_4/CSG nanocomposites are readily dispersible in nonpolar solvents and feasible for separation with external field from a permanent magnet.

7.3 Experimental

7.3.1 Chemicals and reagents

Iron III acetylacetonate (Aldrich, 99.95%), oleic acid (Aldrich, tech 90%), oleylamine (Aldrich, tech), benzyl ether (ACS 99.9%, Aldrich), dimethyl sulfoxide (ACS 99.9%, Alfa Aesar), Graphite (natural, high purity,-200 mesh, 99.9999%, metal basis, Alfa Aesar), sulfuric acid (Fisher Scientific, Certified ACS), potassium permanganate (Analyt Reag., low in mercury, Mallinckrodt), hydrogen peroxide (30%, KMG), and ethanol.

7.3.2 General synthetic method

In a typical synthesis of magnetite nanocrystals, a pre-determined amount of iron acetylacetonate, ([Fe $(acac)_3$]), was mixed with 105 mmol benzyl ether and stirred vigorously until complete dissolution. Oleylamine and/or oleic acid were/were then added to the solution under stirring and the reaction vessel was transferred to a domestic microwave oven. The whole mixture was microwave irradiated for 20 minutes (15 sec on cycles). After cooling down to room temperature, the formed magnetite particles were separated with ethanol and centrifuge and then washed with hexane/ethanol cycles. Although separation was conducted using centrifugation the prepared nanocrystals respond to external field from a small magnet and can be collected using a permanent magnet.

7.3.3 Synthesis of Fe_3O_4 nanospheres

For the synthesis of Fe_3O_4 nanospheres, 280 µmol of Fe $(acac)_3$ was dissolved in 105 mmol benzyl ether and then a mixture of 4.2 mmol of oleylamine and 11.2 mmol oeic acid was added to the solution under vigorous stirring. The mixture was microwave irradiated for 20 min at 1000 W. Upon microwave irradiation, the reaction mixture turned rapidly into dark red and finally to black

when temperature was about 280 ^{o}C. The final product was collected and washed as described earlier.

7.3.4 Synthesis of Fe_3O_4 nanocubes

The mixture for the synthesis of Fe_3O_4 nanocubes contained 280 µmol of $Fe(acac)_3$, 4.2 mmol of oleylamine and 2.8 mmol of oleic acid in 105 mmol benzyl ether. The reaction mixture was microwave irradiated for 20 min at the same power. Separation and washing steps are the same of the spheres.

7.3.5 Synthesis of Fe_3O_4 triangles

The typical synthetic mixture of Fe_3O_4 triangles included 280 µmol of $Fe(acac)_3$, 2.1 mmol of oleylamine and 2.8 of oleic acid in 105 mmol benzyl ether. The rest of reactions steps, separation and washing are the same as the spheres.

7.3.6 Synthesis of shape-controlled Fe_3O_4-decorated graphene

The different syntheses of shaped-controlled Fe_3O_4 nanostructures on RGO adopted same respective molar ratios between the precursors and surfactants mixtures for different shapes. A summary of different experimental conditions and resulting morphologies of Fe_3O_4 and Fe_3O_4/RGO is outlined in **Table 7.1**. The synthesis of Fe_3O_4 nanoplates/RGO involved the dissolution of 280 µmol of Fe $(acac)_3$ in 105 mmol benzyl ether followed by the addition of a mixture of 4.2 mmol of oleylamine and 5.6 mmol oeic acid under vigorous stirring. Prior to MWI, a GO/DMSO suspension was added to the reaction mixture and finally the reaction vessel was microwaved micorwaved for 20 min at 1000 W. Upon completion, the final product was collected and washed as described before.

7.4 Results and Discussion

Magnetic iron oxide nanocrystals (e.g. magnetite Fe_3O_4) are particularly promising in many applications such as soft magnetic materials, electromagnetic shielding, drug delivery, color imaging and others.[325] They have been brought into sharp focus mainly due to their superior magnetic properties, low toxicity and biocompatibility.[326] As a simple and fast route, microwave irradiation (MWI) has been used extensively for the large scale synthesis of high crystalline nanostructures that minimizes the thermal gradient effects.[107, 125] Heating of a substance by microwave irradiation is based on dipole rotation and ionic conduction, that is, by reversal of solvent dipoles and the resulting replacement of charged ions of a solute.[107, 125] Due to the difference in the solvent and reactant dielectric constants, selective dielectric heating can provide significant enhancement in reaction rates. The rapid transfer of energy directly to the reactants causes an instantaneous internal temperature rise. Thus, the activation energy is essentially decreased as compared with conventional heating methods and the reaction rate increases accordingly. This also allows the rapid decomposition of the precursors thus creating highly supersaturated solutions where nucleation and growth can take place to produce the desired nanocrystals.

The potential of oleic acid (OAc) and oleylamine (OAm) mixture in a molecular solvent has been explored over the past several years as an effective approach for the fabrication of various metallic nanostructures of various morphologies, including cubes, prisms, hexagons, rods and nanowires.[353-355] The cooperative interaction between OAc and OAm in presence of metal ions to form diolamide upon MWI has been shown by our group to be a rational behind formation of various Au anisotropic shapes.[260] The same approach is extended herein to decorate graphene

nanosheets with Fe_3O_4 architectures of various sizes and shapes in a controllable fashion adopting MWI.

In our controlled synthesis of Fe_3O_4/RGO nanocomposites, natural graphite and iron acetylacetonate were used as molecular precursors to graphene and magnetite, respectively. Through a slightly modified Hummer's method and as described in the experimental section, graphite was treated with strong oxidizing agent in presence of H_2SO_4 to yield graphene oxide (GO). Unlike graphene, the lots of oxygen-containing functional groups possessed on GO enable its dispersion and formation of homogenous colloidal solutions in polar organic solvents and water. Although being a suitable substitute for graphene, the thermal instability and poor electrical conductivity of GO handicap its applications in functional composite materials. Therefore, various chemical, electrochemical and thermal methods have been introduced to convert GO into graphene. Recently, we have reported a microwave-assisted method for the efficient reduction of GO in very short time using dimethylsulfoxide (DMSO) as a solvent.[46]

Generally, there are three strategies to prepare graphene-based functional nanocomposites starting from GO. In one strategy, the targeted nanoparticles are first loaded on GO sheets followed by its reduction after achieving the desired composite structure.[45, 356] However, in such strategy some alterations to the nanoparticles counterpart in the prepared composite structure are likely to take place upon the complete reduction of GO all the way to reduced graphene oxide (RGO). For instance, anchored nanoparticles may detach from the surface during the reduction process. In a second strategy, GO is separately converted to RGO first and targeted nanoparticles are then loaded on existing RGO sheets.[102] However, RGO sheets possess rare functional moieties on the surface and consequently poor dispersibility in most solvents, which leads to serious aggregation of RGO sheets. In a third strategy, the desired nanoparticles are synthesized on the existing GO

sheets with the contemporary reduction to RGO in a one-pot and single-step fashion.[46, 87, 330, 331] The feasibility of the one-pot reduction of GO sheets with the simultaneous nucleation and growth of nanoparticles counterparts on RGO surface makes the third strategy superior to fabricate diverse graphene-based functional nanocomposites. In this work, the Fe_3O_4/RGO nanocomposites were fabricated in a single-step directly from GO and $Fe(acac)_3$ through a facile one-pot microwave-assisted reduction.

7.4.1 Morphological characterization and shape transformation

Various shaped- and sized- Fe_3O_4 nanocrystals were prepared individually and anchored to graphene by MWI of $Fe(acac)_3$ precursors in benzyl ether and a mixture of oleylamine and oleic acid. The MWI delivers a great amount of heat that accelerate the decomposition of $Fe(acac)_3$ precursors leading to the burst of nucleation and further growth. When supersaturation is reached in reaction medium, the Fe-O species start to cluster in the reaction medium of benzyl ether to give numerous nuclei. The aggregation of these numerous nuclei above the saturation threshold leads to sintering resulting in formation of primary Fe_3O_4 nanocrystals. The primary formed Fe_3O_4 nanocrystals are then further grown by diffusion and stacking the respective atomic species derived from the partial reduction and decomposition of $Fe(oleate)_3$ in presence of oleylamine-oleic acid mixture onto the primary nanocrystals.

To better understand the effect of different experimental parameters on the growth process, the synthesis of magnetite nanoparticles was first conducted in presence of the single components of the surfactant mixture, i.e oleylamine or oleic acid. The various morohologies with their corresponding synthetic experimental conditions and parameters are summarized in **Table 7.1**. As shown in **Fig. 7.1**, Fe_3O_4 nanoparticles prepared by MWI of Fe(acac)3 in benzylether and using 3.2 mmol or 4.2 mmol of oleylamine or oleic acid, respectively, are spherical in shape. The very

small size of nanoparticles prepared under these conditions, relative to those prepared in the mixture implies the efficient passivation of growing nanoparticles by the self-assembly of fatty chains from OAm or OAc into a micellar structure within which the Fe_3O_4 nuclei form and grow.[355] Moreover, the dilution of OAm or OAc by the benzyl ether could have result in smaller micelles or inefficient decomposition and/or reduction process leading to formation of tiny spheres. A fine control of the shape and the size of Fe_3O_4 growing under MWI were achieved using a mixture of OAc and OAm. Our findings show that tuning the molar ratio between OAm and OAc provides a feasible mean to control both shape and size of Fe_3O_4 nanostructures.

Table 7-1 Fe_3O_4 different morphologies with corresponding experimental parameters

Fe_3O_4 Shape	**OAm (mmol)**	**OAc (mmol)**	**$Fe(acac)_3$ (mmol)**	**Size**	**Figure**	
Tiny spheres	3.2	0	0.28	4-5 nm	Fig 1	A-D
Tiny spheres	0	4.2	0.28	3-4 nm	Fig 1	E-F
Spheres (small)	4.2	5.6	0.28	10±2 nm	Fig 2	A,B
Spheres (large)	4.2	11.2	0.28	13±2 nm	Fig 2	C,D
Cubes	4.2	2.8	0.28	Edge 15±1 nm	Fig 3	A,B
Triangles	2.1	2.8	0.28	Edge 28±2 nm	Fig 3	C,D
Spheres/RGO	4.2	5.6	0.28	13-15 nm	Fig 4	A-C
Spheres/RGO	4.2	5.6	0.28	13-15 nm	Fig 4	D-F
Cubes/RGO	4.2	2.8	0.28	Edge 11-17 nm	Fig 5	A,B
Triangles/RGO	2.1	2.8	0.28	Edge 30-35 nm	Fig 5	C,D
Hexgonal Plates	4.2	5.6	0.28	G,K edge 0.9 μm	Fig 6	A-L
Hexgons/Graphene	4.2	5.6	0.28	STEM, SEM	Fig 7	A-F

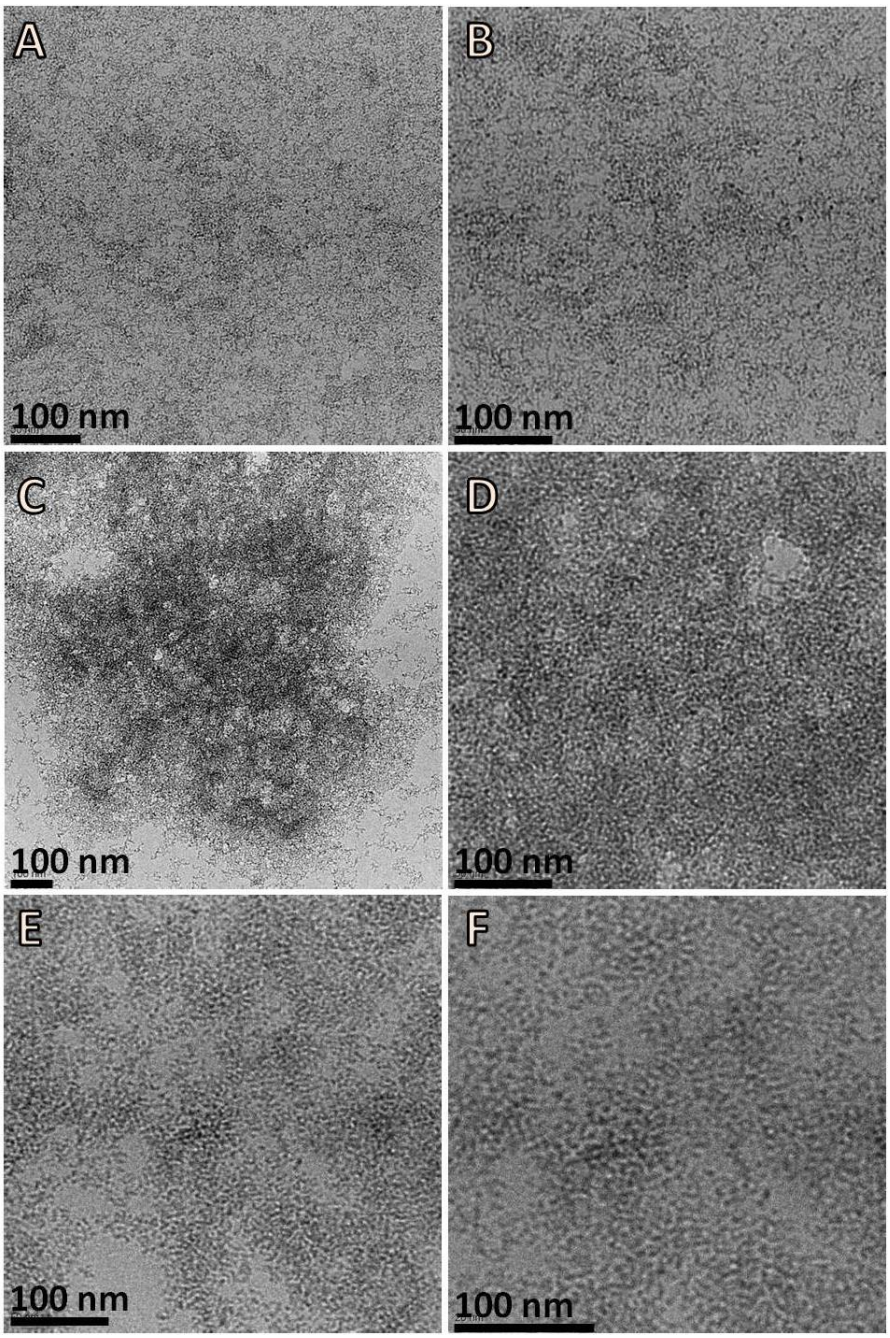

Figure 7-1 TEM images of Fe_3O_4 nanocrystals prepared by MWI of Fe(acac)3 in benzyl ether for 20 min using 3.2 mmol OAm (A-D, average size ~ 4-5 nm) or 4.2 mmol OAc (E-F, average size ~ 3-4 nm).

Figure 7.2 shows TEM images of Fe_3O_4 prepared by MWI in OAm-OAc mixture with different ratios. When 4.2 mmol of OAm was mixed with 5.6 mmol spherical Fe_3O_4 of uniform shape and size and an average diameter of 10±2 nm were obtained. The Fe_3O_4 nanospheres are arranged in a closed pack array which reveals the uniformity of size and shape of as-prepared particles. When OAc fraction was increased to 11.2 mmol the Fe_3O_4 retained the spherical shape but the size of the nanoparticles increased slightly to 13±2 nm. Interestingly, well-defined Fe_3O_4 cubes of monodisperse size and uniform shape with average edge length of 15±1 nm were successfully prepared by changing the molar ratio between OAM and OAc, where OAc fraction was decreased to 2.8 mmol while keeping OAm at 4.2 mmol. **Figure 7.3** shows typical TEM images of Fe_3O_4 cubes and triangle structures. TEM images of Fe_3O_4 nanocubes displayed in

Figure 7.3-A,B, suggests a very narrow size distribution and shape uniformity of as-synthesized cubes which spontaneously self-assemble in two-dimensions on the copper TEM grids after the evaporation of the solvent. When OAc was kept at 2.8 mmol and OAm fraction was decreased to 2.1 mmol the shape of the resulting Fe_3O_4 nanocrystals transforms into triangular ones as can be seen in **TEM images (Figure 7.3-C,D)** that show mostly triangular nanoparticles and a few polyhedral nanostructures. All triangles possess flat facets and regular edge sides with an average edge length of 28±2 nm. The results deduced from TEM clearly indicate that the size and morphology of the Fe_3O_4 nanostructures can be controlled by altering the fractions of surfactants. The 2D self-assemblies observed to greater extent in spherical and cubic nanoparticles suggest the promise of the as-prepared structures in high-density data storage applications.

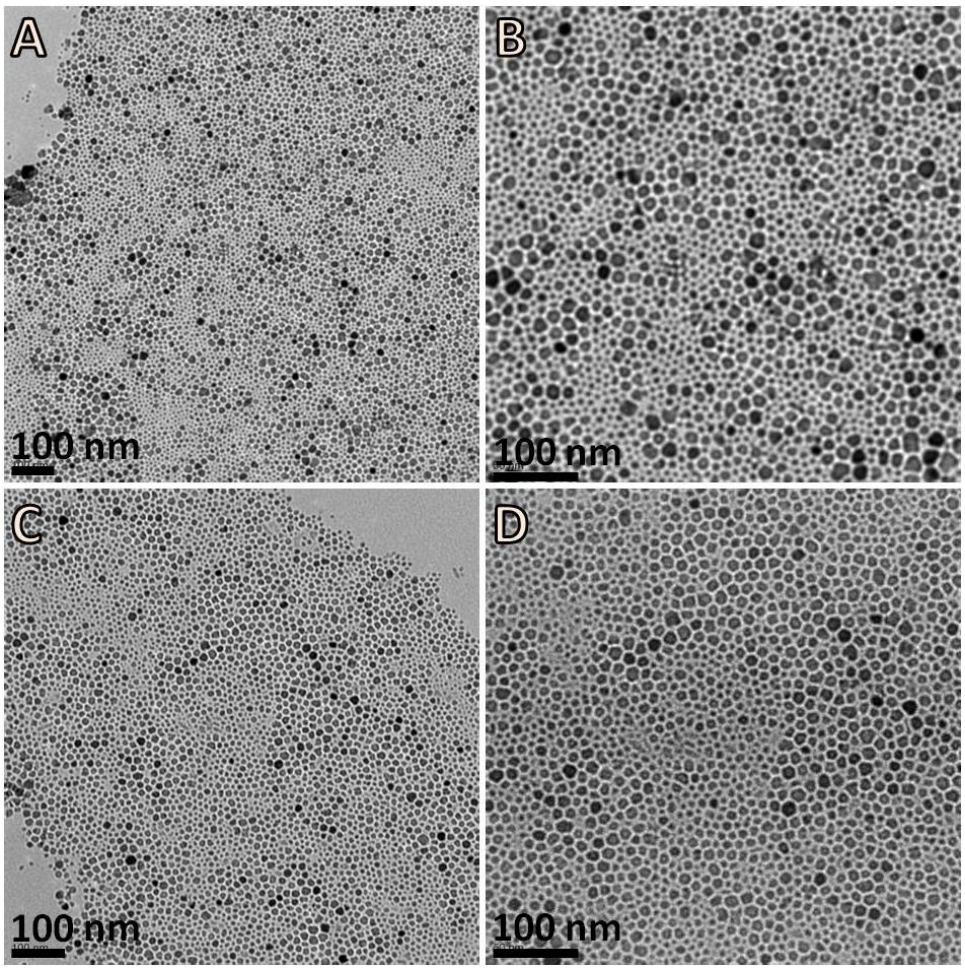

Figure 7-2 TEM images of spherical Fe_3O_4 nanocrystals prepared by MWI of Fe(acac)3 in benzyl ether for 20 min using 4.2 mmol OAm and 5.6 mmol (A,B) or 11.2 mmol (C,D) OAc. Average size of A,B and C,D is ~10 nm and ~13 nm, respectively.

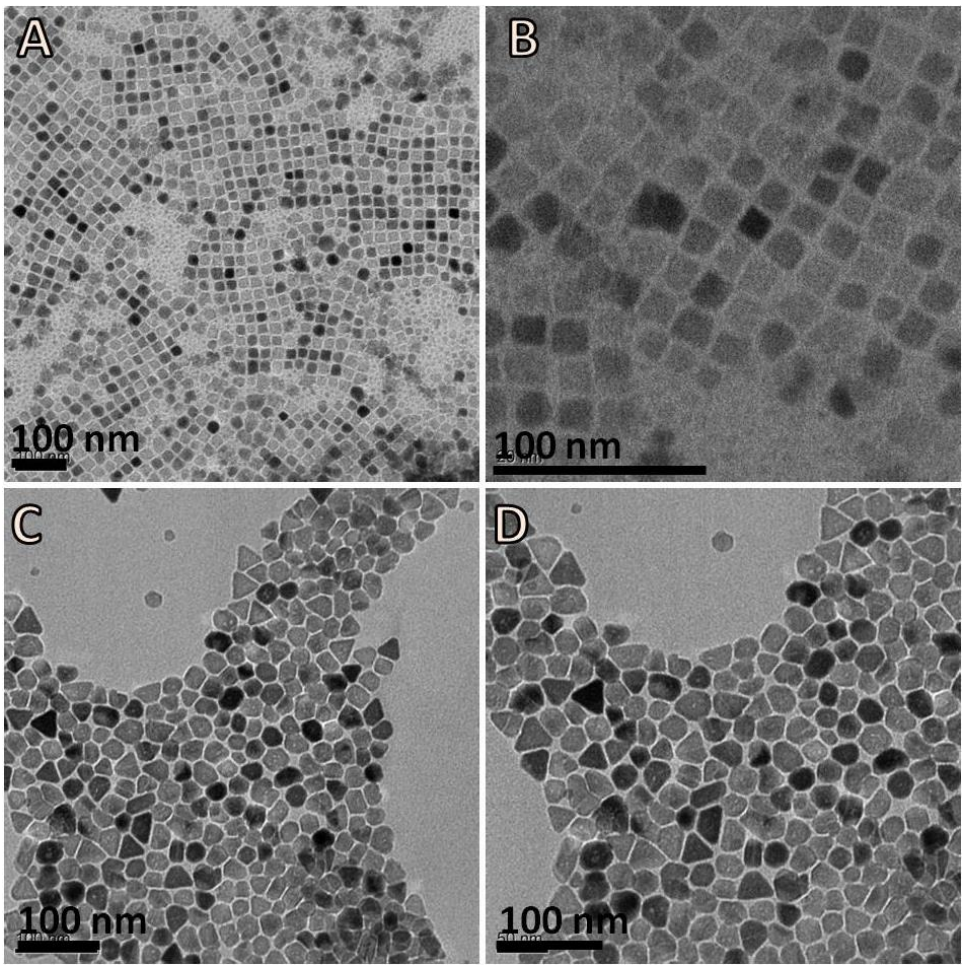

Figure 7-3 TEM images of cubic (A,B) and triangular (C,D) Fe_3O_4 nanocrystals prepared by MWI of Fe(acac)3 in benzyl ether for 20 min using 4.2 mmol OAm and 5.6 mmol or 11.2 mmol OAc, respectively. Edge length of cubes in A,B is ~ 15 nm and edge length in triangles ~28 nm.

The abundant oxygen-containing functional groups on the surface cause graphene oxide to readily disperse in DMSO by ultrasonication to form a stable colloidal solution.[46] The addition of this solution to the iron precursor $Fe(acac)_3$ in presence of OAm/OA mixture likely leads to coordination of the Fe^{3+} ions to the COOH groups of GO. Upon microwaving the reaction mixture, the original light brown color of the mixture turns into dark brown and finally into black when reaction is complete, which indicates both the formation of Fe_3O_4 nanocrystals and conversion of GO to RGO. The microwave-assisted solvothermal reduction of GO in DMSO have been demonstrated earlier by our group.[46] The high reaction temperature provided by MWI greatly accelerate the decomposition of $Fe(acac)_3$ precursors and the consequent Fe_3O_4 nucleation process, leading to the burst of nucleation within several seconds and this fast nucleation helps formation of small nuclei of narrow size distribution. In the next stage, the nuclei formed in the early stage rapidly grow larger through a slow process (20 min MWI). The MWI time along with the selective adsorption of OAm/OA co-surfactants provide means for the size control of growing particles. Finally a stable homogenous black dispersion of Fe_3O_4/RGO nanocomposites could be readily prepared by the contemporaneous microwave-assisted chemical reduction of Fe $(acac)_3$ and starting GO in benzylether.

The anchoring of Fe_3O_4 on the RGO sheets in the composite matrix is clear as can be seen in the transmission electron microscopy studies and wells as structural characterization. Representative TEM images of RGO sheets nicely decorated with Fe_3O_4 nanospheres are displayed in **Figs. 7.4-A-C**. The nice distribution of mostly 13-15 nm Fe_3O_4 spheres on the surface of RGO sheets is clear in low-resolution STEM (**Fig. 7.4-D**) and SEM (**Fig. 7.4-E-F**) images recorded for the spherical Fe_3O_4/RGO nanocomposite structures, as shown in **Fig. 7.4-D-F**. All TEM, STEM and SEM images reveal that the surfaces of RGO sheets are densely covered by Fe_3O_4 nanocrystals

of different uniform size and shape. The distribution of the nanocrystals on the sheets is even without large conglomeration of nanocrystals or large uncovered areas of RGO sheets. In a similar way to that adopted to control the shape of individual Fe_3O_4 nanocrystals, RGO sheets supporting Fe_3O_4 nanostructures of cubic and triangular morphologies were successfully prepared by altering the ratio between OAm and OAc (4.2 mmol OAm/2.8 mmol OAc and 2.1 mmol OAm/2.8 mmol OAc, respectively). **Figure 7.5-A,B** shows low resolution TEM images of Fe_3O_4 cubes supported on RGO sheets. TEM images of Fe_3O_4/RGO nanocomposites showing mostly prismatic nanocrystals are shown in **Fig. 7.5-C,D**. In both cases, the two-dimensional RGO sheets are well decorated by a significant quantity of cubic or prismatic Fe_3O_4 nanostructures and the outlines of both RGO and Fe_3O_4 can be observed; however, some other shapes such spheres or irregular morphologies also are formed (**Figure 7.5**).

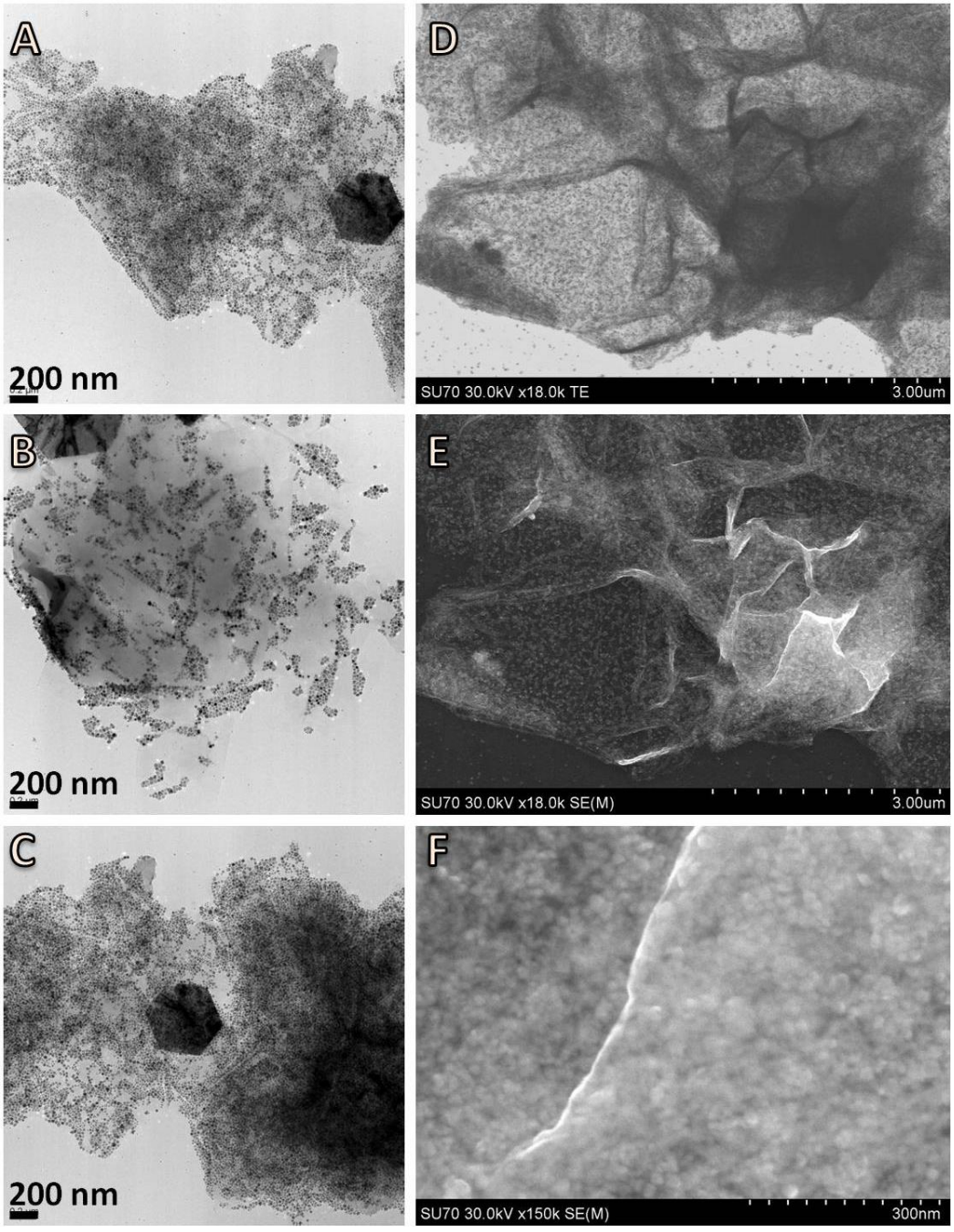

Figure 7-4 TEM (A-C), STEM (D) and low-reoslution SEM (E-F) images of spherical Fe_3O_4/RGO nanocomposite structures prepared by MWI of $Fe(acac)_3$ in benzyl ether for 20 min using 4.2 mmol OAm and 5.6 mmol OAc and in presence of GO/DMSO. Average size range is 13-15 nm.

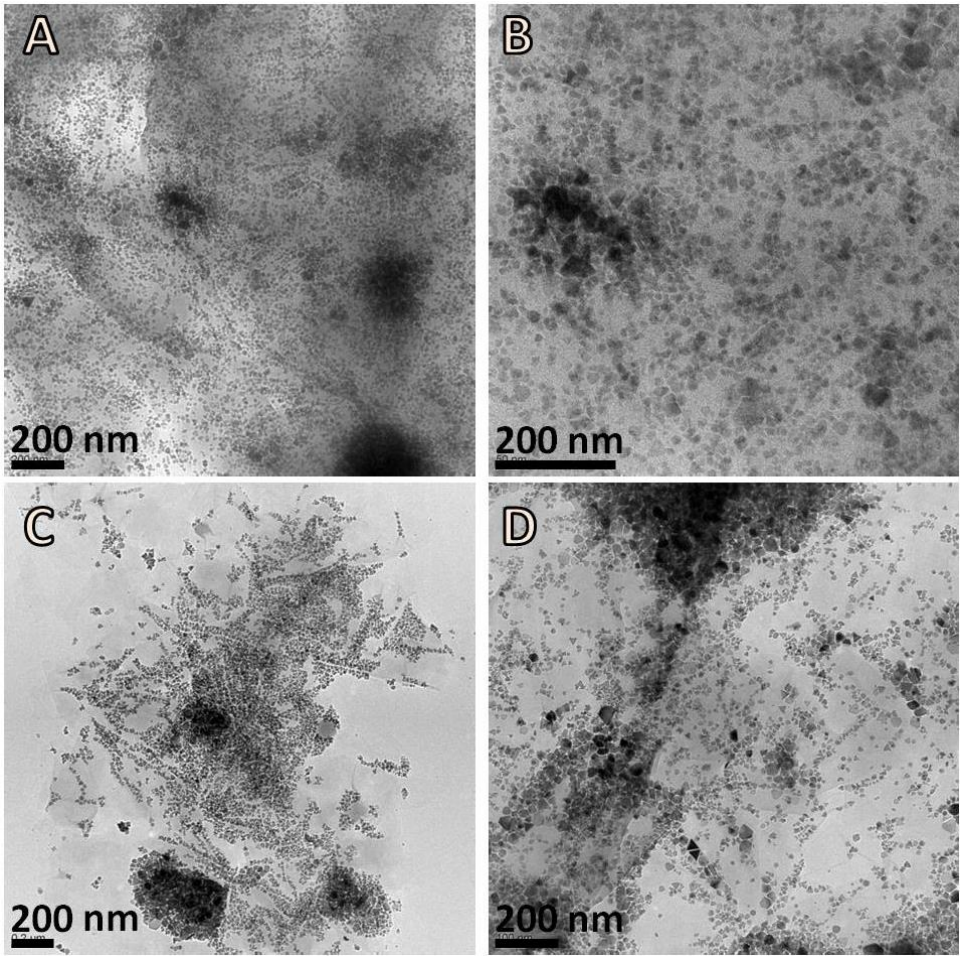

Figure 7-5 Low-resolution TEM images of cubic (A,B) and triangular (C,D) Fe_3O_4 nanocrystals supported on RGO sheets and prepared by MWI of Fe(acac)3 in benzyl ether for 20 min using 4.2 mmol OAm and 2.8 mm OAc or 2.1 mmol of OAm and 2.8 mmol of OAc, respectively. For A,B edge length is 11-17 nm and for C,D edge is 30-35 nm.

Of particular interest, large single crystal of Fe_3O_4 hexagonal nanoplates were successfully prepared when the growth conditions of growing spherical Fe_3O_4 (4.2 mmol OAm/5.6 mmol OAc) were altered by introducing GO suspension in DMSO. Some of these hexagonal nanoplates formed along with the spherical Fe_3O_4 in presence of RGO are shown in TEM images displayed in **Fig. 7.6-A-L**. Low-resolution STEM and SEM images of Fe_3O_4 hexagonal nanoplates are shown in

Fig. 7.7-A-C and **Figs. 7.7-D-F** and **7.8-A-F,** respectively. Presumably, the microwave irradiation during the first 10 min. led to formation of reduced graphene oxide (RGO) with fewer oxygen moieties and defects followed by the deposition of primary magnetite nanocrystals nucleated onto RGO sheets. Upon completion of the reaction course these primary nanocrystals anchored on RGO sheets are transformed into single crystal hexagonal nanoplates by recrystallization due to the elevated reaction temperature from the continuing microwave irradiation.[352] Finally, large and uniform magnetite hexagonal nanoplates with an average edge length of 0.9 μm nm were grown on RGO sheets, as can be seen in TEM and SEM images in **Figs. 7.6-7.7** .

It can be hypothesized that the prolonged microwave irradiation of reaction mixture leads first to thermal decomposition of iron precursors in benzyl ether that serve as a high-boiling point solvent. When the supersatuartion is reached this triggers the formation of Fe_3O_4 nuclei followed by the subsequent growth of these nuclei to primary nanoparticles. On the basis of the TEM results combined with the experimental conditions, thermodynamic and kinetic factors could lead to shape evolution at different stages of the microwave irradiation process. The adsorption of surfactants to different extents under different conditions combined with altering the molar ratio between the two surfactants could play a crucial role in selective passivation of different crystal planes and hence different growth rates at those faces.[357] This could stabilize the {100} facets of growing Fe_3O_4 nanocrystals and thus led to termination or slower relative growth rate. For instance, the shape transformation of the isotropically growing nuclei from spheres to cubic or prismatic nanostructures could result from the favored growth along the {111} crystal facet in particles with terminated {100} planes. [346] The relative fractions of oleic acid and oleyamine play a crucial role in the anisotropic shape growth process which strongly influences the formed morphology. The higher oxophilicity of oleic acid compared to oleylamine may cause oleic acid to from a stronger

bond to surface atoms of primary growing particles.[358] However, further studies are necessary to explore the exact mechanism of binding of the organic surfactants onto the surface of the growing crystals.

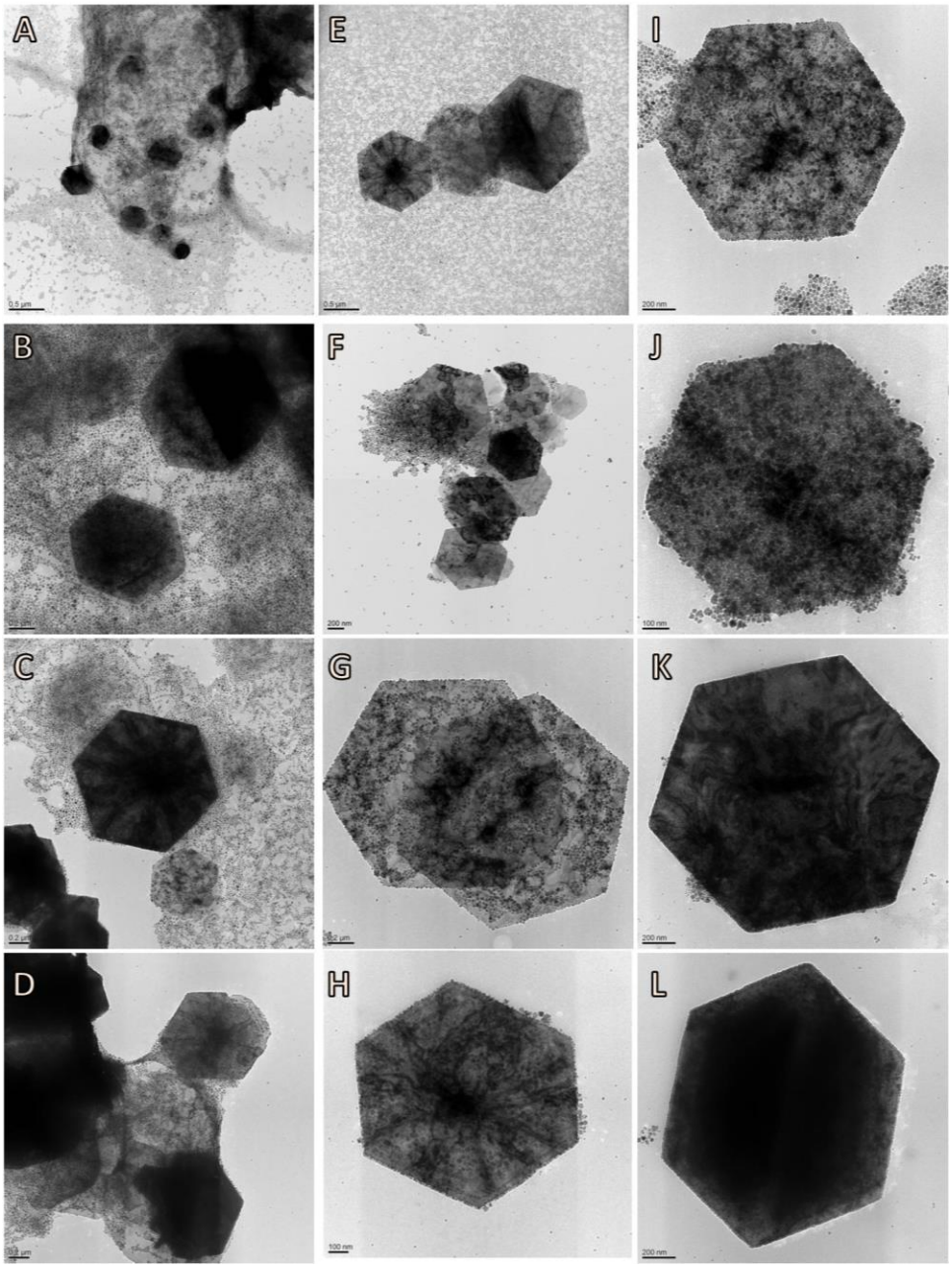

Figure 7-6 TEM images of single-crystalline Fe_3O_4 hexagonal nanoplates prepared with spherical Fe_3O_4 in presence of RGO sheets. Edge length in image G and K is ~0.9 µm.

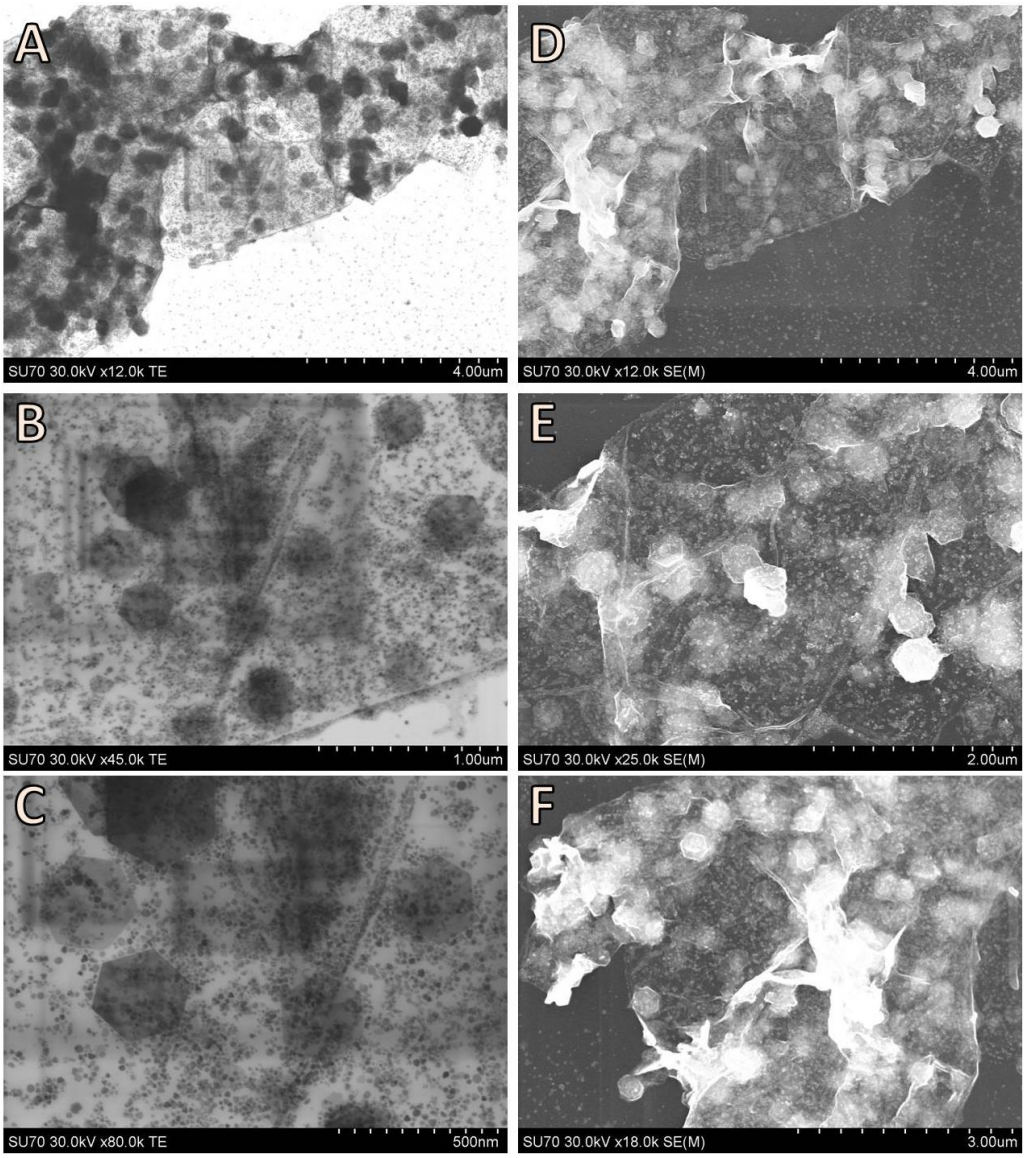

Figure 7-7 Low-resolution STEM (A-C) and SEM (D-F) images of Fe_3O_4 hexagonal nanoplates.

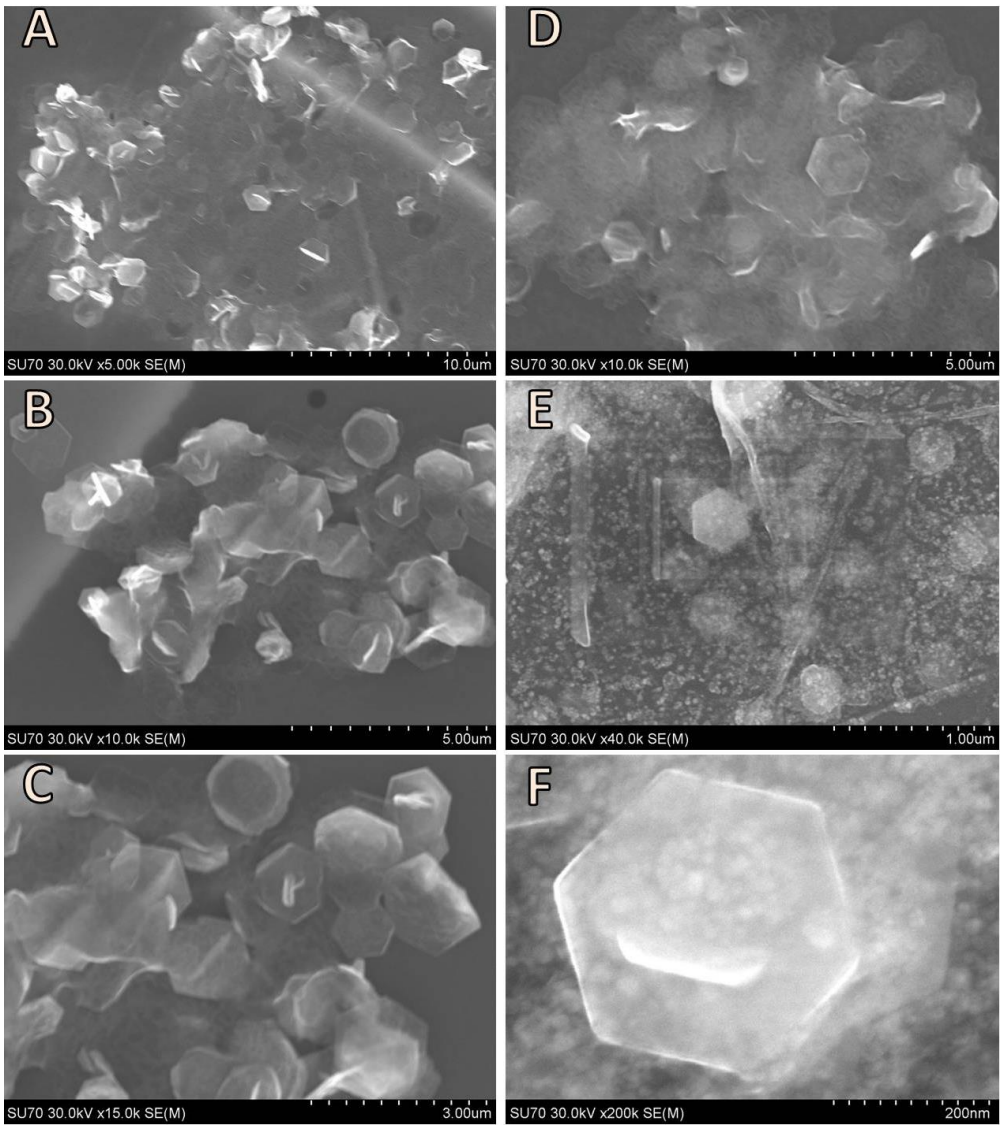

Figure 7-8 Low-resolution SEM images of Fe_3O_4 hexagonal nanoplates wrapped in RGO sheets.

7.4.2 Structural Characterization:

Figure 7.9 shows the powder X-ray diffraction patterns of different Fe_3O_4 and Fe_3O_4/RGO nanostructures of various shapes, namely, spheres, cubes and triangles. The XRD peaks can be indexed to the standard spinnel Fe_3O_4 structure, in a good agreement to the literature.[327] The diffraction patterns of all nanostructures both free-standing and anchored on RGO sheets feature strong reflections indicating all prepared nanostructures are well-crystalline. The spectra are characterized by seven peaks at 18.34°, 30.18°, 35.54°, 43.24°, 53.66°, 57.14° and 62.78°, corresponding to the (111), (220), (311), (400), (422), (511), and (440) planes. [359]

X-ray photoelectron spectroscopy (XPS) measurements were conducted to further reveal structural characteristics of prepared nanostructures and probe the extent of reduction of GO. **Figure 7.10** shows the C1s high-resolution spectra of GO before and after the microwave irradiation. Spectrum of GO before the microwave irradiation reveals five different convoluted peaks at 284.5, 286.1, 286.5, 287.9 and 288.4 eV which are corresponding to sp^2 carbon, sp^3 carbon, hydroxyl/epoxy groups (C-O), carbonyl groups (C=O) and carboxyl groups (O-C=O), respectively.[112, 113] After the microwave irradiation of GO dispersed in DMSO, the fraction related to the oxygen content between 286.1-288.4 eV obviously decreased with a relative increase in the fraction of the C-C bonding indicating the efficient microwave-assisted deoxygentaion of GO sheets. The sensitivity of XPS to difference between Fe^{2+} and Fe^{3+} cations allows distinguishing the Fe_3O_4 and γ-Fe_2O_3 phases. **Figure 7.11** shows comparisons of XPS high-resolution Fe3d spectra of various-shaped Fe_3O_4 and Fe_3O_4/RGO nanocomposites. The presence of the two main peaks at around 710-711 and 724-725 eV which are characteristic binding energies of $Fe2p_{3/2}$ and $Fe2p_{1/2}$, respectively, and the absence of significant peaks in the 718-720 eV range, characteristics to γ-Fe_2O_3, reveal the formation of crystalline Fe_3O_4 phase in different nanocomposites, as

compared to values reported in the literature.[343] The studies from XRD and XPS show that the crystalline phase of free-standing and anchored iron oxide nanostructures is magnetite. Further structural details of Fe_3O_4 nanopsheres and hexagonal nanoplates were obtained from the selected area diffraction (SAED) patterns. **Figure 7.12** compares SAED pattern obtained from spherical Fe_3O_4 and a single Fe_3O_4 hexagonal nanoplate with the electron beam perpendicular to the basal facet. The SAED pattern shown in **Figure 7.12-a** can be indexed to the [111] zone axis of FCC Fe_3O_4 which reveals the characteristic spinel crystal structure of magnetite. [348]

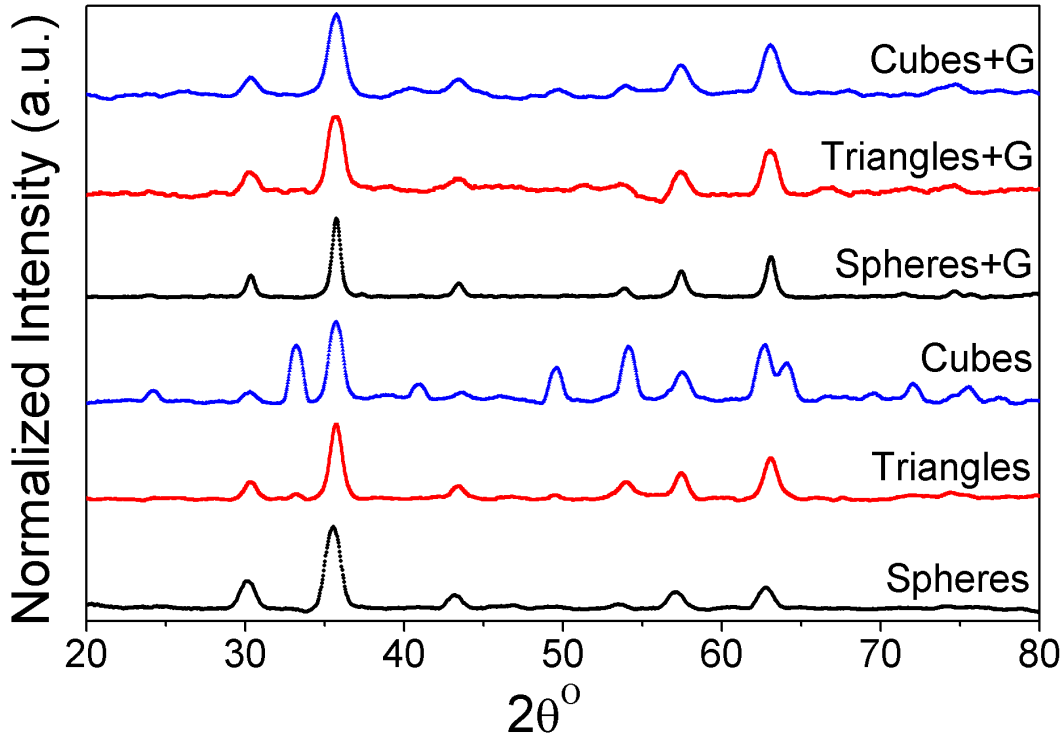

Figure 7-9 X-ray diffraction patterns of various shaped-Fe_3O_4 and Fe_3O_4/RGO nanostructures prepared by MWI of molecular precursors in OA-OAm mixture.

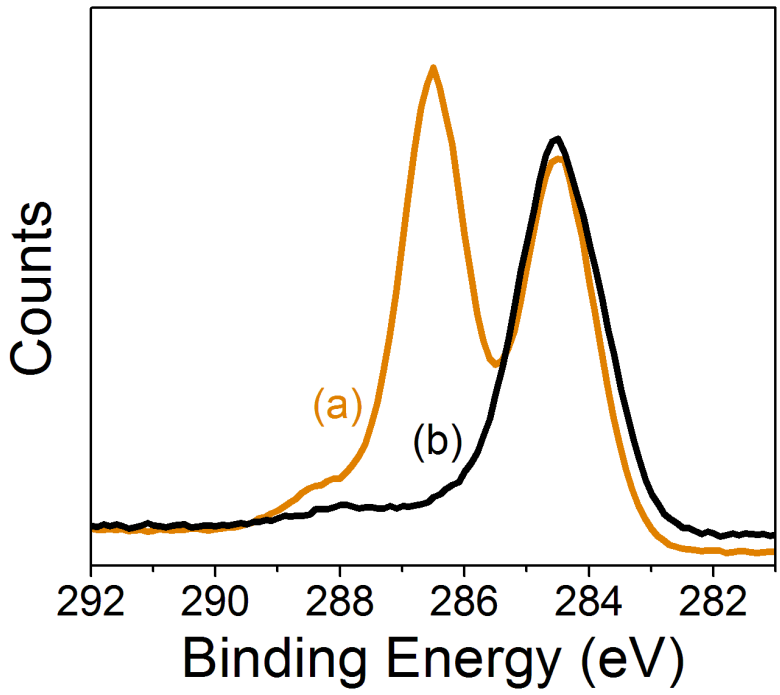

Figure 7-10 XPS high-resolution C1s spectra of GO (a) and RGO (b) prepared by MWI.

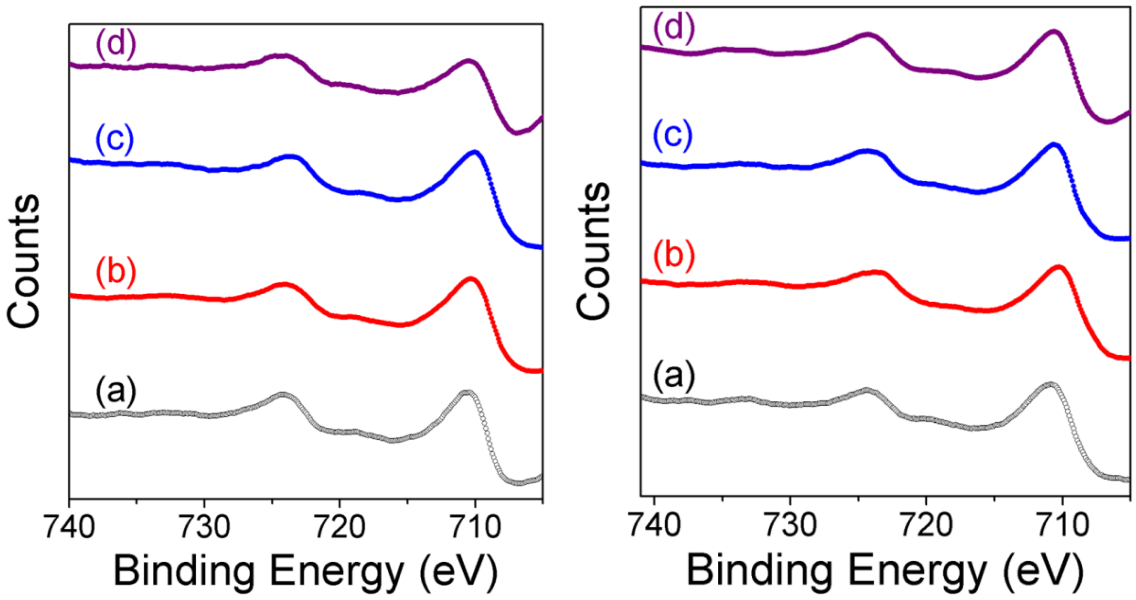

Figure 7-11 XPS high resolution spectrum of Fe2p of various-shaped Fe_3O_4 (left) and Fe_3O_4/RGO nanocomposites (right)

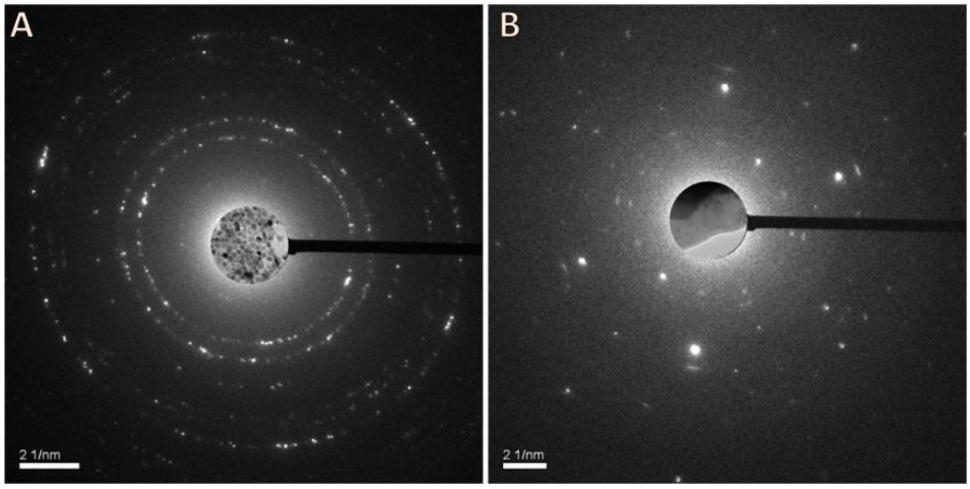

Figure 7-12 SAED diffraction patterns of Fe_3O_4 nanospheres (a) and hexagonal nanoplates (b) prepared by MWI.

7.4.3 Magnetic characterization

The effect of the structure and morphology on the magnetite properties was studied by measuring magnetic behaviors of various samples adopting a vibrating sample magnetometer (VSM). The magnetization curves of as-prepared Fe_3O_4 and Fe_3O_4/RGO nanostructures were recorded at room temperature by measuring the saturation magnetization as a function of the external applied magnetic field. **Fig. 7.13** shows the hysteresis curves obtained for different morphologies with an applied field sweeping from -30 to 30 kOe. The hysteresis loops of all prepared samples reveal superparamagnetic behavior at room temperature with nearly zero coercivity and extremely low remnant magnetization values, as listed in **Table 7.2**. The lack of remaining magnetization when the external magnetic field is removed is in agreement with a superparamagnetic behavior observed in graphene nanosheets coated with Fe_3O_4 nanoparticles.[360] The size reduction of our prepared nanostructures to less than the critical size of single domain particles, which is 54 nm for magnetite,[60] led to a significant change in magnetic properties from

bulk counterpart and superparamgnetic behavior is observed in different synthesized morphologies. The shrinkage in size makes the magnetic anisotropic energy, KV, where K is the magnetic anisotropy constant and V is the volume of the particle, comparable to the thermal energy, kT, and this causes randomization in moment and superparamgentic behavior.

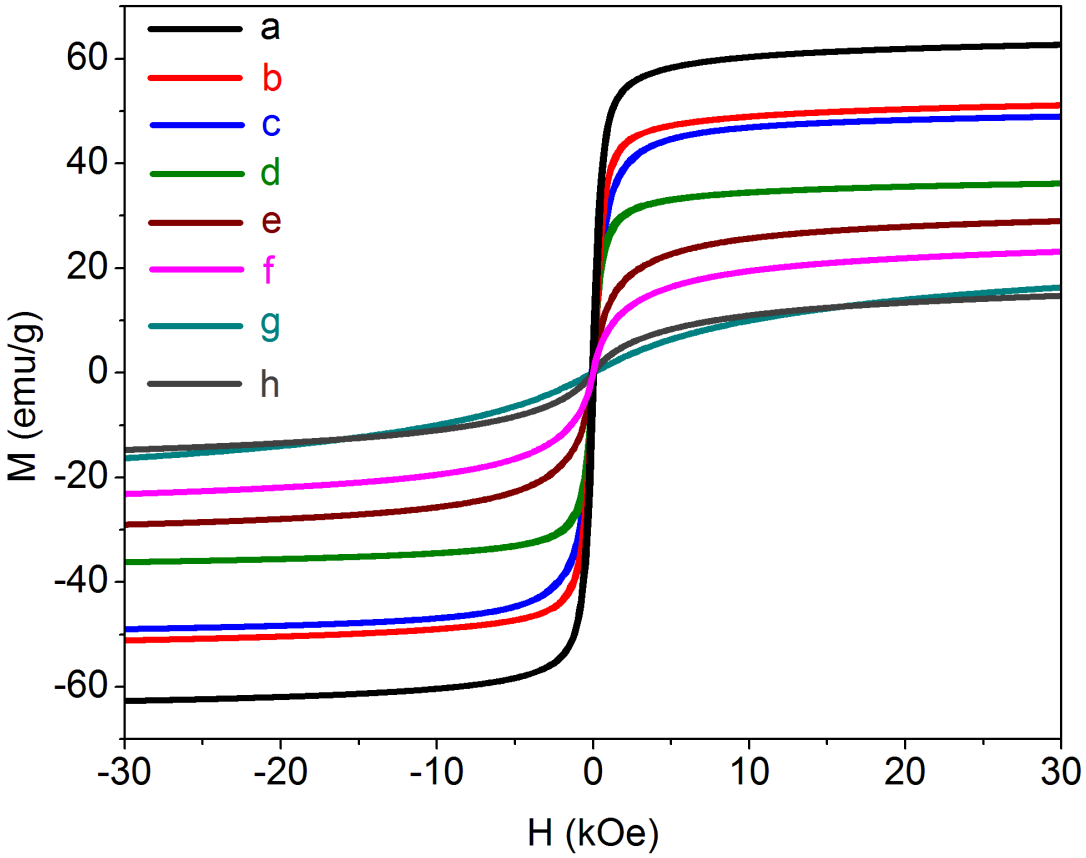

Figure 7-13 Hysteresis curves of various-shaped Fe_3O_4 and Fe_3O_4/RGO nanostructures measured at 300 K. a) Fe_3O_4 Triangles/RGO, b) Triangles, c) Cubes, d) Spheres/RGO, e) Spheres (large, ~13 nm), f) Cubes/RGO, g) Dots by OAm (~5 nm) and h) Spheres (small, ~10 nm).

In addition, It is generally accepted that the degree of saturation magnetization increases with increasing size or crystallinity.[60] **Table 7.2** compares the different values of saturation magnetization of our prepared magnetite nanostructures. The Ms values of different magnetite samples are smaller than those reported for 2-5 mm bulk magnetite grains (93 emu/g),[344] probably due to the decrease of the particle size, the increase in surface defects or the adsorption of surfactants on the surface. Such structural disorders may lead to noncollinear spin structure which results in spin canting and magnetic moment reduction. [348, 361]

Table 7-2 Comparison of values of M_s, M_r and H_c of prepared Fe_3O_4 samples of various shapes

Shape/Composition	T (K)	M_s (emu/g)	M_r (emu/g)	H_c (kOe)
Fe_3O_4 Triangles/RGO	300	62.67	6.72	0.058
Fe_3O_4 Triangles	300	51.11	4.18	0.041
Fe_3O_4 Cubes	300	48.95	5.82	0.094
Fe_3O_4 Large spheres/RGO	300	36.16	2.60	0.035
Fe_3O_4 Large Spheres (~13 nm)	300	29.00	1.78	0.085
Fe_3O_4 Cubes/RGO	300	23.15	0.20	0.019
Fe_3O_4 Dots by OAm (~5 nm)	300	16.32	0.11	0.072
Fe_3O_4 Small Spheres (~10 nm)	300	14.72	0.08	0.017

It can be seen that generally with shape transformation from isotropic to anisotropic morphology, the magnitude of saturation magnetization becomes larger, probably due to the increase in shape and magnetiocrytsalline anisotropy.[342] The saturation magnetization of the Fe_3O_4 triangles anchored on RGO sheets is a little higher than non-anchored ones possibly due to the different surface conditions. The transformation of the shape from spheres to triangles or cubes results in a remarkable increase in the saturation magnetization to 62 emu/g for triangles and 51 emu/g for cubes, compared to 36 emu/g in case of spherical samples, which is a good agreement with similar studies of hollow spheres,[344] cubes,[348] octahedrons, [342] and hexapods [342] of saturation magnetization as 56-65, 60.3, 72.5 and 96.2 emu/g, respectively. Although saturation

magnetization of Fe_3O_4 spheres and spherical Fe_3O_4 anchored on RGO is less than other anisotropic shapes, still higher than those reported for spherical magnetite (17.96 emu/g) and spherical magnetite supported on graphene (10.23 emu/g).[43] The magnetic measurements clearly show the effects of shape and size control on the magnetic properties of prepared Fe_3O_4 and Fe_3O_4/RGO nanostructures.

7.5 Conclusions

In conclusion, a single-step and rapid, yet facile, microwave-assisted synthesis of magnetite nanospheres, nanocubes, and triangles on graphene sheets using iron acetylacetnate is developed. The morphology of the magnetite nanocrystals grown on graphene can be tailored by tuning the molar ratio of oleic acid and oleylamine. The strategy developed provide a mean to control the shape of magnetite nanocrystals, both free standing and those attached to graphene sheets, integrating in such way the superparamagnetic properties of magnetite nanoparticles of different morphologies and the superior conductivity of graphene in a single compartment composite structure. On the basis of the TEM results combined with the experimental conditions, thermodynamic and kinetic factors could lead to shape evolution at different stages of the microwave irradiation process. The magnetic measurements clearly show the effects of shape and size control on the magnetic properties of prepared Fe_3O_4 and Fe_3O_4/RGO nanostructures.

List of References

List of References

1. Novoselov, K. S.; Geim, A. K.; Morozov, S. V.; Jiang, D.; Zhang, Y.; Dubonos, S. V.; Grigorieva, I. V.; Firsov, A. A., Electric Field Effect in Atomically Thin Carbon Films. *Science* **2004,** 306, (5696), 666-669.

2. Li, D.; Muller, M. B.; Gilje, S.; Kaner, R. B.; Wallace, G. G., Processable aqueous dispersions of graphene nanosheets. *Nat Nano* **2008,** 3, (2), 101-105.

3. Geim, A. K.; Novoselov, K. S., The rise of graphene. *Nat Mater* **2007,** 6, (3), 183-191.

4. Novoselov, K. S.; Jiang, D.; Schedin, F.; Booth, T. J.; Khotkevich, V. V.; Morozov, S. V.; Geim, A. K., Two-dimensional atomic crystals. *Proceedings of the National Academy of Sciences of the United States of America* **2005,** 102, (30), 10451-10453.

5. Novoselov, K. S.; Geim, A. K.; Morozov, S. V.; Jiang, D.; Katsnelson, M. I.; Grigorieva, I. V.; Dubonos, S. V.; Firsov, A. A., Two-dimensional gas of massless Dirac fermions in graphene. *Nature* **2005,** 438, (7065), 197-200.

6. Zhang, Y.; Tan, Y.-W.; Stormer, H. L.; Kim, P., Experimental observation of the quantum Hall effect and Berry's phase in graphene. *Nature* **2005,** 438, (7065), 201-204.

7. Dresselhaus, M. S.; Dresselhaus, G., Intercalation compounds of graphite. *Advances in Physics* **2002,** 51, (1), 1-186.

8. Lui, C. H.; Li, Z.; Mak, K. F.; Cappelluti, E.; Heinz, T. F., Observation of an electrically tunable band gap in trilayer graphene. *Nat Phys* **2011,** 7, (12), 944-947.

9. Charlier, J. C.; Issi, J. P., Electrical conductivity of novel forms of carbon. *Journal of Physics and Chemistry of Solids* 57, (6-8), 957-965.

10. Saito, R.; Dresselhaus, G.; Dresselhaus, M. S., *Physical Properties of Carbon Nanotubes*. World Scientific: 1998; p 272.

11. Park, S.; Ruoff, R. S., Chemical methods for the production of graphenes. *Nat Nano* **2009,** 4, (4), 217-224.

12. Allen, M. J.; Tung, V. C.; Kaner, R. B., Honeycomb Carbon: A Review of Graphene. *Chemical Reviews* **2009,** 110, (1), 132-145.

13. Peres, N. M. R., The transport properties of graphene. *Journal of Physics: Condensed Matter* **2009,** 21, (32), 323201.

14. Fowler, J. D.; Allen, M. J.; Tung, V. C.; Yang, Y.; Kaner, R. B.; Weiller, B. H., Practical Chemical Sensors from Chemically Derived Graphene. *ACS Nano* **2009,** 3, (2), 301-306.

15. Schedin, F.; Geim, A. K.; Morozov, S. V.; Hill, E. W.; Blake, P.; Katsnelson, M. I.; Novoselov, K. S., Detection of individual gas molecules adsorbed on graphene. *Nat Mater* **2007,** 6, (9), 652-655.

16. Stolyarova, E.; Rim, K. T.; Ryu, S.; Maultzsch, J.; Kim, P.; Brus, L. E.; Heinz, T. F.; Hybertsen, M. S.; Flynn, G. W., High-resolution scanning tunneling microscopy imaging of mesoscopic graphene sheets on an insulating surface. *Proceedings of the National Academy of Sciences* **2007,** 104, (22), 9209-9212.

17. Dresselhaus, M. S.; Jorio, A.; Saito, R., Characterizing Graphene, Graphite, and Carbon Nanotubes by Raman Spectroscopy. *Annual Review of Condensed Matter Physics* **2010,** 1, (1).

18. Ferrari, A. C.; Meyer, J. C.; Scardaci, V.; Casiraghi, C.; Lazzeri, M.; Mauri, F.; Piscanec, S.; Jiang, D.; Novoselov, K. S.; Roth, S.; Geim, A. K., Raman Spectrum of Graphene and Graphene Layers. *Physical Review Letters* **2006,** 97, (18), 187401.

19. Zhu, Y.; Murali, S.; Cai, W.; Li, X.; Suk, J. W.; Potts, J. R.; Ruoff, R. S., Graphene and Graphene Oxide: Synthesis, Properties, and Applications. *Advanced Materials* **2010,** 22, (35), 3906-3924.

20. Bai, H.; Li, C.; Shi, G., Functional Composite Materials Based on Chemically Converted Graphene. *Advanced Materials* **2011,** 23, (9), 1089-1115.

21. Xia, F.; Farmer, D. B.; Lin, Y.-m.; Avouris, P., Graphene Field-Effect Transistors with High On/Off Current Ratio and Large Transport Band Gap at Room Temperature. *Nano Letters* 10, (2), 715-718.

22. Eda, G.; Chhowalla, M., Graphene-based Composite Thin Films for Electronics. *Nano Letters* **2009,** 9, (2), 814-818.

23. Wu, J.; Pisula, W.; MÃ¼llen, K., Graphenes as Potential Material for Electronics. *Chemical Reviews* **2007,** 107, (3), 718-747.

24. Wang, G.; Shen, X.; Yao, J.; Park, J., Graphene nanosheets for enhanced lithium storage in lithium ion batteries. *Carbon* **2009,** 47, (8), 2049-2053.

25. Kamat, P. V., Graphene-Based Nanoassemblies for Energy Conversion. *The Journal of Physical Chemistry Letters* **2011,** 2, (3), 242-251.

26. Liu, C.; Yu, Z.; Neff, D.; Zhamu, A.; Jang, B. Z., Graphene-Based Supercapacitor with an Ultrahigh Energy Density. *Nano Letters* 10, (12), 4863-4868.

27. Gwon, H.; Kim, H.-S.; Lee, K. U.; Seo, D.-H.; Park, Y. C.; Lee, Y.-S.; Ahn, B. T.; Kang, K., Flexible energy storage devices based on graphene paper. *Energy & Environmental Science* 4, (4), 1277-1283.

28. Yavari, F.; Fard, H. R.; Pashayi, K.; Rafiee, M. A.; Zamiri, A.; Yu, Z.; Ozisik, R.; Borca-Tasciuc, T.; Koratkar, N., Enhanced Thermal Conductivity in a Nanostructured Phase Change Composite due to Low Concentration Graphene Additives. *The Journal of Physical Chemistry C* **2011,** 115, (17), 8753-8758.

29. Rafiee, M. A.; Lu, W.; Thomas, A. V.; Zandiatashbar, A.; Rafiee, J.; Tour, J. M.; Koratkar, N. A., Graphene Nanoribbon Composites. *ACS Nano* **2010,** 4, (12), 7415-7420.

30. Rao, C. N. R.; Sood, A. K.; Voggu, R.; Subrahmanyam, K. S., Some Novel Attributes of Graphene. *The Journal of Physical Chemistry Letters* 1, (2), 572-580.

31. Gomez-Navarro, C.; Weitz, R. T.; Bittner, A. M.; Scolari, M.; Mews, A.; Burghard, M.; Kern, K., Electronic Transport Properties of Individual Chemically Reduced Graphene Oxide Sheets. *Nano Letters* **2007,** 7, (11), 3499-3503.

32. Castro, E. V.; Novoselov, K. S.; Morozov, S. V.; Peres, N. M. R.; dos Santos, J. M. B. L.; Nilsson, J.; Guinea, F.; Geim, A. K.; Neto, A. H. C., Biased Bilayer Graphene: Semiconductor with a Gap Tunable by the Electric Field Effect. *Physical Review Letters* **2007,** 99, (21), 216802.

33. Dikin, D. A.; Stankovich, S.; Zimney, E. J.; Piner, R. D.; Dommett, G. H. B.; Evmenenko, G.; Nguyen, S. T.; Ruoff, R. S., Preparation and characterization of graphene oxide paper. *Nature* **2007,** 448, (7152), 457-460.

34. Wang, X.; Zhi, L.; Mullen, K., Transparent, Conductive Graphene Electrodes for Dye-Sensitized Solar Cells. *Nano Letters* **2007,** 8, (1), 323-327.

35. Watcharotone, S.; Dikin, D. A.; Stankovich, S.; Piner, R.; Jung, I.; Dommett, G. H. B.; Evmenenko, G.; Wu, S.-E.; Chen, S.-F.; Liu, C.-P.; Nguyen, S. T.; Ruoff, R. S., Grapheneâˆ’Silica Composite Thin Films as Transparent Conductors. *Nano Letters* **2007,** 7, (7), 1888-1892.

36. Kim, K.; Park, H. J.; Woo, B.-C.; Kim, K. J.; Kim, G. T.; Yun, W. S., Electric Property Evolution of Structurally Defected Multilayer Graphene. *Nano Letters* **2008,** 8, (10), 3092-3096.

37. Cheng, Z.; Li, Q.; Li, Z.; Zhou, Q.; Fang, Y., Suspended Graphene Sensors with Improved Signal and Reduced Noise. *Nano Letters* 10, (5), 1864-1868.

38. Meyer, J. C.; Girit, C. O.; Crommie, M. F.; Zettl, A., Imaging and dynamics of light atoms and molecules on graphene. *Nature* **2008,** 454, (7202), 319-322.

39. Shahil, K. M. F.; Balandin, A. A., Grapheneâ€“Multilayer Graphene Nanocomposites as Highly Efficient Thermal Interface Materials. *Nano Letters* **2012**

12, (2), 861-867.

40. Yoonessi, M.; Shi, Y.; Scheiman, D. A.; Lebron-Colon, M.; Tigelaar, D. M.; Weiss, R. A.; Meador, M. A., Graphene Polyimide Nanocomposites; Thermal, Mechanical, and High-Temperature Shape Memory Effects. *ACS Nano* **2012,** 6, (9), 7644-7655.

41. Song, Z.; Xu, T.; Gordin, M. L.; Jiang, Y.-B.; Bae, I.-T.; Xiao, Q.; Zhan, H.; Liu, J.; Wang, D., Polymerâ€“Graphene Nanocomposites as Ultrafast-Charge and -Discharge Cathodes for Rechargeable Lithium Batteries. *Nano Letters* **2012,** 12, (5), 2205-2211.

42. Guo, Y.; Han, Y.; Shuang, S.; Dong, C., Rational synthesis of graphene-metal coordination polymer composite nanosheet as enhanced materials for electrochemical biosensing. *Journal of Materials Chemistry* **2012,** 22, (26), 13166-13173.

43. Su, J.; Cao, M.; Ren, L.; Hu, C., Fe3O4â€“Graphene Nanocomposites with Improved Lithium Storage and Magnetism Properties. *The Journal of Physical Chemistry C* **2011,** 115, (30), 14469-14477.

44. Zhang, Y.; Tang, Z.-R.; Fu, X.; Xu, Y.-J., TiO2âˆ’Graphene Nanocomposites for Gas-Phase Photocatalytic Degradation of Volatile Aromatic Pollutant: Is TiO2âˆ’Graphene Truly Different from Other TiO2âˆ’Carbon Composite Materials? *ACS Nano* **2010,** 4, (12), 7303-7314.

45. Williams, G.; Seger, B.; Kamat, P. V., TiO2-Graphene Nanocomposites. UV-Assisted Photocatalytic Reduction of Graphene Oxide. *ACS Nano* **2008,** 2, (7), 1487-1491.

46. Zedan, A. F.; Sappal, S.; Moussa, S.; El-Shall, M. S., Ligand-Controlled Microwave Synthesis of Cubic and Hexagonal CdSe Nanocrystals Supported on Graphene. Photoluminescence Quenching by Graphene. *The Journal of Physical Chemistry C* **2010,** 114, (47), 19920-19927.

47. Weller, H., Quantized Semiconductor Particles: A novel state of matter for materials science. *Advanced Materials* **1993,** 5, (2), 88-95.

48. Weller, H., Colloidal Semiconductor Q-Particles: Chemistry in the Transition Region Between Solid State and Molecules. *Angewandte Chemie International Edition in English* **1993,** 32, (1), 41-53.

49. Quantum Dots: A Primer. *Applied Spectroscopy* **2002,** 56, 16A-27A.

50. Bruchez, M.; Moronne, M.; Gin, P.; Weiss, S.; Alivisatos, A. P., Semiconductor Nanocrystals as Fluorescent Biological Labels. *Science* **1998,** 281, (5385), 2013-2016.

51. Michalet, X.; Pinaud, F.; Lacoste, T. D.; Dahan, M.; Bruchez, M. P.; Alivisatos, A. P.; Weiss, S., Properties of Fluorescent Semiconductor Nanocrystals and their Application to Biological Labeling. *Single Molecules* **2001,** 2, (4), 261-276.

52. Mansur, H. S., Quantum dots and nanocomposites. *Wiley Interdisciplinary Reviews: Nanomedicine and Nanobiotechnology* 2, (2), 113-129.

53. El-Sayed, M. A., Some Interesting Properties of Metals Confined in Time and Nanometer Space of Different Shapes. *Accounts of Chemical Research* **2001,** 34, (4), 257-264.

54. Zhu, M.; Diao, G., Synthesis of Porous Fe3O4 Nanospheres and Its Application for the Catalytic Degradation of Xylenol Orange. *The Journal of Physical Chemistry C* **2011,** 115, (39), 18923-18934.

55. Zhang, Y.; Sun, L.; Fu, Y.; Huang, Z. C.; Bai, X. J.; Zhai, Y.; Du, J.; Zhai, H. R., The Shape Anisotropy in the Magnetic Field-Assisted Self-Assembly Chain-like Structure of Magnetite. *The Journal of Physical Chemistry C* **2009,** 113, (19), 8152-8157.

56. Zhang, D.; Liu, Z.; Han, S.; Li, C.; Lei, B.; Stewart, M. P.; Tour, J. M.; Zhou, C., Magnetite (Fe3O4) Coreâ^'Shell Nanowires:â€‰ Synthesis and Magnetoresistance. *Nano Letters* **2004,** 4, (11), 2151-2155.

57. Yang, D.; Hu, J.; Fu, S., Controlled Synthesis of Magnetiteâ^'Silica Nanocomposites via a Seeded Solâ^'Gel Approach. *The Journal of Physical Chemistry C* **2009,** 113, (18), 7646-7651.

58. Xu, Z.; Shen, C.; Hou, Y.; Gao, H.; Sun, S., Oleylamine as Both Reducing Agent and Stabilizer in a Facile Synthesis of Magnetite Nanoparticles. *Chemistry of Materials* **2009,** 21, (9), 1778-1780.

59. Xu, S.; Ma, W.-F.; You, L.-J.; Li, J.-M.; Guo, J.; Hu, J. J.; Wang, C.-C., Toward Designer Magnetite/Polystyrene Colloidal Composite Microspheres with Controllable Nanostructures and Desirable Surface Functionalities. *Langmuir* **2012,** 28, (6), 3271-3278.

60. Xiong, Y.; Ye, J.; Gu, X.; Chen, Q.-w., Synthesis and Assembly of Magnetite Nanocubes into Flux-Closure Rings. *The Journal of Physical Chemistry C* **2007,** 111, (19), 6998-7003.

61. Xiong, Q. Q.; Tu, J. P.; Lu, Y.; Chen, J.; Yu, Y. X.; Qiao, Y. Q.; Wang, X. L.; Gu, C. D., Synthesis of Hierarchical Hollow-Structured Single-Crystalline Magnetite (Fe3O4) Microspheres: The Highly Powerful Storage versus Lithium as an Anode for Lithium Ion Batteries. *The Journal of Physical Chemistry C* **2012,** 116, (10), 6495-6502.

62. Suh, S. K.; Yuet, K.; Hwang, D. K.; Bong, K. W.; Doyle, P. S.; Hatton, T. A., Synthesis of Nonspherical Superparamagnetic Particles: In Situ Coprecipitation of Magnetic Nanoparticles in Microgels Prepared by Stop-Flow Lithography. *Journal of the American Chemical Society* **2012,** 134, (17), 7337-7343.

63. Kievit, F. M.; Zhang, M., Surface Engineering of Iron Oxide Nanoparticles for Targeted Cancer Therapy. *Accounts of Chemical Research* **2011,** 44, (10), 853-862.

64. Schniepp, H. C.; Li, J.-L.; McAllister, M. J.; Sai, H.; Herrera-Alonso, M.; Adamson, D. H.; Prud'homme, R. K.; Car, R.; Saville, D. A.; Aksay, I. A., Functionalized Single Graphene Sheets Derived from Splitting Graphite Oxide. *The Journal of Physical Chemistry B* **2006,** 110, (17), 8535-8539.

65. Gao, L.; Guest, J. R.; Guisinger, N. P., Epitaxial Graphene on Cu(111). *Nano Letters* 10, (9), 3512-3516.

66. Li, X.; Magnuson, C. W.; Venugopal, A.; An, J.; Suk, J. W.; Han, B.; Borysiak, M.; Cai, W.; Velamakanni, A.; Zhu, Y.; Fu, L.; Vogel, E. M.; Voelkl, E.; Colombo, L.; Ruoff, R. S., Graphene Films with Large Domain Size by a Two-Step Chemical Vapor Deposition Process. *Nano Letters* **2010,** 10, (11), 4328-4334.

67. Eda, G.; Fanchini, G.; Chhowalla, M., Large-area ultrathin films of reduced graphene oxide as a transparent and flexible electronic material. *Nature Nanotechnology* **2008,** 3, (5), 270-274.

68. GoÌ • mez-Navarro, C.; Meyer, J. C.; Sundaram, R. S.; Chuvilin, A.; Kurasch, S.; Burghard, M.; Kern, K.; Kaiser, U., Atomic Structure of Reduced Graphene Oxide. *Nano Letters* **2010,** 10, (4), 1144-1148.

69. Jung, I.; Dikin, D. A.; Piner, R. D.; Ruoff, R. S., Tunable Electrical Conductivity of Individual Graphene Oxide Sheets Reduced at Ã¢â‚¬Å“LowÃ¢â‚¬Â • Temperatures. *Nano Letters* **2008,** 8, (12), 4283-4287.

70. Tung, V. C.; Allen, M. J.; Yang, Y.; Kaner, R. B., High-throughput solution processing of large-scale graphene. *Nat Nano* **2009,** 4, (1), 25-29.

71. Xu, C.; Wang, X.; Zhu, J.; Yang, X.; Lu, L., Deposition of Co3O4 nanoparticles onto exfoliated graphite oxide sheets. *Journal of Materials Chemistry* **2008,** 18, (46), 5625-5629.

72. Rao, C. N. R.; Biswas, K., Characterization of Nanomaterials by Physical Methods. *Annual Review of Analytical Chemistry* **2009,** 2, (1), 435-462.

73. Heide, P., *X-ray Photoelectron Spectroscopy: An Introduction to Principles and Practices*. John Wiley & Sons: 2011.

74. IR Spectrometer. https://www.thermo.com/eThermo/CMA/PDFs/Various/File_52263.pdf

75. Geim, A. K., Graphene: Status and Prospects. *Science* **2009,** 324, (5934), 1530-1534.

76. Rao, C. N. R.; Sood, A. K.; Subrahmanyam, K. S.; Govindaraj, A., Graphene: The New Two-Dimensional Nanomaterial. *Angewandte Chemie International Edition* **2009,** 48, (42), 7752-7777.

77. Ponomarenko, L. A.; Schedin, F.; Katsnelson, M. I.; Yang, R.; Hill, E. W.; Novoselov, K. S.; Geim, A. K., Chaotic Dirac Billiard in Graphene Quantum Dots. *Science* **2008,** 320, (5874), 356-358.

78. Novoselov, K. S.; Jiang, Z.; Zhang, Y.; Morozov, S. V.; Stormer, H. L.; Zeitler, U.; Maan, J. C.; Boebinger, G. S.; Kim, P.; Geim, A. K., Room-Temperature Quantum Hall Effect in Graphene. *Science* **2007,** 315, (5817), 1379.

79. Stankovich, S.; Dikin, D. A.; Dommett, G. H. B.; Kohlhaas, K. M.; Zimney, E. J.; Stach, E. A.; Piner, R. D.; Nguyen, S. T.; Ruoff, R. S., Graphene-based composite materials. *Nature* **2006,** 442, (7100), 282-286.

80. Hummers, W. S.; Offeman, R. E., Preparation of Graphitic Oxide. *Journal of the American Chemical Society* **1958,** 80, (6), 1339-1339.

81. Sasha Stankovich, R. D. P., Xinqi Chen, Nianqiang Wu, SonBinh T. Nguyen and Rodney S. Ruoff, Stable aqueous dispersions of graphitic nanoplatelets via the reduction of exfoliated graphite oxide in the presence of poly(sodium 4-styrenesulfonate). *J. Mater. Chem.* **2006,** 16, (2).

82. Stankovich, S.; Dikin, D. A.; Piner, R. D.; Kohlhaas, K. A.; Kleinhammes, A.; Jia, Y.; Wu, Y.; Nguyen, S. T.; Ruoff, R. S., Synthesis of graphene-based nanosheets via chemical reduction of exfoliated graphite oxide. *Carbon* **2007,** 45, (7), 1558-1565.

83. Muszynski, R.; Seger, B.; Kamat, P. V., Decorating Graphene Sheets with Gold Nanoparticles. *The Journal of Physical Chemistry C* **2008,** 112, (14), 5263-5266.

84. Li, X.; Wang, X.; Zhang, L.; Lee, S.; Dai, H., Chemically Derived, Ultrasmooth Graphene Nanoribbon Semiconductors. *Science* **2008,** 319, (5867), 1229-1232.

85. Li, X.; Zhang, G.; Bai, X.; Sun, X.; Wang, X.; Wang, E.; Dai, H., Highly conducting graphene sheets and Langmuir-Blodgett films. *Nat Nano* **2008,** 3, (9), 538-542.

86. Hernandez, Y.; Nicolosi, V.; Lotya, M.; Blighe, F. M.; Sun, Z.; De, S.; McGovern, I. T.; Holland, B.; Byrne, M.; Gun'Ko, Y. K.; Boland, J. J.; Niraj, P.; Duesberg, G.; Krishnamurthy, S.; Goodhue, R.; Hutchison, J.; Scardaci, V.; Ferrari, A. C.; Coleman, J. N., High-yield production of graphene by liquid-phase exfoliation of graphite. *Nat Nano* **2008,** 3, (9), 563-568.

87. Hassan M. A. Hassan, a. V. A., a Abd El Rahman S. Khder,a Khaled M. AbouZeid,a James Terner,a M. Samy El-Shall,*a Saud I. Al-Resayesb and Adel A. El-Azharyb, Microwave synthesis of graphene sheets supporting metal nanocrystals in aqueous and organic media†. *J. Mater. Chem.* **2009,** 19, 3832-3837.

88. JuaÌ • rez, B. H.; Meyns, M.; Chanaewa, A.; Cai, Y.; Klinke, C.; Weller, H., Carbon Supported CdSe Nanocrystals. *Journal of the American Chemical Society* **2008,** 130, (46), 15282-15284.

89. Seger, B.; Kamat, P. V., Electrocatalytically Active Graphene-Platinum Nanocomposites. Role of 2-D Carbon Support in PEM Fuel Cells. *The Journal of Physical Chemistry C* **2009,** 113, (19), 7990-7995.

90. Xu, C.; Wang, X.; Zhu, J., Grapheneâˆ'Metal Particle Nanocomposites. *The Journal of Physical Chemistry C* **2008,** 112, (50), 19841-19845.

91. Aoneng Cao, Z. L., Saisai Chu, Minghong Wu, Zhangmei Ye, A Facile One-step Method to Produce Graphene–CdS Quantum Dot Nanocomposites as Promising Optoelectronic Materials. *Adv. Mater.* **2010,** 22, (1).

92. GÃ³mez-Navarro, C.; Burghard, M.; Kern, K., Elastic Properties of Chemically Derived Single Graphene Sheets. *Nano Letters* **2008,** 8, (7), 2045-2049.

93. Luo, Z.; Somers, L. A.; Dan, Y.; Ly, T.; Kybert, N. J.; Mele, E. J.; Johnson, A. T. C., Size-Selective Nanoparticle Growth on Few-Layer Graphene Films. *Nano Letters* **2010,** 10, (3), 777-781.

94. Kamat, P. V., Graphene-Based Nanoarchitectures. Anchoring Semiconductor and Metal Nanoparticles on a Two-Dimensional Carbon Support. *The Journal of Physical Chemistry Letters* **2009,** 1, (2), 520-527.

95. Williams, G.; Kamat, P. V., Grapheneâ^'Semiconductor Nanocomposites: Excited-State Interactions between ZnO Nanoparticles and Graphene Oxideâ€ *Langmuir* **2009,** 25, (24), 13869-13873.

96. Chen, Z.; Berciaud, S.; Nuckolls, C.; Heinz, T. F.; Brus, L. E., Energy Transfer from Individual Semiconductor Nanocrystals to Graphene. *ACS Nano* **2010,** 4, (5), 2964-2968.

97. Murray, C. B.; Kagan, C. R.; Bawendi, M. G., SYNTHESIS AND CHARACTERIZATION OF MONODISPERSE NANOCRYSTALS AND CLOSE-PACKED NANOCRYSTAL ASSEMBLIES. *Annual Review of Materials Science* **2003,** 30, (1), 545-610.

98. Peng, X.; Manna, L.; Yang, W.; Wickham, J.; Scher, E.; Kadavanich, A.; Alivisatos, A. P., Shape control of CdSe nanocrystals. *Nature* **2000,** 404, (6773), 59-61.

99. Nirmal, M.; Brus, L., Luminescence Photophysics in Semiconductor Nanocrystals. *Accounts of Chemical Research* **1998,** 32, (5), 407-414.

100. Gur, I.; Fromer, N. A.; Geier, M. L.; Alivisatos, A. P., Air-Stable All-Inorganic Nanocrystal Solar Cells Processed from Solution. *Science* **2005,** 310, (5747), 462-465.

101. Farrow, B.; Kamat, P. V., CdSe Quantum Dot Sensitized Solar Cells. Shuttling Electrons Through Stacked Carbon Nanocups. *Journal of the American Chemical Society* **2009,** 131, (31), 11124-11131.

102. Lin, Y.; Zhang, K.; Chen, W.; Liu, Y.; Geng, Z.; Zeng, J.; Pan, N.; Yan, L.; Wang, X.; Hou, J. G., Dramatically Enhanced Photoresponse of Reduced Graphene Oxide with Linker-Free Anchored CdSe Nanoparticles. *ACS Nano* **2010,** 4, (6), 3033-3038.

103. Goncalves, G.; Marques, P. A. A. P.; Granadeiro, C. M.; Nogueira, H. I. S.; Singh, M. K.; GraÌ • cio, J., Surface Modification of Graphene Nanosheets with Gold Nanoparticles: The Role of Oxygen Moieties at Graphene Surface on Gold Nucleation and Growth. *Chemistry of Materials* **2009,** 21, (20), 4796-4802.

104. Park, S.; An, J.; Jung, I.; Piner, R. D.; An, S. J.; Li, X.; Velamakanni, A.; Ruoff, R. S., Colloidal Suspensions of Highly Reduced Graphene Oxide in a Wide Variety of Organic Solvents. *Nano Letters* **2009,** 9, (4), 1593-1597.

105. Abdelsayed, V.; Moussa, S.; Hassan, H. M.; Aluri, H. S.; Collinson, M. M.; El-Shall, M., Photothermal Deoxygenation of Graphite Oxide with Laser Excitation in Solution and Graphene-Aided Increase in Water Temperature. *The Journal of Physical Chemistry Letters* 1, (19), 2804-2809.

106. Kappe, C. O., Controlled Microwave Heating in Modern Organic Synthesis. *Angewandte Chemie International Edition* **2004,** 43, (46), 6250-6284.

107. Abdelsayed, V.; Aljarash, A.; El-Shall, M. S.; Al Othman, Z. A.; Alghamdi, A. H., Microwave Synthesis of Bimetallic Nanoalloys and CO Oxidation on Ceria-Supported Nanoalloys. *Chemistry of Materials* **2009,** 21, (13), 2825-2834.

108. Mohamed, M. B.; AbouZeid, K. M.; Abdelsayed, V.; Aljarash, A. A.; El-Shall, M. S., Growth Mechanism of Anisotropic Gold Nanocrystals via Microwave Synthesis: Formation of Dioleamide by Gold Nanocatalysis. *ACS Nano* 4, (5), 2766-2772.

109. Lerf, A.; He, H.; Forster, M.; Klinowski, J., Structure of Graphite Oxide Revisitedâ€–. *The Journal of Physical Chemistry B* **1998,** 102, (23), 4477-4482.

110. Gilje, S.; Han, S.; Wang, M.; Wang, K. L.; Kaner, R. B., A Chemical Route to Graphene for Device Applications. *Nano Letters* **2007,** 7, (11), 3394-3398.

111. Hirata, M.; Gotou, T.; Ohba, M., Thin-film particles of graphite oxide. 2: Preliminary studies for internal micro fabrication of single particle and carbonaceous electronic circuits. *Carbon* **2005,** 43, (3), 503-510.

112. Fan, X.; Peng, W.; Li, Y.; Li, X.; Wang, S.; Zhang, G.; Zhang, F., Deoxygenation of Exfoliated Graphite Oxide under Alkaline Conditions: A Green Route to Graphene Preparation. *Advanced Materials* **2008,** 20, (23), 4490-4493.

113. Zhou, Y.; Bao, Q.; Tang, L. A. L.; Zhong, Y.; Loh, K. P., Hydrothermal Dehydration for the Ã¢â‚¬Å“GreenÃ¢â‚¬Â• Reduction of Exfoliated Graphene Oxide to Graphene and Demonstration of Tunable Optical Limiting Properties. *Chemistry of Materials* **2009,** 21, (13), 2950-2956.

114. Bourlinos, A. B.; Gournis, D.; Petridis, D.; SzabÃ³, T. s.; Szeri, A.; DÃ©kÃ¡ny, I., Graphite Oxide:â€‰ Chemical Reduction to Graphite and Surface Modification with Primary Aliphatic Amines and Amino Acids. *Langmuir* **2003,** 19, (15), 6050-6055.

115. Paredes, J. I.; Villar-Rodil, S.; MartiÌ • nez-Alonso, A.; TascoÌ • n, J. M. D., Graphene Oxide Dispersions in Organic Solvents. *Langmuir* **2008,** 24, (19), 10560-10564.

116. Mohamed, M. B.; Tonti, D.; Al-Salman, A.; Chemseddine, A.; Chergui, M., Synthesis of High Quality Zinc Blende CdSe Nanocrystals. *The Journal of Physical Chemistry B* **2005,** 109, (21), 10533-10537.

117. Mahler, B. t.; Lequeux, N.; Dubertret, B. t., Ligand-Controlled Polytypism of Thick-Shell CdSe/CdS Nanocrystals. *Journal of the American Chemical Society* **2009,** 132, (3), 953-959.

118. Cullity, B., *Elements of X-Ray Diffraction*. 2nd ed.; Addison-Wesley, Redding: 1978.

119. Yu, W. W.; Qu, L.; Guo, W.; Peng, X., Experimental Determination of the Extinction Coefficient of CdTe, CdSe, and CdS Nanocrystals. *Chemistry of Materials* **2003,** 15, (14), 2854-2860.

120. Manna, L.; Scher, E. C.; Alivisatos, A. P., Shape Control of Colloidal Semiconductor Nanocrystals. *Journal of Cluster Science* **2002,** 13, (4), 521-532.

121. Talapin, D. V.; Rogach, A. L.; Kornowski, A.; Haase, M.; Weller, H., Highly Luminescent Monodisperse CdSe and CdSe/ZnS Nanocrystals Synthesized in a Hexadecylamineâˆ'Trioctylphosphine Oxideâˆ'Trioctylphospine Mixture. *Nano Letters* **2001,** 1, (4), 207-211.

122. Bullen, C. R.; Mulvaney, P., Nucleation and Growth Kinetics of CdSe Nanocrystals in Octadecene. *Nano Letters* **2004,** 4, (12), 2303-2307.

123. Park, J.; Joo, J.; Kwon, S. G.; Jang, Y.; Hyeon, T., Synthesis of Monodisperse Spherical Nanocrystals. *Angewandte Chemie International Edition* **2007,** 46, (25), 4630-4660.

124. Wang, D.; Yu, D.; Mo, M.; Liu, X.; Qian, Y., Preparation and characterization of wire-like Sb2Se3 and flake-like Bi2Se3 nanocrystals. *Journal of Crystal Growth* **2003,** 253, (1-4), 445-451.

125. Abdelsayed, V.; El-Shall, M. S., Vapor phase nucleation on neutral and charged nanoparticles: Condensation of supersaturated trifluoroethanol on Mg nanoparticles. *The Journal of Chemical Physics* **2007,** 126, (2), 024706-6.

126. Jiang, Z.-J.; Kelley, D. F., Role of Magic-Sized Clusters in the Synthesis of CdSe Nanorods. *ACS Nano* 4, (3), 1561-1572.

127. Blake, P.; Brimicombe, P. D.; Nair, R. R.; Booth, T. J.; Jiang, D.; Schedin, F.; Ponomarenko, L. A.; Morozov, S. V.; Gleeson, H. F.; Hill, E. W.; Geim, A. K.; Novoselov, K. S., Graphene-Based Liquid Crystal Device. *Nano Letters* **2008,** 8, (6), 1704-1708.

128. Abdelsayed, V.; Moussa, S.; Hassan, H. M.; Aluri, H. S.; Collinson, M. M.; El-Shall, M., Photothermal Deoxygenation of Graphite Oxide with Laser Excitation in Solution and Graphene-Aided Increase in Water Temperature. *The Journal of Physical Chemistry Letters* **2010,** 1, (19), 2804-2809.

129. Du, A.; Ng, Y. H.; Bell, N. J.; Zhu, Z.; Amal, R.; Smith, S. C., Hybrid Graphene/Titania Nanocomposite: Interface Charge Transfer, Hole Doping, and Sensitization for Visible Light Response. *The Journal of Physical Chemistry Letters* **2011,** 2, (8), 894-899.

130. Fan, W.; Lai, Q.; Zhang, Q.; Wang, Y., Nanocomposites of TiO2 and Reduced Graphene Oxide as Efficient Photocatalysts for Hydrogen Evolution. *The Journal of Physical Chemistry C* **2011,** 115, (21), 10694-10701.

131. Jia, L.; Wang, D.-H.; Huang, Y.-X.; Xu, A.-W.; Yu, H.-Q., Highly Durable N-Doped Graphene/CdS Nanocomposites with Enhanced Photocatalytic Hydrogen Evolution from Water under Visible Light Irradiation. *The Journal of Physical Chemistry C* **2011,** 115, (23), 11466-11473.

132. Moussa, S.; Atkinson, G.; SamyEl-Shall, M.; Shehata, A.; AbouZeid, K. M.; Mohamed, M. B., Laser assisted photocatalytic reduction of metal ions by graphene oxide. *Journal of Materials Chemistry* **2011**.

133. Siamaki, A. R.; Khder, A. E. R. S.; Abdelsayed, V.; El-Shall, M. S.; Gupton, B. F., Microwave-assisted synthesis of palladium nanoparticles supported on graphene: A highly active and recyclable catalyst for carbon-carbon cross-coupling reactions. *Journal of Catalysis* **2011,** 279, (1), 1-11.

134. Karakoti, A. S.; Kuchibhatla, S. V. N. T.; Babu, K. S.; Seal, S., Direct Synthesis of Nanoceria in Aqueous Polyhydroxyl Solutions. *The Journal of Physical Chemistry C* **2007,** 111, (46), 17232-17240.

135. Patsalas, P.; Logothetidis, S.; Sygellou, L.; Kennou, S., Structure-dependent electronic properties of nanocrystalline cerium oxide films. *Physical Review B* **2003,** 68, (3), 035104.

136. Li, C.; Sun, N.; Ni, J.; Wang, J.; Chu, H.; Zhou, H.; Li, M.; Li, Y., Controllable preparation and properties of composite materials based on ceria nanoparticles and carbon nanotubes. *Journal of Solid State Chemistry* **2008,** 181, (10), 2620-2625.

137. Andersson, D. A.; Simak, S. I.; Skorodumova, N. V.; Abrikosov, I. A.; Johansson, B. r., Optimization of ionic conductivity in doped ceria. *Proceedings of the National Academy of Sciences of the United States of America* **2006,** 103, (10), 3518-3521.

138. Glaspell, G.; Fuoco, L.; El-Shall, M. S., Microwave Synthesis of Supported Au and Pd Nanoparticle Catalysts for CO Oxidation. *The Journal of Physical Chemistry B* **2005,** 109, (37), 17350-17355.

139. Tsunekawa, S.; Fukuda, T.; Kasuya, A., Blue shift in ultraviolet absorption spectra of monodisperse CeO[sub 2 - x] nanoparticles. *Journal of Applied Physics* **2000,** 87, (3), 1318-1321.

140. S. Patil, S. C. K. a. S. S., Nanocrystalline Ceria Imparts Better High-Temperature Protection. *Proceedings: Mathematical, Physical and Engineering Sciences* **2004,** 460, (2052), 3569-3587

141. Zhang, F.; Wang, P.; Koberstein, J.; Khalid, S.; Chan, S.-W., Cerium oxidation state in ceria nanoparticles studied with X-ray photoelectron spectroscopy and absorption near edge spectroscopy. *Surface Science* **2004,** 563, (1-3), 74-82.

142. Asati, A.; Santra, S.; Kaittanis, C.; Nath, S.; Perez, J. M., Oxidase-Like Activity of Polymer-Coated Cerium Oxide Nanoparticles. *Angewandte Chemie International Edition* **2009,** 48, (13), 2308-2312.

143. Asati, A.; Kaittanis, C.; Santra, S.; Perez, J. M., pH-Tunable Oxidase-Like Activity of Cerium Oxide Nanoparticles Achieving Sensitive Fluorigenic Detection of Cancer Biomarkers at Neutral pH. *Analytical Chemistry* **2011,** 83, (7), 2547-2553.

144. Asati, A.; Santra, S.; Kaittanis, C.; Perez, J. M., Surface-Charge-Dependent Cell Localization and Cytotoxicity of Cerium Oxide Nanoparticles. *ACS Nano* **2010,** 4, (9), 5321-5331.

145. Doussier-Brochard, C.; Chavillon, B.; Cario, L.; Jobic, S. p., Synthesis of p-Type Transparent LaOCuS Nanoparticles via Soft Chemistry. *Inorganic Chemistry* **2010,** 49, (7), 3074-3076.

146. Kim, M. R.; Park, S.-Y.; Jang, D.-J., Composition Variation and Thermal Treatment of ZnxCd1âˆ’xS Alloy Nanoparticles to Exhibit Controlled and Efficient Luminescence. *The Journal of Physical Chemistry C* **2010,** 114, (14), 6452-6457.

147. Biswas, S.; Kar, S.; Santra, S.; Jompol, Y.; Arif, M.; Khondaker, S. I., Solvothermal Synthesis of High-Aspect Ratio Alloy Semiconductor Nanowires: Cd1âˆ’xZnxS, a Case Study. *The Journal of Physical Chemistry C* **2009,** 113, (9), 3617-3624.

148. Kar, S.; Patel, C.; Santra, S., Direct Room Temperature Synthesis of Valence State Engineered Ultra-Small Ceria Nanoparticles: Investigation on the Role of Ethylenediamine as a Capping Agent. *The Journal of Physical Chemistry C* **2009,** 113, (12), 4862-4867.

149. Goncalves, G.; Marques, P. A. A. P.; Granadeiro, C. M.; Nogueira, H. I. S.; Singh, M. K.; GraÃŒÂ • cio, J., Surface Modification of Graphene Nanosheets with Gold Nanoparticles: The Role of Oxygen Moieties at Graphene Surface on Gold Nucleation and Growth. *Chemistry of Materials* **2009,** 21, (20), 4796-4802.

150. Haruta, M., Nanoparticulate Gold Catalysts for Low-Temperature CO Oxidation. *J. New. Mat. Electrochem. Systems* **2004,** 7, (3), 163-172.

151. Costello, C. K.; Yang, J. H.; Law, H. Y.; Wang, Y.; Lin, J. N.; Marks, L. D.; Kung, M. C.; Kung, H. H., On the potential role of hydroxyl groups in CO oxidation over Au/Al2O3. *Applied Catalysis A: General* **2003,** 243, (1), 15-24.

152. Haruta, M., Catalysis of Gold Nanoparticles Deposited on Metal Oxides. *CATTECH* **2002,** 6, (3), 102-115.

153. Chen, Y.-J.; Yeh, C.-t., Deposition of Highly Dispersed Gold on Alumina Support. *Journal of Catalysis* **2001,** 200, (1), 59-68.

154. Haruta, M., Novel catalysis of gold deposited on metal oxides. *Catalysis Surveys from Japan* **1997,** 1, (1), 61-73-73.

155. Oh, H. S.; Yang, J. H.; Costello, C. K.; Wang, Y. M.; Bare, S. R.; Kung, H. H.; Kung, M. C., Selective Catalytic Oxidation of CO: Effect of Chloride on Supported Au Catalysts. *Journal of Catalysis* **2002,** 210, (2), 375-386.

156. Lin, C.-H.; Lin, S. D.; Lee, J.-F., Chlorine Residue in the Au/γ-Al₂O₃ Prepared by AuCl₃ Impregnation—an EXAFS Analysis. *Catalysis Letters* **2003,** 89, (3), 235-242.

157. Kung, M. C.; Davis, R. J.; Kung, H. H., Understanding Au-Catalyzed Low-Temperature CO Oxidation. *The Journal of Physical Chemistry C* **2007,** 111, (32), 11767-11775.

158. Luo, D.; Zhang, G.; Liu, J.; Sun, X., Evaluation Criteria for Reduced Graphene Oxide. *The Journal of Physical Chemistry C* **2011,** 115, (23), 11327-11335.

159. Shang, N.; Papakonstantinou, P.; Wang, P.; Zakharov, A.; Palnitkar, U.; Lin, I. N.; Chu, M.; Stamboulis, A., Self-Assembled Growth, Microstructure, and Field-Emission High-Performance of Ultrathin Diamond Nanorods. *ACS Nano* **2009,** 3, (4), 1032-1038.

160. Mazali, I. O.; Viana, B. C.; Alves, O. L.; Mendes Filho, J.; Souza Filho, A. G., Structural and vibrational properties of CeO2 nanocrystals. *Journal of Physics and Chemistry of Solids* **2007,** 68, (4), 622-627.

161. Zhong, L.-S.; Hu, J.-S.; Cao, A.-M.; Liu, Q.; Song, W.-G.; Wan, L.-J., 3D Flowerlike Ceria Micro/Nanocomposite Structure and Its Application for Water Treatment and CO Removal. *Chemistry of Materials* **2007,** 19, (7), 1648-1655.

162. Sutradhar, N.; Sinhamahapatra, A.; Pahari, S.; Jayachandran, M.; Subramanian, B.; Bajaj, H. C.; Panda, A. B., Facile Low-Temperature Synthesis of Ceria and Samarium-Doped Ceria Nanoparticles and Catalytic Allylic Oxidation of Cyclohexene. *The Journal of Physical Chemistry C* **2011,** 115, (15), 7628-7637.

163. Calla, J. T.; Bore, M. T.; Datye, A. K.; Davis, R. J., Effect of alumina and titania on the oxidation of CO over Au nanoparticles evaluated by 13C isotopic transient analysis. *Journal of Catalysis* **2006,** 238, (2), 458-467.

164. Taniguchi, T.; Watanabe, T.; Sugiyama, N.; Subramani, A. K.; Wagata, H.; Matsushita, N.; Yoshimura, M., Identifying Defects in Ceria-Based Nanocrystals by UV Resonance Raman Spectroscopy. *The Journal of Physical Chemistry C* **2009,** 113, (46), 19789-19793.

165. Zhang, F.; Chan, S.-W.; Spanier, J. E.; Apak, E.; Jin, Q.; Robinson, R. D.; Herman, I. P., Cerium oxide nanoparticles: Size-selective formation and structure analysis. *Applied Physics Letters* **2002,** 80, (1), 127-129.

166. Mazali, I. O.; Filho, A. G.; Viana, B. C.; Filho, J.; Alves, O. L., Size-controllable synthesis of nanosized-TiO₂ anatase using porous Vycor glass as template. *Journal of Nanoparticle Research* **2006,** 8, (1), 141-148.

167. CorreÌ‚a, D. N.; de Souza e Silva, J. M.; Santos, E. B.; Sigoli, F. A.; Souza Filho, A. G.; Mazali, I. O., TiO2- and CeO2-Based Biphasic Coreâ€“Shell Nanoparticles with Tunable Core Sizes and Shell Thicknesses. *The Journal of Physical Chemistry C* **2011,** 115, (21), 10380-10387.

168. Spanier, J. E.; Robinson, R. D.; Zhang, F.; Chan, S.-W.; Herman, I. P., Size-dependent properties of CeO2-y nanoparticles as studied by Raman scattering. *Physical Review B* **2001,** 64, (24), 245407.

169. Suresh, B.; et al., Dopant-mediated oxygen vacancy tuning in ceria nanoparticles. *Nanotechnology* **2009,** 20, (8), 085713.

170. Wang, X.; Rodriguez, J. A.; Hanson, J. C.; Gamarra, D.; MartÃ-nez-Arias, A.; FernÃ¡ndez-GarcÃ-a, M., Unusual Physical and Chemical Properties of Cu in Ce1-xCuxO2 Oxides. *The Journal of Physical Chemistry B* **2005,** 109, (42), 19595-19603.

171. Yeung, C. M. Y.; Tsang, S. C., Noble Metal Coreâˆ'Ceria Shell Catalysts For Waterâˆ'Gas Shift Reaction. *The Journal of Physical Chemistry C* **2009,** 113, (15), 6074-6087.

172. Deng, W.; Flytzani-Stephanopoulos, M., On the Issue of the Deactivation of Au–Ceria and Pt–Ceria Water–Gas Shift Catalysts in Practical Fuel-Cell Applications. *Angewandte Chemie* **2006,** 118, (14), 2343-2347.

173. Deng, W.; Flytzani-Stephanopoulos, M., On the Issue of the Deactivation of Au–Ceria and Pt–Ceria Water–Gas Shift Catalysts in Practical Fuel-Cell Applications. *Angewandte Chemie International Edition* **2006,** 45, (14), 2285-2289.

174. Shelef, M.; McCabe, R. W., Twenty-five years after introduction of automotive catalysts: what next? *Catalysis Today* **2000,** 62, (1), 35-50.

175. Ligthart, D. A. J. M.; van Santen, R. A.; Hensen, E. J. M., Supported Rhodium Oxide Nanoparticles as Highly Active CO Oxidation Catalysts. *Angewandte Chemie International Edition* **2011,** 50, (23), 5306-5310.

176. Glaspell, G.; Hassan; Elzatahry, A.; Fuoco, L.; Radwan, N. R. E.; El-Shall, M. S., Nanocatalysis on Tailored Shape Supports:â€‰ Au and Pd Nanoparticles Supported on MgO Nanocubes and ZnO Nanobelts. *The Journal of Physical Chemistry B* **2006,** 110, (43), 21387-21393.

177. Hashmi, A. S. K.; Hutchings, G. J., Gold Catalysis. *Angewandte Chemie International Edition* **2006,** 45, (47), 7896-7936.

178. Hickey, N.; Arneodo Larochette, P.; Gentilini, C.; Sordelli, L.; Olivi, L.; Polizzi, S.; Montini, T.; Fornasiero, P.; Pasquato, L.; Graziani, M., Monolayer Protected Gold Nanoparticles on Ceria for an Efficient CO Oxidation Catalyst. *Chemistry of Materials* **2007,** 19, (4), 650-651.

179. Nolan, M.; Verdugo, V. S.; Metiu, H., Vacancy formation and CO adsorption on gold-doped ceria surfaces. *Surface Science* **2008,** 602, (16), 2734-2742.

180. Minato, T.; Susaki, T.; Shiraki, S.; Kato, H. S.; Kawai, M.; Aika, K.-i., Investigation of the electronic interaction between TiO2(1 1 0) surfaces and Au clusters by PES and STM. *Surface Science* **2004,** 566-568, (Part 2), 1012-1017.

181. Xu, Y.; Mavrikakis, M., Adsorption and Dissociation of O2 on Gold Surfaces:â€‰ Effect of Steps and Strain. *The Journal of Physical Chemistry B* **2003,** 107, (35), 9298-9307.

182. Esch, F.; Fabris, S.; Zhou, L.; Montini, T.; Africh, C.; Fornasiero, P.; Comelli, G.; Rosei, R., Electron Localization Determines Defect Formation on Ceria Substrates. *Science* **2005,** 309, (5735), 752-755.

183. Lu, J. L.; Gao, H. J.; Shaikhutdinov, S.; Freund, H. J., Gold supported on well-ordered ceria films: nucleation, growth and morphology in CO oxidation reaction. *Catalysis Letters* **2007,** 114, (1), 8-16.

184. Liu, Z.-P.; Jenkins, S. J.; King, D. A., Origin and Activity of Oxidized Gold in Water-Gas-Shift Catalysis. *Physical Review Letters* **2005,** 94, (19), 196102.

185. Hammer, B.; Norskov, J. K., Why gold is the noblest of all the metals. *Nature* **1995,** 376, (6537), 238-240.

186. Burda, C.; Chen, X.; Narayanan, R.; El-Sayed, M. A., Chemistry and Properties of Nanocrystals of Different Shapes. *Chemical Reviews* **2005,** 105, (4), 1025-1102.

187. Yoon, B.; HÃ¤kkinen, H.; Landman, U.; WÃ¶rz, A. S.; Antonietti, J.-M.; Abbet, S. p.; Judai, K.; Heiz, U., Charging Effects on Bonding and Catalyzed Oxidation of CO on Au8 Clusters on MgO. *Science* **2005,** 307, (5708), 403-407.

188. Fierro-Gonzalez, J. C.; Gates, B. C., Catalysis by gold dispersed on supports: the importance of cationic gold. *Chemical Society Reviews* **2008,** 37, (9), 2127-2134.

189. Lopez, N.; Janssens, T. V. W.; Clausen, B. S.; Xu, Y.; Mavrikakis, M.; Bligaard, T.; Nørskov, J. K., On the origin of the catalytic activity of gold nanoparticles for low-temperature CO oxidation. *Journal of Catalysis* **2004,** 223, (1), 232-235.

190. Gottfried, J. M.; Schmidt, K. J.; Schroeder, S. L. M.; Christmann, K., Adsorption of carbon monoxide on Au(1 1 0)-(1 × 2). *Surface Science* **2003,** 536, (1-3), 206-224.

191. Yoon, B.; HÃ¤kkinen, H.; Landman, U., Interaction of O2 with Gold Clusters:â€‰ Molecular and Dissociative Adsorption. *The Journal of Physical Chemistry A* **2003,** 107, (20), 4066-4071.

192. Mills, G.; Gordon, M. S.; Metiu, H., The adsorption of molecular oxygen on neutral and negative Aun clusters (n=2-5). *Chemical Physics Letters* **2002,** 359, (5-6), 493-499.

193. Weststrate, C. J.; Resta, A.; Westerstrom, R.; Lundgren, E.; Mikkelsen, A.; Andersen, J. N., CO Adsorption on a Au/CeO2 (111) Model Catalyst. *The Journal of Physical Chemistry C* **2008,** 112, (17), 6900-6906.

194. Shang, C.; Liu, Z.-P., Is Transition Metal Oxide a Must? Moisture-Assisted Oxygen Activation in CO Oxidation on Gold/Î³-Aluminaâ€ *The Journal of Physical Chemistry C* 114, (40), 16989-16995.

195. Guzman, J.; Gates, B. C., A mononuclear gold complex catalyst supported on MgO: spectroscopic characterization during ethylene hydrogenation catalysis. *Journal of Catalysis* **2004,** 226, (1), 111-119.

196. Zanella, R.; Delannoy, L.; Louis, C., Mechanism of deposition of gold precursors onto TiO2 during the preparation by cation adsorption and deposition-precipitation with NaOH and urea. *Applied Catalysis A: General* **2005,** 291, (1-2), 62-72.

197. Cargnello, M.; Gentilini, C.; Montini, T.; Fonda, E.; Mehraeen, S.; Chi, M.; Herrera-Collado, M.; Browning, N. D.; Polizzi, S.; Pasquato, L.; Fornasiero, P., Active and Stable Embedded Au@CeO2 Catalysts for Preferential Oxidation of CO. *Chemistry of Materials* **2010,** 22, (14), 4335-4345.

198. HernaÌ • ndez, W. Y.; Romero-Sarria, F.; Centeno, M. A.; Odriozola, J. A., In Situ Characterization of the Dynamic Goldâ^'Support Interaction over Ceria Modified Eu3+. Influence of the Oxygen Vacancies on the CO Oxidation Reaction. *The Journal of Physical Chemistry C* **2010,** 114, (24), 10857-10865.

199. Huang, P. X.; Wu, F.; Zhu, B. L.; Gao, X. P.; Zhu, H. Y.; Yan, T. Y.; Huang, W. P.; Wu, S. H.; Song, D. Y., CeO2 Nanorods and Gold Nanocrystals Supported on CeO2 Nanorods as Catalyst. *The Journal of Physical Chemistry B* **2005,** 109, (41), 19169-19174.

200. Yuan, Z.-Y.; Idakiev, V.; Vantomme, A.; Tabakova, T.; Ren, T.-Z.; Su, B.-L., Mesoporous and nanostructured CeO2 as supports of nano-sized gold catalysts for low-temperature water-gas shift reaction. *Catalysis Today* **2008,** 131, (1-4), 203-210.

201. Venezia, A. M.; Pantaleo, G.; Longo, A.; Di Carlo, G.; Casaletto, M. P.; Liotta, F. L.; Deganello, G., Relationship between Structure and CO Oxidation Activity of Ceria-Supported Gold Catalysts. *The Journal of Physical Chemistry B* **2005,** 109, (7), 2821-2827.

202. Sun, C.; Li, H.; Chen, L., Study of flowerlike CeO2 microspheres used as catalyst supports for CO oxidation reaction. *Journal of Physics and Chemistry of Solids* **2007,** 68, (9), 1785-1790.

203. Carrettin, S.; Concepción, P.; Corma, A.; López Nieto, J. M.; Puntes, V. F., Nanocrystalline CeO2 Increases the Activity of Au for CO Oxidation by Two Orders of Magnitude. *Angewandte Chemie International Edition* **2004,** 43, (19), 2538-2540.

204. Wang, D.; Ma, Z.; Dai, S.; Liu, J.; Nie, Z.; Engelhard, M. H.; Huo, Q.; Wang, C.; Kou, R., Low-Temperature Synthesis of Tunable Mesoporous Crystalline Transition Metal Oxides and Applications as Au Catalyst Supports. *The Journal of Physical Chemistry C* **2008,** 112, (35), 13499-13509.

205. Yang, Y.; Saoud, K. M.; Abdelsayed, V.; Glaspell, G.; Deevi, S.; El-Shall, M. S., Vapor phase synthesis of supported Pd, Au, and unsupported bimetallic nanoparticle catalysts for CO oxidation. *Catalysis Communications* **2006,** 7, (5), 281-284.

206. Han, M.; Wang, X.; Shen, Y.; Tang, C.; Li, G.; Smith, R. L., Preparation of Highly Active, Low Au-Loaded, Au/CeO2 Nanoparticle Catalysts That Promote CO Oxidation at Ambient Temperatures. *The Journal of Physical Chemistry C* **2009,** 114, (2), 793-798.

207. Mendes, D.; Garcia, H.; Silva, V. B.; Mendes, A. l.; Madeira, L. M., Comparison of Nanosized Gold-Based and Copper-Based Catalysts for the Low-Temperature Waterâ˚'Gas Shift Reaction. *Industrial & Engineering Chemistry Research* **2008,** 48, (1), 430-439.

208. Cao, C.-Y.; Cui, Z.-M.; Chen, C.-Q.; Song, W.-G.; Cai, W., Ceria Hollow Nanospheres Produced by a Template-Free Microwave-Assisted Hydrothermal Method for Heavy Metal Ion Removal and Catalysis. *The Journal of Physical Chemistry C* **2010,** 114, (21), 9865-9870.

209. Ma, T.-Y.; Cao, J.-L.; Shao, G.-S.; Zhang, X.-J.; Yuan, Z.-Y., Hierarchically Structured Squama-like Cerium-Doped Titania: Synthesis, Photoactivity, and Catalytic CO Oxidation. *The Journal of Physical Chemistry C* **2009,** 113, (38), 16658-16667.

210. Li, Q.; Zhang, Y.; Chen, G.; Fan, J.; Lan, H.; Yang, Y., Ultra-low-gold loading Au/CeO2 catalysts for ambient temperature CO oxidation: Effect of preparation conditions on surface composition and activity. *Journal of Catalysis* **2010,** 273, (2), 167-176.

211. Carabineiro, S. A. C.; Silva, A. M. T.; Drazic, G.; Tavares, P. B.; Figueiredo, J. L., Gold nanoparticles on ceria supports for the oxidation of carbon monoxide. *Catalysis Today* **2010,** 154, (1-2), 21-30.

212. Carabineiro, S. A. C.; Bastos, S. S. T.; Órfão, J. J. M.; Pereira, M. F. R.; Delgado, J. J.; Figueiredo, J. L., Exotemplated ceria catalysts with gold for CO oxidation. *Applied Catalysis A: General* **2010,** 381, (1-2), 150-160.

213. Niu, F.; Zhang, D.; Shi, L.; He, X.; Li, H.; Mai, H.; Yan, T., Facile synthesis, characterization and low-temperature catalytic performance of Au/CeO2 nanorods. *Materials Letters* **2009,** 63, (24–25), 2132-2135.

214. Tana; Wang, F.; Li, H.; Shen, W., Influence of Au particle size on Au/CeO2 catalysts for CO oxidation. *Catalysis Today* **2011,** 175, (1), 541-545.

215. Sanchez-Dominguez, M.; Liotta, L. F.; Di Carlo, G.; Pantaleo, G.; Venezia, A. M.; Solans, C.; Boutonnet, M., Synthesis of CeO2, ZrO2, Ce0.5Zr0.5O2, and TiO2 nanoparticles by a novel oil-in-water microemulsion reaction method and their use as catalyst support for CO oxidation. *Catalysis Today* **2010,** 158, (1-2), 35-43.

216. Dobrosz-Gómez, I.; Kocemba, I.; Rynkowski, J. M., Au/Ce1-xZrxO2 as effective catalysts for low-temperature CO oxidation. *Applied Catalysis B: Environmental* **2008,** 83, (3-4), 240-255.

217. Chen, Z.; Gao, Q., Enhanced carbon monoxide oxidation activity over gold-ceria nanocomposites. *Applied Catalysis B: Environmental* **2008,** 84, (3-4), 790-796.

218. Zou, X.; Xu, J.; Qi, S.; Suo, Z.; An, L.; Li, F., Effects of preparation conditions of Au/FeOx/Al2O3 catalysts prepared by a modified two-step method on the stability for CO oxidation. *Journal of Natural Gas Chemistry* 20, (1), 41-47.

219. Huang, X.; Neretina, S.; El-Sayed, M. A., Gold Nanorods: From Synthesis and Properties to Biological and Biomedical Applications. *Advanced Materials* **2009,** 21, (48), 4880-4910.

220. Eustis, S.; El-Sayed, M. A., Why gold nanoparticles are more precious than pretty gold: Noble metal surface plasmon resonance and its enhancement of the radiative and nonradiative properties of nanocrystals of different shapes. *Chemical Society Reviews* **2006,** 35, (3), 209-217.

221. Murphy, C. J.; Thompson, L. B.; Alkilany, A. M.; Sisco, P. N.; Boulos, S. P.; Sivapalan, S. T.; Yang, J. A.; Chernak, D. J.; Huang, J., The Many Faces of Gold Nanorods. *The Journal of Physical Chemistry Letters* **2010,** 1, (19), 2867-2875.

222. Jain, P. K.; Huang, X.; El-Sayed, I. H.; El-Sayed, M. A., Noble Metals on the Nanoscale: Optical and Photothermal Properties and Some Applications in Imaging, Sensing, Biology, and Medicine. *Accounts of Chemical Research* **2008,** 41, (12), 1578-1586.

223. Ringe, E.; Langille, M. R.; Sohn, K.; Zhang, J.; Huang, J.; Mirkin, C. A.; Van Duyne, R. P.; Marks, L. D., Plasmon Length: A Universal Parameter to Describe Size Effects in Gold Nanoparticles. *The Journal of Physical Chemistry Letters* **2012,** 3, (11), 1479-1483.

224. Link, S.; El-Sayed, M. A., Size and Temperature Dependence of the Plasmon Absorption of Colloidal Gold Nanoparticles. *The Journal of Physical Chemistry B* **1999,** 103, (21), 4212-4217.

225. Chou, C.-H.; Chen, C.-D.; Wang, C. R. C., Highly Efficient, Wavelength-Tunable, Gold Nanoparticle Based Optothermal Nanoconvertors. *The Journal of Physical Chemistry B* **2005,** 109, (22), 11135-11138.

226. Huang, X.; Jain, P.; El-Sayed, I.; El-Sayed, M., Plasmonic photothermal therapy (PPTT) using gold nanoparticles. *Lasers in Medical Science* **2008,** 23, (3), 217-228.

227. Gobin, A. M.; Lee, M. H.; Halas, N. J.; James, W. D.; Drezek, R. A.; West, J. L., Near-Infrared Resonant Nanoshells for Combined Optical Imaging and Photothermal Cancer Therapy. *Nano Letters* **2007,** 7, (7), 1929-1934.

228. Tong, L.; Wei, Q.; Wei, A.; Cheng, J.-X., Gold Nanorods as Contrast Agents for Biological Imaging: Optical Properties, Surface Conjugation and Photothermal Effects†. *Photochemistry and Photobiology* **2009,** 85, (1), 21-32.

229. Hirsch, L. R.; Stafford, R. J.; Bankson, J. A.; Sershen, S. R.; Rivera, B.; Price, R. E.; Hazle, J. D.; Halas, N. J.; West, J. L., Nanoshell-mediated near-infrared thermal therapy of tumors under magnetic resonance guidance. *Proceedings of the National Academy of Sciences* **2003,** 100, (23), 13549-13554.

230. Zhang, J. Z., Biomedical Applications of Shape-Controlled Plasmonic Nanostructures: A Case Study of Hollow Gold Nanospheres for Photothermal Ablation Therapy of Cancer. *The Journal of Physical Chemistry Letters* **2010,** 1, (4), 686-695.

231. Kamat, P. V., Photophysical, Photochemical and Photocatalytic Aspects of Metal Nanoparticles. *The Journal of Physical Chemistry B* **2002,** 106, (32), 7729-7744.

232. Raschke, G.; Brogl, S.; Susha, A. S.; Rogach, A. L.; Klar, T. A.; Feldmann, J.; Fieres, B.; Petkov, N.; Bein, T.; Nichtl, A.; Kürzinger, K., Gold Nanoshells Improve Single Nanoparticle Molecular Sensors. *Nano Letters* **2004,** 4, (10), 1853-1857.

233. Schwartzberg, A. M.; Zhang, J. Z., Novel Optical Properties and Emerging Applications of Metal Nanostructures†. *The Journal of Physical Chemistry C* **2008,** 112, (28), 10323-10337.

234. Kam, N. W. S.; O'Connell, M.; Wisdom, J. A.; Dai, H., Carbon nanotubes as multifunctional biological transporters and near-infrared agents for selective cancer cell destruction. *Proceedings of the National Academy of Sciences of the United States of America* **2005,** 102, (33), 11600-11605.

235. Chakravarty, P.; Marches, R.; Zimmerman, N. S.; Swafford, A. D. E.; Bajaj, P.; Musselman, I. H.; Pantano, P.; Draper, R. K.; Vitetta, E. S., Thermal ablation of tumor cells with antibody-functionalized single-walled carbon nanotubes. *Proceedings of the National Academy of Sciences* **2008**.

236. Zhou, F.; Xing, D.; Ou, Z.; Wu, B.; Resasco, D. E.; Chen, W. R., Cancer photothermal therapy in the near-infrared region by using single-walled carbon nanotubes. *Journal of Biomedical Optics* **2009,** 14, (2), 021009-021009.

237. Ghosh, S.; Dutta, S.; Gomes, E.; Carroll, D.; D'Agostino, R.; Olson, J.; Guthold, M.; Gmeiner, W. H., Increased Heating Efficiency and Selective Thermal Ablation of Malignant Tissue with DNA-Encased Multiwalled Carbon Nanotubes. *ACS Nano* **2009,** 3, (9), 2667-2673.

238. Liu, Z.; Robinson, J. T.; Sun, X.; Dai, H., PEGylated Nanographene Oxide for Delivery of Water-Insoluble Cancer Drugs. *Journal of the American Chemical Society* **2008,** 130, (33), 10876-10877.

239. Yang, K.; Zhang, S.; Zhang, G.; Sun, X.; Lee, S.-T.; Liu, Z., Graphene in Mice: Ultrahigh In Vivo Tumor Uptake and Efficient Photothermal Therapy. *Nano Letters* **2010,** 10, (9), 3318-3323.

240. Robinson, J. T.; Tabakman, S. M.; Liang, Y.; Wang, H.; Sanchez Casalongue, H.; Vinh, D.; Dai, H., Ultrasmall Reduced Graphene Oxide with High Near-Infrared Absorbance for Photothermal Therapy. *Journal of the American Chemical Society* **2011,** 133, (17), 6825-6831.

241. Takami, A.; Kurita, H.; Koda, S., Laser-Induced Size Reduction of Noble Metal Particles. *The Journal of Physical Chemistry B* **1999,** 103, (8), 1226-1232.

242. Inasawa, S.; Sugiyama, M.; Yamaguchi, Y., Bimodal Size Distribution of Gold Nanoparticles under Picosecond Laser Pulses. *The Journal of Physical Chemistry B* **2005,** 109, (19), 9404-9410.

243. Yamada, K.; Tokumoto, Y.; Nagata, T.; Mafuné, F., Mechanism of Laser-induced Size-reduction of Gold Nanoparticles as Studied by Nanosecond Transient Absorption Spectroscopy. *The Journal of Physical Chemistry B* **2006,** 110, (24), 11751-11756.

244. Muto, H.; Miyajima, K.; Mafune, F., Mechanism of Laser-Induced Size Reduction of Gold Nanoparticles As Studied by Single and Double Laser Pulse Excitation. *The Journal of Physical Chemistry C* **2008,** 112, (15), 5810-5815.

245. Pyatenko, A.; Yamaguchi, M.; Suzuki, M., Mechanisms of Size Reduction of Colloidal Silver and Gold Nanoparticles Irradiated by Nd:YAG Laser. *The Journal of Physical Chemistry C* **2009,** 113, (21), 9078-9085.

246. Werner, D.; Hashimoto, S.; Uwada, T., Remarkable Photothermal Effect of Interband Excitation on Nanosecond Laser-Induced Reshaping and Size Reduction of Pseudospherical Gold Nanoparticles in Aqueous Solution. *Langmuir* **2010,** 26, (12), 9956-9963.

247. EnÃ¼stÃ¼n, B. V.; Turkevich, J., Coagulation of Colloidal Gold. *Journal of the American Chemical Society* **1963,** 85, (21), 3317-3328.

248. Gole, A.; Murphy, C. J., Seed-Mediated Synthesis of Gold Nanorods:â€‰ Role of the Size and Nature of the Seed. *Chemistry of Materials* **2004,** 16, (19), 3633-3640.

249. Sau, T. K.; Murphy, C. J., Seeded High Yield Synthesis of Short Au Nanorods in Aqueous Solution. *Langmuir* **2004,** 20, (15), 6414-6420.

250. Murphy, C. J.; Sau, T. K.; Gole, A. M.; Orendorff, C. J.; Gao, J.; Gou, L.; Hunyadi, S. E.; Li, T., Anisotropic Metal Nanoparticles:â€‰ Synthesis, Assembly, and Optical Applications. *The Journal of Physical Chemistry B* **2005,** 109, (29), 13857-13870.

251. Kim, F.; Song, J. H.; Yang, P., Photochemical Synthesis of Gold Nanorods. *Journal of the American Chemical Society* **2002,** 124, (48), 14316-14317.

252. Yu; Chang, S.-S.; Lee, C.-L.; Wang, C. R. C., Gold Nanorods:â€‰ Electrochemical Synthesis and Optical Properties. *The Journal of Physical Chemistry B* **1997,** 101, (34), 6661-6664.

253. Jana, N. R.; Gearheart, L.; Murphy, C. J., Seed-Mediated Growth Approach for Shape-Controlled Synthesis of Spheroidal and Rod-like Gold Nanoparticles Using a Surfactant Template. *Advanced Materials* **2001,** 13, (18), 1389-1393.

254. Kou, X.; Zhang, S.; Tsung, C.-K.; Yeung, M. H.; Shi, Q.; Stucky, G. D.; Sun, L.; Wang, J.; Yan, C., Growth of Gold Nanorods and Bipyramids Using CTEAB Surfactant. *The Journal of Physical Chemistry B* **2006,** 110, (33), 16377-16383.

255. Liu; Guyot-Sionnest, P., Mechanism of Silver(I)-Assisted Growth of Gold Nanorods and Bipyramids. *The Journal of Physical Chemistry B* **2005,** 109, (47), 22192-22200.

256. Nikoobakht, B.; El-Sayed, M. A., Preparation and Growth Mechanism of Gold Nanorods (NRs) Using Seed-Mediated Growth Method. *Chemistry of Materials* **2003,** 15, (10), 1957-1962.

257. Stone, J.; Jackson, S.; Wright, D., Biological applications of gold nanorods. *Wiley Interdisciplinary Reviews: Nanomedicine and Nanobiotechnology* 3, (1), 100-109.

258. Sau, T. K.; Murphy, C. J., Room Temperature, High-Yield Synthesis of Multiple Shapes of Gold Nanoparticles in Aqueous Solution. *Journal of the American Chemical Society* **2004,** 126, (28), 8648-8649.

259. Link, S.; Mohamed, M. B.; El-Sayed, M. A., Simulation of the Optical Absorption Spectra of Gold Nanorods as a Function of Their Aspect Ratio and the Effect of the Medium Dielectric Constant. *The Journal of Physical Chemistry B* **1999,** 103, (16), 3073-3077.

260. Mohamed, M. B.; AbouZeid, K. M.; Abdelsayed, V.; Aljarash, A. A.; El-Shall, M. S., Growth Mechanism of Anisotropic Gold Nanocrystals via Microwave Synthesis: Formation of Dioleamide by Gold Nanocatalysis. *ACS Nano* **2010,** 4, (5), 2766-2772.

261. Varnavski, O.; Ramakrishna, G.; Kim, J.; Lee, D.; Goodson, T., Critical Size for the Observation of Quantum Confinement in Optically Excited Gold Clusters. *Journal of the American Chemical Society* **2009,** 132, (1), 16-17.

262. Pérez-Juste, J.; Pastoriza-Santos, I.; Liz-Marzán, L. M.; Mulvaney, P., Gold nanorods: Synthesis, characterization and applications. *Coordination Chemistry Reviews* **2005,** 249, (17-18), 1870-1901.

263. Meyer, J. C.; Kisielowski, C.; Erni, R.; Rossell, M. D.; Crommie, M. F.; Zettl, A., Direct Imaging of Lattice Atoms and Topological Defects in Graphene Membranes. *Nano Letters* **2008,** 8, (11), 3582-3586.

264. Girit, Ç. Ö.; Meyer, J. C.; Erni, R.; Rossell, M. D.; Kisielowski, C.; Yang, L.; Park, C.-H.; Crommie, M. F.; Cohen, M. L.; Louie, S. G.; Zettl, A., Graphene at the Edge: Stability and Dynamics. *Science* **2009,** 323, (5922), 1705-1708.

265. Bagri, A.; Mattevi, C.; Acik, M.; Chabal, Y. J.; Chhowalla, M.; Shenoy, V. B., Structural evolution during the reduction of chemically derived graphene oxide. *Nat Chem* **2010,** 2, (7), 581-587.

266. Kim, G.; Jhi, S.-H., Carbon Monoxide-Tolerant Platinum Nanoparticle Catalysts on Defect-Engineered Graphene. *ACS Nano* **2011,** 5, (2), 805-810.

267. Matsumoto, Y.; Koinuma, M.; Ida, S.; Hayami, S.; Taniguchi, T.; Hatakeyama, K.; Tateishi, H.; Watanabe, Y.; Amano, S., Photoreaction of Graphene Oxide Nanosheets in Water. *The Journal of Physical Chemistry C* **2011,** 115, (39), 19280-19286.

268. Moussa, S.; Siamaki, A. R.; Gupton, B. F.; El-Shall, M. S., Pd-Partially Reduced Graphene Oxide Catalysts (Pd/PRGO): Laser Synthesis of Pd Nanoparticles Supported on PRGO Nanosheets for Carbon–Carbon Cross Coupling Reactions. *ACS Catalysis* **2011,** 2, (1), 145-154.

269. Liu, L.; Ryu, S.; Tomasik, M. R.; Stolyarova, E.; Jung, N.; Hybertsen, M. S.; Steigerwald, M. L.; Brus, L. E.; Flynn, G. W., Graphene Oxidation: Thickness-Dependent Etching and Strong Chemical Doping. *Nano Letters* **2008,** 8, (7), 1965-1970.

270. Ferrari, A. C., Raman spectroscopy of graphene and graphite: Disorder, electron-phonon coupling, doping and nonadiabatic effects. *Solid State Communications* **2007,** 143, (1-2), 47-57.

271. Cançado, L. G.; Jorio, A.; Ferreira, E. H. M.; Stavale, F.; Achete, C. A.; Capaz, R. B.; Moutinho, M. V. O.; Lombardo, A.; Kulmala, T. S.; Ferrari, A. C., Quantifying Defects in Graphene via Raman Spectroscopy at Different Excitation Energies. *Nano Letters* **2011,** 11, (8), 3190-3196.

272. Subrahmanyam, K. S.; Manna, A. K.; Pati, S. K.; Rao, C. N. R., A study of graphene decorated with metal nanoparticles. *Chemical Physics Letters* **2010,** 497, (1–3), 70-75.

273. Lee, Y. H.; Polavarapu, L.; Gao, N.; Yuan, P.; Xu, Q.-H., Enhanced Optical Properties of Graphene Oxide–Au Nanocrystal Composites. *Langmuir* **2011,** 28, (1), 321-326.

274. Jain, P. K.; Lee, K. S.; El-Sayed, I. H.; El-Sayed, M. A., Calculated Absorption and Scattering Properties of Gold Nanoparticles of Different Size, Shape, and Composition:â€‰ Applications in Biological Imaging and Biomedicine. *The Journal of Physical Chemistry B* **2006,** 110, (14), 7238-7248.

275. Sönnichsen, C.; Franzl, T.; Wilk, T.; von Plessen, G.; Feldmann, J.; Wilson, O.; Mulvaney, P., Drastic Reduction of Plasmon Damping in Gold Nanorods. *Physical Review Letters* **2002,** 88, (7), 077402.

276. Wang, X.; Wang, C.; Cheng, L.; Lee, S.-T.; Liu, Z., Noble Metal Coated Single-Walled Carbon Nanotubes for Applications in Surface Enhanced Raman Scattering Imaging and Photothermal Therapy. *Journal of the American Chemical Society* **2012,** 134, (17), 7414-7422.

277. Jin, L.; Yang, K.; Yao, K.; Zhang, S.; Tao, H.; Lee, S.-T.; Liu, Z.; Peng, R., Functionalized Graphene Oxide in Enzyme Engineering: A Selective Modulator for Enzyme Activity and Thermostability. *ACS Nano* **2012,** 6, (6), 4864-4875.

278. Liu, Q.; Wei, L.; Wang, J.; Peng, F.; Luo, D.; Cui, R.; Niu, Y.; Qin, X.; Liu, Y.; Sun, H.; Yang, J.; Li, Y., Cell imaging by graphene oxide based on surface enhanced Raman scattering. *Nanoscale* **2012,** 4, (22), 7084-7089.

279. Liu, Z.; Hu, C.; Li, S.; Zhang, W.; Guo, Z., Rapid Intracellular Growth of Gold Nanostructures Assisted by Functionalized Graphene Oxide and Its Application for Surface-Enhanced Raman Spectroscopy. *Analytical Chemistry* **2012**.

280. Ma, X.; Tao, H.; Yang, K.; Feng, L.; Cheng, L.; Shi, X.; Li, Y.; Guo, L.; Liu, Z., A functionalized graphene oxide-iron oxide nanocomposite for magnetically targeted drug delivery, photothermal therapy, and magnetic resonance imaging. *Nano Research* **2012,** 5, (3), 199-212.

281. Mu, Q.; Su, G.; Li, L.; Gilbertson, B. O.; Yu, L. H.; Zhang, Q.; Sun, Y.-P.; Yan, B., Size-Dependent Cell Uptake of Protein-Coated Graphene Oxide Nanosheets. *ACS Applied Materials & Interfaces* **2012,** 4, (4), 2259-2266.

282. Shen, H.; Liu, M.; He, H.; Zhang, L.; Huang, J.; Chong, Y.; Dai, J.; Zhang, Z., PEGylated Graphene Oxide-Mediated Protein Delivery for Cell Function Regulation. *ACS Applied Materials & Interfaces* **2012**.

283. Vila, M.; Portolés, M. T.; Marques, P. A. A. P.; Feito, M. J.; Matesanz, M. C.; Ramírez-Santillán, C.; Gonçalves, G.; Cruz, S. M. A.; Nieto, A.; Vallet-Regi, M., Cell uptake survey of pegylated nanographene oxide. *Nanotechnology* **2012,** 23, (46), 465103.

284. Yue, H.; Wei, W.; Yue, Z.; Wang, B.; Luo, N.; Gao, Y.; Ma, D.; Ma, G.; Su, Z., The role of the lateral dimension of graphene oxide in the regulation of cellular responses. *Biomaterials* **2012,** 33, (16), 4013-4021.

285. Zhou, X.; Zhang, Y.; Wang, C.; Wu, X.; Yang, Y.; Zheng, B.; Wu, H.; Guo, S.; Zhang, J., Photo-Fenton Reaction of Graphene Oxide: A New Strategy to Prepare Graphene Quantum Dots for DNA Cleavage. *ACS Nano* **2012,** 6, (8), 6592-6599.

286. Yang, K.; Hu, L.; Ma, X.; Ye, S.; Cheng, L.; Shi, X.; Li, C.; Li, Y.; Liu, Z., Multimodal Imaging Guided Photothermal Therapy using Functionalized Graphene Nanosheets Anchored with Magnetic Nanoparticles. *Advanced Materials* **2012,** 24, (14), 1868-1872.

287. Akhavan, O.; Ghaderi, E.; Emamy, H., Nontoxic concentrations of PEGylated graphene nanoribbons for selective cancer cell imaging and photothermal therapy. *Journal of Materials Chemistry* **2012,** 22, (38), 20626-20633.

288. Khlebtsov, B. N.; Panfilova, E. V.; Terentyuk, G. S.; Maksimova, I. L.; Ivanov, A. V.; Khlebtsov, N. G., Plasmonic Nanopowders for Photothermal Therapy of Tumors. *Langmuir* **2012,** 28, (24), 8994-9002.

289. Cheng, L.; Yang, K.; Chen, Q.; Liu, Z., Organic Stealth Nanoparticles for Highly Effective in Vivo Near-Infrared Photothermal Therapy of Cancer. *ACS Nano* **2012,** 6, (6), 5605-5613.

290. Liu, X.; Tao, H.; Yang, K.; Zhang, S.; Lee, S.-T.; Liu, Z., Optimization of surface chemistry on single-walled carbon nanotubes for in vivo photothermal ablation of tumors. *Biomaterials* **2011,** 32, (1), 144-151.

291. Wu, X.; Ming, T.; Wang, X.; Wang, P.; Wang, J.; Chen, J., High-Photoluminescence-Yield Gold Nanocubes: For Cell Imaging and Photothermal Therapy. *ACS Nano* **2009,** 4, (1), 113-120.

292. Jang, B.; Park, J.-Y.; Tung, C.-H.; Kim, I.-H.; Choi, Y., Gold Nanorodâˆ’Photosensitizer Complex for Near-Infrared Fluorescence Imaging and Photodynamic/Photothermal Therapy In Vivo. *ACS Nano* **2011,** 5, (2), 1086-1094.

293. Huang, X.; El-Sayed, I. H.; Qian, W.; El-Sayed, M. A., Cancer Cell Imaging and Photothermal Therapy in the Near-Infrared Region by Using Gold Nanorods. *Journal of the American Chemical Society* **2006,** 128, (6), 2115-2120.

294. Gu, H.; Yang, Z.; Gao, J.; Chang, C. K.; Xu, B., Heterodimers of Nanoparticles: Formation at a Liquidâˆ’Liquid Interface and Particle-Specific Surface Modification by Functional Molecules. *Journal of the American Chemical Society* **2004,** 127, (1), 34-35.

295. Gu, H.; Zheng, R.; Zhang, X.; Xu, B., Facile One-Pot Synthesis of Bifunctional Heterodimers of Nanoparticles: A Conjugate of Quantum Dot and Magnetic Nanoparticles. *Journal of the American Chemical Society* **2004,** 126, (18), 5664-5665.

296. Kwon, K.-W.; Shim, M., Î³-Fe2O3/IIâˆ’VI Sulfide Nanocrystal Heterojunctions. *Journal of the American Chemical Society* **2005,** 127, (29), 10269-10275.

297. Gui Huan Du1, Z., 3, QiangHua Lu1, Xing Xia1, LiHui Jia1, Kai Lun Yao1, Qian Chu2 and SuMing Zhang2, Fe3O4/CdSe/ZnS magnetic fluorescent bifunctional nanocomposites. *Nanotechnology* **2006,** 17, 2850-2854.

298. Gao, J.; Zhang, B.; Gao, Y.; Pan, Y.; Zhang, X.; Xu, B., Fluorescent Magnetic Nanocrystals by Sequential Addition of Reagents in a One-Pot Reaction: A Simple Preparation for Multifunctional Nanostructures. *Journal of the American Chemical Society* **2007,** 129, (39), 11928-11935.

299. Gao, J.; Zhang, W.; Huang, P.; Zhang, B.; Zhang, X.; Xu, B., Intracellular Spatial Control of Fluorescent Magnetic Nanoparticles. *Journal of the American Chemical Society* **2008,** 130, (12), 3710-3711.

300. Liu, B.; Xie, W.; Wang, D.; Huang, W.; Yu, M.; Yao, A., Preparation and characterization of magnetic luminescent nanocomposite particles. *Materials Letters* **2008,** 62, (17â€“18), 3014-3017.

301. Liu, X.; Hu, Q.; Zhang, X.; Fang, Z.; Wang, Q., Generalized and Facile Synthesis of Fe3O4/MS (M = Zn, Cd, Hg, Pb, Co, and Ni) Nanocomposites. *The Journal of Physical Chemistry C* **2008,** 112, (33), 12728-12735.

302. Marco Zanella, A. F., Stefan Kudera, Liberato Manna, Maria F. Casula and Wolfgang J. Parak, Growth of colloidal nanoparticles of group II–VI and IV–VI semiconductors on top of magnetic iron–platinum nanocrystals. *J. Mater. Chem.* **2008,** 18.

303. Beaulac, R. m.; Schneider, L.; Archer, P. I.; Bacher, G.; Gamelin, D. R., Light-Induced Spontaneous Magnetization in Doped Colloidal Quantum Dots. *Science* **2009,** 325, (5943), 973-976.

304. Deka, S.; Falqui, A.; Bertoni, G.; Sangregorio, C.; Poneti, G.; Morello, G.; Giorgi, M. D.; Giannini, C.; Cingolani, R.; Manna, L.; Cozzoli, P. D., Fluorescent Asymmetrically Cobalt-Tipped CdSe@CdS Core@Shell Nanorod Heterostructures Exhibiting Room-Temperature Ferromagnetic Behavior. *Journal of the American Chemical Society* **2009,** 131, (35), 12817-12828.

305. Fan, L.-Y.; Yu, S.-H., ZnO@Co hybrid nanotube arrays growth from electrochemical deposition: structural, optical, photocatalytic and magnetic properties. *Physical Chemistry Chemical Physics* **2009,** 11, (19), 3710-3717.

306. Jin, Y.; Gao, X., Plasmonic fluorescent quantum dots. *Nat Nano* **2009,** 4, (9), 571-576.

307. Tao, K.; Zhou, H.; Dou, H.; Xing, B.; Li, W.; Sun, K., Direct Deposition of Fluorescent Emission-Tunable CdSe on Magnetite Nanocrystals. *The Journal of Physical Chemistry C* **2009,** 113, (20), 8762-8766.

308. Wang, L.; Wei, H.; Fan, Y.; Gu, X.; Zhan, J., One-Dimensional CdS/Î±-Fe2O3 and CdS/Fe3O4 Heterostructures: Epitaxial and Nonepitaxial Growth and Photocatalytic Activity. *The Journal of Physical Chemistry C* **2009,** 113, (32), 14119-14125.

309. Chiu, W.; Khiew, P.; Cloke, M.; Isa, D.; Lim, H.; Tan, T.; Huang, N.; Radiman, S.; Abd-Shukor, R.; Hamid, M. A. A.; Chia, C., Heterogeneous Seeded Growth: Synthesis and Characterization of Bifunctional Fe3O4/ZnO Core/Shell Nanocrystals. *The Journal of Physical Chemistry C* **2010,** 114, (18), 8212-8218.

310. Lee, J.-S.; Bodnarchuk, M. I.; Shevchenko, E. V.; Talapin, D. V., â€œMagnet-in-the-Semiconductorâ€□ FePtâˆ’PbS and FePtâˆ’PbSe Nanostructures: Magnetic Properties, Charge Transport, and Magnetoresistance. *Journal of the American Chemical Society* **2010,** 132, (18), 6382-6391.

311. Lu, W.; Shen, Y.; Xie, A.; Zhang, X.; Chang, W., Novel Bifuncitonal One-Dimensional Fe3O4/Se Nanocomposites via Facile Green Synthesis. *The Journal of Physical Chemistry C* **2010,** 114, (11), 4846-4851.

312. Sun, P.; Zhang, H.; Liu, C.; Fang, J.; Wang, M.; Chen, J.; Zhang, J.; Mao, C.; Xu, S., Preparation and Characterization of Fe3O4/CdTe Magnetic/Fluorescent Nanocomposites and Their Applications in Immuno-Labeling and Fluorescent Imaging of Cancer Cells. *Langmuir* **2010,** 26, (2), 1278-1284.

313. Xu, Y.; Karmakar, A.; Wang, D.; Mahmood, M. W.; Watanabe, F.; Zhang, Y.; Fejleh, A.; Fejleh, P.; Li, Z.; Kannarpady, G.; Ali, S.; Biris, A. R.; Biris, A. S., Multifunctional Fe3O4 Cored Magnetic-Quantum Dot Fluorescent Nanocomposites for RF Nanohyperthermia of Cancer Cells. *The Journal of Physical Chemistry C* **2010,** 114, (11), 5020-5026.

314. Zhou, T.; Lu, M.; Zhang, Z.; Gong, H.; Chin, W. S.; Liu, B., Synthesis and Characterization of Multifunctional FePt/ZnO Core/Shell Nanoparticles. *Advanced Materials* **2010,** 22, (3), 403-406.

315. Jang, Y.; Chung, J.; Kim, S.; Jun, S. W.; Kim, B. H.; Lee, D. W.; Kim, B. M.; Hyeon, T., Simple synthesis of Pd-Fe3O4 heterodimer nanocrystals and their application as a magnetically recyclable catalyst for Suzuki cross-coupling reactions. *Physical Chemistry Chemical Physics* **2011,** 13, (7), 2512-2516.

316. Wu, H.; Chen, O.; Zhuang, J.; Lynch, J.; LaMontagne, D.; Nagaoka, Y.; Cao, Y. C., Formation of Heterodimer Nanocrystals: UO2/In2O3 and FePt/In2O3. *Journal of the American Chemical Society* **2011,** 133, (36), 14327-14337.

317. Kim, H.; Achermann, M.; Balet, L. P.; Hollingsworth, J. A.; Klimov, V. I., Synthesis and Characterization of Co/CdSe Core/Shell Nanocomposites: Bifunctional Magnetic-Optical Nanocrystals. *Journal of the American Chemical Society* **2004,** 127, (2), 544-546.

318. Suchita Kalele1, S. W. G., J. Urban2 and S. K. Kulkarni1,*, Nanoshell particles: synthesis, properties and applications. *CURRENT SCIENCE* **2006,** 91, (8).

319. Sen, T.; Sebastianelli, A.; Bruce, I. J., Mesoporous Silicaâ^'Magnetite Nanocomposite:â€‰ Fabrication and Applications in Magnetic Bioseparations. *Journal of the American Chemical Society* **2006,** 128, (22), 7130-7131.

320. Yang, H.-H.; Zhang, S.-Q.; Chen, X.-L.; Zhuang, Z.-X.; Xu, J.-G.; Wang, X.-R., Magnetite-Containing Spherical Silica Nanoparticles for Biocatalysis and Bioseparations. *Analytical Chemistry* **2004,** 76, (5), 1316-1321.

321. Shi, W.; Zeng, H.; Sahoo, Y.; Ohulchanskyy, T. Y.; Ding, Y.; Wang, Z. L.; Swihart, M.; Prasad, P. N., A General Approach to Binary and Ternary Hybrid Nanocrystals. *Nano Letters* **2006,** 6, (4), 875-881.

322. Mokari, T.; Sztrum, C. G.; Salant, A.; Rabani, E.; Banin, U., Formation of asymmetric one-sided metal-tipped semiconductor nanocrystal dots and rods. *Nat Mater* **2005,** 4, (11), 855-863.

323. Panda, A. B.; Glaspell, G.; El-Shall, M. S., Microwave Synthesis of Highly Aligned Ultra Narrow Semiconductor Rods and Wires. *Journal of the American Chemical Society* **2006,** 128, (9), 2790-2791.

324. Herring, N. P.; AbouZeid, K.; Mohamed, M. B.; Pinsk, J.; El-Shall, M. S., Formation Mechanisms of Goldâ€“Zinc Oxide Hexagonal Nanopyramids by Heterogeneous Nucleation using Microwave Synthesis. *Langmuir* **2011,** 27, (24), 15146-15154.

325. Salado, J.; Insausti, M.; Lezama, L.; Gil de Muro, I.; Goikolea, E.; Rojo, T. f., Preparation and Characterization of Monodisperse Fe3O4 Nanoparticles: An Electron Magnetic Resonance Study. *Chemistry of Materials* **2011,** 23, (11), 2879-2885.

326. Mahmoudi, M.; Sahraian, M. A.; Shokrgozar, M. A.; Laurent, S., Superparamagnetic Iron Oxide Nanoparticles: Promises for Diagnosis and Treatment of Multiple Sclerosis. *ACS Chemical Neuroscience* 2, (3), 118-140.

327. Sun, S.; Zeng, H., Size-Controlled Synthesis of Magnetite Nanoparticles. *Journal of the American Chemical Society* **2002,** 124, (28), 8204-8205.

328. Moussa, S.; Atkinson, G.; SamyEl-Shall, M.; Shehata, A.; AbouZeid, K. M.; Mohamed, M. B., Laser assisted photocatalytic reduction of metal ions by graphene oxide. *Journal of Materials Chemistry*.

329. Zhang, Y.; Tang, Z.-R.; Fu, X.; Xu, Y.-J., TiO2âˆ'Graphene Nanocomposites for Gas-Phase Photocatalytic Degradation of Volatile Aromatic Pollutant: Is TiO2âˆ'Graphene Truly Different from Other TiO2âˆ'Carbon Composite Materials? *ACS Nano* 4, (12), 7303-7314.

330. Siamaki, A. R.; Khder, A. E. R. S.; Abdelsayed, V.; El-Shall, M. S.; Gupton, B. F., Microwave-assisted synthesis of palladium nanoparticles supported on graphene: A highly active and recyclable catalyst for carbon-carbon cross-coupling reactions. *Journal of Catalysis* 279, (1), 1-11.

331. Izadi-Najafabadi, A.; Yamada, T.; Futaba, D. N.; Yudasaka, M.; Takagi, H.; Hatori, H.; Iijima, S.; Hata, K., High-Power Supercapacitor Electrodes from Single-Walled Carbon Nanohorn/Nanotube Composite. *ACS Nano* **2011,** 5, (2), 811-819.

332. Lin, Y.; Baggett, D. W.; Kim, J.-W.; Siochi, E. J.; Connell, J. W., Instantaneous Formation of Metal and Metal Oxide Nanoparticles on Carbon Nanotubes and Graphene via Solvent-Free Microwave Heating. *ACS Applied Materials & Interfaces* 3, (5), 1652-1664.

333. Cong, H.-P.; He, J.-J.; Lu, Y.; Yu, S.-H., Water-Soluble Magnetic-Functionalized Reduced Graphene Oxide Sheets: In situ Synthesis and Magnetic Resonance Imaging Applications. *Small* 6, (2), 169-173.

334. Chandra, V.; Park, J.; Chun, Y.; Lee, J. W.; Hwang, I.-C.; Kim, K. S., Water-Dispersible Magnetite-Reduced Graphene Oxide Composites for Arsenic Removal. *ACS Nano* 4, (7), 3979-3986.

335. Lee, J.-K.; Gwinner, M. C.; Berger, R.; Newby, C.; Zentel, R.; Friend, R. H.; Sirringhaus, H.; Ober, C. K., High-Performance Electron-Transporting Polymers Derived from a Heteroaryl Bis(trifluoroborate). *Journal of the American Chemical Society* **2011,** 133, (26), 9949-9951.

336. Yang, X.; Zhang, X.; Ma, Y.; Huang, Y.; Wang, Y.; Chen, Y., Superparamagnetic graphene oxide-Fe3O4 nanoparticles hybrid for controlled targeted drug carriers. *Journal of Materials Chemistry* **2009,** 19, (18), 2710-2714.

337. Liang, J.; Xu, Y.; Sui, D.; Zhang, L.; Huang, Y.; Ma, Y.; Li, F.; Chen, Y., Flexible, Magnetic, and Electrically Conductive Graphene/Fe3O4 Paper and Its Application for Magnetic-Controlled Switches. *The Journal of Physical Chemistry C* 114, (41), 17465-17471.

338. Yang, J.; Fang, H.-H.; Ding, R.; Lu, S.-Y.; Zhang, Y.-L.; Chen, Q.-D.; Sun, H.-B., High-Quality Large-Size Organic Crystals Prepared by Improved Physical Vapor Growth Technique and Their Optical Gain Properties. *The Journal of Physical Chemistry C* **2011,** 115, (18), 9171-9175.

339. Zhou, G.-W.; Wang, J.; Gao, P.; Yang, X.; He, Y.-S.; Liao, X.-Z.; Yang, J.; Ma, Z.-F., Facile Spray Drying Route for the Three-Dimensional Graphene-Encapsulated Fe2O3 Nanoparticles for Lithium Ion Battery Anodes. *Industrial & Engineering Chemistry Research* **2012,** 52, (3), 1197-1204.

340. Sun, S.; Zeng, H.; Robinson, D. B.; Raoux, S.; Rice, P. M.; Wang, S. X.; Li, G., Monodisperse MFe2O4 (M = Fe, Co, Mn) Nanoparticles. *Journal of the American Chemical Society* **2003,** 126, (1), 273-279.

341. Shavel, A.; Rodríguez-González, B.; Pacifico, J.; Spasova, M.; Farle, M.; Liz-Marzán, L. M., Shape Control in Iron Oxide Nanocrystal Synthesis, Induced by Trioctylammonium Ions. *Chemistry of Materials* **2009,** 21, (7), 1326-1332.

342. Wang, X.; Zhao, Z.; Qu, J.; Wang, Z.; Qiu, J., Shape-Control and Characterization of Magnetite Prepared via a One-Step Solvothermal Route. *Crystal Growth & Design* **2010,** 10, (7), 2863-2869.

343. Li, X.; Si, Z.; Lei, Y.; Tang, J.; Wang, S.; Su, S.; Song, S.; Zhao, L.; Zhang, H., Direct hydrothermal synthesis of single-crystalline triangular Fe3O4 nanoprisms. *CrystEngComm* **2010,** 12, (7), 2060-2063.

344. Ye, Q.-L.; Kozuka, Y.; Yoshikawa, H.; Awaga, K.; Bandow, S.; Iijima, S., Effects of the unique shape of submicron magnetite hollow spheres on magnetic properties and domain states. *Physical Review B* **2007,** 75, (22), 224404.

345. Chalasani, R.; Vasudevan, S., Form, Content, and Magnetism in Iron Oxide Nanocrystals. *The Journal of Physical Chemistry C* **2011,** 115, (37), 18088-18093.

346. Ho, C.-H.; Tsai, C.-P.; Chung, C.-C.; Tsai, C.-Y.; Chen, F.-R.; Lin, H.-J.; Lai, C.-H., Shape-Controlled Growth and Shape-Dependent Cation Site Occupancy of Monodisperse Fe3O4 Nanoparticles. *Chemistry of Materials* **2011,** 23, (7), 1753-1760.

347. Hwang, S. O.; Kim, C. H.; Myung, Y.; Park, S.-H.; Park, J.; Kim, J.; Han, C.-S.; Kim, J.-Y., Synthesis of Vertically Aligned Manganese-Doped Fe3O4 Nanowire Arrays and Their Excellent Room-Temperature Gas Sensing Ability. *The Journal of Physical Chemistry C* **2008,** 112, (36), 13911-13916.

348. Gao, G.; Liu, X.; Shi, R.; Zhou, K.; Shi, Y.; Ma, R.; Takayama-Muromachi, E.; Qiu, G., Shape-Controlled Synthesis and Magnetic Properties of Monodisperse Fe3O4 Nanocubes. *Crystal Growth & Design* **2010,** 10, (7), 2888-2894.

349. Li, L.; Yang, Y.; Ding, J.; Xue, J., Synthesis of Magnetite Nanooctahedra and Their Magnetic Field-Induced Two-/Three-Dimensional Superstructure. *Chemistry of Materials* **2010,** 22, (10), 3183-3191.

350. Chen, Y.-J.; Zhang, F.; Zhao, G.-g.; Fang, X.-y.; Jin, H.-B.; Gao, P.; Zhu, C.-L.; Cao, M.-S.; Xiao, G., Synthesis, Multi-Nonlinear Dielectric Resonance, and Excellent Electromagnetic

Absorption Characteristics of Fe3O4/ZnO Core/Shell Nanorods. *The Journal of Physical Chemistry C* **2010,** 114, (20), 9239-9244.

351. Shen, J.; Hu, Y.; Shi, M.; Li, N.; Ma, H.; Ye, M., One Step Synthesis of Graphene Oxideâ^'Magnetic Nanoparticle Composite. *The Journal of Physical Chemistry C* 114, (3), 1498-1503.

352. Wang, H.; Robinson, J. T.; Diankov, G.; Dai, H., Nanocrystal Growth on Graphene with Various Degrees of Oxidation. *Journal of the American Chemical Society* **2010,** 132, (10), 3270-3271.

353. Jeong, U.; Teng, X.; Wang, Y.; Yang, H.; Xia, Y., Superparamagnetic Colloids: Controlled Synthesis and Niche Applications. *Advanced Materials* **2007,** 19, (1), 33-60.

354. Peng, S.; Wang, C.; Xie, J.; Sun, S., Synthesis and Stabilization of Monodisperse Fe Nanoparticles. *Journal of the American Chemical Society* **2006,** 128, (33), 10676-10677.

355. Wang, C.; Hou, Y.; Kim, J.; Sun, S., A General Strategy for Synthesizing FePt Nanowires and Nanorods. *Angewandte Chemie International Edition* **2007,** 46, (33), 6333-6335.

356. Li, B.; Cao, H.; Shao, J.; Li, G.; Qu, M.; Yin, G., Co3O4@graphene Composites as Anode Materials for High-Performance Lithium Ion Batteries. *Inorganic chemistry* 50, (5), 1628-1632.

357. Manna, L.; Scher, E. C.; Alivisatos, A. P., Synthesis of Soluble and Processable Rod-, Arrow-, Teardrop-, and Tetrapod-Shaped CdSe Nanocrystals. *Journal of the American Chemical Society* **2000,** 122, (51), 12700-12706.

358. Si, R.; Zhang, Y.-W.; You, L.-P.; Yan, C.-H., Rare-Earth Oxide Nanopolyhedra, Nanoplates, and Nanodisks. *Angewandte Chemie International Edition* **2005,** 44, (21), 3256-3260.

359. Liu, Z.; Wang, J.; Xie, D.; Chen, G., Polyaniline-Coated Fe3O4 Nanoparticle–Carbon-Nanotube Composite and its Application in Electrochemical Biosensing. *Small* **2008,** 4, (4), 462-466.

360. He, H.; Gao, C., Supraparamagnetic, Conductive, and Processable Multifunctional Graphene Nanosheets Coated with High-Density Fe3O4 Nanoparticles. *ACS Applied Materials & Interfaces* **2010,** 2, (11), 3201-3210.

361. Morales, M. P.; Serna, C. J.; Bødker, F.; Mørup, S., Spin canting due to structural disorder in maghemite. *Journal of Physics: Condensed Matter* **1997,** 9, (25), 5461.